

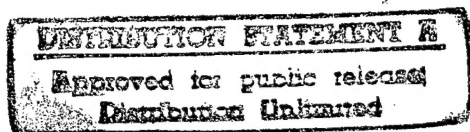
JPRS-JST-90-014

9 MARCH 1990



**FOREIGN
BROADCAST
INFORMATION
SERVICE**

JPRS Report



19980129 107

Science & Technology

Japan

6TH JAPAN-KOREA CERAMICS SEMINAR

REPRODUCED BY
U.S. DEPARTMENT OF COMMERCE
NATIONAL TECHNICAL INFORMATION SERVICE
SPRINGFIELD, VA. 22161

[DMC QUALITY INSPECTED 3]

22161

SPRINGFIELD, VA
5285 PORT ROYAL RD
ATTN: PROCESS 103
NTIS

45
22161

JPRS-JST-90-014

9 MARCH 1990

SCIENCE & TECHNOLOGY
JAPAN
6TH JAPAN-KOREA CERAMICS SEMINAR

43070721 Osaka PROCEEDINGS OF THE 6TH JAPAN-KOREA SEMINAR ON
CERAMICS in English 6-7 Dec 89 pp 7-490

[Selected papers presented at the 6th Japan-Korea Seminar on
Ceramics, held 6-7 Dec 89 in Osaka and sponsored by the Organizing
Committee of the 6th Japan-Korea Seminar on Ceramics]

CONTENTS

Agenda.....	1
Effect of SiO ₂ on Grain Growth and Densification of Alumina Prepared by SOL-Gel Technique [Hai-Doo Kim, Hwan-Kyu Kang].....	15
The Interfacial Segregation of Mg and Ca During Sintering of Alumina [S. Baik, J. H. Moon].....	23
In-Situ Observation of Structural Changes of Y-TZP by X-Ray Diffraction [Y. Kitano, Y. Mori, et al.].....	28
Microstructure Control and Thermoelectric Characteristics of Porous SiC Ceramics [K. Koumto, C. H. Pai, et al.].....	34
Mechanical Properties and Fatigue of Piezoelectric Ceramics [T. Tanimoto, T. Yamamoto, et al.].....	39
Direct Preparation of BaTiO ₃ Powders and Thin Films From Titanium Metal by Hydrothermal-Electrochemical Method [Seung-Eul Yoo, Nobuo Ishizawa, et al.].....	44

Growth of Superconducting Oxide Single Crystals by TSFZ Method [H. Kojima, I Tanaka].....	50
Preparation of Bi-Oxide High Tc Superconducting Cuprates in the Form of Ceramics and Thin Films [Tomoji Kawai, Masaki Kanai, et al.].....	55
Hot-Pressing and Superconducting Properties of Bi-Pb-Sr-Ca-Cu-O Ceramics [Norimitsu Murayama, Senzo Kuwabara, et al.].....	61
Preparation of Superconducting Whiskers of Bi System and Their Electrical Properties [Ichiro Matsubara, Hideo Tanigawa, et al.].....	66
Direct Preparation of Porous Silica Glasses by the Sol-Gel Method [H, Kozuka, J. Yamaguchi, et al.].....	70
Preparation of B ₂ O ₃ -SiO ₂ and Al ₂ O ₃ -SiO ₂ Coating Films by the Sol-Gel Method [Byung-Hoon Kim, Seok-Jin Choi, et al.].....	74
Crystallization of BaTiO ₃ Based Dielectric Glass Ceramics [H, S. Kim, U. Kang].....	79
Effect of Modifiers on the Structures and Hydroxyapatite [Cheol Y. Kim, Hopil Lee].....	86
Dispersion-Flocculation Behaviors of Mullite Slip and Their Effects on the Microstructures of Green Casts [Ki G. Lee, Han N. Cheong, et al.].....	91
Synthesis of Al ₂ O ₃ -Coated TiO ₂ and Al ₂ O ₃ -Coated Cr ₂ O ₃ Composite Powder by Homogeneous Precipitation Method [Byung-Kwan Kim, Itaru Yasui].....	97
Formation and Some Properties of Needle-Like Mullite From Kaolin Minerals [Hiroaki Katsuki].....	102
Effects of Attitives and Atmosphere on Morphology and Growth of Silicon Carbide Whiskers [Thae-Khapp Kang, Soon-Dong Park, et al.].....	108
Metallization of Alumina Ceramics by Electroless Plating [S. G. Kang, B. S. Jeon, et al.].....	113
Microstructure and Phase Transformation of Plasma-Sprayed ZrO ₂ -Y ₂ O ₃ Thermal Barrier Coatings [Dong-Soo Shur].....	118
Cutting Tool of SiC Whisker/Al ₂ O ₃ Composite [Kazuo Ueno, Tsutomu Yamamoto, et al.].....	124

Development and Application of High Thermal Conductivity AlN Substrates [Y. Kurokawa, Y. Shimada, et al.].....	130
Superconducting Ceramic Artificial Superstructured Films [Kenji Kawaguchi, Mitsugu Sohma, et al.].....	136
Microstructure and Properties of Hot-Worked $\text{YBa}_2\text{Cu}_3\text{O}_{7-x}$ Superconducting Wire [J. T. Song, H. J. Chang, et al.].....	142
Properties of Carbon Ceramic Composite Made by Pressureless Sintering [Yoshio Takashima, Ichitaro Ogawa, et al.].....	147
The Grain-Growth Behavior and Mechanical Properties of Al_2O_3 -TiC Composite [H. S. Song, Y. H. You].....	152
Sintering Behavior and α/β Transformation of Si_3N_4 in Si_3N_4 - ZrO_2 Composite [Chong Hee Kim, Jae Ryong Kim, et al.].....	159
Properties of Al_2O_3 -15v/o ZrO_2 (+3m/o Y_2O_3) Ceramics Prepared by a Precipitation Method [Hong Lim Lee, Gi Gon Hong].....	169
Preparation of Al_2O_3 and Si_3N_4 Ceramics by Low Pressure Injection Molding Method [K. Miyamoto, Y. Takahashi, et al.].....	175
Synthesis of β -Sialon From Porous Glass and Properties of Its Sintered Body [Byong-Ho Kim, Gun-Hun Lee, et al.].....	181
Effect of Carbide Addition on Sintering of SiC-B-C System [Toshiaki Mizutani, Akihiko Tsuge].....	184
Morphology of Coiled Whiskers of Si_3N_4 and Their Mechanical Properties [H. Iwanaga, T. Iwasaki, et al.].....	188
Dynamic Fatigue Properties of Mullite Silica Fiber Ceramics [M. Yonemura, T. Kusuda, et al.].....	194
Evaluation of Fracture Toughness by a Single Edge V-Notched Beam Method [T. Watanabe, H. Awaji, et al.].....	199
Multilayer Ceramic Capacitor Fabrication by Infiltration Process of Internal Electrode Material [Moon G. Kim, J. W. Ko, et al.].....	205
Dielectric Material With Resistance to Reduction and Multilayer Ceramic Capacitor With Copper Electrode [H. Kagata, J. Kato, et al.].....	210
Effect of Excess MgO on the Dielectric Properties of $\text{Pb}(\text{Mg}_{1/3}\text{Nb}_{2/3})\text{O}_3$ Ceramics [D. H. Kang, K. H. Yoon].....	216

Osaka Hall of Commerce & Industry

- 10:00 (司会 小見山亨 Tohru Komiyama, 趙 相喜 Sang Hee Cho)
「縁と研究」..... 3
韓 準石 Jun Sok Han (Contacts and Research)
- 10:40 (司会 福長 脩 Osamu Fukunaga, 李 卿喜 Kyung Hee Lee)
「共沈法によるセラミック粉末の調製」..... 7
Coprecipitation Processes in Ceramic Methods of Preparation on
Crystalline Materials
崔 圭源 Q. Won Choi (ソウル大學校 名誉教授)
- 11:20 (司会 古澤義文 Yoshifumi Furusawa, 朴 容浣 Yong Wan Park)
「おそ過ぎた隣国理解」..... 11
荻野吉和 Yoshikazu Ogino (Belated Understanding of Neighboring
Countries)

○一般講演 マイドーム大阪8F

12月6日(水)午後 A会場

[Basic Science]

(13:30)(座長 正木孝樹 Takaki Masaki, 金 銀玉 Eun Ok OH-Kim)

- 1A01 ゾル-ゲル法により調製されたアルミナの粒成長と緻密化に及ぼす SiO_2 の影響.....15

Effect of SiO_2 on Grain Growth and Densification of Alumina Prepared by Sol-Gel Technique

○金 海斗 Hai-Doo Kim, Hwan-Kyu Kang (韓国機械研)

- 1A02 Al_2O_3 の焼結時におけるMgとCaの界面偏析.....23

The Interfacial Segregation of Mg and Ca during Sintering of Alumina

○白 聖基 Sung Gi Baik, J. H. Moon (産業科学技術研)

- 1A03 セラミックスの緻密化に及ぼす閉じ込められたガスと気孔収縮の影響.....28

Entrapped Gases and Pore Shrinkage in Ceramics Sintering

Kyung Jin Yoon, ○姜 錫重 Suk-Joong L. Kang (韓国科学技術院)

- 1A04 酸化物における化学的に誘起された界面の移動.....32

Chemically Induced Grain Boundary Migration in Oxides

J. W. Jeong, H. Y. Lee, S. C. Han, Suk-Joong L. Kang, ○尹 徳龍

Duk Nong Yoon (韓国科学技術院)

- 1A05 高温X線回折法によるY-TZP焼結体の構造解析.....38

In-Situ Observation of Structural Changes of Y-TZP by X-ray Diffraction

○北野幸重 Yukishige Kitano, 森 由爾 Yuuji Mori, 石谷 炯 Akira Ishitani, 正木孝樹* Takaki Masaki* (東レリサーチセンター, 東レ*)

[Functional Materials]

(15:40)(座長 金丸文一 Fumikazu Kanamaru, 金 昊起 Ho Gi Kim)

- 1A06 多孔質SiCセラミックスの微細構造制御と熱電特性.....47

Microstructure Control and Thermoelectric Characteristics of Porous SiC Ceramics

○河本邦仁 Kunihito Koumoto, 裴 哲薫 Chul Hoon Pai, 竹田俊二 Shunji Takeda, 柳田博明 Hiroaki Yanagida (東京大学)

- 1 A 0 7 (Zr, Ti)O₂水熱合成粉体を用いたPb(Zr_{0.53}Ti_{0.47})O₃
セラミックスの合成と評価52
Fabrication and Evaluation of Pb(Zr_{0.53}Ti_{0.47})O₃ Ceramics Using
Hydrothermal Produced (Zr,Ti)O₂ Powder
○山本 孝 Takashi Yamamoto, 田中亮二 Ryouji Tanaka, 岡崎 清*
Kiyoshi Okazaki* (防衛大学校, 相模工大*)
- 1 A 0 8 圧電セラミックスの機械的性質と疲労.....57
Mechanical Properties and Fatigue of Piezoelectric Ceramics
○谷本敏夫 Toshio Tanimoto, 山本 孝* Takashi Yamamoto*, 岡崎 清
Kiyoshi Okazaki (相模工大, 防衛大学校*)
- 1 A 0 9 水熱電気化学法によるチタン金属からのBaTiO₃粉末及び薄膜の直接作製...62
Direct Preparation of BaTiO₃ Powders and Thin Films from Titanium
Metal by Hydrothermal-Electrochemical Method
○柳 承己 Seung-Eul Yoo, 石澤伸夫 Nobuo Ishizawa, 吉村昌弘
Masahiro Yoshimura (東京工大)
- 1 2 月 6 日 (水) 午後 B 会場
[Superconducting Ceramics]
(13:30) (座長 小野修一郎 Shuichiro Ono, 尹 冀鉉 Ki Hyun Yoon)
- 1 B 0 1 TSFZ法による高温超伝導酸化物単結晶の育成71
Growth of Superconducting Oxide Single Crystals by TSFZ Method
○児嶋弘直 Hironao Kojima, 田中 功 Isao Tanaka (山梨大学)
- 1 B 0 2 近接効果によるY₁Ba₂Cu₃O_{7-δ}のJ_c改良の試み76
An Attempt to Improve the Critical Current Density of the High T_c
Superconductor Y₁Ba₂Cu₃O_{7-δ} by the Proximity Effect
○土信田豊 Yutaka Doshida, 清水賢司 Kenji Shimizu, 渡部安広
Yasuhiro Watanabe, 秋濱良三 Ryoza Akihama (秩父セメント)
- 1 B 0 3 YBa₂Cu_{3-x}Co_xO_{7±δ}超伝導相の分光学的研究82
Spectroscopic Studies on the Superconducting Phase of YBa₂Cu_{3-x}Co_xO_{7±δ}
○崔 珍鎬 Jin Ho Choy, W. Y. Choe, D. Y. Jung, S. G. Kang
(Seoul大)

- 1 B 0 4 Bi系高温超伝導セラミックス及び薄膜の研究88
 Preparation of Bi-Oxide High Tc Superconducting Cuprates in the Form of Ceramics and Thin Films
 ○川合知二 Tomoji Kawai, 金井真樹 Masaki Kanai, 田畑 仁* Hitoshi Tabata*, 江上賢洋** Yoshihiro Egami**, 堀内 健 Takeshi Horiuchi, 三井克時***, Katsutoki Mitsui***, 堀内 健 Ken Horiuchi, 堀 洋一 Youichi Hori, 北浜 克熙 Katsuki Kitahama, 小倉 涉*** Kiyoshi Ogura***, 高木定雄*** Sadao Takagi***, P. J. Chong****, 河合七雄 Shichio Kawai (大阪大学, 川崎重工*, TAYCA Co.Ltd.***, 近畿大学***, Korean Research Institute of Chemical Technology****)
- 1 B 0 5 Bi系超伝導セラミックスのホットプレス焼結とその性質94
 Hot-Pressing and Superconducting Properties of Bi-Pb-Sr-Ca-Cu-O Ceramics
 ○村山宣光 Norimitsu Murayama, 桑原千三 Senzo Kuwabara, 鳥居保良 Yasuyoshi Torii (名古屋工業技術試験所)
- (15:40) (座長 川合知二 Tomoji Kawai, 白 聖基 Sun Gi Baik)
- 1 B 0 6 $\text{Bi}_2\text{Sr}_2\text{Ca}_2\text{Cu}_3\text{O}_x$ 超伝導セラミックスの作製101
 Preparation of $\text{Bi}_2\text{Sr}_2\text{Ca}_2\text{Cu}_3\text{O}_x$ Superconductive Ceramics
 ○宮本大樹 Hiroki Miyamoto, 宮本 敬 Kei Miyamoto, 稲村 偉 Suguru Inamura, 高橋弓弦 Yuzuru Takahashi (大阪府立産業技術総合研究所)
- 1 B 0 7 Bi系超伝導ウィスカーの作製と性質.....107
 Preparation of Superconducting Whiskers of Bi-System and Their Electrical Properties
 ○松原一郎 Ichiro Matsubara, 谷川秀夫 Hideo Tanigawa, 小倉 透 Toru Ogura, 山下博志 Hiroshi Yamashita, 木下 実 Makoto Kinoshita, 川合知二* Tomoji Kawai* (大阪工業技術試験所, 大阪大学*)
- 1 B 0 8 Bi, Pb-Sr-Ca-Cu-O系物質の相関係.....111
 Phase Relations in the Bi,Pb-Sr-Ca-Cu-O System
 ○下村真一 Shinichi Shimomura, 高野幹夫* Mikio Takano*, 池田靖訓* Yasunori Ikeda*, 伊藤浩之 Hiroyuki Ito, 広井善二* Zenji Hiroi*, 坂東尚周* Yoshichika Bando*, 高田 潤** Jun Takada**, 小田喜一** Kiichi Oda**, 北口 仁** Hitoshi Kitaguchi** (大阪窯業, 京都大学*, 岡山大学**)

- 1 B 0 9 ラマン分光法によるBi(Pb)-Sr-Ca-Cu-O系超伝導物質の
 キャラクタリゼーション.....117
 Homogeneous Cu-O Bonding due to Pb Doping in $\text{Bi}_4\text{Sr}_3\text{Ca}_3\text{Cu}_4\text{O}_{16-\delta}$
 Superconducting Materials detected by Raman Spectroscopy
 ○金 銀玉 Eun Ok OH-Kim, Pham V. Huong*, Keu Hong Kim** (東西
 産業素材研, Laboratoire de Spectroscopie Moleculaire et Cristalline
 Universite de Bordeaux*, 延世大**)
- 1 B 1 0 Tl-Sr-Ca-Cu-OセラミックスおよびTl-Bi-Sr-Ca-
 Cu-Oセラミックスの超伝導転移.....123
 Superconductive Transitions in Tl-Sr-Ca-Cu-O and Tl-Bi-Sr-Ca-Cu-O
 Ceramics
 ○井上 修 Osamu Inoue, 安達成司 Seiji Adachi, 河島俊一郎
 Syunichiro Kawashima (松下電器産業)
- 1 2 月 6 日 (水) 午後 C 会場
 [Glass]
 (13:30) (座長 大里信義 Nobuyoshi Ohsato, 金 炳憲 Byung Hoon Kim)
- 1 C 0 1 ゼルーゲル法による多孔質シリカガラスの直接合成.....131
 Direct Preparation of Porous Silica Glasses by the Sol-Gel Method
 ○幸塚広光 Hiromitsu Kozuka, 山口 淳 Jun Yamaguchi, 作花清夫
 Sumio Sakka (京都大学)
- 1 C 0 2 ゼルーゲル法による $\text{B}_2\text{O}_3\text{-SiO}_2$ 及び $\text{Al}_2\text{O}_3\text{-SiO}_2$ 系ガラス被膜の
 作製.....135
 Preparation of $\text{B}_2\text{O}_3\text{-SiO}_2$ and $\text{Al}_2\text{O}_3\text{-SiO}_2$ Coating Films by the Sol-Gel
 Method
 ○金 炳勲 Byung-Hoon Kim, Seok-Jin Choi, Kyu-Soek Hwang (全南大)
- 1 C 0 3 ゼルーゲル法による光ディスク用プリグルーブの形成.....140
 Formation of Pregrooves for Optical Disks by the Sol-Gel Method
 ○峠 登 Noboru Tohge, 南 努 Tsutomu Minami, 松田厚範* Atsunori
 Matsuda*, 松野好洋* Yoshihiro Matsuno*, 片山 慎也* Shinya
 Katayama*, 角 俊雄* Toshio Tsuno* (大阪府立大学, 日本板硝子*)
- 1 C 0 4 透光性ガラスセラミックスに関する研究.....144
 A Study on Transparent Glass Ceramics
 ○朴 容浣 Yong-Wan Park (漢陽大)

- 1 C 0 5 誘電ガラスセラミックス中におけるBaTiO₃の結晶化148
 Crystallization of BaTiO₃ Based Dielectric Glass Ceramics
 ○金 亨植 Hyung Sik Kim, U. Kang (韓国電機研)
- (15:40) (座長 守屋喜郎 Yoshiro Moriya, 金 炳勳 Byung Hoon Kim)
- 1 C 0 6 Rotary Gas Jet (RGJ) 法によるグラスウールの製造157
 The Rotary Gas Jet Process for Glass Wool Formation
 ○池田 薫 Kaoru Ikeda, 音田新治 Shinji Onda, 大里信義 Nobuyoshi Osato (日本板硝子)
- 1 C 0 7 非球面レンズの高精度モールドイング成形163
 High Precision Moulding of Aspherical Glass Lenses
 ○泉谷徹郎 Tetsuro Izumitani (HOYA)
- 1 C 0 8 生体用ガラスの構造と水酸化アパタイトの形成に及ぼす修飾剤の影響168
 Effect of Modifiers on the Structures and Hydroxyapatite Formation of Bioglass
 ○金 喆泳 Cheol Young Kim, Hopil Lee (仁荷大)
- 1 C 0 9 TeO₂含有ガラスの構造と性質173
 Structure and Properties of TeO₂-Containing Glasses
 ○横尾俊信 Toshinobu Yokoo, 藤田政行 Masayuki Fujita, 幸塚広光 Hiromitsu Kozuka, 作花清夫 Sumio Sakka (京都大学)
- 1 C 1 0 イオン交換によるガラスのキャラクタリゼーション179
 Characterization of Glasses by Ion Exchange
 Dong-In Lee, ○李 喜洙 Hee Soo Lee (延世大)
- 12月7日(木) 午前～午後 A会場
 [Ceramic Raw Materials]
 (9:30) (座長 奥谷 猛 Takeshi Okutani, 李 秉夏 Byung Ha Lee)
- 2 A 0 1 京都府のセラミックス原料について — 陶石資源と現用原料187
 Ceramic Raw Materials in Kyoto Prefecture — Toseki Resources and Today's Using Ceramic Raw Materials
 ○矢野秀樹 Hideki Yano, 宮村 学* Manabu Miyamura* (京都府立中小企業総合指導所, 元地質調査所*)

- 2 A 0 2 カルシアのクリンカー及びレンガの特性について193
 The Characteristics of Calcia Clinker and Brick
 金 鐘聲 Jong Sung Kim, ○金 永國 (三華化成)
- 2 A 0 3 酸化物系セラミックスの原料合成技術201
 Synthetic Techniques of Oxide Powder with High Qualities
 ○高木弘義 Hiroyoshi Takagi, 淡野正信 Masanobu Awano, 山田豊章
 Toyoaki Yamada, 中村和雄 Kazuo Nakamura (名古屋工業技術試験所)
- (10:40) (座長 石井敏次 Toshitsugu Ishii, 徐 東瑋 Dong Soo Suhr)
- 2 A 0 4 ムライトスリップの分散-凝集の挙動と鑄込み成形体の微構造上及ぼす影響 ...209
 Dispersion-Flocculation Behaviors of Mullite Slip and Their Effects on
 the Microstructures of Green Casts
 ○Ki G. Lee, Han N. Cheong, Hyun M. Jang*, 金 義勲** Eui Hoon
Kim** (産業科学技術研, Pohang Institute of Science and Technology*,
 Sam Hwa Chemical Co., Ltd.**)
- 2 A 0 5 Al_2O_3 を被覆した TiO_2 と Cr_2O_3 からなる複合粉末の均一沈澱法による
 合成215
 Synthesis of Al_2O_3 -Coated TiO_2 and Al_2O_3 -Coated Cr_2O_3 Composite Powder
 by Homogeneous Precipitation Method
 ○金 秉官 Byung Kwan Kim, Itaru Yasui* (昌原大, 東京大*)
- 2 A 0 6 カオリン鉱物からの針状ムライトの生成と特性220
 Formation and Some Properties of Needle-like Mullite from Kaolin
 Minerals
 ○勝木宏昭 Hiroaki Katsuki (佐賀県窯業試験場)
- 2 A 0 7 ゾル-ゲル法による高純度微粉ムライトの合成法226
 Synthesis of Pure Fine Mullite Powder by Sol-Gel Process
 李 卿喜 Kyung Hee Lee, ○李 秉夏 Byung Ha Lee, 黄 牛淵 Woo
 Youn Hwang, 李 隆傑 Yung Kul Lee (明知大)

(13:30) (座長 勝木宏昭 Hiroaki Katsuki, 金 秉官 Byun Kwan Kim)

- 2A08 ころがり台上の炭素熱還元窒化による窒化ケイ素粉末の合成233
Synthesis of Silicon Nitride Powders by Carbothermal Reduction and Nitridation in a Rolling Bed

○李 康浩 Kang Ho Lee, B. H. Park, S. Baik (産業科学技術研)

- 2A09 SiO_2 -Hydrocarbon- NH_3 系による α - Si_3N_4 粉末の合成 ...237
Synthesis of α - Si_3N_4 Powder by SiO_2 -Hydrocarbon- NH_3 System

○石井敏次 Toshitsugu Ishii, 今井 功 Isao Imai, 佐野 省 Akira Sano, 小松通泰* Michiyasu Komatsu* (東芝セラミックス, 東芝*)

- 2A10 エチルけい酸塩からの高純度 β - SiC 微粉末の合成の研究243
A Study on Synthesis of High Purity β - SiC Fine Powders from Ethyl Silicate

○崔 鏞植 Yong-Sik Choi, Keum-Churl Park* (国立工業試験院, 漢陽大*)

- 2A11 SiC ウィスカーの形状と成長に及ぼす添加物と雰囲気の影響249
Effects of Additives and Atmosphere on Morphology and Growth of Silicon Carbide Whiskers

○姜 大甲 Thae-Khapp Kang, Soon-Dong Park, Chang-Kyu Rhee, Il-Hyun Kuk (韓国 Energy 研)

- 2A12 籾殻燃焼灰からの SiCl_4 の製造254
Preparation of SiCl_4 from Rice Hull Ashes and Its Utilization

○奥谷 猛 Takeshi Okutani, 中田善徳 Yoshinori Nakata, 鈴木正昭 Masaaki Suzuki, 山口宗宏 Munehiro Yamaguchi (北海道工業開発試験所)

[Ceramic Applications]

(15:40) (座長 山本 勉 Tsutomu Yamamoto, 洪 良基 Yang Ki Hong)

- 2A13 高温発熱体用ジルコニア成形体の特性評価263
Evaluation of the Zirconia Form as a High Temperature Heating Element

○浅見 肇 Hajime Asami (品川白煉瓦)

- 2A14 無電解メッキによるアルミナセラミックスのメタライズ269
Metallization of Alumina Ceramics by Electroless Plating

S. G. Kang*, B. S. Jeon, ○朴 光子 Kwang Ja Park (国立工業試験院, 漢陽大*)

- 2 A 1 5 プラズマ溶射された $ZrO_2-Y_2O_3$ 断熱コーティング膜の微構造と相転移274
 Microstructure and Phase Transformation of Plasma-sprayed $ZrO_2-Y_2O_3$
 Thermal Barrier Coatings

○徐 東琇 Dong-Soo Shur (忠南大)

- 2 A 1 6 SiC ウィスカー/ Al_2O_3 系複合セラミックス切削工具280
 Cutting Tool of SiC Whisker/ Al_2O_3 Composite

○上野和夫 Kazuo Ueno, 山本 勉* Tsutomu Yamamoto*, 浅野 誠*
 Makoto Asano* (大阪工業技術試験所, ダイジェット工業*)

- 2 A 1 7 高熱伝導性 AlN 基板の開発と応用286
 Development and Application of High Thermal Conductivity AlN Substrate

○黒川泰弘 Yasuhiro Kurokawa, 嶋田勇三 Yuzo Shimada, 高見沢秀男
 Hideo Takamizawa (日本電気)

1 2 月 7 日 (木) 午前～午後 B 会場

[Superconducting Ceramics]

(9:30) (座長 宮本大樹 Hiroki Miyamoto, 崔 珍鎬 Jin Ho Choy)

- 2 B 0 1 超伝導セラミックス人工格子295
 Superconducting Ceramic Artificial Superstructured Films

○川口建二 Kenji Kawaguchi, 相馬 貢 Mitsugu Sohma, 新 重光
 Shigemitsu Shin (化学技術研究所)

- 2 B 0 2 $(Ca_{0.86}Sr_{0.14})CuO_2$ のラマン散乱301
 Raman Scattering in $(Ca_{0.86}Sr_{0.14})CuO_2$

○渦巻拓也 Takuya Uzumaki, Kazunori Yamanaka, Atsushi Tanaka,
 亀原伸男 Nobuo Kamehara, 丹羽紘一 Koichi Niwa (富士通研究所)

- 2 B 0 3 高温 YBCO 超伝導線の微構造と性質306
 Microstructure and Properties of Hot-Worked $YBa_2Cu_3O_{7-x}$ Super-
 conducting Wire

○J. T. Song, H. J. Chang, 秋濱良三* Ryouzou Akihama* (漢陽大,
 秩父セメント*)

[Composite Ceramics]

(10:40) (座長 新原 晴一 Koichi Niihara, 金 海斗 Hai Doo Kim)

2B04 常圧焼結による炭素セラミック複合材料の諸性質313

Properties of Carbon Ceramic Composite Made by Pressureless Sintering

○高嶋好夫 Yoshio Takashima, 小川一太郎* Ichitaro Ogawa*, 古川満彦 Mitsuhiko Furukawa, 吉田久良* Hisayoshi Yoshida* (日本タングステン, 九州工業技術試験所*)

2B05 Al_2O_3 -TiC 複合体の粒成長挙動と機械的性質318

The Grain-Growth Behavior and Mechanical Properties of Al_2O_3 -TiC Composite

○宋 瀚植 Han Shik Song, Y. H. You (雙龍中央研)

2B06 Si_3N_4 - ZrO_2 複合体の焼結挙動と Si_3N_4 の α/β 転移325

Sintering Behavior and α/β Transformation of Si_3N_4 in Si_3N_4 - ZrO_2 Composite

○金 宗熙 Chong Hee Kim, Jae Ryong Kim, Chae Hyun Lee (韓國科學技術院)

[Structural Ceramics]

(13:30) (座長 木下 実 Makoto Kinoshita, 金 泰玉 Tae Ok Kim)

2B07 沈澱法により作られた Al_2O_3 - ZrO_2 セラミックスの特性337

Properties of Al_2O_3 -15v/o ZrO_2 (+3m/o Y_2O_3) Ceramics Prepared by Precipitation Method

○李 弘林 Hong Lim Lee, Gi Gon Hong (延世大)

2B08 低圧射出成形法による Al_2O_3 および Si_3N_4 の作製343

Preparation of Al_2O_3 and Si_3N_4 Ceramics by Low Pressure Injection Molding Method

○宮本 敬 Kei Miyamoto, 高橋弓弦 Yuzuru Takahashi, 稲村 偉 Suguru Inamura, 宮本大樹 Hiroki Miyamoto (大阪府立産業技術総合研究所)

2B09 多孔質ガラスからの β -サイアロンの合成と焼結体の特性349

Synthesis of β -Sialon from Porous Glass and Properties of its Sintered Body

○金 炳旭 Byong-Ho Kim, Gun-Hun Lee, Hyung-Woo Jun (高麗大)

- 2 B 1 0 SiC-B-C系の焼結に及ぼす炭化物添加の影響352
 Effect of Carbide Addition on Sintering of SiC-B-C System
 ○水谷敏昭 Toshiaki Mizutani, 柘植章彦 Akihiko Tsuge (東芝)
- 2 B 1 1 Si₃N₄コイル状ウィスカーのモルフォロジーと機械的性質356
 Morphology of Coiled Whiskers of Si₃N₄ and Their Mechanical Properties
 ○岩永 浩 Hiroshi Iwanaga, 岩崎 武 Takeshi Iwasaki, 元島栖二*
 Seiji Motozima*, 服部達彦** Tatsuhiko Hattori**, 竹内 伸*** Shin
Takeuchi*** (長崎大学、岐阜大学*, 東亜合成化学工業**, 東京大学***)
- (15:40) (座長 吉田久良 Hisayoshi Yoshida, 李 弘林 Hong Lim Lee)
- 2 B 1 2 ムライト-シリカ質繊維セラミックスの動疲労特性365
 Dynamic Fatigue Properties of Mullite Silica Fiber Ceramics
 ○米村正明 Masaaki Yonemura, 楠田隆男 Takao Kusuda, 若宮正行
 Masayuki Wakamiya (松下電器産業)
- 2 B 1 3 セラミック転がり軸受の概要371
 Outline of Ceramic Antifriction Bearings
 ○安井啓剛 Hiroyoshi Yasui (光洋精工)
- 2 B 1 4 構造用セラミックスの比研削エネルギー377
 Specific Grinding Energies of Structural Ceramics
 田中芳雄 Yoshio Tanaka, ○朴 吉煥 Gillhwan Park, 水谷勝己*
 Katsumi Mizutani* (大阪府立大学, 大阪府立産業技術総合研究所*)
- 2 B 1 5 SENB (Vノッチ) 法による破壊靱性評価383
 Evaluation of Fracture Toughness by a Single Edge V-Notched Beam
 Method
 ○渡部忠男 Tadao Watanabe, 淡路英夫 Hideo Awaji, 山田達也 Tatsuya
Yamada, 坂井田喜久 Yoshihisa Sakaida, 田宮博道 Hiromichi Tamiya,
 中川平三郎* Heizaburo Nakagawa* ((財)ファインセラミックスセンター,
 鳥取大学*)
- 2 B 1 6 ボールオンディスク法によるセラミックスの摩擦・摩耗評価389
 Friction and Wear of Ceramics by Ball-On-Disk Method
 ○岩佐美喜男 Mikio Iwasa, 木下 実 Makoto Kinoshita (大阪工業技術
 試験所)

12月7日(木) 午前～午後 C会場

[Functional Ceramics]

(9:30)(座長 河本邦仁 Kunihito Koumoto, 呉 根鎬 K. K. Orr)

2C01 ガラス基板上に作製したPt-TiO₂薄膜とその光触媒作用……………397

Preparation and Photocatalytic Properties of Pt-TiO₂ Thin Films on Glass Substrate

○見田啓介 Keisuke Mita, 高橋雅也 Masanari Takahashi, 川舟功朗
Isao Kawafune, 頓行 宏 Hiroshi Toyuki (大阪市立工業研究所)

2C02 中止

2C03 固相法による透光性PLZTセラミックスの作製……………403

Transparent PLZT Ceramics Prepared by Mixed Oxide Technique

○山内 洋 You Yamauchi, 植田安孝 Yasutaka Ueda (住友精化)

(10:40)(座長 釘宮公一 Koichi Kugimiya, 金 喆泳 Cheol Young Kim)

2C04 HIPによるPLZT磁器の作製と光スイッチへの応用……………411

PLZT Ceramics Prepared by HIP and Its Application to Optical Switches

高田光裕 Mitsuhiro Takata, ○豊田幸夫 Sachio Toyota (住友特殊金属)

2C05 圧電セラミックスにおけるポーリングメカニズムの考察……………416

Review on Poling Mechanism in Piezoelectric Ceramics

C. M. Chun, J. H. Lim, G. J. Wee, ○洪 良基 Yang Ki Hong
(東洋化学研)

2C06 PbO過剰量がPb(Ni_{1/3}Nb_{2/3})O₃-PbTiO₃-PbZrO₃系の
焼結及び圧電特性に及ぼす影響……………421

Effects of Excess PbO Addition on Sintering and Piezoelectric
Properties in Pb(Ni_{1/3}Nb_{2/3})O₃-PbTiO₃-PbZrO₃ System

○趙 相熙 Sang Hee Cho, 金 正柱 J. J. Kim, 金 道然* D. Y. Kim*
(慶北大, Seoul大*)

2C07 Pb(Zr, Ti)O₃-Pb(Ni_{1/3}Nb_{2/3})O₃-
Pb(Zn_{1/3}Nb_{2/3})O₃系における新規相境界での圧電特性……………428

Piezoelectric Properties of the New Phase Boundary in the

Pb(Zr, Ti)O₃-Pb(Ni_{1/3}Nb_{2/3})O₃-Pb(Zn_{1/3}Nb_{2/3})O₃ System

○長田裕也 Hiroya Nagata, 渡辺正広 Masahiro Watanabe, 窪田吉孝
Yoshitaka Kubota, 山村 博 Hiroshi Yamamura (東ソー)

(13:30) (座長 岡本祥一 Shoichi Okamoto, 姜 錫重 Suk Joong Kang)

- 2C08 湿式直接法による (Ba-Sr) TiO_3 の生成反応機構437
Reaction Mechanism on the Synthesis of (Ba-Sr) TiO_3 by Direct Wet Process
○李 卿喜 Kyung Hee Lee, 李 秉夏 Byung Ha Lee, ○金 大雄 Dea Ung Kim (明知大)
- 2C09 内部電極物質浸透法による積層セラミックコンデンサの作製442
Multilayer Ceramic Capacitor Fabrication by Infiltration Process of Internal Electrode Material
○金 文圭 Mun Gyu Kim, J. W. Ko, Y. H. Kim* (Seoul大, Fine Ceramic Materials Lab., KAIST*)
- 2C10 耐還元性を有する誘電体材料と銅内部電極セラミック積層コンデンサ447
Dielectric Material with Resistance to Reduction and Multilayer Ceramic Capacitor with Copper Electrode
○加賀田博司 Hiroshi Kagata, 横谷洋一郎 Yoichiro Yokotani, 加藤純一 Junichi Kato, 釘宮公一 Koichi Kugimiya (松下電器産業)
- 2C11 Pb ($Mg_{1/3}Nb_{2/3}$) O_3 セラミックスの誘電特性に及ぼす過剰の MgO の影響453
Effect of Excess MgO on the Dielectric Properties of Pb($Mg_{1/3}Nb_{2/3}$) O_3 Ceramics
D. H. Kang, ○尹 冀鉉 Ki Hyun Yoon (延世大)
- 2C12 AES 法によるチタン酸鉛薄膜の組成分析とその電気的特性458
Compositional Analysis of Lead Titanate Thin Films by Auger Electron Spectroscopy(AES) and Their Electrical Properties
Soon-Gil Yoon, ○金 昊起 Ho Gi Kim (韓國科學技術院)
- (15:40) (座長 頼行 宏 Hiroshi Toyuki, 金 亨植 Hyung Sik Kim)
- 2C13 La 修飾された Pb TiO_3 の化学的合成とその特性471
Chemical Preparation of La-Modified Pb TiO_3 and its Properties
B. W. Lee, ○吳 根鎬 K. K. Orr, J. K. Choi (漢陽大)

- 2 C 1 4 $\text{TiN}-\text{MN}$ ($\text{M}=\text{Al}, \text{Mo}$) 系窒化物固溶体の電子状態と物性473
 Electronic State and Properties for Solid Solution of $\text{TiN}-\text{MN}$
 ($\text{M}=\text{Al}, \text{Mo}$) System
 ○高橋昌男 Masao Takahashi, 延谷宏治 Kohji Nobugai, 金丸文一
 Fumikazu Kanamaru (大阪大学)
- 2 C 1 5 酸素および窒素イオンを高濃度に注入したコバルト薄膜の構造と磁気特性479
 The Structure and Magnetic Properties of Cobalt-Base Films Implanted
 with High-Dose Oxygen and Nitrogen Ions
 ○中島健介 Kensuke Nakajima, 岡本祥一 Shoichi Okamoto
 (長岡技術科学大学)
- 2 C 1 6 $\delta-\text{FeOOH}-\text{BaCO}_3-\text{Zn}(\text{OH})_2$ 共沈物による Zn_2Y 微細単結晶
 粒子の製造485
 Preparation of Single Crystallites of Zn_2Y by Using Coprecipitate
 $\delta-\text{FeOOH}-\text{BaCO}_3-\text{Zn}(\text{OH})_2$
 ○金 泰玉 Tae-Ok Kim (釜山大)

EFFECT OF SiO_2 ON GRAIN GROWTH AND DENSIFICATION OF ALUMINA PREPARED BY SOL-GEL TECHNIQUE

Hai-Doo KIM and Hwan-Kyu Kang
Korea Institute of Machinery & Metals
66 Sangnam-dong, Changwon 641-010, Korea

1. Introduction

Alumina is one of the most important technical ceramics and has been intensively investigated because of its versatile applications. In alumina technology each property is strongly dependent on the microstructure. For example, mechanical and electrical properties will be improved when grain size and porosity are reduced to minimum; that means, grain growth should be suppressed and densification be enhanced during sintering process.

There are many ways to meet such requirements, one of which is the use of additives. If small amount of additive (normally 2+ or 4+) is dissolved in alumina lattice, Al^{3+} site is replaced by the additive cation, which increases the concentration of defects, thus, enhances the diffusion process.

The most popular additive for alumina sintering is MgO . The most widely accepted Coble theory (1-3) says oxygen ions transport faster along grain boundaries accompanied with the volume diffusion of aluminium ions which is the rate-determining, which leads to the idea that both 2+ and 4+ additives enhance the sintering of alumina due to the formation of aluminium interstitials and aluminium vacancies, respectively.

Recently, the enhanced grain boundary diffusion of oxygen ion has been argued by Reynen and Kim (4), based on the works of Kröger (5-7), in which the diffusing species on grain boundaries is not oxygen ions but oxygen atoms. Reynen and Readey theory (8-11) predicts that sintering process of alumina would be retarded by doping 4+ due to the decrease in oxygen vacancy concentration .

In this study, change in sintering behavior with a SiO_2 additive (4+) is discussed in relation with microstructural development.

In particular, the general sintering temperature of alumina is over 1600°C, which is above the eutectic temperature in binary system of Al_2O_3 - SiO_2 and, therefore, the use of SiO_2 as sintering additive for alumina of which sintering temperature is over 1600°C has not been considered in previous. However, recent research trend in alumina technology is towards the low temperature sintering of alumina; Yeh and Sacks (12) succeeded to sinter alumina near theoretical density (TD) at 1150 °C, which was difficult to imagine in previous days. Furthermore, some alumina powders produced in industries sinter to near TD at < 1550 °C which is below the eutectic temperature of Al_2O_3 - SiO_2 system. Therefore, it's meaningful to assess the effect of SiO_2 as an additive for alumina powder which sinters at very low temperature.

2. Experiments

0, 100, 1000, 10000 ppm of SiO_2 were doped to alumina through sol - gel process in order to be sure that small amounts of SiO_2 additive are homogeneously mixed (Fig. 1) . Table 1 shows the impurities of the starting materials . Especially alumina seed (< 0.5 μm) has been prepared by sedimentation method . Gels have been dried at 70 ° C for two weeks in drying oven and gel fragments of over 1 cm in size were collected for sintering experiments.

DTA-TG analysis was performed in order to determine the transformation temperature of boehmite to α - Al_2O_3 .

A series of gel fragments was sintered at 1350 °C, 1450 °C, 1550°C for 3, 30, 300 mins. in air . Up to 900 °C heating rate was 3 °C/min in order to avoid the cracks followed by 10 °C/min to the desired temperatures.

The bulk density after sintering was measured by Archimedes principle and, for the specimen with open pores, they were coated with lacquer before measuring density.

The microstructures were investigated by scanning electron microscope after polishing and thermal etching.

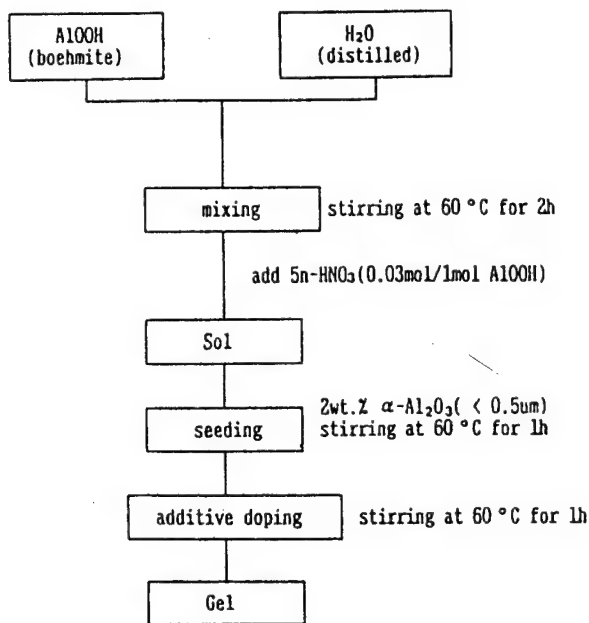


Table 1. The impurities of the materials used (wt.%)

	AlOOH*	SiO ₂ **	Al ₂ O ₃ ***
Al ₂ O ₃		0.05	
SiO ₂	0.022		0.04
TiO ₂		0.03	
Fe ₂ O ₃	0.016	0.003	0.01
Na ₂ O	0.002		0.03
carbon	0.4		
HCl		0.005	
average particle size (nm)	11	7	300
BET(m ² /gr)	180	380	5
LOI		< 2.5	0.1
H ₂ O		< 1.5	0.2

* AlOOH Disperal R Alumina, Condea Chemie, W. Germany

** SiO₂ Amorphous fumed silica, Degussa, W. Germany

*** Al₂O₃ Ceralox HPA alumina, Ceralox, U. S. A.

Fig. 1. Schematic diagram for the preparation of gel specimens

3. Results and Discussions

Fig.2 shows the DTA - TG results of each gels which has been dried for 2 weeks at 70 °C. Boehmite transforms to α - Al₂O₃ at 1210 °C while seeded specimen as well as seeded specimen doped with SiO₂ transform to α - Al₂O₃ at 1100 °C. The transformation temperature of 1100 °C is relatively higher than the previous reports (13-15) which may reflect no special treatment for boehmite powder to eliminate the agglomerates.

The density of the sintering at various conditions were shown in Fig. 3. At low temperature and short sintering time, seeded specimens without SiO₂ additive show higher density than those with SiO₂ additive while, at higher temperature and prolonged sintering time, they show at least same density or reverse.

Without SiO₂ additive sintered density does not go above 99 % TD even with 1550 °C, 300 min sintering while , with SiO₂ additive, it goes above 99 % TD.

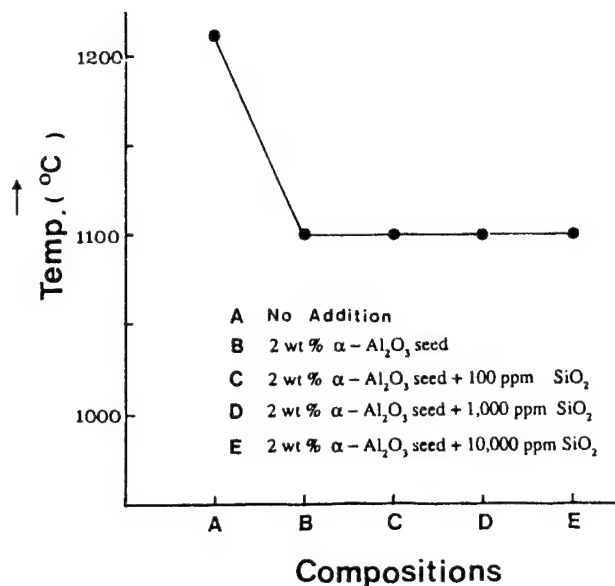


Fig. 2. Phase transformation temperatures to α - Al_2O_3 determined by DTA for different compositions

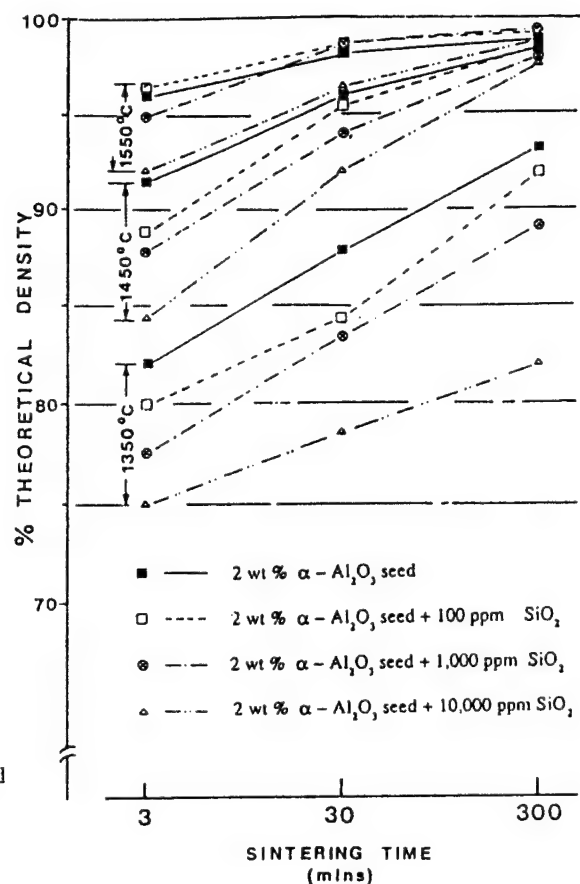


Fig. 3. Change in density at various conditions

This possibly suggests that SiO_2 additive decreases the grain growth and densification during initial and intermediate stage sintering, however, also inhibits the onset of discontinuous grain growth, thus, leading to higher density.

This view is further supported by the plot of grain size against percent theoretical density (Fig. 4).

The seeded specimen without SiO_2 additive shows the increase in grain size with the increase in density followed by the rapid increase in grain size as the density approaches the theoretical density. The seeded specimens with SiO_2 additive show very little grain growth until ~93 - 95 % TD, beyond which relatively lesser grain growth occurs than the above case.

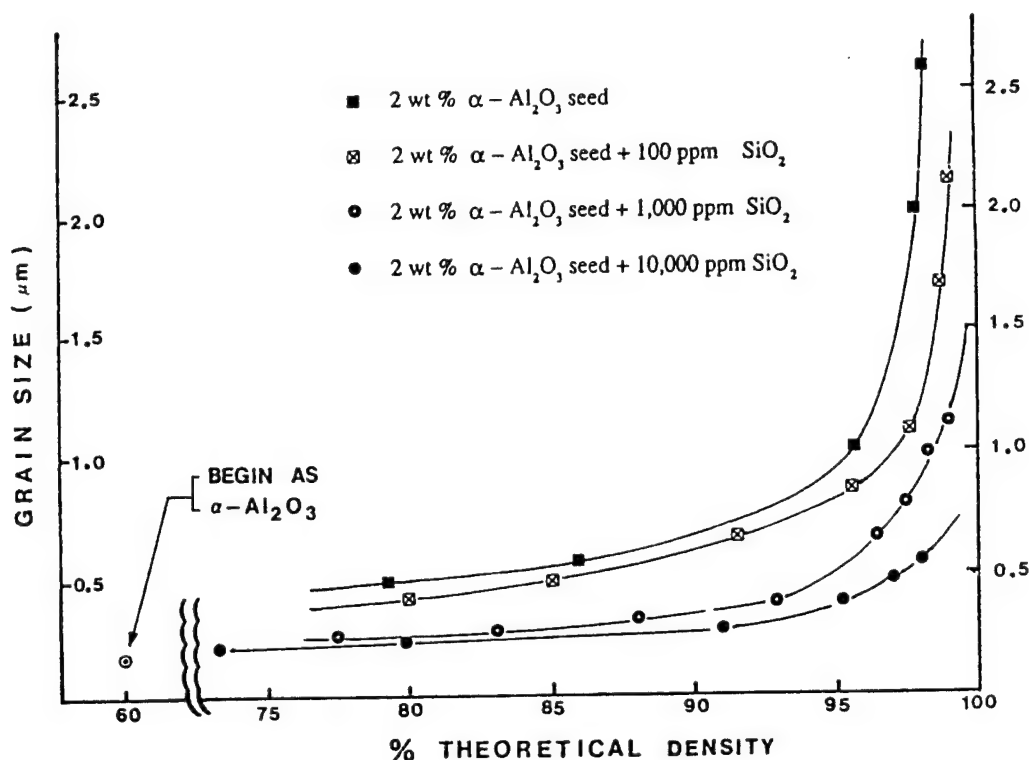


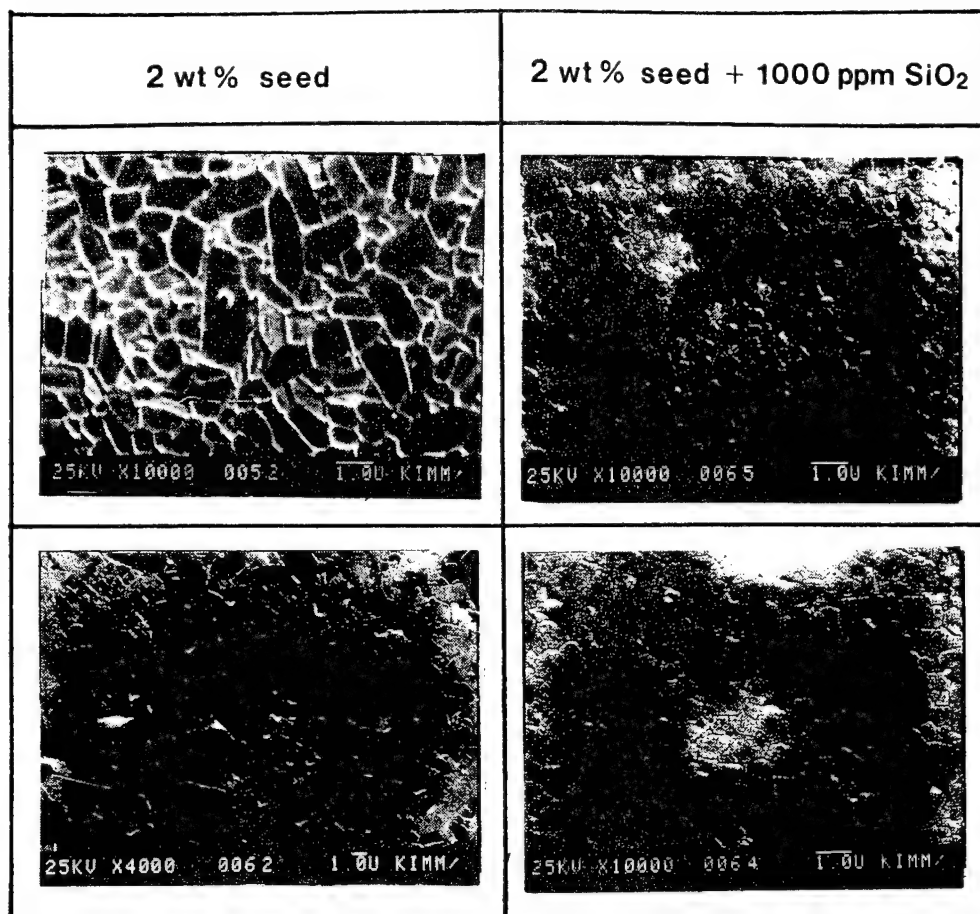
Fig. 4. The plot of grain size vs percent theoretical density. The sintered density just after transformation to α -alumina (sintered at 1120°C) was measured to 60 % TD and grain size was calculated from BET data.

It seems clear that SiO_2 additive retards the grain growth of alumina until the end of intermediate stage, enables the pores remain attached to grain boundaries, thus , enables them to sinter to near theoretical density. This also means that grain growth rate is relatively slow when pores are interconnected while it becomes relatively rapid when pores are isolated. Without SiO_2 additive grain growth is not retarded and , thus , an isotropic grain growth and discontinuous grain growth are quite possible.

The microstructural evidence for above arguments is presented in Fig. 5.

Fig. 5 shows the difference in microstructures between seeded specimen and seeded + 1000 ppm SiO_2 specimen sintered at 1550°C for 3 and 300 mins.

Without SiO_2 additive, large anisotropic and discontinuous grain growth occurred at 1550°C , 300 mins sintering while, with SiO_2 additive, no anisotropic and discontinuous grain growth occurred and its microstructure is characterised by high density with small grain size.



3	3
300	300
mins.	

Fig. 5. Microstructural development of seeded specimen with and without SiO₂ additive sintered at 1550 °C in air

Especially, the seeded specimen with 1000 ppm SiO₂ sintered at 1550 °C, 3 min shows ~ 95 % TD and 0.6 mm mean grain size, which seems to be just the end of intermediate stage. This specimen shows that all the pores remain at grain corners or grain boundaries, which is the favourable situation for densification to TD, thus, resulting in the near TD.

The solubility of SiO₂ in Al₂O₃ at high temperature is not known. If we assume that the solubility of SiO₂ in Al₂O₃ is very low, the remarkable retarding effect of SiO₂ on the grain growth is possibly due to the second phase formation, i.e. mullite. The formation of mullite through sol - gel process has been reported by Ismael et al. (16) in which mullite starts to be observed at 1300 °C and , at 1400 °C - 1 hour, all XRD

peaks correspond to mullite. The sintering temperatures employed in this experiment are high enough to give mullite, which was, however, not yet detected because of its extreme small grain size and small quantity.

4. Conclusions

Without additive grain growth is not retarded and, thus, anisotropic and discontinuous grain growth are inevitable at high temperature.

SiO₂ additive retards the grain growth of alumina until the end of intermediate stage, enables the pores remain attached to grain boundaries, thus, enables them to sinter to near theoretical density.

The remarkable retarding effect of SiO₂ on grain growth of alumina is possibly due to the second phase formation, i.e. mullite.

References

1. Coble, R. L. " Sintering crystalline solids : I. Intermediate and final stage diffusion models", J. Appl. Phys. 32, 787 - 92, (1961)
2. Coble, R. L. " Sintering crystalline solids : II. Experimental test of diffusion models in powder compacts", J. Appl. Phys. 32, 793 - 99, (1961)
3. Paladino, A. E. and Coble, R. L. " Effect of grain boundaries on diffusion-controlled processes in aluminium oxide", J. Am. Ceram. Soc. 46, 133-36, (1963)
4. Reynen, P. and Kim, H.D. "The influence of Na₂O on sintering and creep of alumina doped with MgO and TiO₂", Ceram. Ber. DKG 63, 272-79, (1986)
5. Hou, L.D., Tiku, S.K., Wang, H.A. and Kröger, F.A. "Conductivity and creep in acceptor-dominated polycrystalline Al₂O₃", J. Mater. Sci. 14, 1877-89, (1979)
6. Wang, H.A., and Kröger, F.A. "Chemical diffusion in polycrystalline Al₂O₃", J. Am. Ceram. Soc. 63, 613-19, (1980)
7. El-Aiat, M.M., Hou, L.D., Tiku, S.K., Wang, H.A. and Kröger, F.A. "High temperature conductivity and creep of polycrystalline Al₂O₃ doped with Fe and/or Ti", *ibid*, 64, 174-82, (1981)
8. Reijnen, P., " Non-stoichiometry and sintering of ionic solid", in Reactivity of Solids, Proc. 6th Int. Symp. Reactivity of Solids, p. 99-114, (1968)
9. Reijnen, P. " Sintering behavior and microstructure of aluminates and ferrites with spinel structure with regard to deviation from stoichiometry", Sci. Ceram., 4, 169-88, (1968)
10. Reijnen, P. "Nonstoichiometry and sintering in ionic solids", in Problems of Nonstoichiometry, Ed. Rabenau, A., North Holland Pub. Co., p, 219-38 (1970)
11. Readey, D.W., " Mass transport and sintering in impure ionic solids", J. Am. Ceram. Soc., 49, 366-69, (1966)

12. Yeh, T.S. and Sacks, M.D., " Low temperature sintering of aluminum oxide", *ibid*, 71, 841-44, (1988)
13. Kumagai, M. and Messing, G.L. "Enhanced densification of boehmite sol - gel by α - alumina seeding ", *ibid*, 67, c-230 - c-231, (1984)
14. Kumagai, M. and Messing G.L. " Controlled transformation and sintering of a boehmite sol - gel by α - alumina seeding ", *ibid*, 68, 500-05, (1985)
15. Kim, H.D. " Microstructure Control in Alumina", ph.D. thesis, Univ. Aachen, W. Germany, (1987)
16. Ismael, M.G.M.U., Nakai, Z., Minegishi, K. and Somiya, S. "Synthesis of mullite powder and its characteristics", *Int. J.High Tech.Ceram.* 2, 123-34, (1986)

THE INTERFACIAL SEGREGATION OF Mg AND Ca DURING SINTERING OF ALUMINA

S. Baik and J.H. Moon

Dept. of Materials Science and Engineering
Pohang Institute of Science and Technology
San 32, Hyo Ja-dong, Pohang 790-600, Korea

Comparative studies on the interfacial segregation behaviors of Mg and Ca using doped single-crystalline and polycrystalline alumina demonstrated that their interfacial segregation behaviors are markedly different each other. Ca tends to segregate on certain crystallographic surfaces or grain boundaries, while Mg enrichment is insensitive to the orientation or structure of interfaces. It is suggested that the anisotropy in the interfacial segregation behaviors of certain impurities, notably CaO, is responsible for the abnormal grain growth, whereas MgO promotes homogeneity of interfacial characteristics and enhance the development of uniform microstructures during final stage of alumina sintering.

I. INTRODUCTION

Production of ceramic components involves, without exception, a sintering process - a final step to achieve a desired density and shape. Through experience, it has been found that sintering of ceramic materials to theoretical densities often requires the addition of small amounts of sintering aids. A classical example is an addition of less than 0.25 wt % MgO in Al₂O₃ [1-2]. Similar instances are found in the addition of boron in SiC [3], Carbon in TiB₂ [4], ThO₂ in Y₂O₃ [5] and so on. However, the role of such additives in the sintering process is yet poorly understood, even though the technique has been used extensively in the commercial production of various ceramic components.

Similarly, certain impurities have to be carefully controlled below a certain limit in order to achieve reasonable densities. Prominent examples are oxygen in SiC [6] and TiB₂ [7] and CaO in Al₂O₃ [8]. Again why these elements are especially harmful if they are present above certain levels is not yet clearly answered.

The system that has been receiving most attention in the ceramic community is MgO (sintering aid) and CaO (harmful impurity) in Al₂O₃. A small addition of MgO prevents premature abnormal grain growth and promotes complete removal of porosities during the final stage of densification of alumina. One of the explanation for the role of MgO is that it tends to segregate to the grain boundaries and reduces the boundary mobility by a "solute drag mechanism" [9,10]. Many attempts [9-12] were made to confirm the hypothesis utilizing various surface chemical analyzers such as Auger electron spectroscopy (AES) and X-ray photoelectron spectroscopy (XPS). Grain boundaries were exposed in the analyzers and examined to see if any traces of Mg were present after sintering. However, Ca segregation always prevailed, while the evidence of Mg segregation was margined or inconclusive in most cases.

Interestingly, Ca is not effective for controlling abnormal grain growth even though it is such a strong grain boundary segregant. With the marginal evidence of Mg segregation, alternative explanations for the role of MgO and CaO in Al₂O₃ have been sought.

* also with Research Institute of Industrial Science and Technology, Pohang, Korea

We have been conducting a series of experiments using doped sapphire to test if Mg and/or Ca tends to segregate on the free surfaces [13-16]. Important kinetic as well as thermodynamic parameters were determined for each component. At least two crystallographic orientations - (0001) and (10 $\bar{1}0$) surfaces - were tested. Then we reexamined the behaviors of grain boundary segregations of Mg and/or Ca using ultra-high purity alumina powder, and compared its results with those of surface segregation experiments. In this paper, important findings are summarized and their implications to the alumina sintering are discussed.

2. SURFACE SEGREGATION

2.1 Magnesium Segregation

(0001) Plane

Strong enrichment of Mg has been observed when a sapphire crystal doped with 40 ppm of Mg was annealed above 1200°C in air [13]. In-situ vacuum annealing and Auger analysis at 900-1800°C failed to reveal Mg segregation presumably due to the fast evaporation of segregating species. The equilibrium surface concentration of Mg in the annealing temperature range 1300-1500°C follows Langmuir-type equilibrium isotherm with an effective heat of segregation, -1.9 eV as shown in Fig. 1. It is interesting to note that the enrichment of Mg is confined only in the top monolayer and its maximum enrichment factors, a ratio of surface concentration to the bulk concentration is as high as 3000 at 1300°C.

(10 $\bar{1}0$) Plane

Annealing the crystal in air also led to surface enrichment of Mg on the prismatic plane of sapphire [16]. In this particular experiment, Mg was doped in the crystal by ion implantation technique and the surface region of high concentration was removed by Ar⁺ ion sputtering. However, its segregation behavior was quite similar with that on the basal plane. Fig. 1. also shows the normalized surface concentration of Mg versus the inverse of annealing temperature. The heat of segregation calculated from its slope is -1.4 eV, which is a bit lower than that for the (0001) plane. The reason, in author's opinion, is due to the differences in ionic structures of each surface.

On the other hand, annealing the crystals in vacuum showed no trace of Mg on the surface at any temperature due to a possible evaporative loss of Mg. Instead, Ca was found to segregate strongly although the bulk concentration of Ca was thought to be in the range of a few ppm or less.

(10 $\bar{1}2$) Plane

This is one of the low energy planes, which is also known to be a primary cleavage plane of sapphire. It is thus expected that thermodynamic driving force for any solute in the crystal lattice to migrate from the lattice site to the surface ionic site in this rhombohedral plane should be comparable or even higher than those for the basal or prism planes. However, no study on the segregation to this plane has been reported yet.

2.2 Calcium Segregation

(0001) Plane

Utilizing the crystals doped intentionally with about 40 ppm of Ca, extensive search for

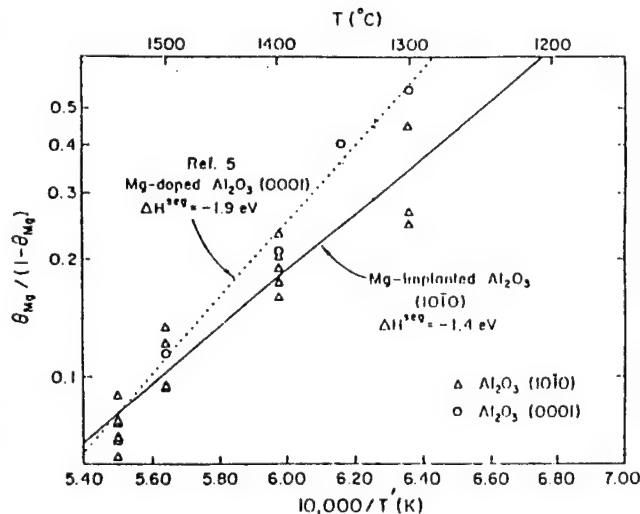


Fig. 1 Experimental results on surface segregation of Ca in alumina

any evidence of Ca enrichment on this surface has been performed [15]. But, unexpectedly, no evidence of Ca presence on the surface could be found under the experimental conditions that have been used in the Mg segregation studies. Regardless of the annealing conditions, in air or in vacuum, the Auger signals corresponding to Ca were shown to be barely above the detectability limits of the Auger Electron Spectroscope used in the experiment. Fig. 2. shows its results. Therefore, the difference in the segregation behaviors between Mg and Ca is quite dramatic for this basal plane. The mechanistic reason is not clearly understood yet. But a plausible reason is that Ca^{2+} ion, having ionic radii almost twice as large as that of Al^{3+} ion can not be accommodated in the basal plane whereas Mg^{2+} ion can easily replace Al^{3+} ion of similar size. In order to substantiate this proposition, it is necessary to understand the surface structures of sapphire.

(10 $\bar{1}$ 0) Plane

Strong enrichment of Ca on this plane was confirmed above 1300°C as shown in Fig.2 [15]. A small but noticeable amount of Ca was detected even below 1300°C. However, as observed in the case of Mg segregation dramatic increase in Ca enrichment occurred above 1300°C. Depth profiling of enriched surface by Ar ion sputtering demonstrated that the segregation was confined only top monolayer and the distribution of surface Ca was uniform across the entire surface. In the temperature range 1300–1500°C, the normalized surface concentration of Ca follows a Langmuir type equilibrium isotherm with a heat of segregation, -1.75eV. However, the lack of its reversibility with respect to the annealing steps whether its temperatures are ascending or descending, makes its adoption only tentative.

As mention above, strong segregation of Ca is also reported for this plane when a sapphire crystal doped with Mg was annealed in vacuum.

Extremely high evaporation rate of Mg in comparison to Ca is believed to be as low as a few ppm or less. In the air annealed samples this was absent due to the presence of Mg. It thus appears that Mg can successfully compete for surface segregation sites and be highly effective in repelling Ca once they occupy surface sites.

McCune and Ku[17] also measured Ca enrichment on this plane and reported similar results even though undoped commercial sapphire crystals were used in the experiments. The reported heat of segregation is also consistent with our values.

(10 $\bar{1}$ 2) Plane

We did not measure the surface segregation for this particular plane, but there exists an evidence that Ca also tends to segregate to the rhombohedral plane in the literature. McCune and Ku [17] reported that the enrichment factor, the ratio of surface to bulk concentration, they measured at 1400°C was 1348 with a sapphire crystal containing 26 ppm of Ca as an impurity. Further studies in wider temperature range are necessary.

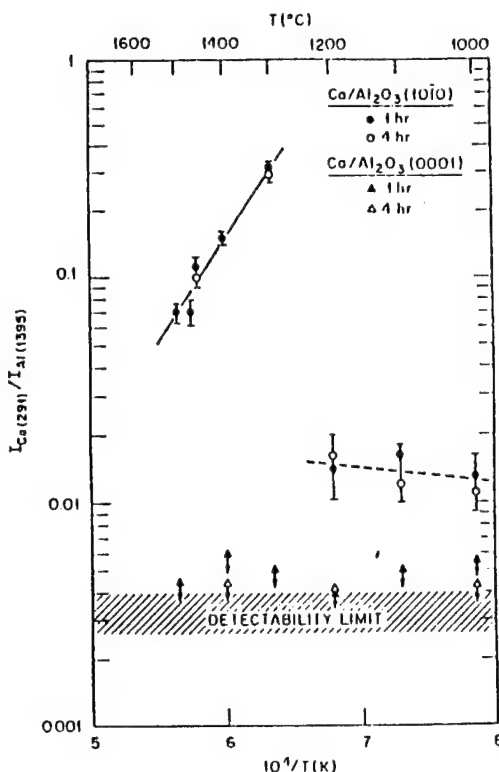


Fig. 2 Experimental results on surface segregation of Ca in alumina

3. GRAIN BOUNDARY SEGREGATION

3.1. Magnesium

We have re-examined using AES grain boundaries of alumina sintered in the temperature range 1300–1500°C in air. This sintering condition was proved to give maximum enrichment of Mg as well as Ca to the free surface. The specimen was made of Alumina powder of ultra-high-purity (>99.999%) doped with 300 ppm MgO. However, we could not achieve the minimum detectability required (e.g. $I(\text{Mg})/I(\text{Al}) > 0.05$ at 1300°C), and failed to identify Mg presence in the grain boundaries.

Interestingly, Ca did not appear on the grain boundaries either in all the experimental conditions, even though its detectability limit [$I(\text{Ca})/I(\text{Al})$] is as low as 0.01. This implies that the Ca content in the powder is sufficiently low, probably below a ppm level.

3.2. Calcium

100 ppm CaO doping

Extremely high concentration of Ca was detected especially in the grain boundaries of alumina specimens sintered at 1300°C and 1400°C. However, the Ca enrichment factor varied markedly depending on the location of the grain boundaries, as shown in Fig.3. This is consistent with the previous results on the anisotropic segregation behaviours of Ca on the free surfaces. Apparently Ca segregation depends strongly on the crystallographic orientation of grain boundaries of alumina.

100 ppm CaO + 300 ppm MgO doping

Further addition of 300 ppm MgO reduced the Ca concentration in the grain boundary particularly at 1300°C and 1400°C. At the same time, anisotropic behavior of Ca segregation disappeared. We failed to locate Mg during AES measurement due to the low detectability of our spectroscope. However, it appears that Mg establishes its grain boundary concentration rapidly and suppresses massive enrichment of Ca in the grain boundaries which are particularly favorable to Ca segregation.

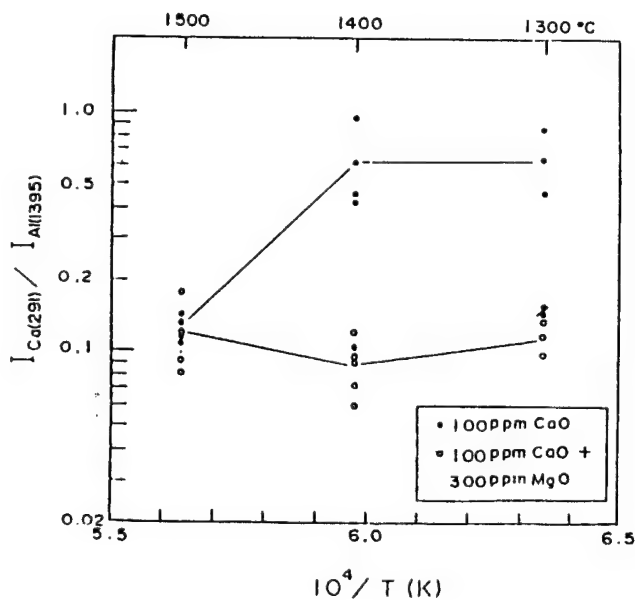


Fig.3 Grain Boundary Segregation of Ca with and without MgO co-doping

4. SUMMARY

Ineffectiveness of CaO as a sintering aid for alumina may be related to the anisotropic segregation behavior of Ca ions to the interfaces including grain boundaries and pore surfaces. Whereas, the reason why MgO is so effective in controlling abnormal grain growth may be because Mg segregation is relatively homogeneous throughout all the interfaces, and enhances structural homogeneity of interfaces. Mg tends to establish uniform concentrations along all the boundaries rapidly and neutralize the orientational and structural anisotropy which is responsible for the abnormal grain growth particularly in the final stage of alumina sintering.

5. REFERENCES

1. R.L. Coble, J. Appl. Phys., 32(5) 7893-99 (1961).
2. R.L. Coble, U.S. Patent, 3,026,210 (1962).
3. S. Prochazka, "Ceramics of High Performance Application," Edited by J.J. Burke et al., Brook Hill, Chestnut Hill (1974). p.239.
4. H.R. Baumgartner and R.A. Steiger, J. Am. Ceram. Soc. 67[3] 207-212 (1984).
5. W.D. Kingery, H.K. Bowen, D.R. Uhlmann, "Introduction to Ceramics," 2nd Edition p.490, John Wiley and Sons (1976).
6. J. Hojo, K. Miyachi, Y. Okabe, and Koto, J. Am. Ceram. Soc. 66[7] C-114-C-115 (1983).
7. S. Baik, P.F. Becher, J.Am. Ceram. Soc. 70[8] 527-30 (1987).
8. S.J. Wu, L.C. DeJonghe, M.N. Rahaman, J. Am. Ceram. Soc. 68[71] 385 (1985).
9. H.L. Marcus, J.M. Harris, and F.J. Szalkowski, pp. 387-98 in Fracture Mechanics of Ceramics, Vol. 1, Edited by R.C. Bradt et al., Plenum Press, New York 1973.
10. R.I. Taylor, J.P. Coad, and R.J. Brook, J.Am. Ceram. Soc. 57[12] 539-40 (1974).
11. W.C. Johnson, J.Am. Ceram. Soc. 61[5-6] 234-37 (1978).
12. P.E.C. Franken and A.P. Gehring, J. Mat. Sci. 16, 384-88 (1981).
13. S. Baik, D.E. Fowler, J.M. Blakely, and R. Raj., J.Am. Ceram. Soc., 68[5] 281-86 (1985).
14. S. Baik, J.Am. Ceram. Soc., 69[5] C101-C103 (1986).
15. Baik, S. and White, C.L., J.Am. Ceram. Soc., 70[9] 682-88 (1987).
16. Mukhopadhyay, S.M., Jardine, A.P., Blakely, J.M. and Baik, S., J.Am. Ceram. Soc., 71[5] 358-62 (1988).
17. McCune, R.C. and Ku, R.C., p.217, vol.10, Advances in Ceramics, Am. Ceram. Soc., Columbus, Ohio (1984).

IN-SITU OBSERVATION OF STRUCTURAL CHANGES OF Y-TZP BY X-RAY DIFFRACTION

KITANO Y., MORI Y., ISHITANI A., and MASAKI T.*

Toray Research Center, Inc., Otsu, Shiga 520, Japan

*Toray Industries, Inc., Otsu, Shiga 520, Japan

Tetragonal to monoclinic phase transformation was studied by in-situ X-ray diffraction technique on the ground and polished surfaces of tetragonal zirconia polycrystals containing 2.5 mol% yttria. Monoclinic phase content by thermal stress-induced transformation has a maximum value at 250°C and much greater (11 $\bar{1}$) peak intensity than (111) was observed similarly as found on the specimens associated with mechanical stresses.

Polycrystalline yttria-stabilized zirconia (Y-TZP) is well known to exhibit high strength and high fracture toughness, which are derived from the transformation of metastable tetragonal (t) to monoclinic (m) zirconia under the action of imposed stresses in the near stress field of a crack tip. T to m transformation is enhanced not only by mechanical stresses but also by thermal stresses. Many experimental observations show that the transformation by thermal stress is induced around 200 to 300°C [1-4].

In the present work, in order to determine the direct martensitic temperature, in-situ observation of the structural changes is carried out on the ground and polished surfaces of 2.5 mol% Y-TZP by X-ray diffraction and the relation of intensity changes between the thermal and mechanical stresses is discussed.

Experimental procedure

Polycrystalline ZrO_2 materials stabilized with 2.5 mol% Y_2O_3 containing 0.5 mol% Al_2O_3 were prepared by the method previously reported [5]. The test specimens were prepared by pressureless sintering and hot isostatic pressing. The powder was first isostatically pressed at 200MPa and heated gradually from room temperature to 900°C at a rate of 50°C/h and finally held at 1450°C for 2h.

Hot isostatic pressing was carried out on samples pressed at 200 MPa and presintered for 2h at 1400°C so as to obtain the material with a density not less than 97% of the theoretical density; an unencapsulated sample was raised from room temperature to the maximum temperature at a rate of 700°C/h in an argon atmosphere; the gas pressure was adjusted to rise slowly so as to reach 200MPa at maximum temperature; the sample was treated at 1400°C for 1.5h. The specimens obtained were ground with a 400-grit diamond wheel and then with 10- μm diamond paste to an optical finish. The surfaces of these specimens received further polishing with 5- and 3- μm diamond pastes.

The X-ray diffraction measurements were performed with graphite monochromated $\text{Cu K}\alpha$ radiation with an electronic furnace on a goniometer under dried nitrogen gas atmosphere. A Rigaku diffractometer (model RU-200B) was used by operating at 50kV-200mA in step scan mode with a 0.01 2θ step and a counting time of 1 sec per step over 2θ range 27° to 40°. This covers the monoclinic $\{111\}$ peaks and tetragonal $\{111\}$ and $\{002\}$ peaks. M-phase contents and intensity ratios of $m(11\bar{1})/m(111)$ and $t(002)/t(200)$ were estimated from the relative areas under $\{111\}$ and $\{002\}$ profiles using the method of Garvie and Nicholson [6].

Results and discussion

Figure 1 shows the XRD profiles for the ground surfaces after heating to 800 °C and then cooling to 200 °C and keeping for 5 to 10h. M-phase contents and X-ray intensity ratios of (002)/(200) tetragonal and $(11\bar{1})/(111)$ monoclinic peaks are summarized in Table 1. M-phase, which appears on the ground surface at room temperature, almost disappears when the sample is heated to 800 °C. When the sample is cooled to 200 °C from 800 °C, the m-phase increases gradually with the increase of heating time.

The reversal of the intensity ratio of the (002)/(200) tetragonal peaks, which might be interpreted as the domain switching, is also observed on the above specimens [7,8]. Figure 1 shows that this reversal of tetragonal peaks is stable when heat treatment is conducted.

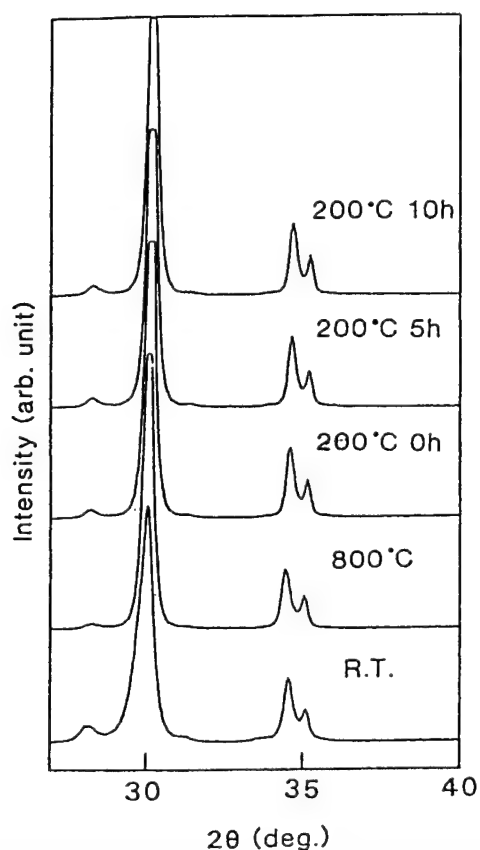


Table 1 Effects of thermal-stresses on the m-phase contents and XRD intensities

	M-phase contents(X)	Intensity ratio	
		T(002)/(200)	M($11\bar{1}$)/M(111)
R.T.	5.0	4.2	10.3
800°C	1.5	3.1	5.8
200°C 0h	2.2	3.5	6.5
200°C 5h	2.7	3.3	7.4
200°C 10h	3.0	3.3	8.1

Fig. 1 XRD profiles for the ground surfaces of 2.5Y-TZP after thermal-stresses.

Figures 2 and 3 show the XRD profiles for the polished surfaces of hipped specimens and pressureless sintered specimens, respectively. Figures 2(a) and 3(a) show the profiles of specimens which are measured immediately after heating to 200, 225, 250, 275, and 300°C. Figures 2(b) and 3(b) show the profiles of specimens which are measured after keeping for 1h at the settled temperature. M-phase contents and $m(11\bar{1})/m(111)$ intensity ratio of these specimens are summarized in Table 2.

M-phase content of hipped specimens measured after keeping for 1h at the settled temperature becomes larger with the increase of heating temperature and reaches maximum at 250°C and then decreases with the increase of heating temperature from 275 to 300°C. When measured immediately after heating to the settled temperature, the amount of m-phase is not so large as that measured after keeping for 1h, although the amount of m-phase reaches to the maximum value at 250°C.

In case of pressureless sintered specimens, on the contrary, comparative amount of m-phase is observed in all range of the heating temperature from 200 to 300°C even on the specimens observed just after heating to the settled temperature.

The difference of the amount of m-phase content can be attributed to the difference of grain size and density between hipped and pressureless sintered specimens. The grain size of the hipped specimen of density of 6.07 Mg m^{-3} , is slightly finer than pressureless sintered specimen, the density of which is about 6.00 Mg m^{-3} due to the lower sintering temperature. Therefore the rate of t to m transformation of hipped specimen is not so high as that of the pressureless sintered specimens.

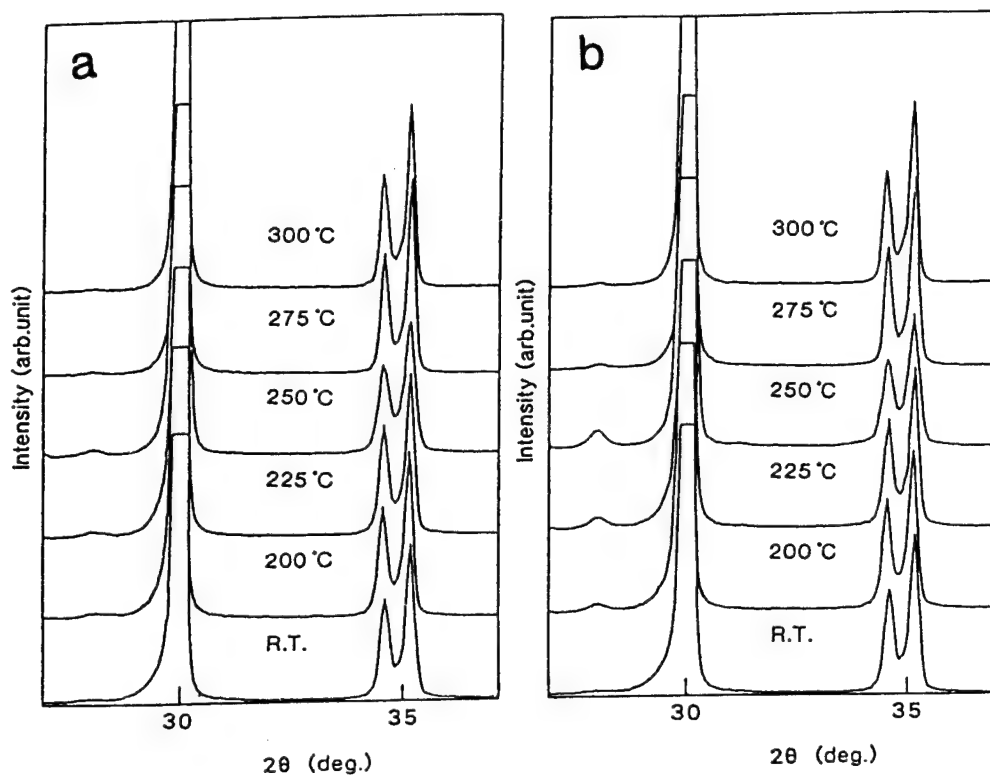


Fig. 2 XRD profiles for the polished surfaces of hipped specimens (a) immediately after heating to and (b) after keeping for 1h at 200, 225, 250, 275 and 300°C.

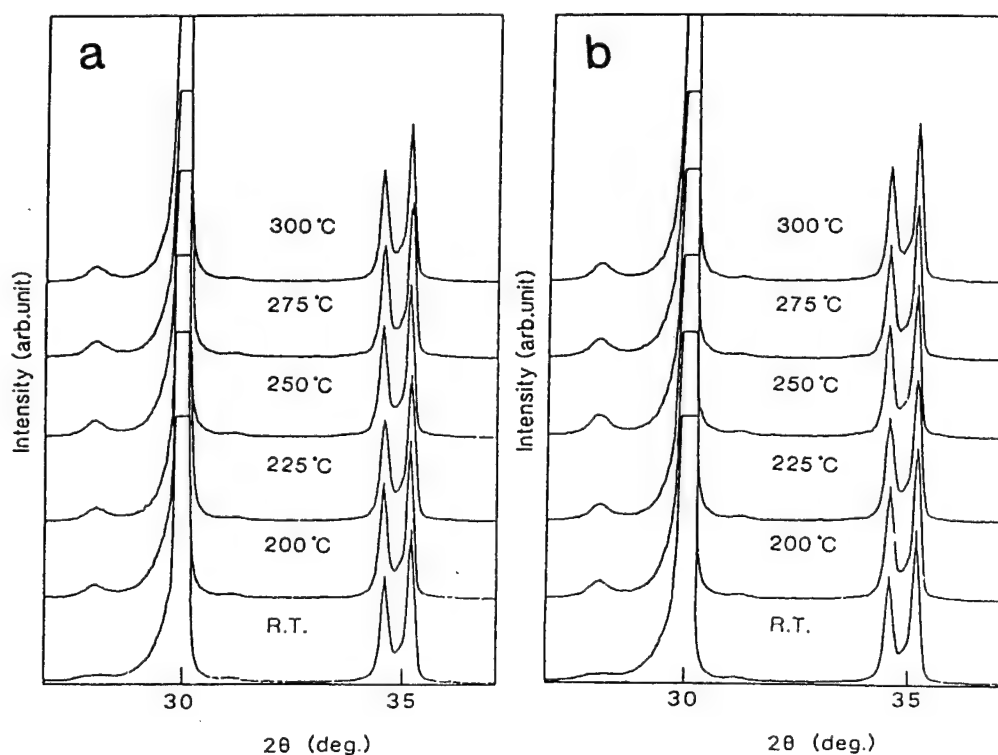


Fig. 3 XRD profiles for the polished surfaces of pressureless sintered specimens (a) immediately after heating to and (b) after keeping for 1h at 200, 225, 250, 275 and 300°C.

Table 2 Effects of thermal-stresses on the m-phase contents and XRD intensities

	H I P		P S	
	M-contents	M(11 $\bar{1}$)/M(111)	M-contents	M(11 $\bar{1}$)/M(111)
R.T.	0. 3	5. 1	0. 8	3. 0
200°C 0h	0. 6	6. 3	1. 8	8. 5
1h	1. 0	6. 2	2. 3	5. 5
225°C 0h	0. 7	8. 0	2. 0	9. 3
1h	1. 4	12. 0	2. 4	5. 2
250°C 0h	1. 2	7. 2	2. 2	6. 3
1h	2. 6	14. 0	3. 0	7. 0
275°C 0h	0. 5	5. 3	2. 2	9. 0
1h	0. 6	6. 3	2. 8	9. 9
300°C 0h	0. 3	2. 7	1. 8	4. 4
1h	0. 5	3. 5	2. 5	9. 0

The $\{111\}$ monoclinic peaks of above specimens show much greater disparity between the $(11\bar{1})$ and (111) peaks than is normally observed in diffraction studies of powders or randomly transformed precipitates of grains within a matrix. These observations indicate a marked preference for the formation of the $(11\bar{1})$ orientation as observed on the specimens of stress state during the mechanical grinding or fracture [8].

References

1. K. Kobayashi, H. Kuwashima & T. Masaki, Solid State Ionics, 3/4, 487-98(1981).
2. T. Saito & M. Shimada, J. Am. Ceram. Soc., 68, 356-59(1985).
3. M. Matsui, T. Soma, & I. Oda, J. Am. Ceram. Soc., 69(3), 198-202(1986).
4. T. Masaki, Int. J. High Technology Ceramics, 2, 85-98(1986).
5. T. Masaki & K. Shinjo, in Advances in Ceramics, Vol. 24, 709-20(1988).
6. R. C. Garvie & P. S. Nicholson, J. Am. Ceram. Soc., 55(6), 303-305(1972).
7. A. V. Virkar & R. L. K. Matsumoto, J. Am. Ceram. Soc., 69(10) C224-26(1986).
8. Y. Kitano, Y. Mori, A. Ishitani & T. Masaki, J. Am. Ceram. Soc., 71(8) C382-84(1988), *ibid.* 72(5) C854-55(1989).

MICROSTRUCTURE CONTROL AND THERMOELECTRIC CHARACTERISTICS OF POROUS SiC CERAMICS

Koumtoi K., Pai C.H., Takeda S., and Yanagida H.*

Department of Industrial Chemistry, Faculty of Engineering,
The University of Tokyo, 7-3-1 Hongo, Bunkyo-ku, Tokyo 113, Japan
*Research Center for Advanced Science and Technology,
The University of Tokyo, 4-6-1 Komaba, Meguro-ku, Tokyo 153, Japan

Porous SiC ceramics were proposed to be promising materials for high-temperature thermoelectric energy conversion. Through the thermoelectric property measurements and microstructure observations on the porous β -SiC, it was experimentally clarified that elimination of stacking faults and twin boundaries by grain growth is effective to increase the Seebeck coefficient and better grain-to-grain connectivity gives rise to higher electrical conductivity.

The development decades ago of thermoelectric materials has recently been resurrected in a flurry of activity once again for high-temperature thermoelectric power generation. For effective utilization of solar heat, nuclear energy and waste heat from industries, materials possessing high thermoelectric energy conversion efficiencies and usable at high temperatures are intensely required.

Thermoelectric semiconductors composed of heavy elements, such as PbTe, Bi_2Te_3 , etc., have already been commercially applied to both refrigeration and power generation /1/. Other materials as FeSi_2 /2/, boron carbide /3/, or BP /4/ are also considered as potential candidates. However, the materials so far developed are easily oxidized, decomposed, or melt above 1000°C and are not satisfactorily suitable to high-temperature applications.

Since ceramic semiconductors in general have high thermal stability and corrosion resistance, it would be highly effective to apply these materials to high-temperature thermoelectric energy conversion. Porous ceramics of silicon carbide have recently been found by the present authors /5/ to show high thermoelectric conversion efficiency at 700-1350K. Electrical conductivity, σ , of porous n-type SiC was comparable to or even higher than the reported values of single crystals, while thermal conductivity, κ , was kept as low as 1/10-1/30 of that for a dense ceramic. The striking phenomenon observed then was that the absolute value of Seebeck coefficient, α , for both n-type and p-type SiC always increases with increasing temperature. In this paper is reviewed how the microstructure of a porous SiC ceramic affects its thermoelectric property and are introduced some newly deduced guiding principles to improve the conversion efficiency.

Phonon-drag effect

The temperature dependences of Seebeck coefficient found in our previous study /5,6/ for porous SiC ceramics (Fig.1) cannot be explained by a simple semiconductor theory taking account only of the electron diffusion generation the thermoelectromotive force under the temperature gradient. Phonon contributions to the Seebeck effect, which is called a phonon-drag effect, have been found for metals and compound semiconductors at low temperatures /7/. Phonon-drag effect is associated with the interaction between current carriers and phonons leading to an apparent increase in the absolute Seebeck coefficient. The temperature dependences of Seebeck coefficient shown in Fig.1 were then postulated to be indicating a phonon-drag effect taking place in porous SiC ceramics /6/.

According to Parrott /8/, the phonon-drag Seebeck coefficient can be expressed as follows:

$$|\alpha| = |\alpha_0| + \frac{\tau_p}{\tau_{ep}} \cdot \frac{m^* s^2}{eT} \quad (2)$$

$$\frac{1}{\tau_p} = \frac{1}{\tau_{pp}} + \frac{1}{\tau_{pb}} + \frac{1}{\tau_{pe}} + \dots \quad (3)$$

where α_0 is the normal Seebeck coefficient without a phonon-drag effect, s the mean velocity of phonons, m^* the effective mass of a charge carrier, e the electronic charge, T the absolute temperature and τ is the relaxation time, respectively. Subscripts for relaxation time τ represent the types of collision process and for example τ_{ep} means the relaxation time for electrons scattered by phonons. Subscripts e , p , and b denote electron, phonon, and boundary, respectively. If phonon scattering by boundaries (stacking faults, dislocations, etc.) is predominant, relaxation time for the responsible phonon scattering would be expressed as follows:

$$\frac{1}{\tau_p} = \frac{1}{\tau_{pb}} = \frac{s}{L^*} \quad (4)$$

and this assumption was the only one which could explain the abnormal temperature dependences of Seebeck coefficient shown in Fig.1. Then, the second term of Eq.(2), α_p , can be written as follows, assuming current carriers (electrons or holes) are predominantly scattered by phonons:

$$\alpha_p = \frac{L^* s}{\mu_0 T} \quad (5)$$

where μ_0 is carrier mobility and its temperature dependence is expressed by the following equation.

$$\mu_0 = CT^{-n} \quad (6)$$

where C is a constant and the value n depends on the phonon mode. Carrier scattering by acoustic and optical phonons would give n values of 1.5 and 2.5, respectively.

Using these equations combined with a usual semiconductor theory, the observed temperature dependencies of Seebeck coefficient were simulated by curve-fitting analysis. Solid lines in Fig.1 represent the best fits obtained by a least squares method.

The L^*s is required to be increased to increase the absolute value of Seebeck coefficient and hence the figure of merit for thermoelectric energy conversion. Since L^* is the mean free path of acoustic phonons and is directly related to the microstructure, microstructural features should be taken into consideration for this purpose. In order to obtain high L^* , average grain size should be increased and structural defects within the SiC grains should be eliminated. However, the microstructural variation would also alter both electrical conductivity and thermal conductivity, so that the optimum microstructure must be sought for to realize the highest thermoelectric conversion efficiency.

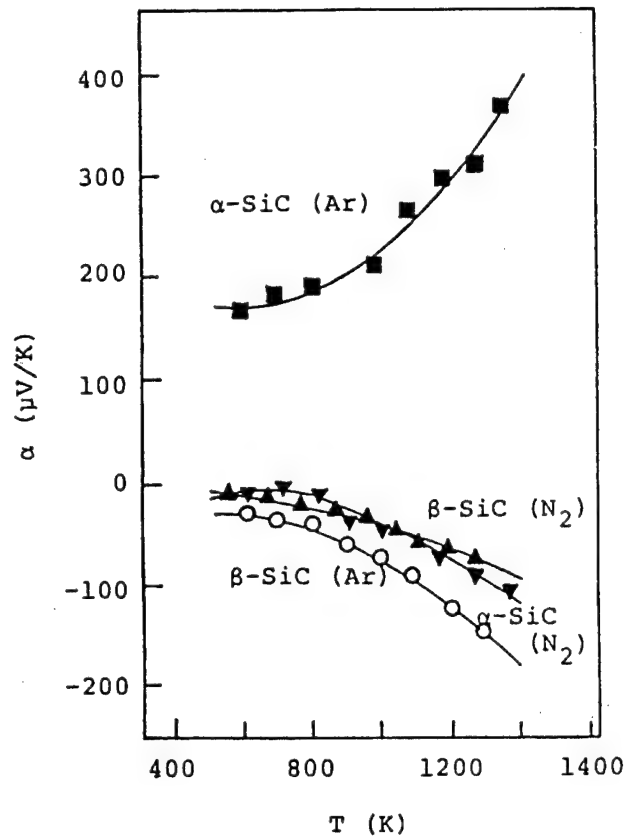


Fig.1 Temperature dependences of the Seebeck coefficient for porous SiC ceramics [5,6].

Role of microstructure

It was attempted to clarify the role of microstructure in thermoelectric properties of porous β -SiC ceramics /9/. Commercially available β -SiC powders (Central Glass Co., Ltd., average particle size $\sim 0.4 \mu\text{m}$) were isostatically pressed and sintered at 1750°C - 2200°C in nitrogen atmosphere. A rectangular bar was cut out from a sintered compact, polished and cleaned. Electrical conductivity and Seebeck coefficient were measured in Ar atmosphere using the technique previously reported /5/. Thermal conductivity was measured by the laser flash method, Scanning electron microscope (SEM) and high-resolution electron microscope (HREM) observations were carried out to examine the microstructure and stacking faults, respectively. XRD measurements were performed on the crushed powders using $\text{CuK}\alpha$ radiation with Ni filter and graphite monochromator.

Thermoelectric properties of β -SiC vary largely with sintering temperature and hence with microstructure variation. The measured σ , α , and κ at 1000°C are plotted against sintering temperature in Fig. 2. Both σ and α increase with increasing sintering temperature up to 2000°C and then decrease at higher temperatures, while κ practically remains unchanged. Similar tendencies were observed at other measuring temperatures.

Average size of β -SiC grains increased remarkably with increasing sintering temperature without noticeable densification as shown in Fig. 2. The authors have already reported /9,10/ that the density of stacking faults, decreased with increasing sintering temperature. The fact that the absolute value of Seebeck coefficient increases with increasing grain size (Fig. 2) and hence decreasing stacking fault density is closely related to the phonon-drag effect explained in the previous section. Decrease in the stacking fault density accompanied by grain growth increased the phonon mean free path, L^* , enhancing the phonon-drag effect leading to apparently larger Seebeck coefficient. That the Seebeck coefficient slightly decreased at above 2000°C (sintering temperature) must have been caused by phase transformation which was detected by both XRD measurement and SEM observation.

Increase in electrical conductivity as increasing sintering temperature up to 2000°C is partly ascribed to the increase in carrier concentration, since nitrogen incorporated into the SiC lattice during sintering temperature. Decrease in electrical conductivity at above 2000°C (sintering temperature) was possibly due to the $\beta \rightarrow \alpha$ transformation, since carrier mobility and hence electrical conductivity of α -SiC is lower in general compared to β -SiC /11/.

We have carried out another experiment in which the pressure of powder compaction was varied while sintering temperature and time were fixed to be 2000°C and 3h, respectively. Figure 3 shows the electrical conductivity and Seebeck coefficient increased at 1000°C as functions of compaction pressure. It can be seen that electrical conductivity increases with increasing pressure, while the Seebeck coefficient remains practically unchanged. As is also shown in Fig.3, relative density and average grain size are almost independent of the compaction pressure, so that the behavior of Seebeck

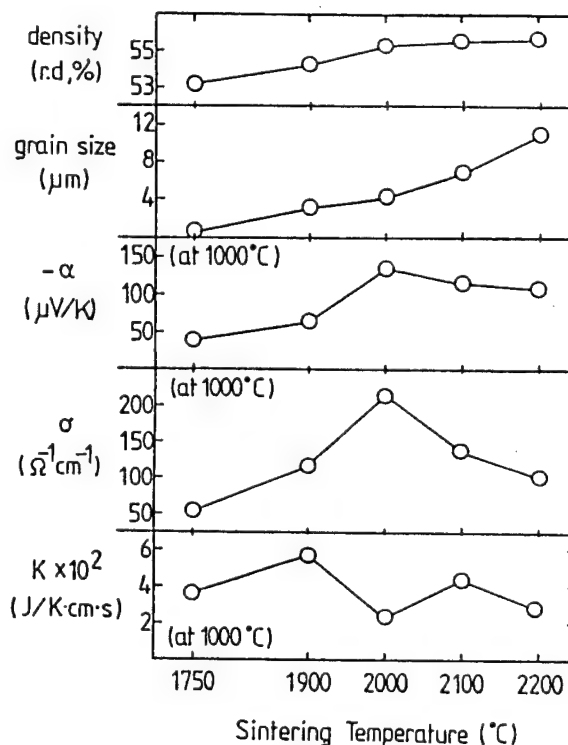


Fig.2 Thermoelectric properties vs. sintering temperature measured at 1000°C . Specimens were sintered for 3h in N_2 atmosphere (compaction pressure = 200kg/cm^2).

coefficient can be explained from the view point of the stacking fault density. Only the difference among four kinds of specimens lied in their grain connectivity, i.e. the grain-to-grain connectivity (in other words the neck radius) became larger as increasing compaction pressure. Thus, better grain-to-grain connectivity must have played a role partly in increasing conductivity.

Finally, thermoelectric properties of the specimens prepared under the same compaction pressure (200 kg/cm²) and sintered for 0.5-3h at 2000°C were compared. Figure 4 shows that the grain size, Seebeck coefficient, and electrical conductivity all increase slightly with increasing sintering time, while relative density remains unchanged. These results are considered to be consistent with the above mentioned tendencies in that slight increase in grain size gives rise to lower stacking fault density and better grain-to-grain connectivity hence causing larger Seebeck coefficient and higher electrical conductivity, respectively.

Conclusion

Some of the guiding principles so far obtained to improve the thermoelectric conversion efficiency of n-type β -SiC can be summarized as follows:

- (1) High grain-to-grain connectivity should be achieved in a porous body.
- (2) Structural defects, such as stacking faults and twin boundaries, ought to be eliminated.
- (3) $\beta \rightarrow \alpha$ phase transformation must be suppressed.

Acknowledgment

The authors are grateful to Mr. T. Ono of Central Glass Co., Ltd. for supplying the SiC powders, Mr. H. Iwasaki of Toa Nenryo Kogyo for sintering the specimens, and Prof. T. Sato of Chiba Institute of Technology for assistance in HREM observations. We are also indebted to Dr. W. Kondo and Dr. S. Mizuda of National Chemical Laboratory for Industry for giving us opportunities to use the apparatus for thermal conductivity measurement. This work was supported by Grant-in-Aid for Scientific Research on Priority Areas from the Japanese Ministry of Education, Science and Culture (No. 01603020).

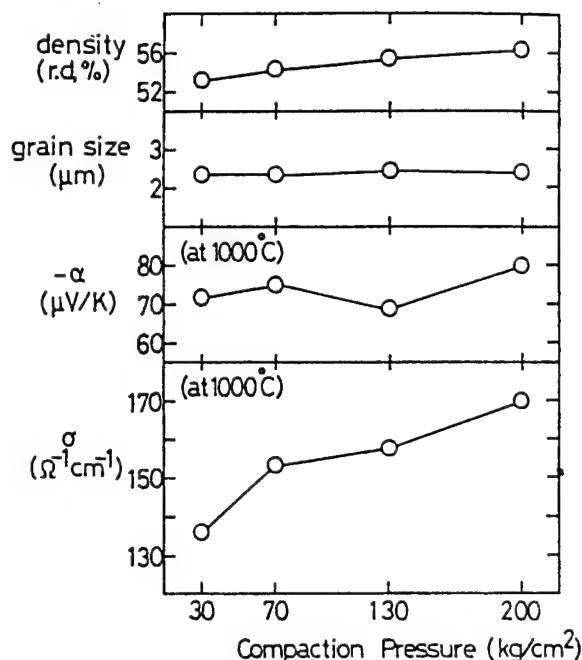


Fig.3 Thermoelectric properties vs. compaction pressure measured at 1000°C. Specimens were sintered at 2000°C for 3h in N₂ atmosphere.

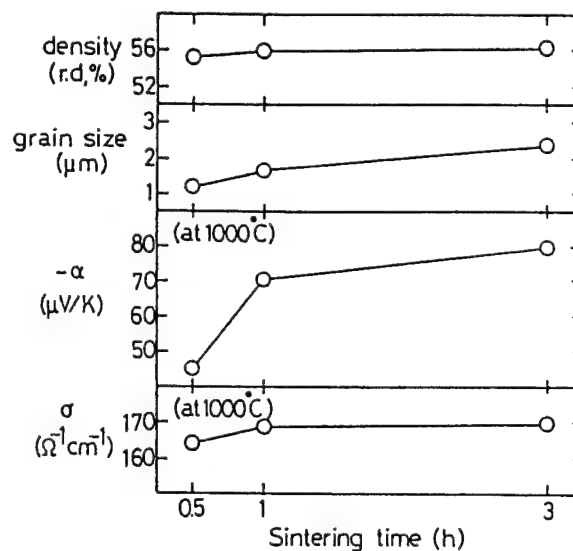


Fig.4 Thermoelectric properties vs. sintering time. Specimens were sintered at 2000°C in N₂ atmosphere (compaction pressure = 200 kg/cm²).

References

1. K.Uemura and I.Nishida, Thermoelectric Semiconductors and Their Applications, Nikkan Kogyo Shinbun (1988). IERE ON PAGE 1
2. T.Kojima, M.Okamoto and I.Nishida, Proc. 5th Int. Conf. Thermoelect. Energy Conversion (1984), 56.
3. D.Emin, Phys. Today, 40 (1987), 55.
4. Y.Kumashiro, M.Hirabayashi and S.Takagi, Abst. Annual Meet. Ceram. Soc. Jpn. (1989), 463.
5. K.Koumoto, M.Shimohigoshi, S.Takeda and H.Yanagida, J. Mater. Sci. Lett., 6 (1987), 1453.
6. K.Koumoto, M.Shimohigoshi, S.Takeda and H.Yanagida, Ceram. Trans., 2 (1989), 501.
7. Y.Suge (ed.), Thermoelectric Semiconductors, Maki Shyoten (1966), 295-355.
8. J.E.Parrott, Proc. Phys. Soc., B70 (1957), 540.
9. K.Koumoto, C.H.Pai, S.Takeda and H.Yanagida, Proc. 2nd Europe. Conf. Thermoelect., in press.
10. K.Koumoto, C.H.Pai, S.Takeda, T.Sato, and H.Yanagida, J. Am. Ceram. Soc., in press.
11. K.Koumoto, Sentan Gijutsu Highlight, 43 (1987), 1-5.

MECHANICAL PROPERTIES AND FATIGUE OF PIEZOELECTRIC CERAMICS

T. Taniimoto^{*}, T. Yamamoto^{**} and K. Okazaki^{*}

^{*} Department of Materials Science and Ceramic Technology, Sagami Institute of Technology,
Fujisawa, Japan

^{**} Department of Electrical Engineering, National Defence Academy, Yokosuka, Japan

Synopsis

An investigation was made on the mechanical properties of piezoelectric ceramics with the special emphases on the effects of poling in the samples. Both the static compression and repeated compression fatigue tests were conducted under the three electrically different conditions. In the first case, the poled samples were subjected to compression, under whose electrodes were electrically connected. In the second case, compression loading was applied on the specimen with both electrodes electrically insulated. In the third case, the compressive strength was measured on the thermally depoled samples. A statistical approach based on a two-parameter Weibull distribution was applied to the test data in order to evaluate the dispersion in the strength and then to compare the strength properties for three different test conditions investigated.

1. Specimen Preparation and Experimental Method

The material used in the present study is a commercial piezoelectric ignitors with the composition of $PbZrO_3$ - $PbTiO_3$ including the third component. The piezoelectric properties are listed in Table 1. The samples were made in the dimensions of 5 mm in diameter and 10 mm in thickness. Polarization was produced by applying a DC field. Depoling was made in such a way that firstly the samples were heated to above its Curie point and then cooled slowly again to below the Curie point. The parallelism of the end surfaces is extremely important in case of the compression test. Therefore each end surface of the sample was polished so that the parallelism could be attained. The specimen was loaded to failure at crosshead speed of 3.5 mm/min in static compression test.

Table 1. Piezoelectric properties of the samples investigated.

Frequency	Permittivity	Coupling factor	Piezoelectric constant	
fr (kHz)	$\epsilon_{33}^T / \epsilon_0$	k_{33} (%)	$d_{33}(10^{-12} \text{ m/V})$	$g_{33}(10^{-3} \text{ Vm/N})$
142.9	1496	69.7	337.4	25.6

Fatigue tests were conducted under axial cyclic compression at a frequency of 20 Hz by a electro-hydraulic fatigue testing machine. Stress ratio R ($\sigma_{\min}/\sigma_{\max}$) is fixed to be constant value of 0.1 in all the fatigue tests. Replication tests were performed to characterize the scatter in the strength.

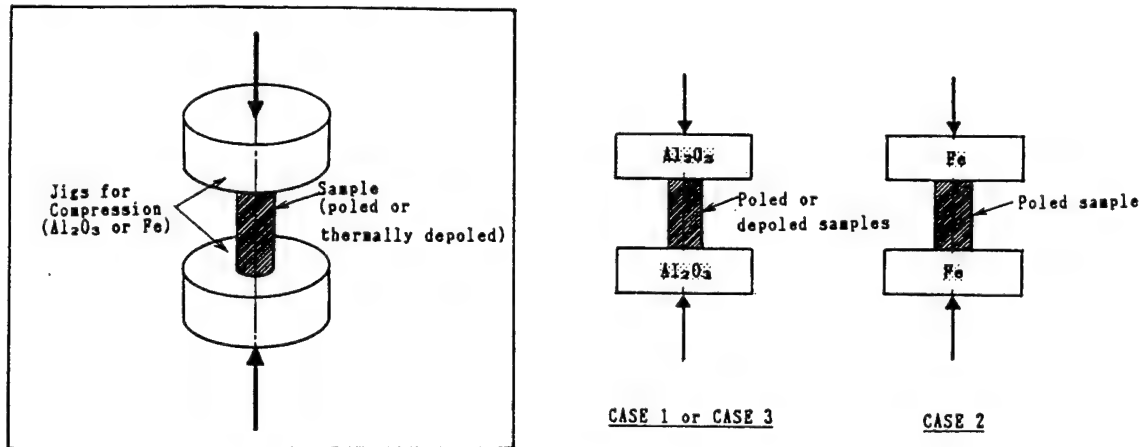


Fig.1. Explanatory illustration of compression tests.

Test conditions were varied in the three different ways. Firstly, the poled samples were subjected to compression, under whose electrodes were electrically connected. Secondly, compression loading was applied on the specimen with both electrodes electrically insulated. Thirdly, the compressive strength was measured on the thermally depoled samples. Hereinafter, these test conditions are referred in this paper to as CASE 1, CASE 2 and CASE 3, respectively. This is the same whichever it may be static compression or cyclic compression. Three different test conditions are illustrated in Figure 1.

2. Experimental Results and Discussion

In static compression test, ten replicates were used to characterize the scatter in the strength. In the statistical evaluation of the strength dispersion, it has been a standard practice to assume the underlying distribution to be of a two-parameter Weibull type. This model is characterized by a probability density function $f(x)$ and the associated cumulative distribution function $F(x)$ as follows:

$$f(x) = \frac{\alpha}{\beta} \left(\frac{x}{\beta}\right)^{\alpha-1} \exp\left\{-\left(\frac{x}{\beta}\right)^{\alpha}\right\} \quad (1)$$

$$F(x) = 1 - \exp\left\{-\left(\frac{x}{\beta}\right)^{\alpha}\right\} \quad (2)$$

where α and β are the shape parameter and scale parameter, respectively.

Mean value, variance and coefficient of variation of the two-parameter Weibull distribution are denoted here by $E[X]$, $V[X]$ and CV , respectively as shown below.

$$E[X] = \beta \cdot \Gamma\left(1 + \frac{1}{\alpha}\right) \quad (3)$$

$$V[X] = E[X^2] - (E[X])^2$$

$$= \beta^2 \left[\Gamma\left(1 + \frac{2}{\alpha}\right) - \Gamma^2\left(1 + \frac{1}{\alpha}\right) \right] \quad (4)$$

$$CV = \sqrt{V[X]} / E[X] \quad (5)$$

Table 2. Estimated Weibull parameters of compressive strength for CASE 1.

Shape parameter	Scale parameter	Mean	Standard deviation	CV
α	β (MPa)	$E[X]$ (MPa)	σ (MPa)	
32.37	777.96	763.23	47.87	0.0627

The results of statistical analysis on the actual compressive strength for CASE 1 are shown in Table 2. Estimation of parameters, α and β in the table was performed by the Least Square Method (LSM). The value of shape parameter in compressive strength is found to be large enough, compared with those of strength data which has been reported for ceramic materials. This indicates that the scatter of piezoelectric ceramics for CASE 1 test conditions is comparatively small, if the specimen preparation and actual testing has been carefully performed. These data were plotted on the Weibull probability paper as shown in Figure 2. The linearity of the test data supports the choice of the Weibull type.

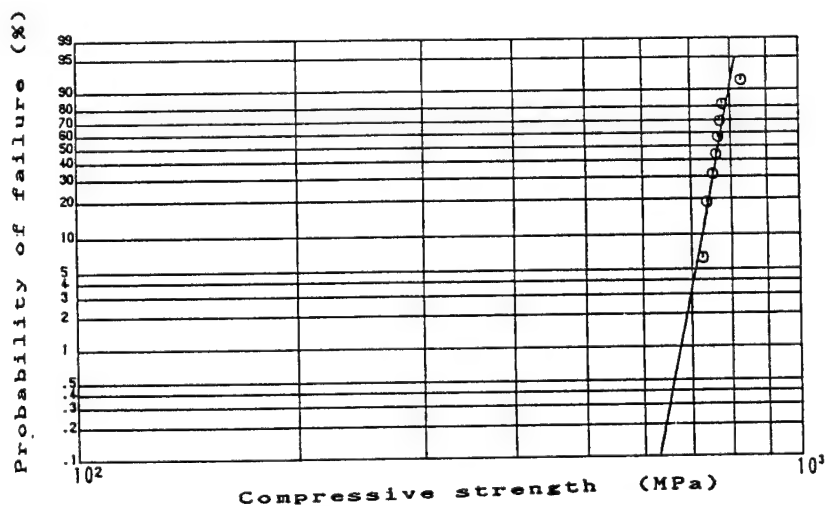


Fig.2. Statistical distribution of compressive strength.

Table 3. Estimated Weibull parameters of compressive strength for CASE 2.

Shape parameter	Scale parameter	Mean	Standard deviation	CV
α	β (MPa)	$E[X]$ (MPa)	σ (MPa)	
19.60	732.90	711.84	58.55	0.0794

Estimated results of Weibull parameters for CASE 2 are shown in Table 3. The value of shape parameter α is small if compared with that for CASE 1, although the scatter is still not large.

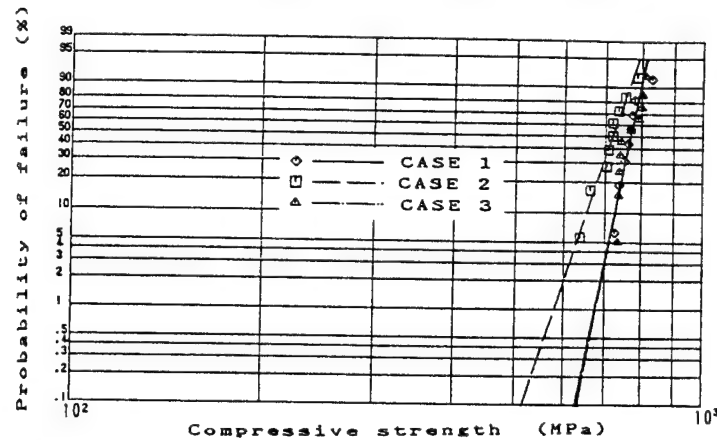


Fig.3. Comparison of compressive strength distribution.

In Figure 3, all the test data are plotted on the Weibull probability paper and the strength distribution for CASE 1, CASE 2 and CASE 3 were compared. As a result, strength distribution has been found to be almost the same between CASE 1 and CASE 3. On the other hand, strength distribution for the CASE 2 which is tested using poled sample placed between iron jigs is in the lower side and the slope of the theoretical line is flatter than those for the other cases. In CASE 2 the samples are supposed to be subject to mechanical depoling effect as the stress value is increased. That means the internal grain structure might be in inhomogeneity and instability. This is considered to be reflected in the larger scatter and lower strength compared with the other cases.

Photographs. 1 and 2 show the fractured surface of the specimens for CASE 1 and CASE 3. Significant difference has not been observed between two cases. However grain boundary fracture is in the tendency to be observed more in CASE 1 than in CASE 3.



Photo.1. Fracture surface of the sample for CASE 1.

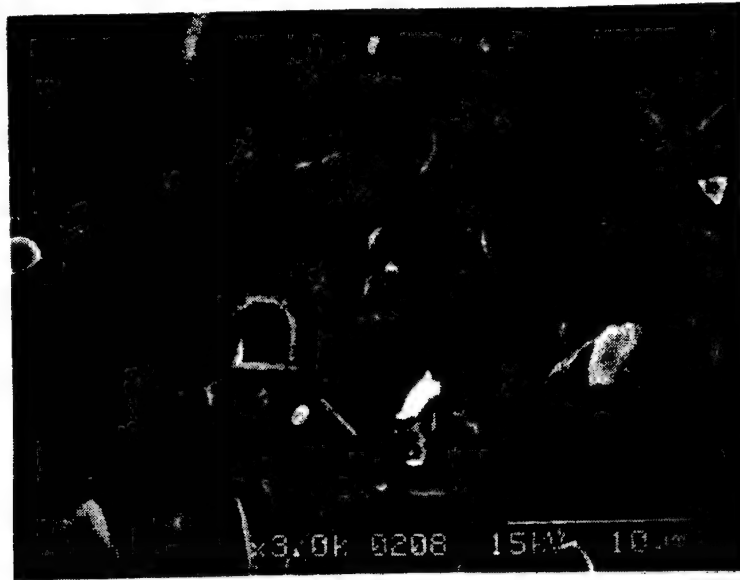


Photo.2. Fracture surface of the sample for CASE 3.

Figure 4 shows the maximum cyclic stress amplitude plotted as a function of the number of cycles to fatigue failure for CASE 1 and CASE 3. The linear approximation between the maximum cyclic stress and expected fatigue life in semi-log scale is drawn by a solid line. Arrow mark in the figure signifies the censored data at 10^7 cycles, indicating that the specimen was not failed within the present work. From the comparison between CASE 1 and CASE 3, it can be seen that the fatigue life at lower stress level for CASE 1 is longer than that for CASE 3. As a conclusion of fatigue test, poled samples have a higher fatigue resistance in a longer life region than thermally depoled samples when it has been used between electrically insulated jigs.

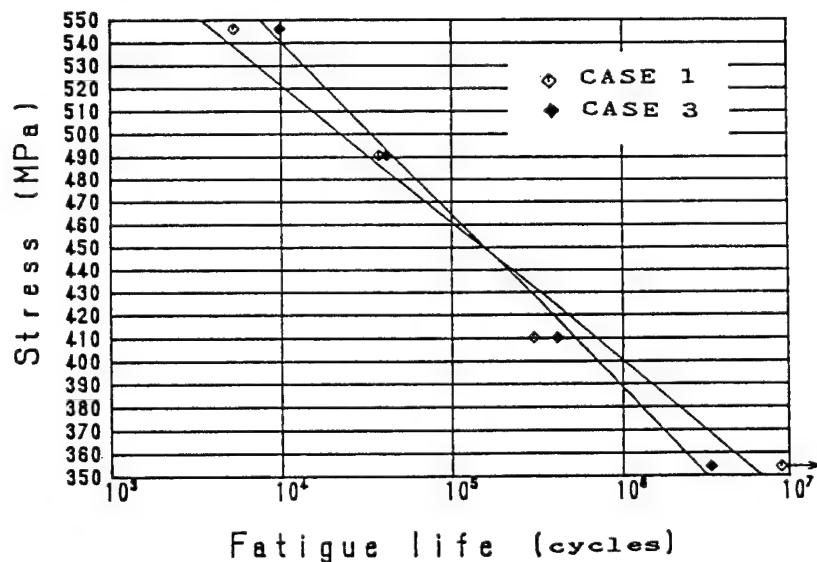


Fig.4. Fatigue S-N diagram.

Direct Preparation of BaTiO₃ Powders and Thin Films from Titanium Metal by Hydrothermal-Electrochemical Method

Seung-Eul Yoo, Nobuo Ishizawa and Masahiro Yoshimura

Research Laboratory of Engineering Materials, Tokyo Institute of Technology, 4259 Nagatsuta, Midori, Yokohama, 227 Japan

ABSTRACT

BaTiO₃ fine powders and thin films have been prepared directly from titanium metal substrates by a new technique, hydrothermal-electrochemical method, where a direct electric current has been applied between the anode of Ti plate and the cathode of Pt plate, placed in a high temperature-high pressure vessel containing Ba²⁺ solutions. Pure and fine powders of BaTiO₃ have been produced in 0.5N-Ba(NO₃)₂ solution at 250°C by applying a constant current density of 100 mA/cm². On the other hand, thin films of polycrystalline cubic BaTiO₃ have been formed on Ti metal plate in 0.25 ~ 0.5N-Ba(OH)₂ solutions above 100°C under the saturated vapor pressures with the current density of 10 ~ 100 mA/cm² and the treatment time of 30 ~ 80 min. The BaTiO₃ films had the thickness of submicrometer order, with no apparent pores nor defects. The crystallinity of the films was quite well in spite of their quite low formation temperatures.

1. INTRODUCTION

Barium titanate, BaTiO₃ is a well-known ferroelectric and piezoelectric material. Its usefulness has attracted much attention in electronics and other branches of engineering as well as in ceramics. A variety of techniques have therefore been developed for preparing powders and thin films of BaTiO₃.

In the most conventional method, BaTiO₃ powders have been prepared by solid-state reactions from powder precursors [1]. In addition to this process, there exist many kinds of chemical processes [2-8], mainly solution techniques, for preparing barium titanate powders at lower temperatures than those required for the solid-state reactions. The advantages of these chemical processes are to form powders with controlled size and shape, having highly pure and homogeneous composition. On the other hand, they have disadvantages i.e., low crystallinity, aggregation of particles and high costs for production. To improve the crystallinity, moderate heating process after the formation of powders is needed in most cases.

Also, many attempts have been performed to obtain BaTiO₃ films [9-12]. They include physical vapor deposition techniques such as vacuum

deposition and sputtering, or chemical processing such as spray coating and dip coating of metal organic compounds using sol-gel techniques. These methods generally need heating processes to crystallize BaTiO_3 after forming an amorphous film on the substrates. The crystallization temperatures are mostly higher than 500°C , which often cause thermal roughening of the film surface and/or the peeling-off problems. Therefore, the alternative processes have been required to be formed in various fields of the electronic industries.

In the present work, we report the preparation of BaTiO_3 powders and thin films [13] by a new technique which we have named "hydrothermal-electrochemical method" and believe to have a variety of superiority to the techniques mentioned above.

2. EXPERIMENTAL

A titanium metal plate(working electrode) was connected to the anode by a platinum wire, then it was set in an autoclave together with a platinum plate(counter electrode) as the cathode as shown in Fig 1. The distance between the working electrode and the counter electrode was 3.0 cm. A direct electric current was applied in the electrolytic solution at elevated temperatures, room temperature $\sim 250^\circ\text{C}$, under the saturated vapor pressures ranging between 0.1 and 1.8 MPa. The treatment was performed in various electrolytic solutions, $\text{Ba}(\text{NO}_3)_2$ (0.01-0.5N), 0.1 N- BaCl_2 , pure H_2O and $\text{Ba}(\text{OH})_2$ (0.25 to 0.5N) for the preparation of BaTiO_3 powders and thin films respectively .

The hydrothermal-electrochemical treatment was carried out galvanostatically with the applied current density between 10 and 100 mA/cm^2 using a galvanostat (Kikusui electronics Co., Type PAD 1K-0.2L) in an electrolytic autoclave (NRD Co., Type AAC-2030). A silica glass or teflon beaker was set for preventing the autoclave wall from corrosion by contacting electrolytic solution. The powders formed at the bottom of the beaker and the thin films formed on the Ti metal plate after the hydrothermal-electrochemical treatment were examined by X-ray diffractometry, Scanning Electron Microscopy (SEM) and Transmission Electron Microscopy (TEM). The capacitance of the film was also mea-

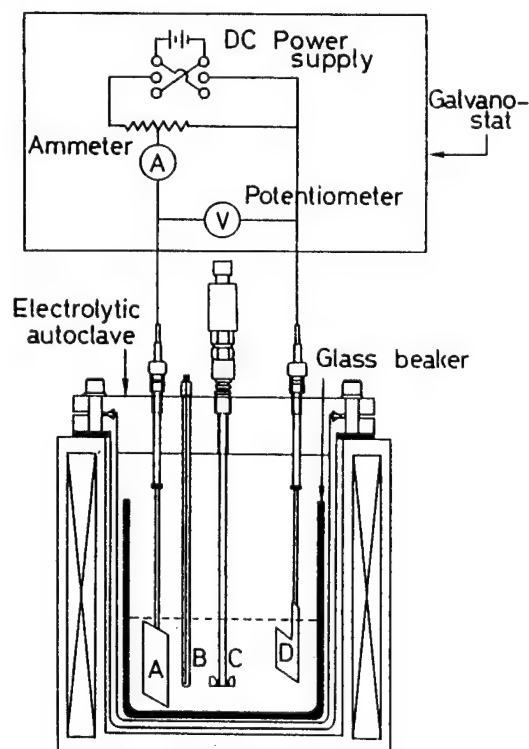


Fig.1 Schematic illustration of the electrochemical cell and circuit arrangements for hydrothermal-electrochemical treatment. (A) Counter electrode (Pt plate), cathode; (B) Thermocouple; (C) Stirrer; (D) Working electrode (Ti plate), anode.

sured using the LCR meter(YHP 4284A) by depositing Ag electrode of 2 mm ϕ in diameter.

3. RESULTS and DISCUSSION

3.1 Preparation of BaTiO₃ powders

Anatase was the only product of hydrothermal- electrochemical treatment of titanium plate in H₂O at 200^o to 250^oC. Similarly, when a 0.1N-BaCl₂ solution was used as an electrolytic solution, only anatase powders were yielded even at 250^oC.

Hydrothermal-electrochemical treatment of titanium metal plate in 0.1N-Ba(NO₃)₂ solution yielded also only TiO₂ (anatase) powders with low crystallinity below 200^oC regardless of the applied current density. However, when the treatment temperature was raised to 250^oC, perovskite BaTiO₃ (cubic or pseudocubic phase) began to form as the product.

On the other hand, BaTiO₃ was formed already at 200^oC in solutions with a higher concentration of barium (0.5N-Ba(NO₃)₂), although a small amount of BaCO₃ or TiO₂ (anatase) formed in addition to BaTiO₃ at this temperature. Figure 2 shows the X-ray diffraction patterns of the powders produced and the surfaces of working electrodes after hydrothermal-electrochemical treatments of titanium metal plates in 0.5N-Ba(NO₃)₂ solution. At 250^oC, pure BaTiO₃ powders could be obtained, whereas the surface of the working electrode was always only TiO₂ after hydrothermal- electrochemical treatment of titanium metal plate in Ba(NO₃)₂ solution under all the conditions studied.

Figure 3 illustrates the formation diagram of the powder products under the various conditions for an applied current density of 100 mA/cm². As shown in this diagram, BaTiO₃ has not been formed at lower temperatures, and in low- concentration barium solutions. When 0.5N-Ba(NO₃)₂ solution was used, pure BaTiO₃ formed at 250^oC as shown in

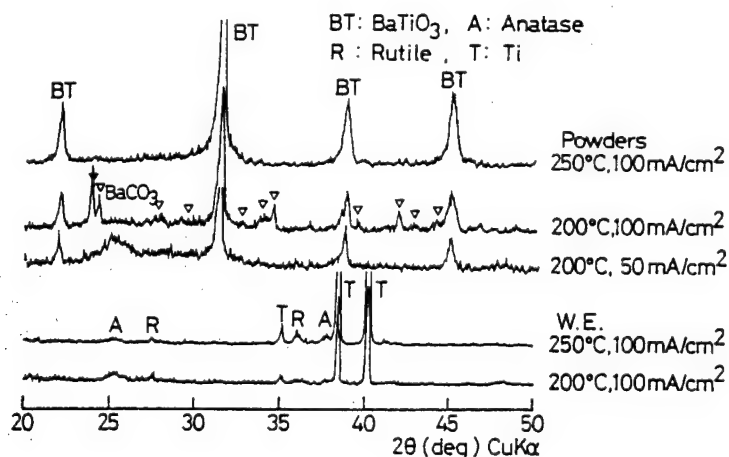


Fig.2 X-ray diffraction patterns of the powders produced and surfaces of working electrodes in 0.5N-Ba(NO₃)₂ solution under various conditions.

Fig.2. These results apparently indicate that the production of BaTiO_3 is dependent on the treatment temperature and/or solution species and concentration.

A transmission electron micrograph of the powder product yielded in 0.5N- $\text{Ba}(\text{NO}_3)_2$ solution at 250°C is shown in Fig.4. The products consisted of submicrometer fine powders of cubic or pseudocubic BaTiO_3 .

Many studies on the preparation of BaTiO_3 , of which the stable form is tetragonal at room temperature, have reported that powders made by wet chemical processes generally have a cubic perovskite-type crystal structure [7,14-16]. Similarly, in the present hydrothermal-electrochemical treatment, the BaTiO_3 powders had a cubic (or pseudocubic) structure. This is considered to be caused by the fine particle sizes (Fig.4).

Figure 5 shows some typical cell voltage-time (V-t) curves, where the voltage between the titanium anode as working electrode and the platinum cathode as counter electrode was measured, during hydrothermal-electrochemical treatment of titanium metal plate in $\text{Ba}(\text{NO}_3)_2$ solution under various conditions.

In the 0.5N- $\text{Ba}(\text{NO}_3)_2$ solution, the cell voltage increased with time up to 40 to 50 V and then showed vigorous fluctuation at 250° and 200°C . In these conditions, BaTiO_3 powders produced after hydrothermal-electrochemical treatment as shown in Fig.2. However, if the cell voltage did not increase to higher values BaTiO_3 was never formed as in the case of 0.1N, 200°C , 50 mA/cm^2 shown in Fig.5. In this case the cell voltage fluctuated within ± 2 V around 10 to 15 V and the powder produced was only anatase. These phenomena clearly suggest that a critical cell voltage is necessary to form BaTiO_3 .

Considering the V-t curves, the considerable fluctuation of cell voltage beyond 20 to 50 V corresponds to dielectric breakdown of surface-oxidized titania film, probably accompanied by sparking, during hydrothermal-electrochemical treatment [17]. A critical cell voltage is

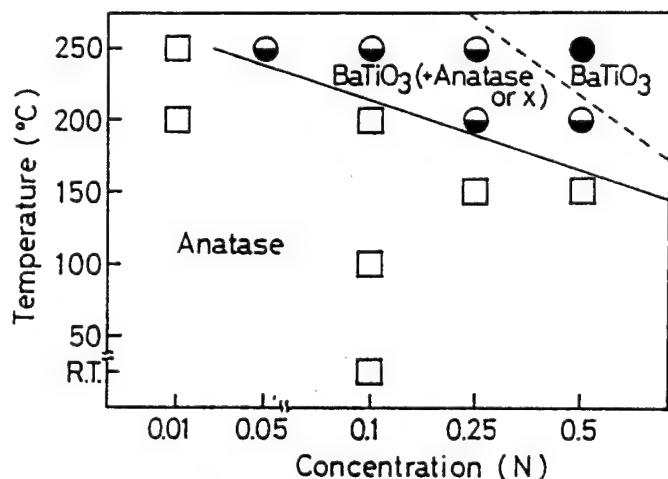


Fig.3 Formation diagram of powder products by hydrothermal-electrochemical treatment of Ti in $\text{Ba}(\text{NO}_3)_2$ solutions. Current density: 100 mA/cm^2 .

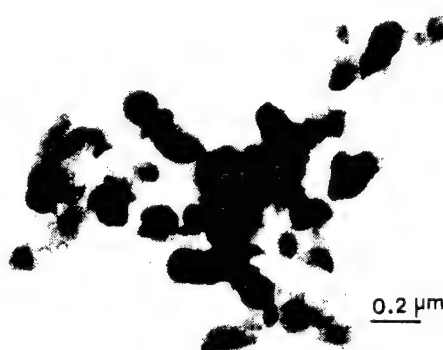


Fig.4 TEM micrograph of the BaTiO_3 powders obtained after hydrothermal-electrochemical treatment of Ti plate in 0.5N- $\text{Ba}(\text{NO}_3)_2$ solution at 250°C .

necessary for adherent surface oxide breakdown or electrochemical dissolution.

Figure 6 shows the relation between initial breakdown voltage and concentration of $\text{Ba}(\text{NO}_3)_2$ solutions at 250°C for an applied current density of 100 mA/cm^2 . The initial breakdown voltage was almost independent of the concentration of the solution. From this result, we can conclude that the surface oxide (TiO_2) grew to a certain thickness and then breakdown occurred resulting in the formation of BaTiO_3 .

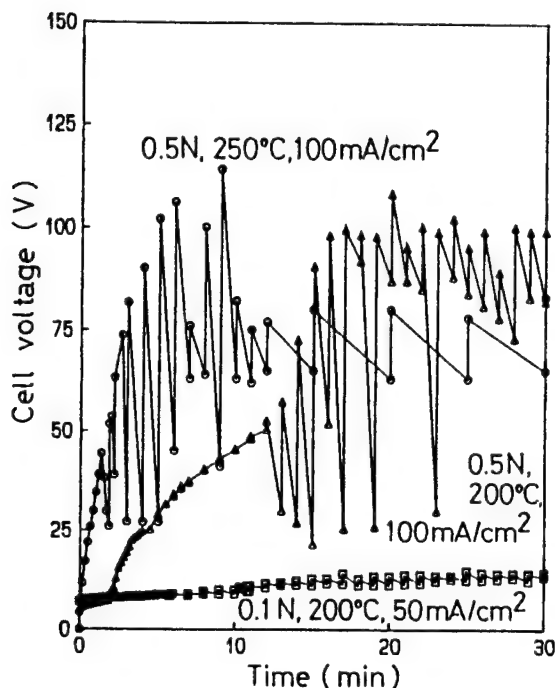


Fig.5 Typical cell voltage-time(V-t) curves during hydrothermal-electrochemical treatment of Ti plate in $\text{Ba}(\text{NO}_3)_2$ solution.

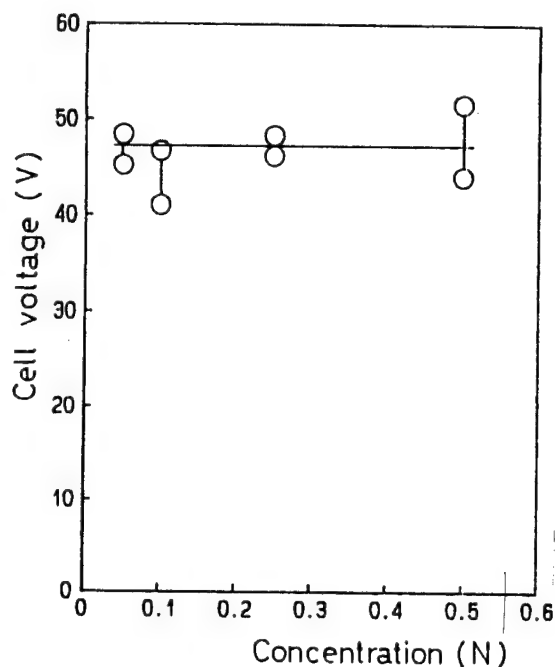


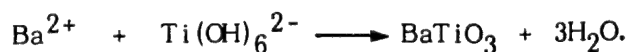
Fig.6 Relation between initial breakdown voltage and concentration at 250°C for an applied current density of 100 mA/cm^2 .

3.2 Preparation of BaTiO_3 thin films

Figure 7 shows the X-ray diffraction patterns of the surface of BaTiO_3 films produced by the hydrothermal-electrochemical method in $\text{Ba}(\text{OH})_2$ solution. According to the X-ray diffraction analysis, the cubic or pseudo-cubic BaTiO_3 was only detected on titanium metal substrate at temperatures above 100°C . At low temperatures such as the room temperature, the product was not BaTiO_3 but TiO_2 . Under the conditions at temperatures above 100°C with the current density of 10 to 100 mA/cm^2 in $0.5\text{N}-\text{Ba}(\text{OH})_2$ solutions, dense thin films showing multiple interference colors were formed. These films had smooth and homogeneous surface without visible pores or defects from the SEM observations.

The formation mechanism of BaTiO_3 thin film in $\text{Ba}(\text{OH})_2$ solution is probably different from that of BaTiO_3 powders which results from the breakdown of surface-oxidized titania film in $\text{Ba}(\text{NO}_3)_2$ solution. One of the possible mechanisms to form BaTiO_3 thin film in the present

technique is as follows:



These reactions may proceed in the hydrothermal $\text{Ba}(\text{OH})_2$ solution near the anode in order to precipitate crystalline BaTiO_3 on the titanium anode plate. The capacitance measured for the film formed at 150°C by the applied current density of 13 mA/cm^2 was 70 nF with $\tan \delta = 15 \%$. The value corresponds to the dielectric constant of ~ 300 for $0.1 \mu\text{m}$ of film thickness estimated from the weight gain of the film.

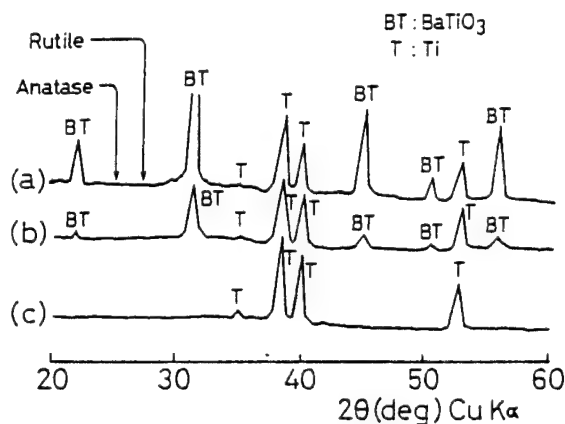


Fig.7 X-ray diffraction patterns of the surface of BaTiO_3 films produced by the hydrothermal-electrochemical method in $\text{Ba}(\text{OH})_2$ solution. (a) 200°C , 30 min; (b) 100°C , 30 min; (c) room temperature, 10 min.

References

1. T. Kubo and K. Shinriki, *Kogyo Kagaku Zasshi* 56 (1953) 335.
2. W. S. Clabaugh, E. M. Swiggard and R. Gilchrist, *J. Res. Natl. Bur. Stand.* 56 (1956) 289.
3. K. Kiss, J. Magder, M. S. Vukasovich and R. J. Lockhart, *J. Am. Ceram. Soc.* 49 (1966) 291.
4. A. N. Virkar, K. Bandyopadhyay and A. Paul, *Trans. Indian Ceram. Soc.* 44 (1985) 78.
5. D. Hennings and W. Mayer, *J. Solid State Chem.* 26 (1978) 329.
6. B. J. Mulder, *Am. Ceram. Soc. Bull.* 49 (1970) 990.
7. K. S. Mazdiasni, R.T. Dolloff and J. S. Smith II, *J. Am. Ceram. Soc.* 52 (1969) 523.
8. S. S. Fiaschen, *J. Am. Chem. Soc.* 77 (1955) 6194.
9. C. Feldman, *Rev. Sci. Instrum.*, 26 (1955) 462.
10. A. E. Feuersanger, A. K. Hangenlocher and A. L. Solomon, *J. Electrochem. Soc.*, 111 (1964) 1387.
11. M. Munekata, *Kogyo Zairyo*, 28 (1980) 32.
12. H. Igarashi and M. Yuasa, *Electronic Ceramics (Japan)*, 89 (1987) 19.
13. M. Yoshimura, S. E. Yoo, M. Hayashi and N. Ishizawa, *Jpn. J. Appl. Phys.*, Submitted.
14. S. Kaneko and F. Imoto, *Nippon-Kagaku-Kaishi* 6 (1975) 985.
15. V. Ern, *J. Am. Ceram. Soc.* 43 (1960) 226.
16. H. Yamamura, S. Shirasaki, K. Takahashi and M. Takagi, *Nippon-kagaku-kaishi* 7 (1974) 1155.
17. S. E. Yoo, M. Yoshimura and S. Sōmiya, *Proceedings of MRS International Meeting on Advanced Materials, Tokyo, May/June, 1988, in Press.*

TSFZ法による高温超伝導酸化物単結晶の育成

児嶋 弘直, 田中 功 (山梨大・工)

GROWTH OF SUPERCONDUCTING OXIDE SINGLE CRYSTALS BY TSFZ METHOD

KOJIMA, H and Tanaka, I

Institute of Inorganic Synthesis, Faculty of Engineering, Yamanashi University, Miyamae 7, Kofu 400, Japan

High quality large single crystals of $\text{La}_{2-x}\text{Sr}_x\text{CuO}_4$ were grown by the traveling solvent floating zone method (TSFZ method). The crystals up to about 6 mm diameter and 40 mm length were obtained. The composition of the grown crystals was uniform and was determined to be $\text{La}_{1.86}\text{Sr}_{0.14}\text{Cu}_{0.97}\text{O}_{3.89}$. The single crystals were superconductors with $T_c = 37.5\text{K}$ and $\Delta T_c = 1.1\text{K}$, and had a significant anisotropy of the electrical resistivities at the non-superconducting state.

INTRODUCTION

Since the recent discovery of high- T_c superconductors of the $(\text{La}_{1-x}\text{M}^{2+}_x)_2\text{CuO}_4$ type, where M^{2+} is Ba or Sr, its crystal structure and the physical properties were investigated actively [1-3]. The measurement of their properties as single crystals gives us further information of the high- T_c superconducting mechanism. Therefore, it is desired to obtain good quality and sizable single crystals of $(\text{La}_{1-x}\text{M}^{2+}_x)_2\text{CuO}_4$.

La_2CuO_4 melts incongruently at 1320°C and decompose to La_2O_3 and the liquid [4]. Cupric oxide (CuO) melts with a loss of oxygen and vaporization of CuO at 1096°C under an oxygen pressure of 1.0 atm [5], so that these phenomena disturb operations for crystal growth of La_2CuO_4 . The single crystals of Sr- or Ba-doped La_2CuO_4 have been grown by the flux method using CuO or PbO as the flux [3, 5-6] and the top seeded solution method with used CuO or $\text{Li}_2\text{CO}_3 + \text{B}_2\text{O}_3$ solvents [7-8]. Directional solidification from eutectic composition by the floating zone method was reported further [9], but the grown boules composed of $(\text{La}, \text{M}^{2+})_2\text{CuO}_4$ and CuO were not single crystals. The $(\text{La}, \text{M}^{2+})_2\text{CuO}_4$ crystals grown by the top seeded solution method were sizable, but they did not too contain Sr^{2+} or Ba^{2+} to be superconducting. The crystals grown by the flux method were sizable and superconductive, but their superconducting transition were broad because of flux inclusion. Therefore, sizable and high quality single crystals of $(\text{La}, \text{M}^{2+})_2\text{CuO}_4$ have not yet been obtained. In this study, the single crystals of $\text{La}_{2-x}\text{Sr}_x\text{CuO}_4$ were grown by the traveling solvent floating zone (TSFZ) method, which has been described in detail elsewhere [10], and the grown crystals were characterized the quality and the superconductive transition.

THE PRINCIPLE OF TSFZ METHOD

According to the reported phase diagram of $\text{La}_2\text{O}_3\text{-CuO}$ system, La_2CuO_4 is known to decompose at the peritectic temperature of 1320°C . The solid of peritectic compound can coexist in equilibrium with the liquidus phase which corresponds to the portion of liquidus curve between the peritectic and eutectic temperature. Such a liquid phase can be used as a solvent for the growth of single crystal of peritectic compound.

The sintered rod of the solvent is put like sandwich between a sintered feeding rod and a seed crystal whose composition are stoichiometric. This rod is placed inside the infrared growth furnace where the floating zone method is applied. At first, the part of solvent phase was melted, then the feeding rod was inserted to molten solvent zone by slow moving down the furnace. The lower part of molten zone was getting to cool to deposit the crystal on the seed crystal because of temperature gradient. If this process is carried out constantly throughout the run, the single crystals of peritectic compound could be obtained on a seed crystal. This procedure is called as the Traveling Solvent Floating Zone method (TSFZ) which is the application of zone levelling technique introduced by Pfann, because the solvent phase had traversed nearly end to end of feeding rod.

EXPERIMENTAL PROCEDURE

The starting materials for preparation of the feed rods and the solvents were La_2O_3 , CuO and SrCO_3 , which had a 99.9% purity respectively. Stoichiometric amounts of the raw materials, in which the content of Sr was $x=0.15$, were mixed in ethanol, dried, and calcined at 850°C for 12 h in air. The pre-heated powder was formed into a cylindrical shape of 6 mm in diameter by 50 mm in length, and pressed at a hydrostatic pressure of about 100 MPa. The rod was sintered at 1000 to 1200°C for 12 h in oxygen and then used as the feed rod. The solvents, in which the compositions were varied, contained CuO from 55 to 80 mol% and SrO from $x=0.15$ to 0.20, and were prepared in the same way as the feed rods.

The apparatus for crystal growth was an infrared heating furnace of the double ellipsoidal type (Nichiden Machinery Ltd.) with two 1.5 kW halogen lamps as the heat source. The growth conditions were as follows. Feed and seed shafts were rotated oppositely at rates of 30 rpm. The growth rate was 1.0 mm/h. The atmosphere in the furnace was an oxygen gas under the pressure of 1.0×10^2 to 2.0×10^2 kPa for preventing the vaporization of CuO from the melt.

The crystals were characterized by using XRD method and EPMA. The superconductive properties of the grown crystals were investigated by measurement of electrical resistivity. The electrical resistivities of the grown crystals were measured by the four-probe method.

RESULTS AND DISCUSSION

K. Oka had reported that the La_2CuO_4 solid was in equilibrium with the liquid between about 75 and 90 mol% in the $\text{La}_2\text{O}_3\text{-CuO}$ system[7]. When the mixture of 80 mol%CuO and 20 mol% La_2O_3 was molten under an oxygen gas of 2.0×10^2 kPa which is higher than an atmospheric pressure, the products were La_2CuO_4 and CuO. This result suggests that the vaporization of CuO from the melt is prevented by increasing the oxygen pressure of the growth atmosphere to be higher than the atmospheric pressure.

Fig.1 shows an as-grown boule of $\text{La}_{2-x}\text{Sr}_x\text{CuO}_4$, which was grown by using a solvent of 78 mol%CuO. The as-grown boule was 6 mm in diameter and 40 mm long and black with metallic luster, and did not contain inclusions such as La_2O_3 . The crystals had two facets perpendicular to the growth direction. The back-reflection Laue X-ray photograph of the facet displayed sharp diffraction spots and revealed a 4-fold rotation axis. The grown crystals were

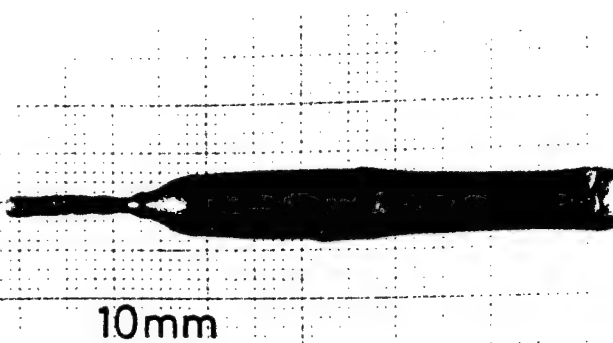


Fig.1 As-grown boule of $\text{La}_{2-x}\text{Sr}_x\text{CuO}_4$

Table 1 Properties of $\text{La}_{2-x}\text{Sr}_x\text{CuO}_4$ grown crystals

	Analysis (wt%)				
	La	Sr	Cu	O	Total
Analyzed values	65.5(2)	3.14(7)	15.67(7)	15.8(2)	100.11
Calculated values ($x=0.15$)	64.82	3.32	16.03	15.83	100.00
Chemical composition	$\text{La}_{1.86}\text{Sr}_{0.14}\text{Cu}_{0.97}\text{O}_{3.89}$				
	Lattice parameters (\AA)				
	a	c			
Measured values	3.793(3)	13.19(2)			
Sintered $\text{La}_{1.85}\text{Sr}_{0.15}\text{CuO}_4$	3.790(3)	13.21(2)			

thus identified as single crystals, and the crystallographic plane of the facet was (001).

The results of the analysis and the lattice parameters of the $\text{La}_{2-x}\text{Sr}_x\text{CuO}_4$ crystals are shown in table 1. The composition of the crystals was uniform along the radius and length of the crystals as analyzed by EPMA. The La concentration of the grown crystals was higher than that of the feeds, and the concentration of Sr and Cu of the crystals were lower than that of the feeds, respectively. Thus the chemical composition of the

crystals was determined to be $\text{La}_{1.86}\text{Sr}_{0.14}\text{Cu}_{0.97}\text{O}_{3.89}$. $\text{La}_{2-x}\text{Sr}_x\text{CuO}_4$ crystals had a tetragonal symmetry, and the lattice parameters were determined to be $a=3.793 \pm 0.003\text{\AA}$ and $c=13.20 \pm 0.02\text{\AA}$, which were close to values obtained from the sintered $\text{La}_{1.85}\text{Sr}_{0.15}\text{CuO}_4$.

Fig. 2 shows the temperature dependence of the electrical resistivities of the $\text{La}_{2-x}\text{Sr}_x\text{CuO}_4$ grown crystals. It was obvious from the resistivities curves that the $\text{La}_{2-x}\text{Sr}_x\text{CuO}_4$ grown crystals are superconductors with $T_c=37.5\text{K}$ and $\Delta T_c = 1.1\text{K}$. The superconducting properties of the $\text{La}_{2-x}\text{Sr}_x\text{CuO}_4$ grown crystals is significantly superior to that of $\text{La}_{2-x}\text{Sr}_x\text{CuO}_4$ single crystals reported previously, $T_c=30\text{K}$ and $\Delta T_c = 15\text{K}$ [6]. Indeed, the resistivity along the c -axis is several hundreds times higher than that parallel to the a -axis at the non-superconducting state. The resistivity along the a -axis at the non-superconducting state increases as the temperature increases, and shows a metallic behavior. However, the resistivity along the c -axis at the non-superconducting state decreases as the temperature increases up to about 200K and shows a semiconductive behavior, but increases as the temperature increases above about 200K, and shows a metallic behavior. Therefore, the $\text{La}_{2-x}\text{Sr}_x\text{CuO}_4$ single crystals have a large anisotropy of the electrical resistivity, and it seems that this anisotropy is related to the K_2NiF_4 -typed crystal structure of $\text{La}_{2-x}\text{Sr}_x\text{CuO}_4$. The details of the resistivities of the $\text{La}_{2-x}\text{Sr}_x\text{CuO}_4$ single crystals will be discussed elsewhere.

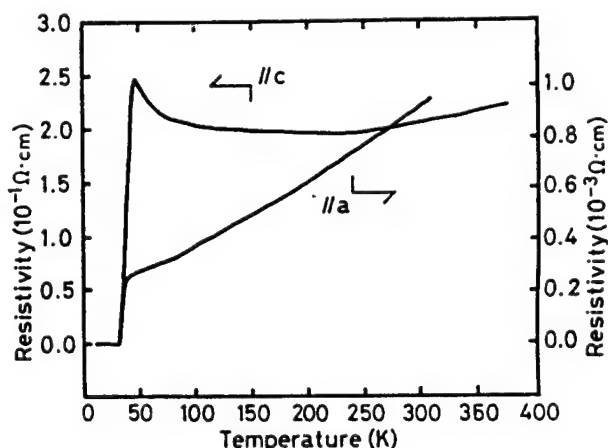


Fig.2 Electrical resistivities of $\text{La}_{2-x}\text{Sr}_x\text{CuO}_4$ grown crystals

CONCLUSIONS

$\text{La}_{2-x}\text{Sr}_x\text{CuO}_4$ single crystals were grown by the TSFZ method. The crystal growth using a solvent with less than 75 mol%CuO caused precipitation of La_2O_3 . Crystal grown with a solvent, containing more than 78 mol%CuO, produced single crystals of $\text{La}_{2-x}\text{Sr}_x\text{CuO}_4$, were black in color with a metallic luster, and contained no inclusions such as La_2O_3 . The grown crystals were identified as single crystals by back-reflection Laue photograph, and had a tetragonal symmetry as determined by powder XRD method. The composition of the grown crystals were radially and axially uniform, and were determined to have the composition of $\text{La}_{1.86}\text{Sr}_{0.14}\text{Cu}_{0.97}\text{O}_{3.89}$ by EPMA. As a result of the electrical resistivity measurement, the $\text{La}_{2-x}\text{Sr}_x\text{CuO}_4$ grown crystals were superconductors with $T_c=37.5\text{K}$ and $\Delta T_c=1.1\text{K}$, and were superior to the $\text{La}_{2-x}\text{Sr}_x\text{CuO}_4$ single crystals reported previously. The electrical resistivities of the grown single crystals had further a significant anisotropy at the non-superconducting state, in which the resistivity along the c -axis was several hundred times higher than that along the a -axis.

ACKNOWLEDGMENTS

The authors wish to thank Professor K. Kitazawa of the University of Tokyo for electrical resistivities measurement.

REFERENCES

1. J.G. Bednorz and K.A. Muller, Z. Phys. B64, 189 (1986).
2. S. Uchida, H. Takagi, K. Kitazawa and S. Tanaka, Japan. J. Appl. Phys. 26, L1 (1987).
3. T. Freltoft, J.E. Fisher, G. Shirane, D.E. Moncton, S.K. Shinha, D. Vaknin, J.P. Remeika, A.S. Cooper and D. Harshman, Phys. Rev. B 36, 826 (1987).
4. A.M.M. Gadalla, W.F. Ford and J. White, Trans. Brit. Ceram. Soc. 62, 45 (1963).
5. H.H. Wang, U. Geiser, R.J. Thorn, K.D. Carlson, M.A. Beno, M.R. Monaghan, T.J. Allen, R.B. Proksch, D.L. Stupka, W.K. Kwok, G.W. Crabtree and J.M. Williams, Inorg. Chem. 26, 1190 (1987).
6. Y. Hidaka, Y. Enomoto, M. Suzuki, M. Oda and T. Murakami, Japan. J. Appl. Phys. 26, L377 (1987); J. Crystal Growth 85, 581 (1987).
7. K. Oka and H. Unoki, Japan. J. Appl. Phys. 26, L1590 (1987).
8. P.L. Picone, H.P. Jenssen and D.R. Gabbe, J. Crystal Growth 85, 576 (1987); 91, 463 (1988).
9. L. Trouilleux, G. Dhalenne and A. Revcolevschi, J. Crystal Growth 91, 268 (1988).
10. S. Kimura and I. Shindo, J. Crystal Growth 41, 192 (1977).

PREPARATION OF Bi-OXIDE HIGH T_c SUPERCONDUCTING CUPRATES IN THE FORM OF CERAMICS AND THIN FILMS

Tomoji KAWAI, Masaki KANAI, Hitoshi TABATA¹⁾, Yoshihiro EGAMI²⁾, Takeshi HORIUCHI, Katsutoki MITSUI³⁾, Ken HORIUCHI, Youichi HORI, Katsuki KITAHAMA, Kiyoshi OGURA³⁾, Sadao TAKAGI³⁾, P.J.CHONG⁴⁾ and Shichio KAWAI

The Institute of Scientific and Industrial Research, Osaka University, Mihogaoka, Ibaraki, Osaka, 567 Japan

1) Technical Institute, Kawasaki Heavy Industries Ltd., Kawasakicho, Akashi, Hyogo 673 Japan

2) TAYCA Co. Ltd., Funamachi, Taishoku, Osaka 551 Japan

3) Faculty of Science, Kinki University, Kowakae, Higashiosaka, Osaka 577 Japan

4) Korean Research Institute of chemical Technology, Daedeog-Danji, Daejeon, Korea 300-31

ABSTRACT

Layer-by-layer successive deposition method is one of the most promising methods to fabricate "Tailored Superconducting Films". The numbers of CuO₂ layers, the distance between the layers and carrier concentration of Bi-Sr-Ca-Cu-O superconductors have been artificially controlled to alter the superconductive properties using this layer-by-layer technique taking advantage of laser ablation. The addition and substitution of exotic atoms and ions to Bi-Sr-Ca-Cu-O superconductor in the bulk samples also alter the superconducting properties. The addition of alkaline metals lowers the formation temperature of the superconductor crystal and raises the T_c. The rise of T_c is also observed for the case of Ba addition.

INTRODUCTION

We report on our recent research activities of the high T_c oxide superconductors, mainly focused on the Bi-Sr-Ca-Cu-O (called BSCCO hereafter) and related compounds. The purpose of our research on bulk Bi-Sr-Ca-Cu-O ceramics is the design and synthesis of new superconductors with better superconductive properties. We found that the substitution of Ba and alkaline metals, Li to Cs, for BSCCO leads to the higher T_c.

The other research activities are the formation of "Tailored Superconducting Thin Films" in which the structure of CuO₂ planes and carrier concentrations are controlled artificially by using layer-by-layer successive deposition method.

(I) Effect of addition and substitution of exotic atoms to BSCCO in the bulk phase

(I-1) Effect of Ba addition ¹⁾

The addition of small amount of Ba to BSCCO enhances the high T_c phase formation. On the addition, the volume percent of the high-T_c phase in the Meissner measurement increases, and simultaneously, the T_{c zero} value rises. The highest T_c obtained is 108.7K. The most striking feature of the addition is the cut off of the low T_c tailing in the R-T curve. This is due to the effect that added Ba decomposes the low T_c phase to get rid of the nucleation of the low T_c structure in the early stage of the solid state reaction, and enhances the high T_c phase formation.

(I-2) Effect of alkaline metal substitution²⁾

The addition of alkaline metal to BSCCO lowers the formation temperature of $\text{Bi}_2\text{Sr}_2\text{Ca}_1\text{Cu}_2\text{O}_y$ phase (2212 phase) drastically. The effect is greatest with Li, having the smallest ionic radius among alkaline metals. Elements with smaller ionic radii, Li and Na, make the superconducting properties better than standard BSCCO. Li-added sample has the highest $T_{c\text{mid}}$ and $T_{c\text{onset}}$. The more the amount of Li is, the lower the formation temperature of the 2212 phase is, and CuO peak in X-ray diffraction pattern becomes stronger. The increase of Li makes the higher $T_{c\text{mid}}$ in R-T curve and Meissner onset temperature. Substitution experiment of Li at Bi, Sr, Ca and Cu site revealed that the exchange of Ca by Li is difficult but possible for Bi, Sr and Cu sites, and the substitution of Li for Cu makes the best superconducting properties. Single 2212 superconducting phase have been obtained with a lot of Li addition to the Sr or Cu site showing $T_{c\text{mid}}$ of 76K and 94K respectively, that is, a big difference was observed for the substitution at the Sr and Cu site. The Meissner onset temperature is 98K for the Li substitution. The substitution of Li for the Cu at the starting composition showed the best result.

(II) Tailored superconducting thin films prepared by layer-by-layer successive deposition

The essential structural features of Cu-based high T_c oxide superconductor are CuO_2 sheets and appropriate amount of charge carriers for the formation of Cooper pairs. Positive ions, such as Ba, Sr, Y, Bi and Tl are playing roles, together with oxygen, to construct structural framework and to control the amount of charge carriers in the superconductor. Accordingly, in order to elucidate the mechanism of high T_c superconductivity and to control the properties of the copper-based superconductor, the control of the structure of the CuO_2 sheet and also the control of the amount of charge carriers are necessary.

The control of the CuO_2 -based structure means the artificial changes of;
(1) the numbers of the CuO_2 layers, (2) the distance between CuO_2 layers, (3) the bond distance of Cu-O and (4) the distance between Cu and O(apex).

The numbers of carriers can be changed by the control of
(1) the amount of oxygen and (2) the substitution of the atoms with different valence state.

Here, we introduce the recent results on the formation of "Tailored Superconducting Films" in which the CuO_2 based structures and carrier concentrations are artificially controlled by using layer-by-layer successive deposition method taking advantage of laser ablation technique. The attention is focused on the Bi-Sr-Ca-Cu-O material, in which (I) the numbers of the CuO_2 layers are changed from one to five layers, (II) the distance between CuO_2 layers are changed by inserting bigger ions, such as Ba, into the layers on the atomic scale, and (III) the numbers of charge carriers are changed by site-selective Pb doping at the Bi_2O_2 layers.

The apparatus used for the film formation is shown in Fig.1.³⁾ The ArF laser beam is sequentially focused on the multi-targets to form a film on a MgO substrate placed at the opposite side of the target in the presence of O_2 or N_2O atmosphere. For deposition, sintered disks of $Bi_{1-x}Pb_xO_y$, $SrCuO_y$, $CaCuO_y$, $BaCuO_y$ and/or $YCuO_y$ are used as targets and each different atomic layer is successively deposited from these targets to form multi-layered structure as we desire. One cycle to form one Bi-Sr-Ca-Cu-O layer consists of for example, the sequence of the deposition from the targets, $Bi(Pb)O_y$ - $SrCuO_y$ - $CaCuO_y$ - $SrCuO_y$, and this cycle is repeated 20 times to form a film

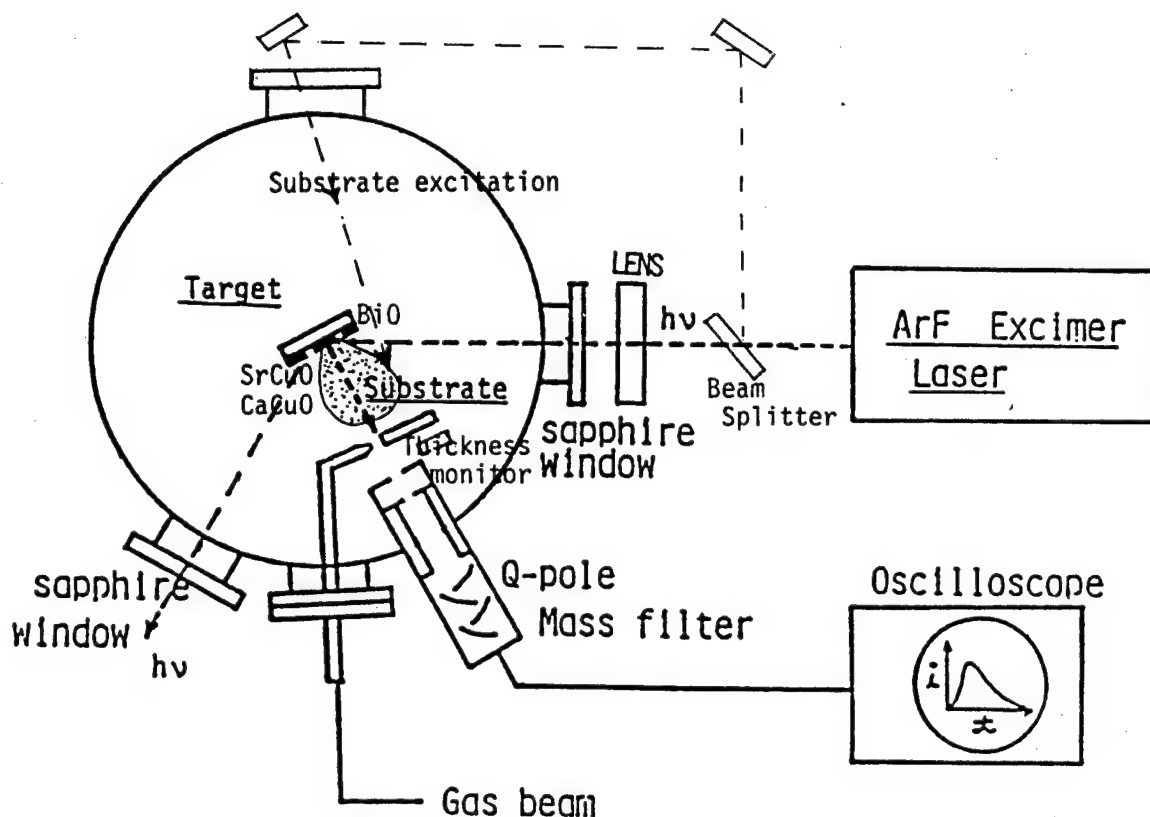


Fig.1. An apparatus for the layer-by-layer successive deposition using ArF excimer.

thickness of about 300Å.

(II-1) Formation of one to five CuO_2 layer structure based on Bi-Sr-Ca-Cu-O compound.⁴⁾

As shown in Fig.2., three phases of the Bi-Sr-Ca-Cu-O are known to exist in a bulk phase, i.e. $\text{Bi}_2\text{Sr}_2\text{Cu}_1\text{O}_6$ (called 2201 phase hereafter) with T_c of 7K or semiconductor, $\text{Bi}_2\text{Sr}_2\text{Ca}_1\text{Cu}_2\text{O}_y$ (2212 phase) with T_c of 80K and $\text{Bi}_2\text{Sr}_2\text{Ca}_2\text{Cu}_3\text{O}_y$ (2223 phase) with T_c of 110K. Furthermore, compounds are conceivable which contain four and five CuO_2 layers. The changes of the structure of these compounds are only the changes of the number of Ca and CuO_2 layers. Accordingly, by using the layer-by-layer successive deposition method, these compounds, containing one to five CuO_2 layers, can be formed by controlling the deposition time from CaCuO_y targets which is sandwiched by Bi_2O_3 layers. Actually, one to three CuO_2 layered structure have been formed. Furthermore, thin films containing four and five CuO_2 layers have been synthesized. In this manner, the numbers of CuO_2 layers can be controlled by the successive deposition method.

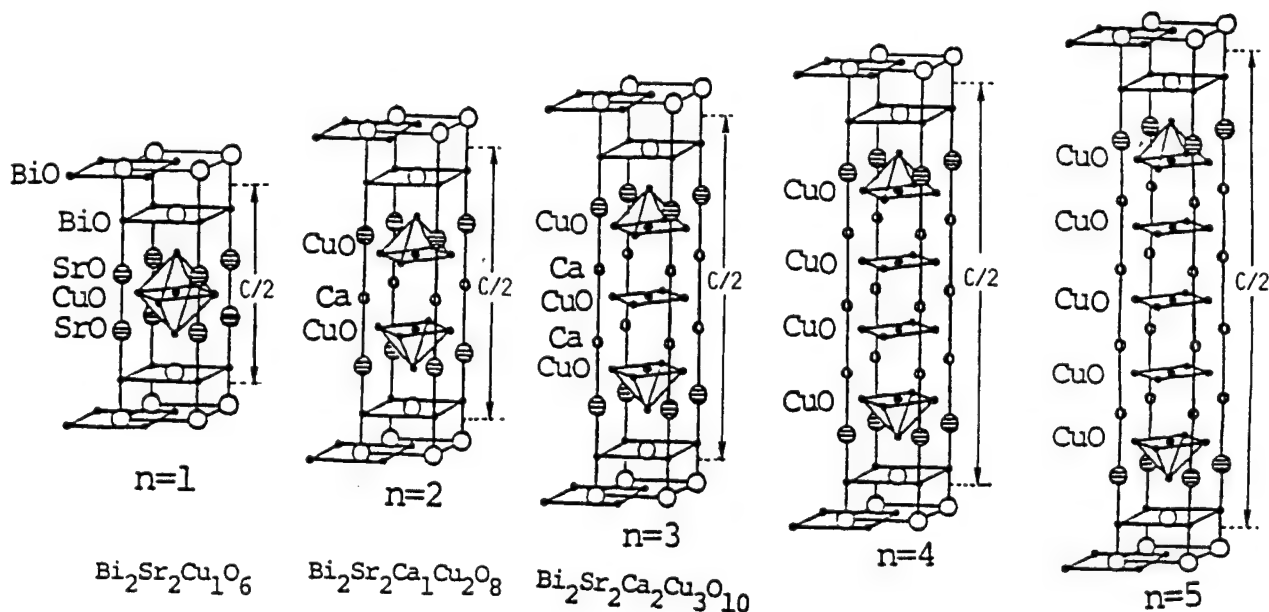


Fig.2. Crystal structure of a superconductor of the Bi-Sr-Ca-Cu-O system. A substance with four or five CuO_2 layers does not exist in bulk. But it can be synthesized by the successive deposition method described here.

(II-2) Incorporation of exotic atoms into BSCCO on the atomic layer scale.-- site selective substitution of Ba for Ca or Sr site⁵⁾--

For the control of the Cu-O bond distance and the distance between CuO_2 layers, atoms having different ionic radii should be incorporated into the desired atomic site of BSCCO. We have examined the incorporation of Ba, the large +2 ion, into Sr and Ca sites of BSCCO (see Fig.2) using layer-by-layer successive deposition. In this experiment, Ba atoms are co-deposited when CaCuO layer or SrCuO layer is formed during the successive deposition. In the former case, Ba is introduced into the Ca site, and in the latter case into the Sr site.

The Ba has been actually incorporated both into Sr and Ca site to give X-ray diffraction patterns of single $\text{Bi}_2\text{Sr}_2\text{Ca}_1\text{Cu}_2\text{O}_y$ phase. The incorporation of Ba was confirmed by EPMA measurement. Considering that the substitution of Ba is very difficult in the bulk phase with solid reaction starting from powdered materials¹⁾, it is understood that the layer-by-layer successive deposition method is a very powerful method to incorporate exotic atoms into the crystal structure. Interestingly, the superconducting properties of the substituted samples at the Sr and Ca sites exhibit quite different behavior in the R-T curve. The Sr site substitution exhibited a semiconductive R-T curve, while Ca site substitution leads to an improvement of the T_c even compared with the standard BSCCO.

In this manner, the the essential part of the Cu-based BSCCO superconductor, the distance between CuO_2 sheets, can be controlled by inserting large or small metal ions between CuO_2 sheets using layer-by-layer successive deposition technique. The bigger distance between CuO_2 layers seems to be desirable to improve the superconductivity by increasing two dimensional character.

(II-3) Site-selective substitution of Pb at Bi_2O_2 layers--control of carrier concentration⁶⁾--

We have tried a site selective substitution of Pb^{2+} for Bi^{3+} using successive deposition method and studied the effect of the substitution of atoms with different valence state on the superconducting properties of $(\text{Bi,Pb})_2\text{Sr}_2\text{Ca}_1\text{Cu}_2\text{O}_y$. The $(\text{Bi}_{1-x}\text{Pb}_x)_2\text{Sr}_2\text{Ca}_2\text{Cu}_2\text{O}_y$ films with systematically altered Pb content have been prepared by this method. The X-ray diffraction pattern shows that all films have almost single phase of double CuO_2 layer structure.⁶⁾ Thus, together with the X-ray and EPMA analysis, we can conclude that the films having the same crystal structures, 2212 structure, with different Pb concentrations have been obtained. The $T_{c\text{zero}}$ and $T_{c\text{mid}}$ values increase drastically, as we expected, against the increase of the Pb substitution from $x=0$ to 0.3. The films having more Pb, such as $x=0.5$, showed two steps of the decrease of resistivity and lower $T_{c\text{zero}}$. In the $(\text{La}_{1-x}\text{Sr}_x)\text{CuO}_4$ superconductor, it has been revealed that T_c increases with the

increase of Sr in the small concentration region, and T_c decreases with large Sr content. This phenomenon is explained by the hole doping and the overdoping, respectively, to La_2CuO_4 by the Sr doping. In the $(\text{Bi}_{1-x}\text{Pb}_x)_2\text{Sr}_2\text{Ca}_1\text{Cu}_2\text{O}_y$ case, we have observed the similar behavior for Pb doping in the samples studied here. Thus, the control of the superconductivity by Pb doping can be successfully carried out.

REFERENCES

1. T.Kawai, S.Kawai, S.Tanaka, T.Horiuchi, S.Takagi, K.Ogura, S.Kambe and M.Kawai, Jpn.J.Appl.Phys., 27, L2296(1988).
2. T.Horiuchi, K.Mitsui, T.Kawai, S.Takagi, K.Ogura and S.Kawai, to be published.
3. M.Kanai, T.Kawai, M.Kawai and S.Kawai, Jpn.J.Appl.Phys., 27, L1293(1988).
4. M.Kanai, T.Kawai, S.Kawai and H.Tabata, Appl.Phys.Lett., 54, 1802(1989).
5. H.Tabata, T.Kawai, M.Kanai, O.Murata and S.Kawai, Jpn.J.Appl.Phys., 28, L823(1989).
6. M.Kanai, T.Kawai and S.Kawai, Vacuum, submitted (1989)

HOT-PRESSING AND SUPERCONDUCTING PROPERTIES OF Bi-Pb-Sr-Ca-Cu-O CERAMICS

Norimitsu Murayama, Senzo Kuwabara and Yasuyoshi Torii

Government Industrial Research Institute, Nagoya,

1-1 Hirate-cho, Kita-ku, Nagoya 462

The bulk density of a normal sintered sample of $\text{Bi}_{0.85}\text{Pb}_{0.15}\text{Sr}_{0.8}\text{CaCu}_{1.4}\text{O}_y$ with a T_c of 98 K was 4.81 g/cm^3 and the shrinkage of the sample was scarcely observed. In hot-pressing in vacuum, the bulk density was saturated above about 770°C . By hot-pressing at a pressure of 400 kg/cm^2 at 770°C in vacuum of 5×10^{-5} Torr for 2 h, the bulk density of the hot-pressed sample was 6.21 g/cm^3 , which was higher than 95 % of the theoretical density. The grains were oriented with the c-axis along the hot-pressing axis. In the sample hot-pressed at a pressure of 300 kg/cm^2 at 770°C in vacuum, the T_c was observed at 67 K. After annealing at 830°C in air for 40 h, the T_c was 102 K and the critical current density at 77 K in zero magnetic field was 646 A/cm^2 , which was an order of magnitude higher than that of a normal sintered sample.

1. INTRODUCTION

Recently, a new high- T_c oxide superconductor has been discovered in the Bi-Sr-Ca-Cu-O system /1/ and it has been found that the partial Pb substitution in Bi-Sr-Ca-Cu-O superconductors resulted in the stabilization of the phase with a transition temperature (T_c) of 105 K (a high- T_c phase) /2/. According to the study on the single crystal of a Y-B-C-O superconductor /3/, an anisotropy in electrical and magnetic properties exists. The critical current density (J_c) of Y-B-C-O ceramics is two or three orders magnitude below that of the single crystal /4/. It is due to the weak link between grains and the random direction of grains. In order to increase J_c , the ceramics need to be densified and grain-oriented. The Bi-Pb-Sr-Ca-Cu-O superconducting powders are in the form of thin plate, which is suitable for grain-orientation. However, it is difficult to prepare dense Bi-Sr-Ca-Cu-O ceramics by normal sintering because the packing of the compact sample is not good. Hot-pressing is considered to be an effective technique for preparing dense and grain-oriented ceramics. We have first succeeded in preparing a grain-oriented dense Bi-Pb-Sr-Ca-Cu-O superconductor by hot-pressing /5/. In the present work, we carried out hot-pressing in vacuum, and investigated the relation between bulk density and hot-pressing condition and the electrical properties of the hot-pressed sample. The study on hot-pressing in air will be reported elsewhere /6/.

2. EXPERIMENTAL

Superconducting ceramic powder with the starting composition of $\text{Bi}_{0.85}\text{Pb}_{0.15}\text{Sr}_{0.8}\text{CaCu}_{1.4}\text{O}_y$ was prepared by a solid-state reaction. Appropriate amounts of Bi_2O_3 , PbO , SrCO_3 , CaCO_3 and CuO of high purity (99.9%) were wet-mixed in ethanol and calcined at 800 °C. The sample was ground, then pressed and heated at 835 °C, and cooled down to room temperature in a furnace, and was finally ground. This process (from pressing to grinding) was repeated several times to ensure a complete solid-state reaction; the total firing time was about 50 h. All firing was done in air. The powder was almost the high- T_c phase. The powder was uniaxially hot-pressed in vacuum of 5×10^{-5} Torr for 2 h using cylindrical dice made of carbon. The hot-pressed brocks were cut into bars. These samples were annealed in air or in O_2 gas. Hot-pressing and annealing conditions are shown in Fig.1 and Table I.

The bulk density was measured by Archimedes method. X-ray powder diffraction (XRD) data were taken at room temperature with graphite-monochromatized Cu radiation. The values of T_c and J_c were measured by a four-probe dc method. The T_c measurement was carried out with the current of 10 mA. The J_c measurement was carried out in liquid nitrogen and in zero magnetic field. The J_c was calculated by dividing critical current by the cross-sectional area of the sample.

3. RESULTS AND DISCUSSION

The bulk density of the compact and the normal sintered sample were 4.98 g/cm³ and 4.81 g/cm³, respectively. The shrinkage of the normal sintered sample was scarcely observed. Figure 1 shows the hot-pressing temperature dependence of the bulk density for the unannealed sample. In the hot-pressing in vacuum, the bulk density was saturated above about 770 °C. The bulk density of the sample hot-pressed at a pressure of 400 kg/cm² was 6.21 g/cm³, which was higher than 95 % of the theoretical density. Despite hot-pressing in vacuum, the high- T_c phase was not decomposed and no appreciable change in the lattice parameters was observed.

Figure 2 shows X-ray diffraction patterns for the perpendicular plane (a) and the parallel plane (b) to the hot-pressing axis of the hot-pressed sample not annealed in air. Figure 3 shows the SEM photographs of the fractured surfaces perpendicular and parallel to the hot-pressing axis of the hot-pressed sample. The grains were found to be oriented with the c-axis along the hot-pressing axis.

The compact sample exhibited semiconductivity above 115 K and metallic conductivity below 115 K, although the resistivity was not zero above 25 K. The normal sintered sample had the T_c of 98 K and exhibited metallic conductivity

above the T_c . It is concluded that in the normal sintered sample, the degree of link between grains increased as compared with the compact sample, although the shrinkage of the sample is scarcely observed. Table I shows the values of T_c and J_c of the sample which was hot-pressed at a pressure of 300 kg/cm^2 at 770°C in vacuum. The detail study on the influence of annealing on superconducting properties of the hot-pressed sample has been investigated elsewhere /6/. In the sample before annealing in air, the T_c was observed at 67 K. After annealing in air, the T_c reached 102 K, which was 4 K higher than that of the normal sintered sample and the resistivity at room temperature was lower than that of the normal sintered sample. After annealing at 830°C in air for 40 h, the J_c reached 646 A/cm^2 , which was an order of magnitude higher than that of a normal sintered sample.

4. CONCLUSIONS

The bulk density of a normal sintered sample of $\text{Bi}_{0.85}\text{Pb}_{0.15}\text{Sr}_{0.8}\text{CaCu}_{1.4}\text{O}_y$ with a T_c of 98 K was 4.81 g/cm^3 and the shrinkage of the sample was scarcely observed. In hot-pressing in vacuum, the bulk density was saturated above about 770°C . By hot-pressing at a pressure of 400 kg/cm^2 at 770°C in vacuum of 5×10^{-5} Torr for 2 h, the bulk density of the hot-pressed sample was 6.21 g/cm^3 , which was higher than 95 % of the theoretical density. The grains were oriented with the c-axis along the hot-pressing axis. In the sample hot-pressed at a pressure of 300 kg/cm^2 at 770°C in vacuum, the T_c was observed at 67 K. After annealing at 830°C in air for 40 h, the T_c was 102 K and the critical current density at 77 K in zero magnetic field was 646 A/cm^2 , which was an order of magnitude higher than that of a normal sintered sample.

REFERENCES

- 1) H.Maeda, Y.Tanaka, M.Fukumoto and T.Asano: Jpn.J.Appl.Phys. 27(1988)L290.
- 2) M.Takano, J.Takada, K.Oda, H.Kitaguchi, Y.Miura, Y.Ikeda, Y.Tomii and H.mazaki: Jpn.J.Appl.Phys. 27(1988)L1041.
- 3) W.J. Gallagher: J.Appl.Phys., 63, (1988)4216.
- 4) J.W.Ekin: Advanced Ceramic Materials 2(3B)(1987)586.
- 5) N.Murayama, E.Sudo, M.Awano, K.Kani and Y.Torii: Jpn.J.Appl.Phys. 27(1988)L1856.
- 6) N.Murayama and Y.Torii: Proceedings of International M²S-Conference (1989).

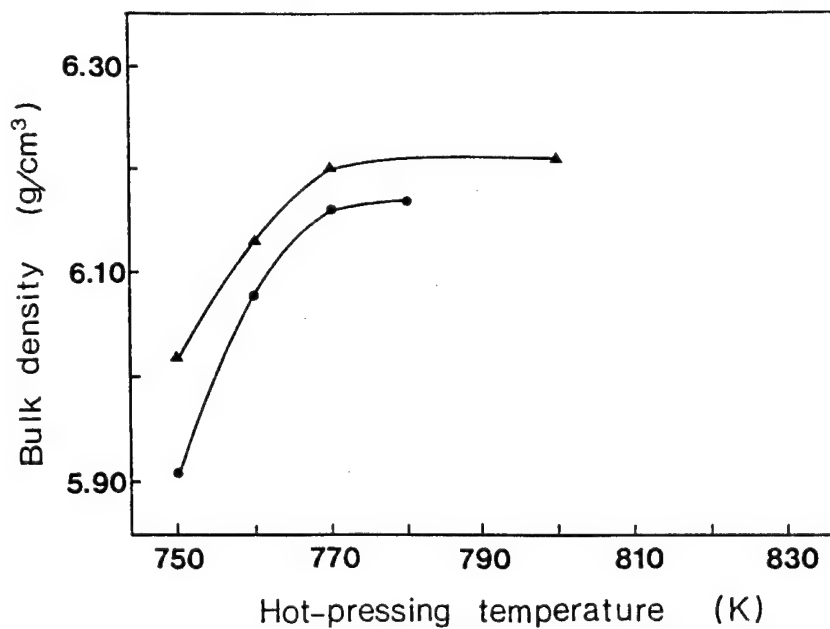


Fig.1 Hot-pressing temperature dependence of the bulk density of $\text{Bi}_{0.85}\text{Pb}_{0.15}\text{Sr}_{0.8}\text{CaCu}_{1.4}\text{O}_y$ ceramics. (●) at 300 kg/cm^2 in vacuum, (▲) at 400 kg/cm^2 in vacuum.

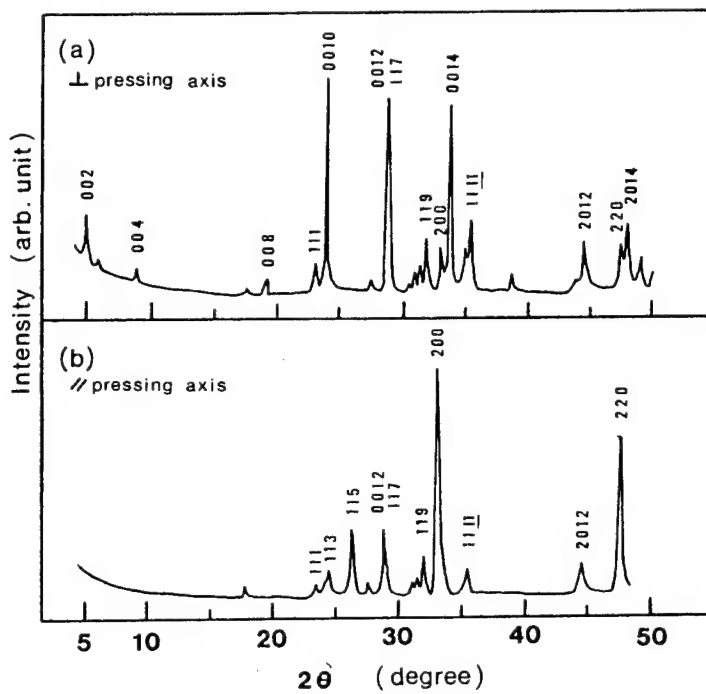


Fig.2 X-rays diffraction patterns for the perpendicular (a) and the parallel (b) planes to the hot-pressing axis of the hot-pressed Bi-Pb-Sr-Ca-Cu-O superconductor.

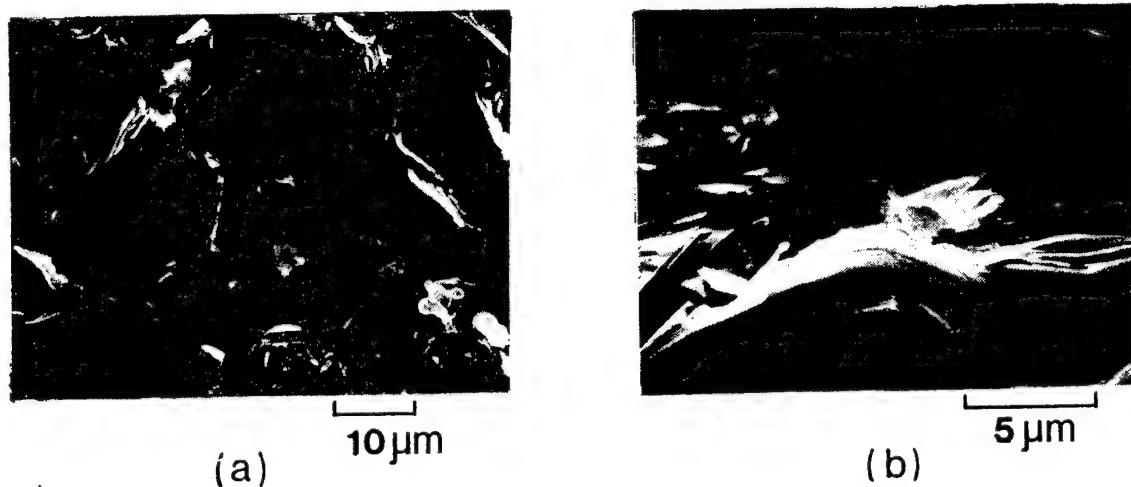


Fig.3 SEM photographs of the fractured surfaces perpendicular (a) and parallel (b) to the hot-pressing axis of the hot-pressed Bi-Pb-Sr-Ca-Cu-O superconductor.

Table I Superconducting properties of the $\text{Bi}_{0.85}\text{Pb}_{0.15}\text{Sr}_{0.8}\text{CaCu}_{1.4}\text{O}_y$ ceramics which was hot-pressed at a pressure of 300 kg/cm^2 at 770°C in vacuum for 2 h.

sample	ρ (g/cm^3)	T_c (K)	$J_c^{\text{a)}}$ (A/cm^2)
V1 as hot-pressed	6.16	67	-
V2 annealed at 830°C in air for 40 h	5.77	102	646
V3 annealed at 500°C in O_2 gas for 60 h	6.17	97	32.8

a) J_c was measured at 77 K in zero magnetic field.

PREPARATION OF SUPERCONDUCTING WHISKERS OF Bi SYSTEM AND THEIR ELECTRICAL PROPERTIES

Ichiro Matsubara, Hideo Tanigawa, Toru Ogura,
Hiroshi Yamashita, Makoto Kinoshita and Tomoji Kawai⁺

Government Industrial Research Institute, Osaka
Midorigaoka, Ikeda, Osaka 563, Japan

⁺The Institute of Scientific and Industrial Research,
Osaka University, Ibaraki, Osaka 567, Japan

Abstract The superconducting whiskers of Bi(Pb)-Sr-Ca-Cu-O system have been prepared by heating a glassy melt-quenched plate in a stream of oxygen gas. The dimension of the whiskers is 2-10 μ m thick, 10-300 μ m wide and 1-15mm long. The whiskers show two steps of the electrical resistance drop at 105K and 73K, and a zero-resistance state around 70K. From the results of SQUID measurements, the volume fraction of the high- T_c phase (2223 phase) is found to be less than 1%. The high- T_c phase is also detected with a microarea X-ray diffractometer, which revealed that the phase is stacked between the low- T_c platelike crystals. The highest T_c (zero) value so far obtained is 96K. The volume fraction of the high- T_c phase depends on the composition of a glassy melt-quenched intermediate.

Introduction

It is well known that the Bi-Sr-Ca-Cu-O superconductor has two different phases: one is $\text{Bi}_2\text{Sr}_2\text{CaCu}_2\text{O}_x$ (low- T_c phase, $T_c=80\text{K}$) and the other is $\text{Bi}_2\text{Sr}_2\text{Ca}_2\text{Cu}_3\text{O}_x$ (high- T_c phase, $T_c=110\text{K}$) (1). Since the discovery of the Bi system superconductor (2), many studies on obtaining a pure 110K phase (high- T_c phase) have been carried out. The single phase of the high- T_c phase was obtained by substituting Pb for Bi (3) and by reacting under low oxygen pressure (4,5). We have reported that the Bi(Pb)-Sr-Ca-Cu-O whiskers which mainly have the 2212 structure with a zero resistance at 70K are formed by heating a melt quenched plate in a stream of O_2 gas (6,7). From the measurements of the temperature dependence of the resistivity, some whiskers were found to show a resistance drop at 105K suggesting a presence of the high- T_c phase in the whiskers. In this report, we determine where the high- T_c phase exists in the whisker and to what extent the volume fraction is. Further, the effects of preparing conditions on the resulting phases are also examined.

Experimental

The Powders of Bi_2O_3 , SrCO_3 , CaCO_3 , CuO and PbO were mixed with an appropriate compositions with a ball mill and the mixed powder was melted in an alumina crucible at 1200°C for 30 minutes in an electric crucible in air. The melts were poured onto a steel plate and were pressed quickly. The thickness of the quenched glassy samples was approximately 1.0mm. This process used to form the starting melt-quenched plate is the same as that used for fabricating a glass ceramic superconductor (8). The obtained samples were heated on an alumina boat at 840°C for 120h in a stream of O_2 (150ml/min) and were cooled to room temperature in the furnace. Then the whiskers grown perpendicularly to the surface of the quenched plates were obtained.

The temperature dependence of the resistance and the critical current density (J_c) was measured by a standard four-probe method. Phase determination was carried out using a microarea X-ray diffractometer at Cu-K wavelength with an X-ray probe 30 μ m in diameter. The sample was mounted on a stage which moved in a manner of precession around the three rotation axes. Magnetic susceptibility was determined with a superconducting quantum interference device (SQUID) magnetometer. The surface structure of the whiskers was investigated by a SEM.

Results and Discussion

Figure 1 shows the photograph of the whiskers grown from a melt-quenched plate by heating at 840°C for 120h under an oxygen gas stream. Its starting composition is $\text{Bi}_2\text{Pb}_{0.5}\text{Sr}_{1.9}\text{Ca}_{2.2}\text{Cu}_4\text{O}_x$. The melt-quenched plates are curved during the heating process suggesting the plates are partially melted. The whisker grows slowly during the long period of heating, reaching a maximum crystal length to 15mm.

The temperature dependences of resistance for several samples are shown in Fig 2. These samples are grown when the starting composition is $\text{Bi}_2\text{Pb}_{0.5}\text{Sr}_{1.9}\text{Ca}_{2.2}\text{Cu}_4\text{O}_x$. For samples A and B, two steps in the resistance curve are observed, at 105K and 73K, and the value of $T_c(\text{zero})$ is 70K. For sample C, the first drop occurs at 105K but $T_c(\text{zero})$ is 96K, higher than that for A or B. The temperature of the first resistance drop is consistent with the data for the high- T_c phase. The ratio between the resistivities for the first and second drops is dependent on samples. This ratio will reflect the fraction of the high- T_c phase in the low- T_c phase along a route between the voltage terminals. Sample C is an example in which the route is connected by the high- T_c phases throughout the voltage terminals. On the other hand, since the high- T_c phase is not detected in the X-ray diffraction pattern of crushed whiskers, the volume fraction of high- T_c phase is rather small. We estimated the volume fraction of the high- T_c phase using a SQUID magnetometer (Fig. 3). The slight diamagnetic susceptibility between 100K and 75K is attributed to the high- T_c phase. From the comparison of the diamagnetic susceptibility at 100K and 70K, the volume fraction of the high- T_c phase is estimated to be about 0.6%.



Fig. 1. Bi(Pb)-Sr-Ca-Cu-O whiskers grown by heating a glassy melt-quenched plate in a stream of O_2 .

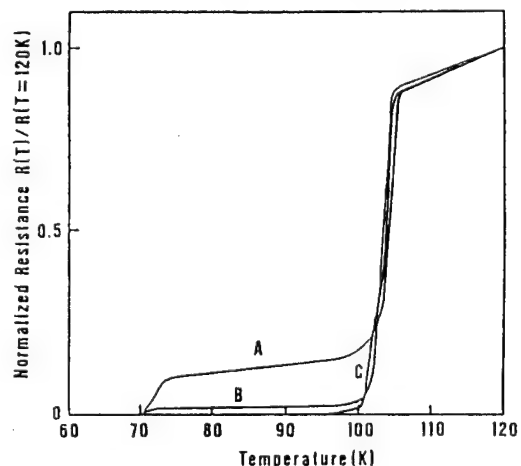


Fig. 2. Temperature dependence of the normalized resistance of the whiskers. A is a typical example, B is an example where the resistance drops close to zero at 105K, and C is a sample which has $T_c(\text{zero})$ at 96K.

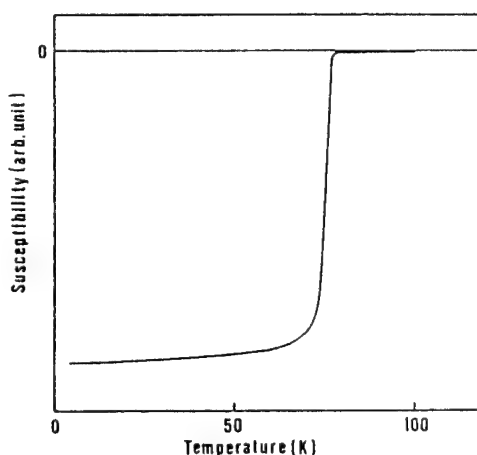


Fig. 3. Temperature dependence of the magnetic susceptibility.

As shown in Fig. 4, each whisker shows a characteristic surface structure consisting of several platelike single crystals ($2\text{-}5\mu\text{m} \times 10\text{-}300\mu\text{m} \times 1\text{-}15\text{m}$) which are stacked in a layered structure along the direction of thickness. The front surface of the whisker is wide and flat consisting of well grown face of single crystal (Fig. 4-a), while the side one is rather rugged piled up with platelike crystals (Fig. 4-b). In the side view, mid layers between the piles are not always connected from top to end parts of the whisker. In order to determine where the high- T_c phase exists in such a layered structure, we carried out diffraction measurements with a microarea X-ray diffractometer equipped with an X-ray probe of $30\mu\text{m}$ diameter.

Figure 5(a) shows the X-ray diffraction patterns for well grown surface taken at eight different positions along the long axis of the whisker. For all the measured positions, each peak can be assigned to that of the low- T_c phase. The high- T_c phase was not detected in the flat surface of the whiskers. Conversely, when the X-ray irradiates on the side surface of the whisker, peaks with (0010) , (0012) , (0014) and (0016) indices due to the high- T_c phase are observed in some positions, as shown in Fig. 5(b). Therefore, we conclude that the high- T_c phase is contained in the intermediate layer sandwiched between the well-grown plates of the low- T_c phase. The crystals of the high- T_c phase are not always connected from top to end of the whiskers, and they exist in the whiskers as mid layers. As for the temperature dependence of resistance, the resistivity ratio between the drops at 105K and 73K changes from sample to sample. This is considered to be due to difference of the fraction of the high- T_c phase between the voltage terminals. The J_c value of a sample having the $T_c(\text{zero})$ at 70K was $67000\text{A}/\text{cm}^2$ at 63K in a zero magnetic field, while the value for another sample with the $T_c(\text{zero})$ at 96K was $45000\text{A}/\text{cm}^2$ at the same condition. At 77K , the latter sample showed the J_c value of $540\text{A}/\text{cm}^2$. Since the J_c current is conducted only through the minority portion of the whisker at 77K , the net J_c value for the high- T_c phase will be far larger than the apparent one.

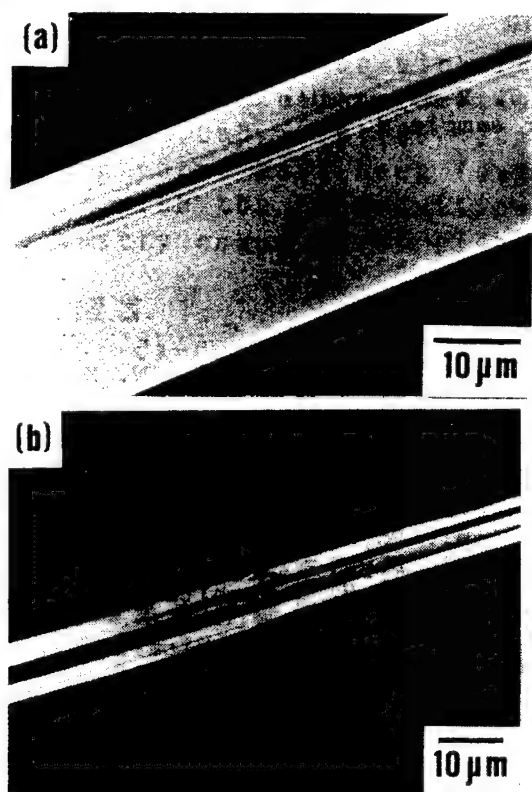


Fig. 4. Scanning electron micrograph of the well-grown surface (a) and the side surface (b) of the Bi(Pb)-Sr-Ca-Cu-O whisker.

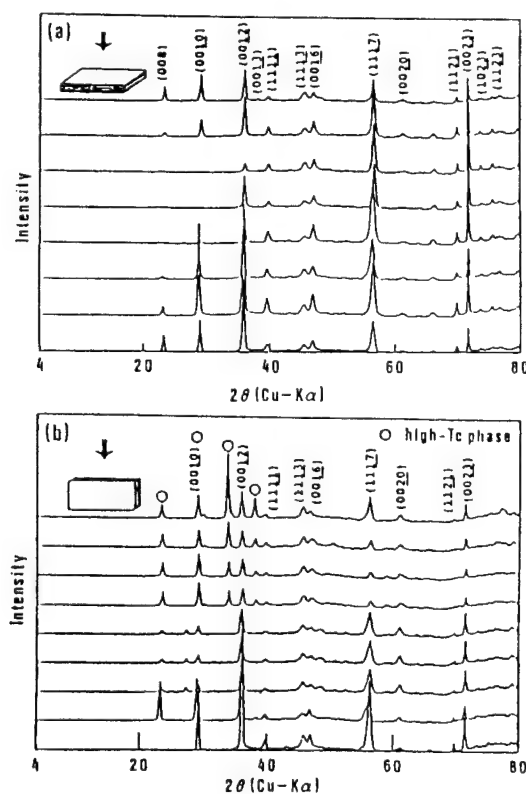


Fig. 5. Microarea X-ray diffraction patterns of the well-grown surface (a), and the side surface (b). Peaks marked with circle coincides with those of high- T_c phase.

In order to increase the volume fraction of the high- T_C phase, we examined the growing phases in the whiskers grown from different starting compositions and under different heating temperatures by using a X-ray diffractometer. Figure 6 shows the composition region where the whiskers grow at 840°C for 120h in a stream of O_2 gas. The starting composition was changed on the triangular diagram, where $Bi_2Sr_2Cu_2O_x$, $CaCuO_x$ and PbO are located at the vertices. The whiskers grow in wide starting composition range for the heating condition. For example, the compositions of a, b and c in Fig. 6 are $Bi_2Pb_{0.4}Sr_2CaCu_3O_x$, $Bi_2PbSr_2Ca_8Cu_{10}O_x$ and $Bi_2Pb_{2.5}Sr_2Ca_{6.5}Cu_{8.5}O_x$ respectively. Each whisker indicated in Fig. 6 has the low- T_C structure except for sample d. The powder X-ray diffraction pattern of the sample d is shown in Fig. 7. Some peaks of the high- T_C phase are observed, and the intensity of the high- T_C phase is comparable to that of the low- T_C phase. We are expecting the volume fraction of the high- T_C phase is able to increase by adjusting the starting composition.

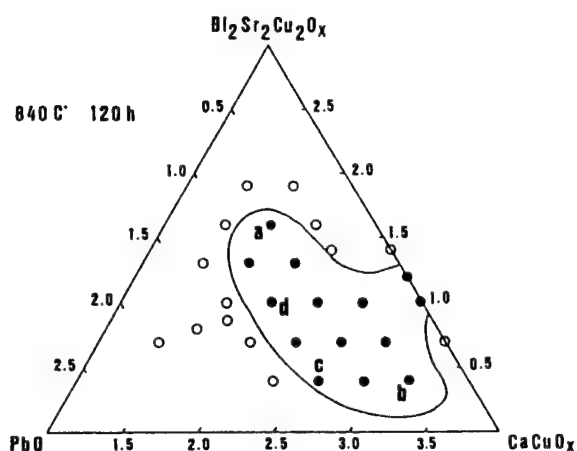


Fig. 6. Starting composition range of growth of the whiskers heating at 840°C for 120h. The closed circle indicate the whisker growth.

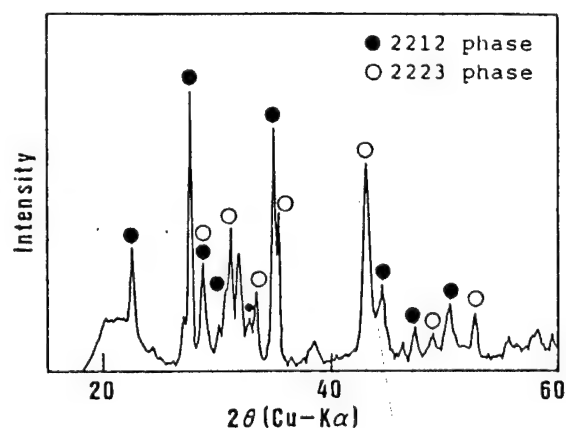


Fig. 7. X-ray powder diffraction pattern for sample d.

References

- (1) J. L. Tallon, R. G. Buckley, P. W. Gilberd, M. R. Presland, I. W. M. Brown M. E. Bowden, L. A. Christian and R. Goguel: Nature 333(1988)153.
- (2) H. Maeda, Y. Tanaka, M. Fukutomi and T. Asano: Jpn. J. Appl. Phys., 27(1988)L209.
- (3) M. Takano, J. Takada, K. Oka, H. Kitaguchi, Y. Miura, Y. Ikeda, Y. Tomii and H. Mazaki: Jpn. J. Appl. Phys., 27(1988)L1041.
- (4) U. Endo, S. Koyama and T. Kawai: Jpn. J. Appl. Phys., 27(1988)L1476.
- (5) S. Koyama, U. Endo and T. Kawai: Jpn. J. Appl. Phys., 27(1988)L1861.
- (6) I. Matsubara, H. Kageyama, H. Tanigawa, T. Ogura, H. Yamashita and T. Kawai Jpn. J. Appl. Phys., 28(1989)L1121.
- (7) I. Matsubara, H. Tanigawa, T. Ogura, H. Yamashita, M. Kinoshita and T. Kawai: Jpn. J. Appl. Phys., 28(1989)L .
- (8) T. Komatsu, K. Iwai, R. Sato, K. Matushita and T. Yamashita: Jpn. J. Appl. Phys., 27(1988)L533.

DIRECT PREPARATION OF POROUS SILICA GLASSES BY THE SOL-GEL METHOD
ゾルーゲル法による多孔質シリカガラスの直接合成

Kozuka H., Yamaguchi J. and Sakka S.

Institute for Chemical Research, Kyoto University
Uji, Kyoto-Fu 611, Japan

Formation of silica gels with micrometer-sized, continuous pores from highly acidic solutions of tetramethoxysilane has been described. The presented gels are shown to be appropriate as the precursor of bulk silica glasses, because of their large pores and monolithity. Characteristics of the constituent particles and sintering behavior of the gels have been discussed.

Introduction

Preparation of shaped silica glasses by the sol-gel method has been attracting much attention, where monolithic silica gels are transformed into bulk silica glasses by heat treatment at relatively low temperatures [1]. The precursor silica gel monoliths are obtained by gelation of hydrolyzed silicon alkoxide solutions and drying of the wet gels. Formation of cracks in the gel bodies during drying of the gels is the problem often encountered in the sol-gel process. Crack formation is thought to be suppressed by making gels with large, continuous pores, which reduce capillary pressure generated on the gel framework [2], and several methods based on this idea have been presented [3,4].

The present authors have developed one method which enables formation of crack-free bulk gels composed of micrometer-sized pores and particles using highly acidic solutions of tetramethoxysilane (TMOS) [5]. The gels may serve as precursors of porous silica glasses as well as pore-free silica glasses, where glasses with continuous pores of submicron or micron order in size are expected to be obtained only by heating the gel monoliths. In the present paper, formation of such gels from alkoxide solutions, properties of the gel constituents and sintering behavior of the gels are described.

Formation of opaque gel monoliths

Flow diagram of the procedure for making gel monoliths is shown in Fig. 1. Methanolic solution containing water and hydrochloric acid is added to methanolic solution of TMOS under vigorous stirring. Gels with micrometer-sized pores and particles are formed when the molar ratio of water to alkoxide is limited as low as 1.5 and the ratio of the acid to alkoxide as high as 0.4 is used. The solution turns opalescent and opaque before gelation, and an opaque gel monolith is obtained as shown in Fig. 2 (a). SEM photograph of the dried gel obtained from the solution of molar composition, $\text{TMOS} : \text{H}_2\text{O} : \text{HCl} : \text{CH}_3\text{OH} = 1 : 1.53 : 0.4 : 2$, (Fig. 2 (b)) indicates that the framework of the gel is composed of connected particles of $5\ \mu\text{m}$ diameter. Smaller amount of HCl and larger amount of water decreases the particle size [5]. When the water to alkoxide molar ratio is kept constant at 1.53, the particles size increases

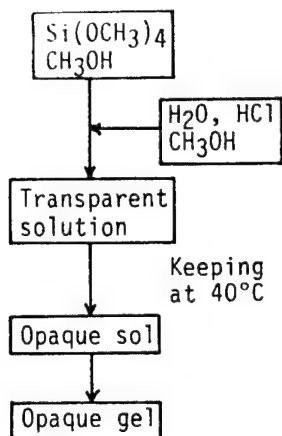


FIGURE 1 Flow diagram of the sol-gel processing for making opaque silica gel monoliths.

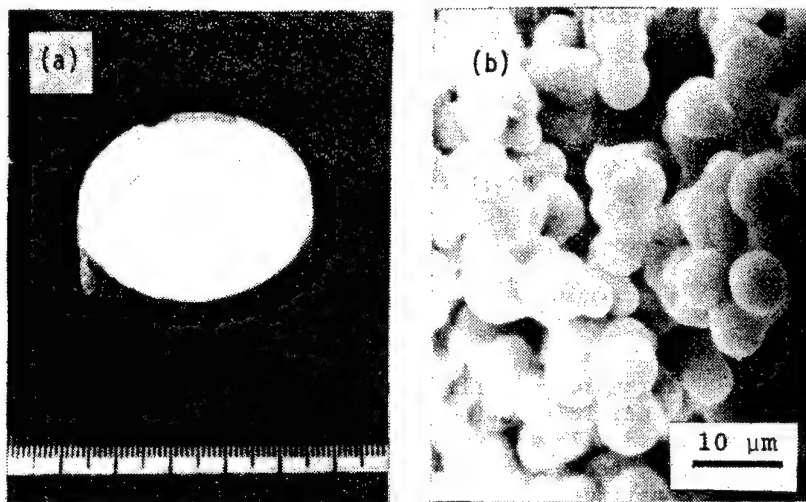


FIGURE 2 Appearance (a) and SEM photograph (b) of the dried gel obtained from the solution of molar composition, $\text{Si}(\text{OCH}_3)_4$: $\text{H}_2\text{O}:\text{HCl}:\text{CH}_3\text{OH} = 1:1.53:0.4:2$.

as the HCl content as shown in Fig. 3.

It should be noted that formation of such opaque gels with micrometer-sized particles is unique in the $\text{TMOS} - \text{H}_2\text{O} - \text{HCl} - \text{CH}_3\text{OH}$ solutions [6]. Alkoxides and alcohols having larger alkyl groups than TMOS and methanol, and acids with smaller dissociation constants than HCl do not work.

Nature of the polymerized species formed in the solutions

The well-known Stöber method [7] can supply round-shaped particles of submicron or micron order in size, where alkoxide solutions containing excess amount of water and ammonia are used. Formation of such particles in highly acidic TMOS solutions is not familiar to us and those particles are quite different in nature from those formed in basic solutions. First, the particles formed in the solution are soluble in non-polar organic solvent. Opaque sols turn transparent when organic liquids such as benzene are added and resultant gels have much finer microstructure [5]. This indicates that the micrometer-sized particles formed in the solution are secondary particles composed of particles or polymers having lipophilic nature. Second, these particles are composed of weakly cross-linked Si-O bonding. The smaller amount of water than needed in the formation of three-dimensional, cross-linked Si-O network may lead to polymerization reaction between partially hydrolyzed alkoxides.

Figure 4 shows ^{29}Si -NMR spectra of the dried silica gel from a highly acidic TMOS solution and silica particles obtained by the method similar to Stöber method. Lower degree of Si-O cross-linking is seen in the gel derived from highly acidic solution; Q^3 component, silicon with

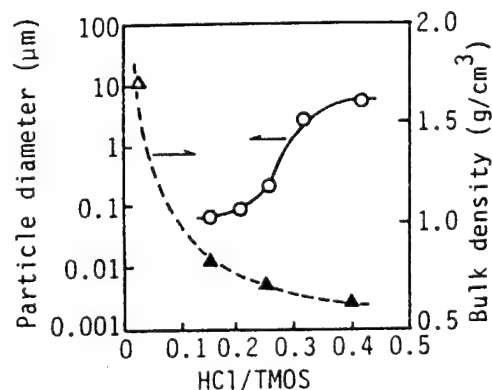


FIGURE 3 The dependence of the particle size and gel bulk density on the HCl content for the solutions of molar composition, $\text{Si}(\text{OCH}_3)_4$: $\text{H}_2\text{O}:\text{HCl}:\text{CH}_3\text{OH} = 1:1.53:0.01-0.40:2$. The solutions were kept at 40°C in an uncovered beaker.

3 bridging oxygens, is the main constituent in the gel, whereas a smaller amount of Q^2 component, silicon with 2 bridging oxygens, and a larger amount of Q^4 , silicon with 4 bridging oxygens, are observed in the spectra of the particles derived from the basic solutions.

These properties of the polymerized species which build up the gel framework affect the surface properties of the gel. Because of the presence of a large amount of unhydrolyzed methoxy groups on the particles, the surface properties are changed when the gel is aged in the ambient atmosphere. Hydrolysis and condensation reaction proceed in the presence of water vapor in the atmosphere even after gelation and removal of the solvent [8,9]. By exposing the dried gel in the 40 °C atmosphere, surface of the gel particles becomes smooth by hydrolysis and condensation reaction as shown in Fig. 5, and the specific surface area decreases from 155 m^2/g after 2 days aging to 60 m^2/g after 13 days aging.

Sintering behavior of the porous gels

Figure 6 shows linear thermal shrinkage curves of the gels derived from the solution of the composition, $TMOS : H_2O : HCl : CH_3OH = 1 : 1.53 : x : 2$ ($x = 0.15, 0.25$ and 0.40). Drastic shrinkage due to viscous sintering is seen in the temperature range of 1000 - 1200 °C, and the temperature where the sintering occurs rises as the particle size increases, namely, the HCl content in the starting solution increases [10]. Larger particle size and smaller specific surface area give smaller driving force for viscous sintering, which increases the temperature for occurrence of the sintering.

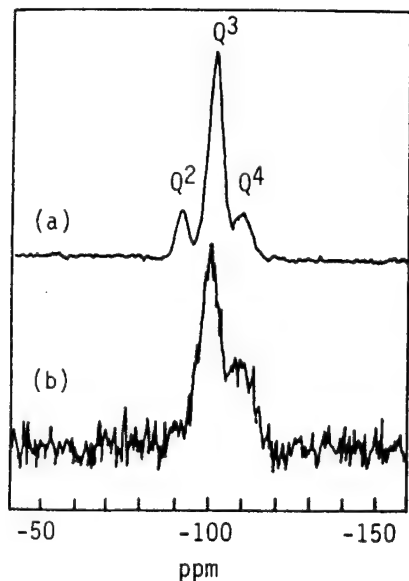


FIGURE 4 ^{29}Si -NMR spectra of the silica gel and particles.
(a) Silica gel derived from the highly acidic solution of molar composition, $Si(OCH_3)_4:H_2O:HCl:CH_3OH = 1:1.53:0.4:2$.
(b) Submicron particles obtained by the method after Stöber's using a basic solution of molar composition, $Si(OCH_3)_4:H_2O:NH_3:CH_3OH = 1:30:5:171$.

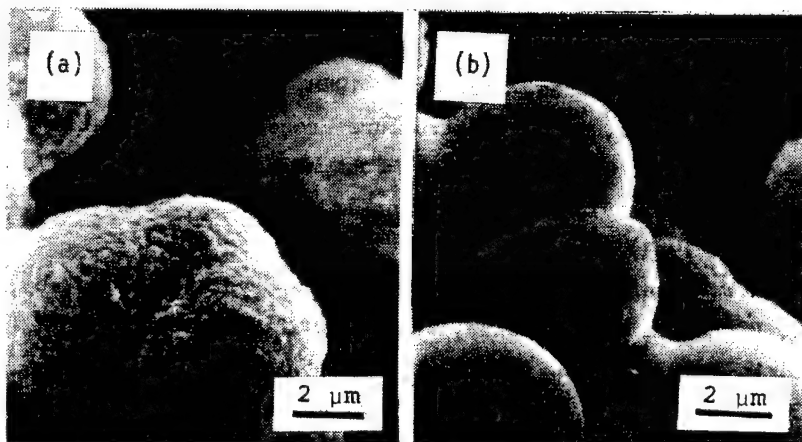


FIGURE 5 Magnified SEM photographs of the surface of the gel framework shown in Fig. 2 (b). (a) Dried for 2 days and (b) dried for 13 days in a 40°C oven.

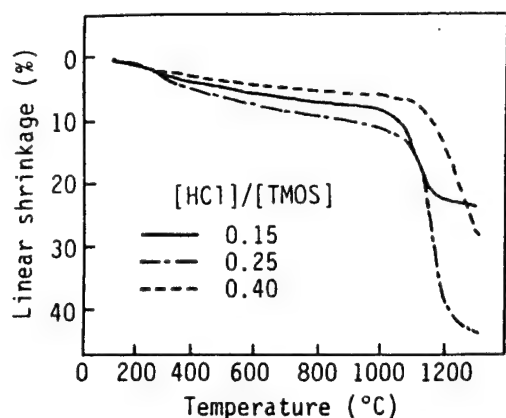


FIGURE 6 Linear thermal shrinkage of the gels derived from the solution of molar composition, $\text{Si}(\text{OCH}_3)_4$: H_2O : HCl : CH_3OH = 1:1.53:0.15-0.40:2.

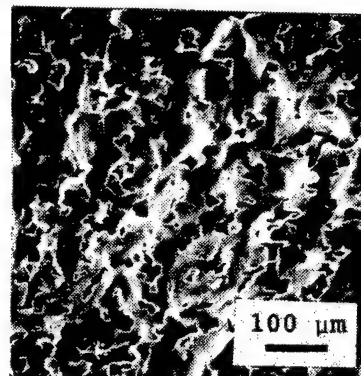


FIGURE 7 SEM photograph of the fracture surface of the porous silica glass obtained by heating the bulk gel shown in Fig. 2 at a rate of $5^\circ\text{C}/\text{min}$ to 1300°C and keeping there for 3h.

Controlled heat treatment can transform the gels into porous silica glasses. The gel shown in Fig. 2 was converted to a bulk porous glass by heating at a rate of $5^\circ\text{C}/\text{min}$ to 1300°C and kept there for 3 h. The microstructure of the fracture surface of the resultant porous glass is shown in Fig. 7, where pores more than $1\ \mu\text{m}$ in size are seen. Controlling the size of the gel particles, degree of hydrolysis and condensation reaction after gelation and heating temperature and time may serve silica glasses with various pore characteristics.

REFERENCES

1. S. Sakka, J. Chem. Soc. Jpn., 1988, 243 (1988).
2. J. Zarzycki, in "Ultrastructure Processing of Ceramics, Glasses and Composites", ed. by L.L. Hench and D.R. Ulrich, John Wiley, NY, 1984, p.27.
3. E.M. Rabinovich, D.W. Johnson Jr., J.B. MacChesney and E.M. Vogel, J. Am. Ceram. Soc., 66, 683 (1983).
4. G.W. Scherer and J.C. Luong, J. Non-Crystal. Solids, 63, 163 (1984).
5. H. Kozuka and S. Sakka, Chemistry of Materials, 1, 398 (1989).
6. H. Kozuka and S. Sakka, Chem. Lett., 1987, 1791 (1987).
7. W. Stober, A. Fink and E. Bohm, J. Colloid Interface Sci., 26, 62 (1968).
8. H. Kozuka, J. Yamaguchi and S. Sakka, Bull. Inst. Chem. Res., Kyoto Univ., 66, 68 (1988).
9. J. Yamaguchi, H. Kozuka and S. Sakka, paper presented at Foundation Memorial Symposium of Advanced Materials Science and Engineering Society, Tokyo, 1989.
10. S. Sakka and H. Kozuka, Sintering '87, ed. by S. Somiya, M. Shimada, M. Yoshimura and R. Watanabe, Elsevier Applied Science, NY, 1988, p.145.

PREPARATION OF $B_2O_3 - SiO_2$ AND $Al_2O_3 - SiO_2$ COATING FILMS BY THE SOL - GEL METHOD

Byung-Hoon Kim, Seok-Jin Choi, Kyu-Soek Hwang

Department of Ceramic Engineering
Cheonnam National University
300 Yongbong-dong, Buk-gu, KwangJu 500-070, Korea

Glass films have been prepared on soda lime silica slide glasses by the sol-gel process using the dip-coating technique from tetraethyl ortho-silicate (TEOS) and aluminum nitrate or boric acid. $M_xO_y-SiO_2$ (M = Al and B) films containing up to 40mol% Al_2O_3 and 20mol% B_2O_3 each other were transparent and adherent to substrates. The various parameters such as viscosity, withdrawal speed, composition were determined. Optical transmission and refractive index of this films were measured. Optical transmittance of substrates increased with increased B_2O_3 or Al_2O_3 content up to 15mol% B_2O_3 and 32.5mol% Al_2O_3 .

1. Introduction

Alkali-free borosilicate glasses exhibit larger energy gaps than composite glasses such as soda-lime-silicates and have a minimum refractive index at an intermediate composition.(1,2) Thus borosilicate glass could serve as a passivation layers for the microelectronic devices based on silicon and cladding material for a pure fused silica core fiber optical waveguide. These glasses, however, are hygroscopic in the boron-rich compositions(3) and require high temperature to prepare the silica-rich compositions. These glass were usually prepared by the reflow of glass powders or the chemical vapor deposition(CVD).

The coating of glasses, ceramics and metals with thin films is probably one of the most important applications of sol-gel process.(4) The deposition of these glassy films greatly modifies the optical, mechanical or electrical properties of the substrates. The process by which to obtain several types of coatings from metal-organic solutions as well as their characterization and applications have been described in several publication.(5)

In the present work the $B_2O_3 - SiO_2$ binary glass layers in the silicon-

rich compositions were prepared by the sol-gel process to obtain transparent coating on glass substrates using the dip-coating technique and the Al_2O_3 - SiO_2 binary system glasses were also prepared for compare.

2. Experimental

2-1. Preparation of solution

To prepare the starting solution for coating, TEOS, ethanol and methanol were mixed, and water containing nitric acid as catalysis was then added slowly. ^{first} This solution was composed of TEOS, ethanol, methanol, water and nitric acid in the volume ratio of 1, 0.35, 2.07, 0.42 and 0.11.

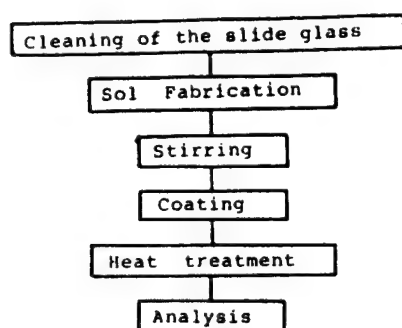


Fig.1. Flow chart

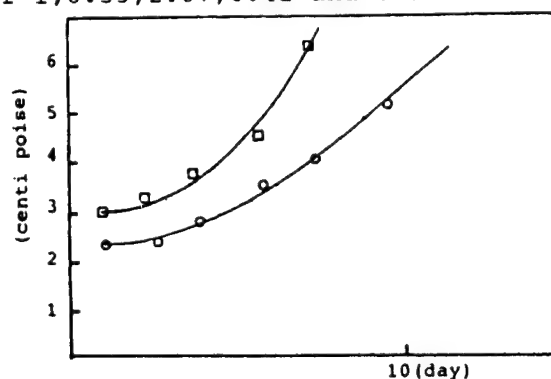


Fig.2. Viscosity of coating solution as a function of time from preparation.
(□: A1 25, ○: B 15)

Fig.1. shows schematic procedure of this experiment and fig.2. shows viscosity of coating solution as a function of time from preparation.

2-2. Coating technique and heat treatment

The coatings were deposited on soda lime silica slide glasses previously cleaned. The cleaning schedule were as follow:

- 1) immersion in NaOH(5 wt%) solution
- 2) washing with distilled water
- 3) cleaning in the ultrasonic bath
- 4) washing with acetone
- 5) drying at room temperature and storage in dessicator

The slide glasses were dipped into the solution and withdrawn at a rate of 10.048 cm/min. After coating, the slide glasses were immediately heated up to 500°C at 10 - 20°C/min.

2-3. Characterization of the coatings

The viscosity of the solution was measured using rotating viscosimeter and Ostwald-Fenske viscosimeter. The thickness of the films were measured

optically. The optical properties such as UV and IR transmittance and refractive index of glass films were measured by UV and IR spectrophotometer, and Ellipsometer.

3. Results

In fig.3, the coating thickness is plotted for films of SiO_2 as a function of the withdrawal speed U . The thickness variation of SiO_2 film with lifting speed of substrates follows Landaw - Levich law.

$$t = (\eta U / \rho g)^{1/2}$$

t = thickness of the film

η = dynamic viscosity

ρ = solution density

g = acceleration due to gravity

Thus, the thickness of films were adjusted below $0.4 \mu\text{m}$.

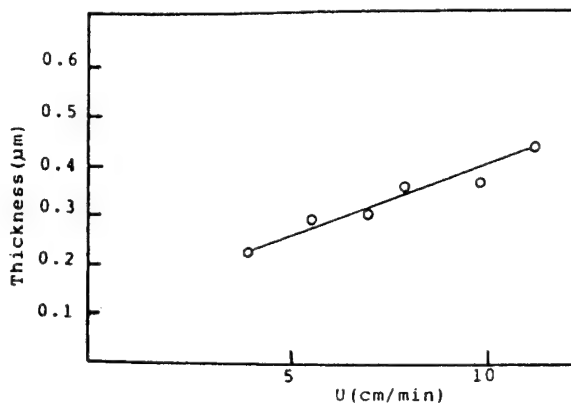


Fig. 3. Thickness variation of dense film of SiO_2 as a function of withdrawal speed.

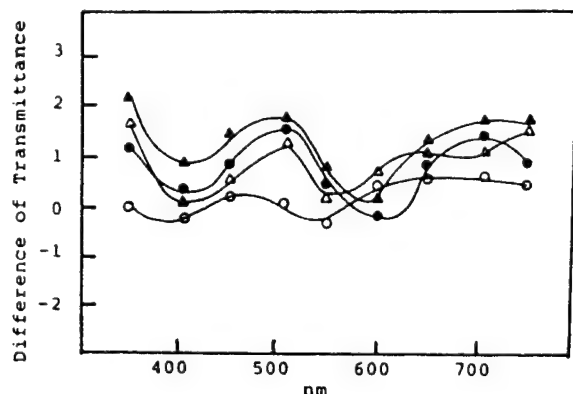


Fig. 4. Transmittance between coated and uncoated slide glasses.
(O: Al10, Δ: Al15, ●: Al25, ▲: Al32.5)

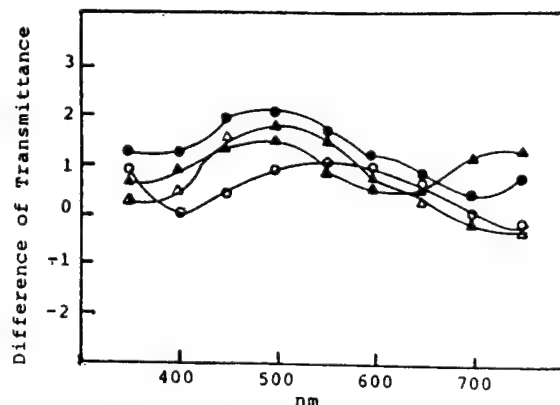


Fig. 5. Transmittance between coated and uncoated slide glasses.
(O: B5, Δ: B10, ●: B15, ▲: B20)

Fig. 4. shows the optical transmission spectra of Al_2O_3 - SiO_2 film coated substrates. Optical transmittance of substrates coated by these films were increased with Al_2O_3 content. The maximum transmittance of substrate at 500nm was obtained at 32.5mol% Al_2O_3 .

Fig. 5. shows the optical transmittance in the B_2O_3 - SiO_2 system. The maximum transmittance was obtained at 15mol% B_2O_3 . The diminution of transmittance at 20mol% B_2O_3 accord with refractive index data followed.

Refractive index as a function of B_2O_3 and Al_2O_3 content for films in the binary system $M_xO_y - SiO_2$ ($M = Al$ and B) was shown in fig.6 and 7. The refractive index of glass films decreased with increased B_2O_3 and Al_2O_3 contents but increased suddenly at 20mol% B_2O_3 . The increase of refractive index at 20mol% B_2O_3 seemed to be caused by the crystallization of HBO_3 .

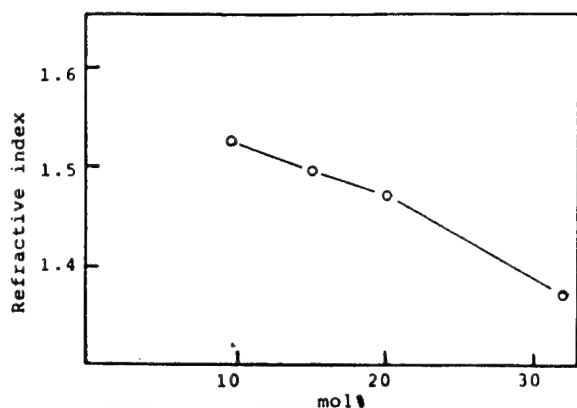


Fig. 6. Refractive index of $Al_2O_3-SiO_2$ films as function of the molar proportion of Al_2O_3 .

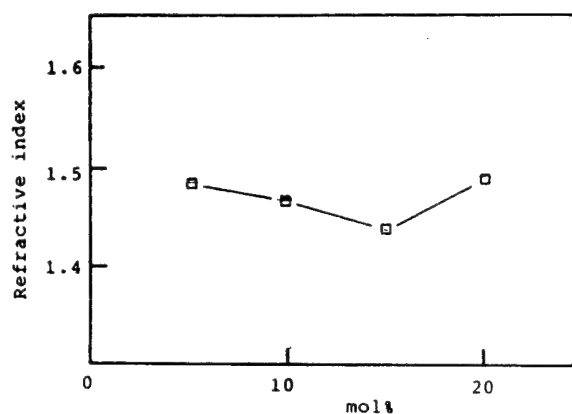


Fig. 7. Refractive index of $B_2O_3-SiO_2$ films as a function of the molar proportion of B_2O_3 .

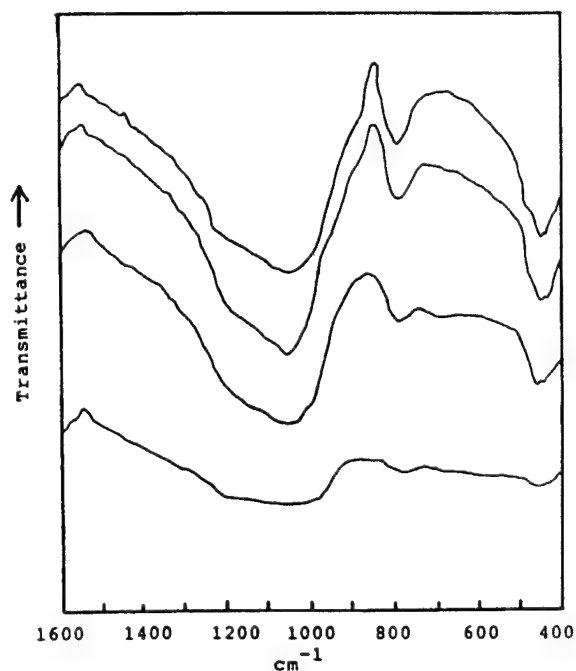


Fig. 8. IR spectra of the $Al_2O_3-SiO_2$ system.

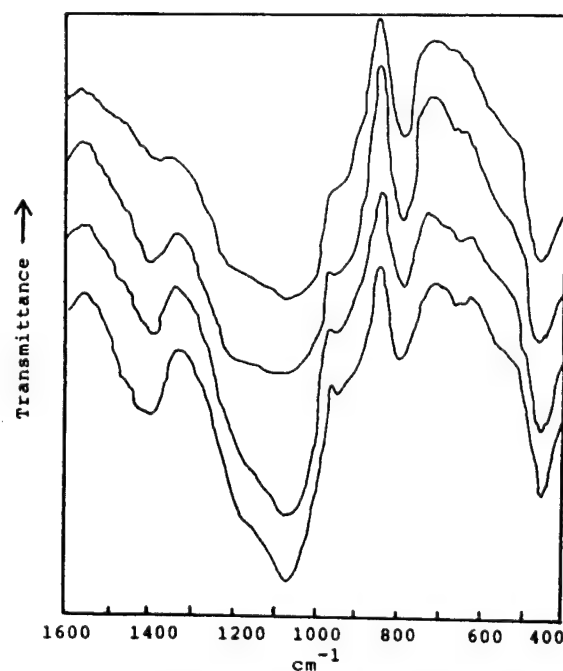


Fig. 9. IR spectra of the $B_2O_3-SiO_2$ system.

Fig.8 shows IR spectra of $\text{Al}_2\text{O}_3 - \text{SiO}_2$. The absorption band at 1100 cm^{-1} in 10mol% Al_2O_3 was assigned to the stretching vibration of Si-O-Si bonds in the amorphous SiO_2 . The absorption band in 32.5mol% Al_2O_3 was observed at 1030 cm^{-1} , a little lower wave number than for 10mol% Al_2O_3 . This shift was considered to be caused by the substitution of Al_2O_3 for SiO_2 .

Fig.9 shows IR spectra of $\text{B}_2\text{O}_3 - \text{SiO}_2$. The following IR bands were observed in the $\text{B}_2\text{O}_3 - \text{SiO}_2$ system : 1400 cm^{-1} (B-O bond), 1070 cm^{-1} (Si-O asymmetric stretching), 960 cm^{-1} (Si-O-B bond), 790 cm^{-1} (Si-O-Si bond), 650 cm^{-1} (Si-O-B bond).

4. Summery

The preparation of $\text{M}_x\text{O}_y - \text{SiO}_2$ (M= Al and B) films by the sol-gel method was investigated. Very transparent thin films containing up to 20mol% B_2O_3 and 40mol% Al_2O_3 were obtained. The maximum transmittance at 500 nm for substrates coated by the film containing 32.5mol% Al_2O_3 and 15mol% B_2O_3 . This process is very convenient and applicable to other compositions.

5. Reference

1. L.G.Van Uibert , D.A.Pinnow , J.C.Williams , T.C.Rich , R.E.Jaeger and W.H.Grodkiewicz , Mat.Res.Bull. 8 , 469 (1973)
2. S.H.Wemple , D.A.Pinnow , T.C.Rich , R.E.Jaeger and L.G.Van Uitert J.App.Phys., 44(12) , 5432 (1973)
3. N.Tohge , A.Matsuda and T.Minami , Yo - Kyo - shi , 95(2) , 182(1987)
4. H.Dislich , E.Hussmann , Thin Solid Films , 77 , 129-139(1981)
5. S.Mukherjee , W.Lowdermilk , J.Non-Cryst.Solids , 63 , 209(1984)

CRYSTALLIZATION OF BaTiO_3 BASED DIELECTRIC GLASS CERAMICS

H.S. Kim and U. Kang

Korea Electrotechnology Research Institute

28-1, Sungju-Dong, Changwon 641-120, Kyeungnam, Korea

In producing dielectric glass ceramics, Ba and Ti were adopted as elements of ferroelectric crystalline phase and Si, Al and B as network formers and Mg as additive. XRD analyses indicated that crystalline phases precipitated in dielectric glass ceramics were BaTiO_3 and $\text{Ba}_2\text{TiSiO}_8$. With adding B_2O_3 , the amount of a ferroelectric phase of BaTiO_3 increased. It also increased when Mg ion was added. Investigating temperature dependence of permittivity, Curie Point was shifted from about 120°C to 50°C . As the grain size of BaTiO_3 approached $1\mu\text{m}$, permittivities increased.

Since discovered in 1950's at first, useful glass ceramics in many fields have been researched and developed. The production process of glass ceramics have the advantage of easing the change of shape as thinner sheets than conventional sintering products and of removing porosity and voids completely. So, those will be used as laminated capacitors which have the character of high dielectric strength. Dielectric properties of the glass ceramics can be controlled by initial glass composition and by its heat treatment. In this report, the kinds of crystals precipitated in the glass matrix according to the changes of heat treatment conditions and electrical properties of its products then were studied.

1. Compositions

It is important which network-forming oxides were used for precipitating crystals of BaTiO_3 in the glass matrix. Generally network-forming oxides are not participated in forming ferroelectric phases and these are the elements of crystalline phases which may have an adverse effect on the electrical properties of product. So, it is necessary to produce no devitrified glass and then precipitate primary phase of BaTiO_3 through controlled heat treatments by adding the minimum amounts of network-forming

oxides. The researches on BaTiO₃ glass ceramics have been chiefly accomplished by Andrew Herczog and the reported results of present research on its compositions have been confined within these of his research. He reported that Si and Al, as network former, must have nearly equal atomic ratio.⁽¹⁾ But excess amounts of Al cause the melting temperature to increase and give difficulty in obtaining stable glass without devitrification. Firstly, the element of Si was chosen as a main network former, while adding a few amounts of Al and B, and mole fractions in the elements of Ba and Ti were changed. Next, precipitated crystalline phases were surveyed with comparatively increasing the amount of B and decreasing that of Si. Permittivities of BaTiO₃ glass ceramics change rapidly near the Curie point like those of BaTiO₃ sintering products. Since ferroelectric ceramics possess useful properties in the solid solutions form, efforts were made to precipitate the ferroelectric phase in the solid solution form by substituting suitable cations such as Sr, Pb and Zr in the glass ceramics. But the solid solution did not seem to crystallize in glass ceramics while the reduction of ferroelectric phase by the precipitation of another phase occurred instead of the formation of solid solution.⁽²⁾ In this study, the effect on the formation of ferroelectric crystalline phase by the variation of network former and by adding Mg ion which might substitute site of Ti ion in perovskite structure and then the shift of Curie Point were investigated. The compositions of various glasses are given in table 1.

Table 1. Compositions of BaTiO₃ glass ceramics (wt %)

조성	SiO ₂	Al ₂ O ₃	B ₂ O ₃	BaCO ₃	TiO ₂	MgO
1	10.79	2.29	1.56	62.02	21.52	1.81
2	10.33	2.19	1.50	63.64	20.61	1.73
3	9.91	2.10	1.44	65.12	19.77	1.66
4	9.60	2.04	1.39	63.04	22.33	1.61
5	10.99	2.33	1.59	63.17	21.92	0.00
6	10.08	2.14	1.46	66.21	20.11	0.00
7	8.19	2.31	3.16	62.74	21.77	1.83
8	7.83	2.22	3.03	64.33	20.84	1.75

2. Glass forming

The melting temperatures of batches were changed at the range of temperatures from 1100 °C to 1400 °C according to initial glass composition. Batches were melted for 2 hours at 1400 °C to shorten melting time in a covered Pt crucible. The melt was

quenched rapidly between two stainless steel slabs preheated at 600 °C to produce glass sheets of about 2mm thick and 10cm diameter and quickly transferred to another pre-heated furnace maintained at 600 °C for annealing. Since the viscosities of melts were relatively low which contained network former as a low rate, these were rapidly crystallized nearby the liquidus temperature. For preventing the crystallization of melt on cooling, the above quenching procedure was necessary from the liquid phase to the glass phase.

3. Heat treatment

Single-step heat treatment is used when nucleation occurs simultaneously with crystallization, when nucleation occurred already during product cooling, or during heating to the crystallization. Fahmy⁽³⁾ reported that glasses containing TiO₂ would require only a single heat treatment to attain the desired glass ceramics, since such additions were found to shift the nucleation peak to higher temperatures, closer to that of the growth peak. Actually since both nucleation and growth rate curves overlapped over a range of temperatures, in the present work single heat treatment was applied to BaTiO₃ glass ceramics. Each grain of BaTiO₃ glass ceramics⁽⁴⁾ will form twins that deteriorate permittivity at above the grain size of about 1 μm in diameter as that of sintering product because the domain wall energy is smaller than that of bulk strain. Heat treatment is therefore important for elevating the permittivity of the produced samples. The heat treatment condition is as follows. The glass products were heated to 550 °C at a rate of 5 °C/min and then to a temperature between 800-1000 °C at a rate of 3 °C/min considering the movement of ions and for 2 hours at the range of above crystallisation temperatures.

4. Discussion

The crystalline phases were identified as BaTiO₃ and Ba₂TiSi₂O₈ by x-ray diffraction analysis(fig.1). DTA curve in fig.2 shows two exothermal peaks at 735 °C and 764 °C representing crystallisation. XRD indicated that fresnoit (Ba₂TiSi₂O₈) crystalline phase was formed near 735 °C and BaTiO₃ crystal phase near 764 °C. So, in

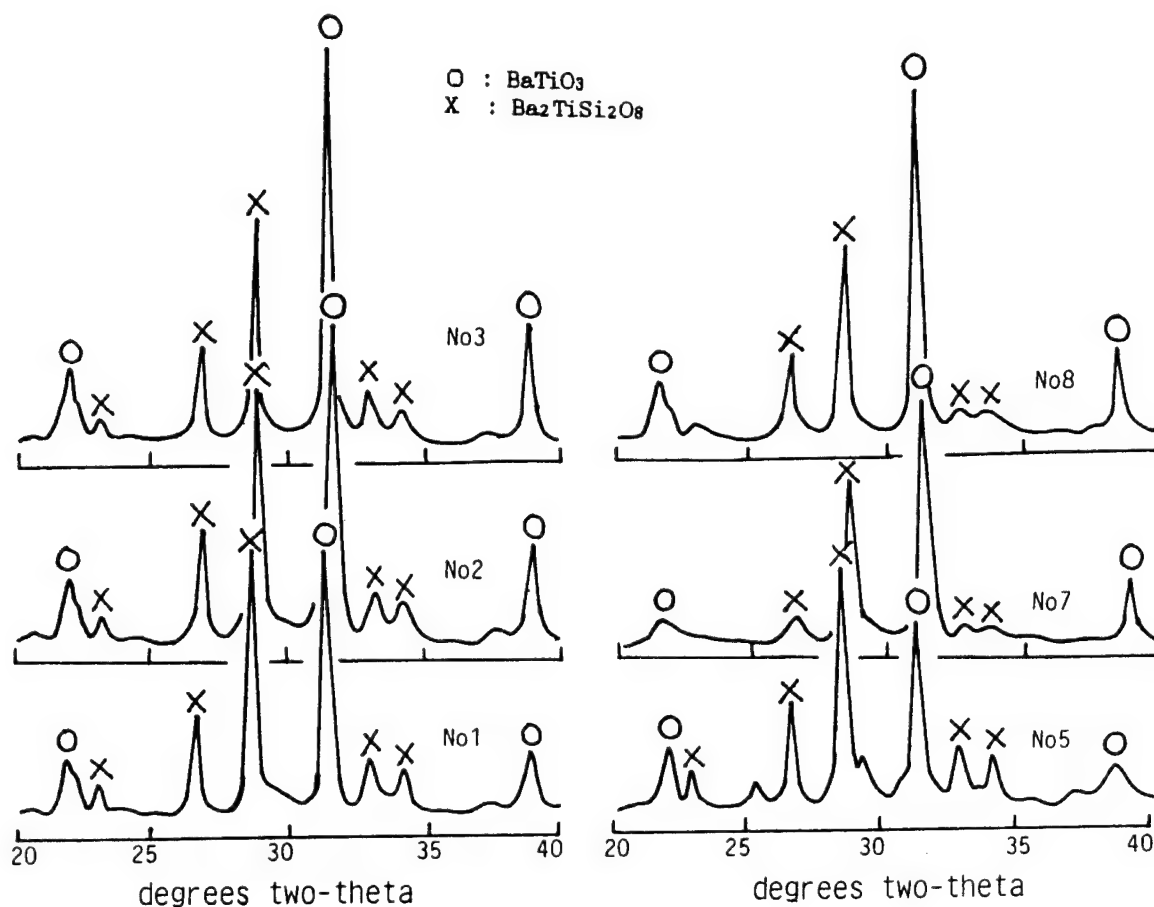


Fig 1. XRD Patterns showing crystallisation of BaTiO_3 and $\text{Ba}_2\text{TiSi}_2\text{O}_8$

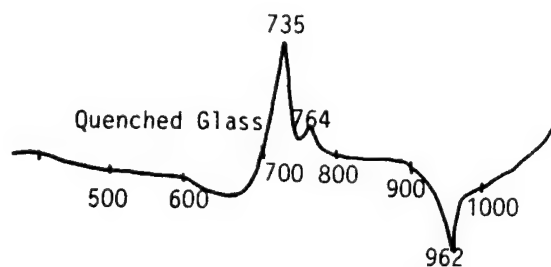


Fig 2. DTA patterns of $\text{BaO-TiO}_2\text{-SiO}_2\text{-B}_2\text{O}_3$ glass

initial glass compositions containing lots of Si ion, the precipitation of fresnoit crystal would be easy. Herczog reported that the permittivity is more larger when Ba and Ti ion have almost stoichiometric values. In that case, Si and Al as network former were added by nearly the same amount and these formed network structure and effectively suppressed to precipitate adverse crystalline phases. On experimental compositions, before being formed BaTiO_3 crystalline phase, fresnoit crystalline phase

was formed. So, it was needed to add much amount of Ba element. As can be seen from fig.1 the more precipitation of BaTiO_3 crystals were obtained with an excess of Ba elements than with stoichiometric compositions. In sample 4, Ti element was relatively more added than in sample 3. Ti ions are the element which forms crystal and simultaneously acted as a network former. So, in above sample 4, more added Ti ions act as a network former instead of forming crystal. As a result, the precipitations of BaTiO_3 and $\text{Ba}_2\text{TiSi}_2\text{O}_8$ decreased. In contrast to samples 1 and 3, Mg ion was not added in samples 5 and 6. X-ray intensities of BaTiO_3 crystal phase decreased in comparison with $\text{Ba}_2\text{TiSi}_2\text{O}_8$ in samples 5 and 6. So, there are some possibilities in the isomorphic substitution of Mg ion for Ti ion. In samples 7 and 8, the amount of B ions increased. To stay Si ions at network which participate in crystal phase of $\text{Ba}_2\text{TiSi}_2\text{O}_8$, it was asked to add strong network former. Since the field strength of P ion is higher than that of Si ion, P ion has stronger attraction in pulling oxygen ions. So, Adding P ions as network former rather caused to devitrify in parent glasses and precipitate adverse crystalline phase of such as $\text{Ba}_4\text{TiP}_2\text{O}_{15}$. The difference of field strength between B and Si is 0.06 and demixing of Si and B ions could occur in network. On the one hand most of Ti ions also function as part of network former and have lower field strength than that of network former. Excess amount of B ion which has a little stronger ionic strength than that of Si therefore cause to devitrify and precipitate crystalline phases such as BaTiB_2O_6 . Therefore, a limited amount of B ions must be added. Fig.3 shows that by adding B ion

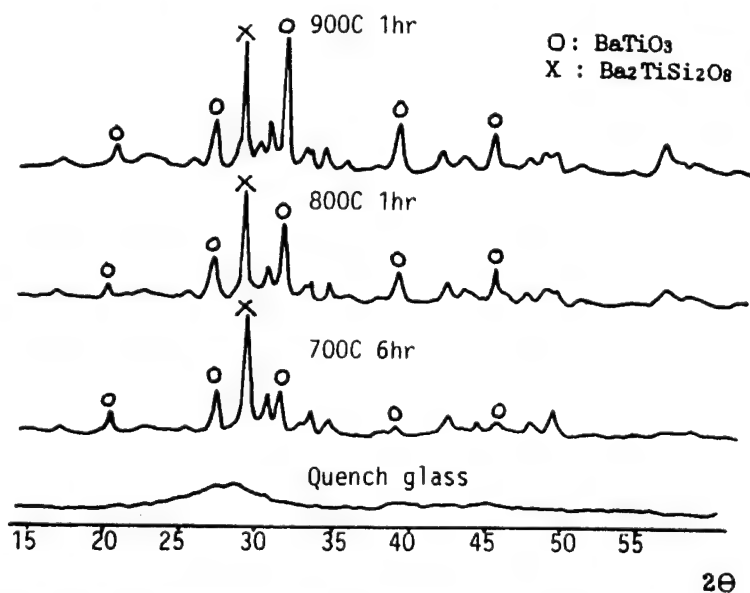


Fig 3. XRD Patterns showing crystallisation of BaTiO_3 and $\text{Ba}_2\text{TiSi}_2\text{O}_8$ in $\text{BaO-TiO}_2\text{-SiO}_2\text{-B}_2\text{O}_3$ glass

the X-ray intensities of BaTiO₃ crystalline phase was increasing in proportion to the elevation of heat treatment temperature while those of fresnoit crystalline phase is nearly fixed. It is deduced therefore many Si ions keeps balance with B ions in network instead of forming phases of Ba₂TiSi₂O₈. Because the grain size of precipitated crystalline phase has much relevance to the improvement of permittivity, the microstructures of samples were observed through SEM. The grain sizes of BaTiO₃ in sample 1 changed from 0.5 μ m to 1 μ m by the elevation of heat treatment temperature from 900 °C to 1000 °C. And then relative permittivity increased as grain size approaches 1 μ m.(fig. 4) Fig.5 shows Dependence of permittivity, K, upon the temperature which indicates the shift of the Curie point from 120 °C to 50 °C. By the well-known displative model(s), the shift of Curie point could be explained. By substituting Mg for Ti, the Cure Point would be lowered from 120 °C to 50 °C because the bonding strength of the Mg ion to oxygen is stronger than that of Ti ion. Adding Mg ion is also attributed to depress the peak around Curie point.

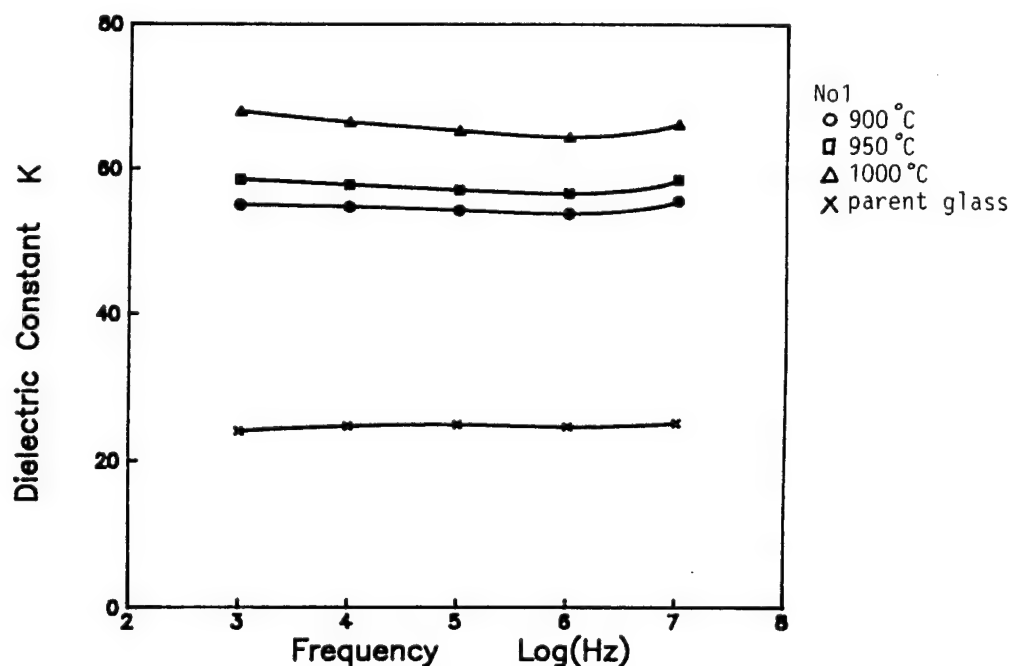


Fig 4. Dielectric constant at various frequencies after heat treatment at the indicated temperature

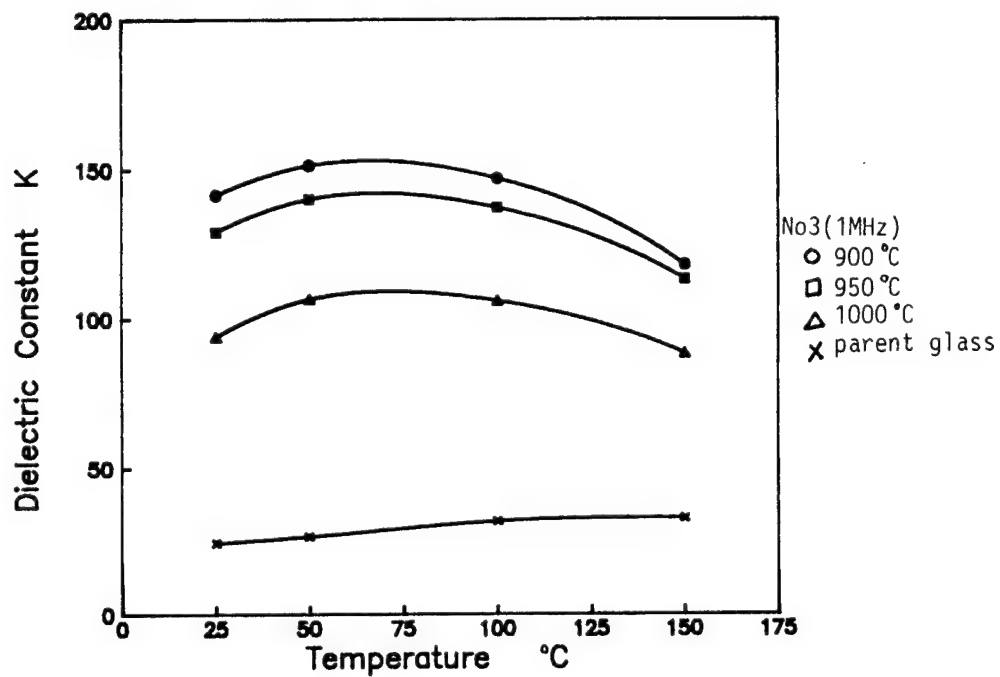


Fig 5. Dielectric constant-temperature relationship after heat treatment at the indicated temperature

References

- (1) U.S.patent 3,195,030 (1965)
- (2) Bull.Mater.Sci., Vol.9, No.4 (1987) 255-262
- (3) Physics Chem.Glasses, Vol.28, No.1 (1987)1-3
- (4) J.Am.Ceram.Soc., Vol.47, No.3 (1964) 107-115
- (5) Dielectrtic Materials and Applications, (1954) 40-46

EFFECT OF MODIFIERS ON THE STRUCTURES AND HYDROXYAPATITE

FORMATION OF BIOGLASS

Cheol Y. Kim, and Hopil Lee

Dept. of Ceramic Engineering, Inha University
253 Yonghyun-dong, Nam-gu, Incheon 402-701, Korea

When K_2O and CaO are substituted for Na_2O in 45S5 Bioglass, their glass structures and hydroxyapatite formation are investigated. Several physical properties, such as density, microhardness, thermal expansion coefficient etc., are measured and interpreted in terms of glass structures. When the glasses are reacted in Tris-buffer solution, K_2O substitution promotes hydroxyapatite formation while CaO substitution prohibits the crystal formation.

Introduction

Many researches have been interested in bioceramics since 1970, and several bioceramic materials, such as alumina, hydroxyapatite and bioactive glass, have been introduced. Among them bioactive glasses show special surface properties when they are implanted in human body. That is, hydroxyapatite crystals form on the glass surface when implanted, which promote the bonding between implant and living tissue. The first bioactive glass was introduced by L.L.Hench[1], and its basic composition is 24.4% Na_2O 26.9% CaO 46.1% SiO_2 2.6% P_2O_5 (mole%), which is called Bioglass (45S5).

45S5 glass has high surface reactivity to body solution, and the glass is getting weaker as time passes after implantation. To prevent this phenomenon, it is needed to study the reaction between Bioglass and living tissue depending on the glass composition, and this reaction should relate closely to the glass structure. Therefore, studies on structure and physical properties of Bioglass should be carried out.

In the present study, K_2O and CaO are systematically substituted for Na_2O in 45S5 Bioglass composition.

Glass structure and physical properties of the resultant glasses are examined. The effect of these glass compositions on the formation of hydroxyapatite are also studied.

Experimental

Table 1 and 2 show the glass compositions in the present study. Premixed batches from the reagent grade of SiO_2 , Na_2CO_3 , H_3PO_4 , CaCO_3 and K_2CO_3 were melted in a covered Pt-crucible at a temperature range of 1200°C to 1300°C depending on the compositions. Infrared and Raman spectroscopic studies were performed to analyze the resultant glass structures, and several physical properties, such as density, thermal expansion coefficient and softening points, are also measured.

The obtained glass samples were reacted in tris hydroxymethyl aminomethane buffer solution (PH=7.2, temp.=37°C) for various time. The reacted surface was examined by FT-IR with diffuse reflection attachment to analyze the formation of surface layer morphology, and layer thickness of hydroxyapatite was examined by SEM.

Table.1 Batch composition of bioglasses (mole%).

Sample	Na ₂ O	K ₂ O	SiO ₂	P ₂ O ₅	CaO	$\frac{\text{K}_2\text{O}}{\text{Na}_2\text{O}+\text{K}_2\text{O}}$
0.0KN	24.4	0.0	46.6	2.6	26.9	0.0
0.2KN	19.5	4.9	'	'	'	0.2
0.4KN	14.6	9.8	'	'	'	0.4
0.6KN	9.8	14.6	'	'	'	0.6
0.8KN	4.9	19.5	'	'	'	0.8
1.0KN	0.0	24.4	'	'	'	1.0

Table.2 Batch composition of bioglasses (mole %).

Sample	Na ₂ O	CaO	SiO ₂	P ₂ O ₅	$\frac{\text{CaO}}{\text{CaO}+\text{Na}_2\text{O}}$
0.4 CN	30.78	20.52			0.4
0.52CN	24.40	26.90			0.52
0.6 CN	20.52	30.78	46.1	2.6	0.6
0.7 CN	15.39	35.91			0.7
0.8 CN	10.26	41.04			0.8

Results and Discussion

(1) KN series

No significant difference in Infrared and Raman spectroscopic spectra was seen as K_2O was substituted for Na_2O in 45S5 Bioglass. This indicates K^+ and Na^+ ions play a similar role in the formation of glass structure.

However significant changes were observed in their physical properties. Density increased while molar volume decreased with K_2O , which indicates the increase in free space in the glass structure. (Fig. 1)

Their thermal expansion coefficient increased with K_2O substitution upto 0.2KN. This is because the bond strength of K-O is much weaker than that of Na-O. Further increase in K_2O reduced thermal expansion coefficient and this is probably due to the absorption of thermal atomic vibration by free space in the glass structure. (Fig. 2)

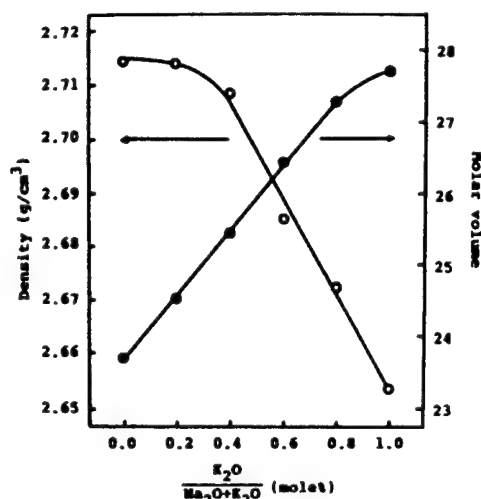


Fig. 1 Density and molar volume of the bioglasses with various $K_2O/(Na_2O+K_2O)$ ratio.

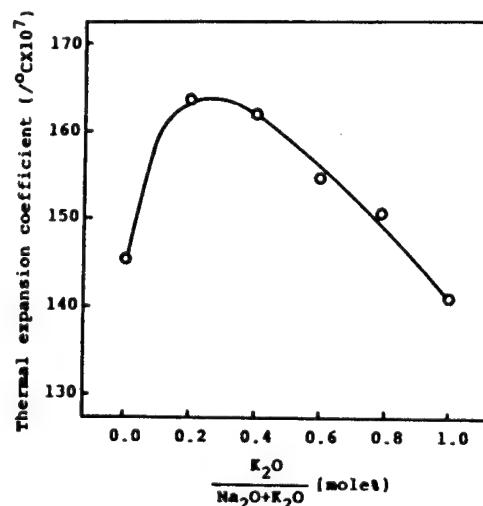


Fig. 2 Thermal expansion coefficient of the bioglasses with various $K_2O/(Na_2O+K_2O)$ ratio.

Fig. 3 shows FT-IRRS spectra of the hydroxyapatite formed on the glass surface when the samples were reacted in Tris-buffer solution. The peaks at 605 cm^{-1} and 560 cm^{-1} are due to the bending vibration of P-O bond, which are very characteristic peaks for hydroxyapatite[2]. The peak at 450 cm^{-1} comes from Si-O bending mode. With increase in K_2O the intensity of P-O bending mode (605 and 560 cm^{-1}) increases, while that of Si-O bending mode (450 cm^{-1}) decreases. This indicates that K_2O substitution for Na_2O helps hydroxyapatite formation.

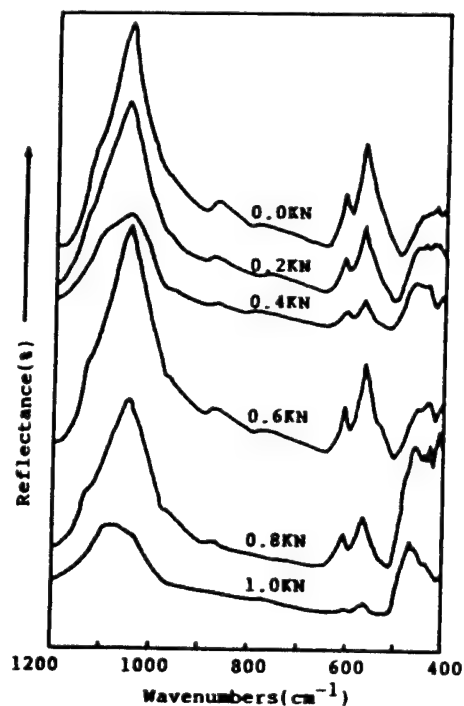


Fig. 3 FT-IRRS spectra of the bioglasses with various $K_2O/(Na_2O+K_2O)$ ratio after 10 hours reaction.

(2) CN series

Densities of the glasses change from 2.68 to 2.80g/cm³ as CaO is substituted for Na₂O in 45S5. When considered the similarity in atomic weight of CaO and Na₂O as well as ionic size of Ca²⁺ and Na⁺, free space in the glass structure will increase by substitution of one Ca²⁺ ion for two Na⁺ ions. Because the bond strength of Ca-O(NBO) is much stronger than that of Na-O(NBO), thermal expansion coefficient of those glasses sharply decrease from 162x10⁻⁷/°C to 113x10⁻⁷/°C with CaO.(Fig. 4)

The glass with low thermal expansion coefficient will reduce stress problem when it is coated on alumina[3].

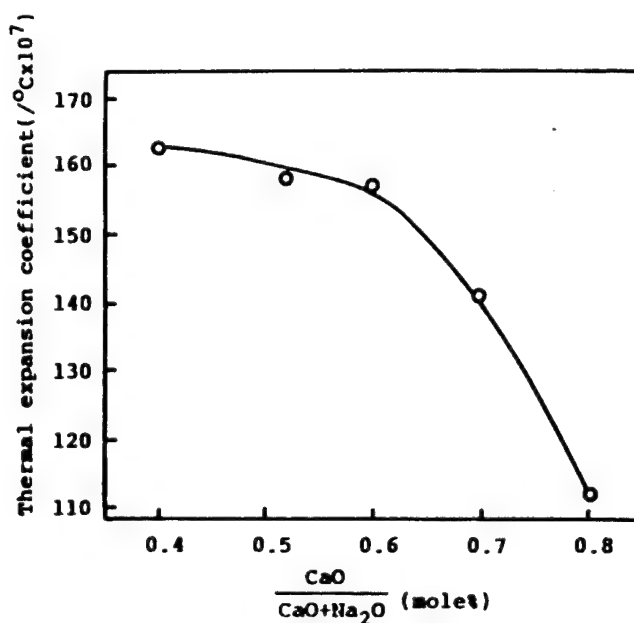


Fig. 4 Thermal expansion coefficient of bioglasses with various CaO/(CaO+Na₂O) ratio.

When the glasses are reacted in Tris-buffer solution, hydroxyapatite forming rate decreased as CaO content increased.(Fig. 5) However hydroxyapatite crystal was formed for all glasses when the samples were reacted for 20hours. Fig. 6 shows the cross-section of 0.4CN and 0.8CN after 100hours of reaction. Narrower Si-rich layer was observed for 0.8CN.

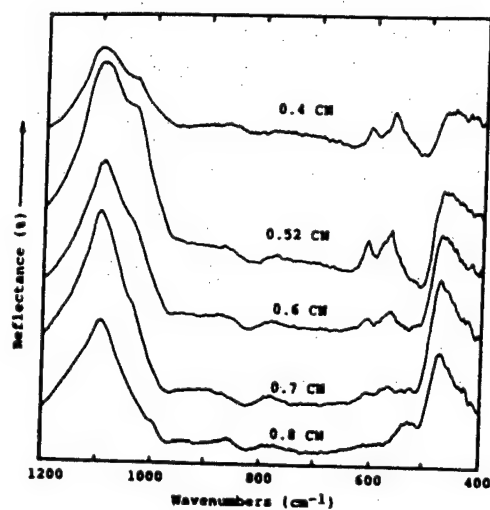


Fig.5 FT-IR spectra of the bioglasses with various $\text{CaO}/(\text{CaO}+\text{Na}_2\text{O})$ ratio after 6 hours reaction.

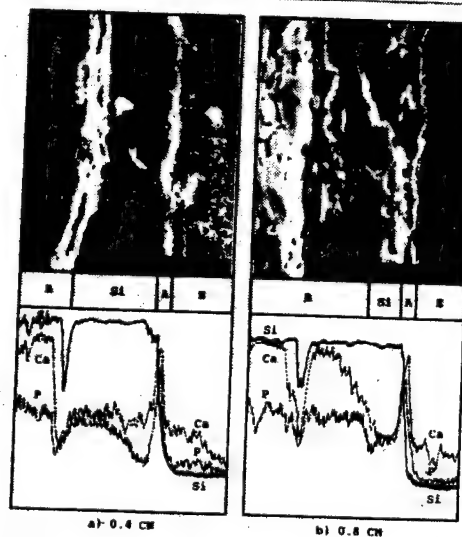


Fig.6 Line profiles of EDS and micrographs of cross sections of 0.4 CM and 0.8 CM bioglasses after 100 hours reaction in tris-buffer solution.

Reference

- 1] L.L.Hench et.al, U.S. Army Report No.1 Contract No. DADA-17-70-C-001 (1970)
- 2] C.Y. Kim et.al, J.Non-Cryst. Solids in print
- 3] D.C. Greenspan et.al, J.Biomed.Res.Sym. No.7 503-509(1976)

DISPERSION-FLOCCULATION BEHAVIORS OF MULLITE SLIP AND THEIR EFFECTS ON THE MICROSTRUCTURES OF GREEN CASTS

Ki G. Lee*, Han N. Cheong*, Hyun M. Jang*, and Eui H. Kim**

* Reserch Institute of Industrial Science and Technology,
Pohang 790-600, Korea

+ Pohang Institute of Science and Technology, Pohang 790-600, Korea

++ Sam Hwa Chemical Co., LTD., Pohang 790-600, Korea

Dispersion - flocculation characteristics of fine mullite powder in aqueous slurry were studied. Zeta potentials and viscosities of the suspensions were correlated with interfacial properties of mullite. The pH range suitable for forming green-casts with dense and homogeneous microstructures was 5 - 6, and this was correlated with viscosity of the slip and the secondary minimum heterocoagulation. The green-casts prepared from the slips with pH 10 or above showed inhomogeneous microstructures. Though magnitude of the zeta potential in this pH range was high, flocculation induced high relative viscosity and deteriorated the microstructures of green-casts. This observation was interpreted in terms of dissolution-reprecipitation phenomena of the silicate species formed above pH 10.

1. Introduction

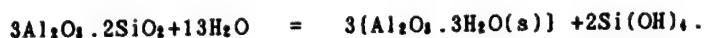
The role of mullite as structural and refractory materials has been extensively documented. Mullite($3\text{Al}_2\text{O}_3 \cdot 2\text{SiO}_2$) is one of few stable materials among many aluminosilicate minerals and is common in porcelain, refractory, electrical insulator etc. due to its excellent spalling resistance, strength and refractoriness. Recently, on the other hand, a great deal of interest has been focused on the homogeneous forming of ceramic green body (such as slip casting) with complicated shape from the colloidal slurry state.

In this work, the dispersion characteristics of fine mullite powder in slurry state were examined, and the green microstructures formed by slip casting were correlate with these dispersion-flocculation characteristics.

2. Solubility of Mullite

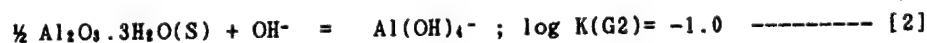
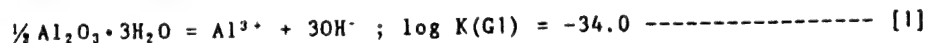
Our colloidal study of mullite slip indicated that the dissolution of mullite in aqueous solution controls stability behavior of the slurry and thus, microstructure of the green body. Therefore, we have estimated the dissolution behavior of mullite as a function of suspension pH.

When mullite is introduced into pure H_2O , it dissolves incongruently. and forms gibbsite and silicic acid by the following reaction:



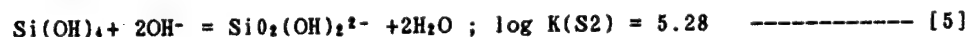
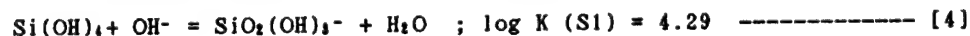
For hydrolysis species of gibbsite ($\text{Al}_2\text{O}_3 \cdot 3\text{H}_2\text{O}$), there is a great deal of uncertainty about the composition and stability, but polynuclear hydroxo complexes formed from the hydrolysis of gibbsite do not materially alter the solubility characteristics of gibbsite (1).

Therefore we carry out our calculations by considering $\text{Al}(\text{OH})_4^-$ and Al^{3+} as the predominant equilibrium species.



The equilibrium constants given above are valid at 25° C. Data for equation [1] to [2] are those given by Stumm(1).

On the other hand, the solubility of silicate species formed from the dissolution of mullite can be characterized by the following set of equilibria (2,3):



The equilibrium constants for equations (1) to (6) permit computation of the solubility of mullite for the entire pH range, and we have constructed a predominance diagram relevant to the dissolution of mullite in an aqueous slurry state.

In an actual calculation, we assumed that mullite dissolved continuously until the equilibrium concentration of $\text{Si}(\text{OH})_4$ in an mullite slurry attained the level predicted by Equation[3], that is, $[\text{Si}(\text{OH})_4] = 10^{-2.7}$.

This assumption is essentially the same as that used by Stumm in the calculation of kaolinite solubility as a function of suspension pH(1).

3. Experimental

The mullite powder used in this study was commercial fused mullite with submicron particle size. By addition of NaOH/ HCl or KOH/ HNO₃ to mullite suspension, a series of aqueous mullite suspensions was prepared varying in pH from 2 to 12.

To determine the surface charge of mullite in the suspensions, zeta potential was estimated by measuring group velocity of particles under a given applied electric field (Lazer Zee Meter; Pen Kem Inc.). Viscosity of the slip was measured using a rotating viscometer. Mullite slurry prepared for slip casting was various in pH from 2 to 12, and mullite to water ratio is 1 in weight. The green bodies prepared by slip casting were fired at 1600° C . The green microstructures of mullite specimen were examined using a scanning electron micrograph. The supernatant of mullite slurry was analyzed by ICP method, and the results were correlated with the solubility of mullite in acidic or alkaline medium. Chemical and morphological characteristics of the precipitates, formed by the dissolution-reprecipitation reactions of mullite, were examined by STEM.

4. Results, Discussion and Conclusions

Fig.1, Fig. 2 and Fig.3 respectively show the zeta potentials, the viscosity data and the solubility-pH diagram of the mullite slip as a function of equilibrium pH. Several conclusions can be made from these results:

- (i) The isoelectric point (IEP) of the mullite slip is 7.8 ;
- (ii) High viscosity of the slip observed around pH 8 (or near IEP) is closely related with flocculation of the mullite slip at low surface charge condition ;
- (iii) The minimum viscosity value observed around pH 5-6 is probably related with the secondary minimum coagulation(4) of mullite particles in the slip;
- (iv) High relative viscosity of the slip observed for pH value above 9.5 is due to reprecipitation of ionic silicate species onto mullite powder surface and heterocoagulation of these precipitates with mullite particles. Fig.3 shows that the negatively charged silicate species dominate over Si(OH)_4 and Al(OH)_4^- above pH 9.5. Thus, the solubility-pH diagram for dissolution of mullite supports the above tentative conclusion.

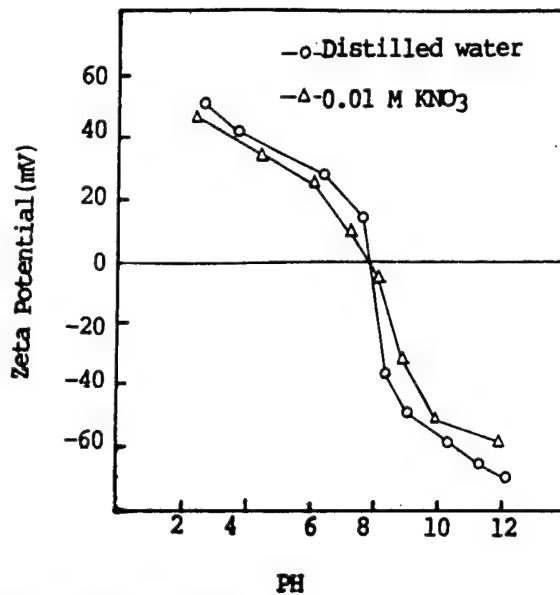


Fig. 1. Zeta potential of mullite as a function of suspension pH with and without the ionic strength control.

Fig. 4 shows SEM of the microstructures of the green casts prepared by slip casting. The green microstructure of the specimen prepared at pH 5.5 shows dense and homogeneous microstructure, indicating the role of viscosity and zeta potential in controlling microstructures of green bodies

Table 1 shows ICP results for the supernatant of mullite

slip prepared by centrifugation of the slip after equilibration. The observed high relative concentration of Al species at extreme pH region, that is, near pH 2 and 12, is consistent with the result of estimated solubility-pH behavior of Al^{3+} and $Al(OH)_4^-$ species (Fig. 3). A rapid decrease of equilibrium silicate concentration (Table 1) above pH 6 is related with the reprecipitation of the ionic silicate species or cooperative precipitation of $Si(OH)_4$ with the ionic silicate species.

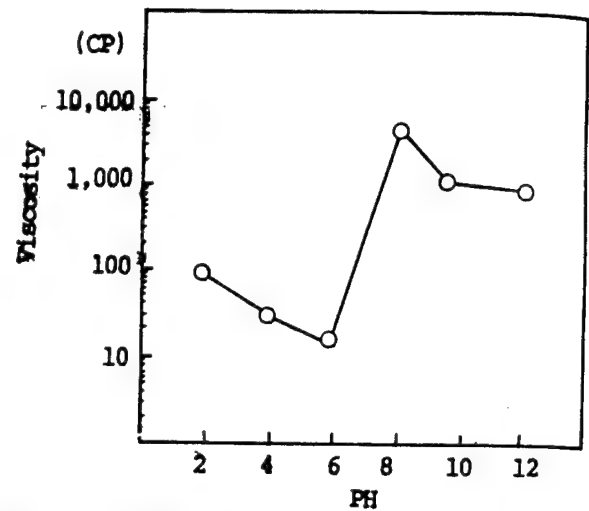


Fig. 2. Viscosity of mullite slip at constant shear rate of 3 sec^{-1} as a function of equilibrium pH.

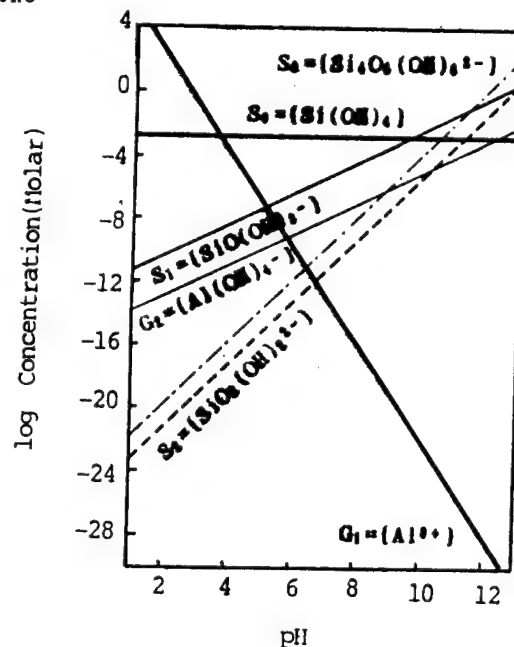


Fig. 3. Solubility-pH diagram of the soluble Al and Si species dissolved from the mullite powder in aqueous slip.

(a)



(b)



(c)

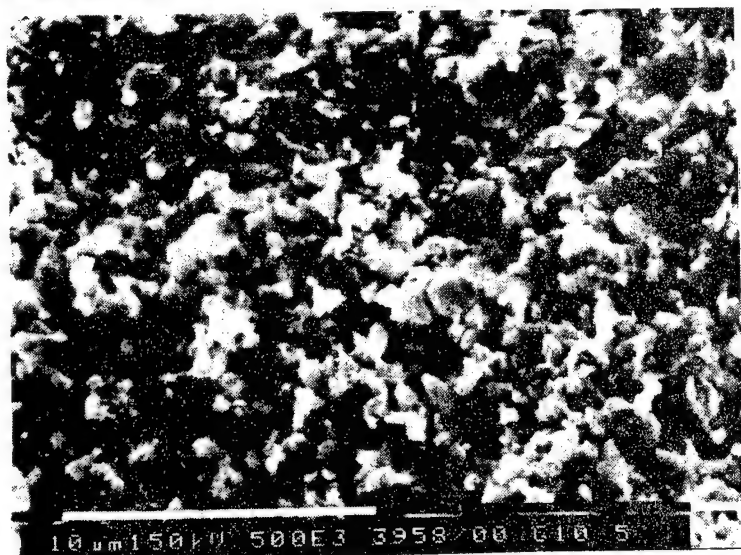
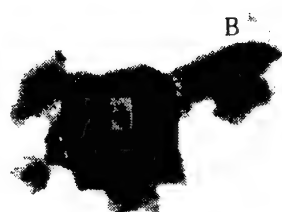


Fig.4. SEM of green-casts prepared by slip casting using slurries of different pH values: (a) pH 5.5; (b)pH8.5; (c)pH 10.5.

The EDS results (Fig.5) show fine precipitates of Si-rich species formed at mullite surface, supporting our hypothesis, that is, the dissolution-reprecipitation of the silicate species onto mullite particles above pH 10.0.

Table 1. ICP result for the supernatant of mullite slips conditioned at several different equilibrium pH values. (PPM)

pH	2	6	10	12
Al	16,520	0.36	29.45	907.0
Si	3,235	1.20	Tr	18.0



(a)

	ELMT.	% CONC.
A	Si	24.817
	Al	75.183
B	Si	82.277
	Al	17.723

(b)

Fig.5 STEM and EDS results for mullite powder derived from the slip at pH 12: (a) STEM (b) EDS

5. References

- (1) W. Stumm and J. J. Morgan, Aquatic Chemistry, 2nd Ed., John Wiley and Sons (1981), Chapter 9.
- (2) R. K. Iler, The Chemistry of Silica, John Wiley and Sons (1979), chapter 2.
- (3) N. Ingri, Acta Chem. Scand., 13, 758 (1959).
- (4) K. furusawa and M. Matsumoto, in Electrical Phenomena at Interfaces, edited by A. Kitahara and a. Watanabe, marcel Dekker, New york (1984), Chapter 8.

SYNTHESIS OF Al_2O_3 -COATED TiO_2 AND Al_2O_3 -COATED Cr_2O_3 COMPOSITE POWDER BY HOMOGENEOUS PRECIPITATION METHOD

Byung-Kwan Kim and Itaru YASUI *

Chang-Won National University
234, Taechon-dong, Changwon 641-240, Korea

* Institute of Industrial Science, The University of Tokyo, Roppongi,
Minato-Ku, Tokyo, 106, Japan

$\text{Al}(\text{OH})_3$ -coated TiO_2 composite powder was prepared from the aqueous solution of $\text{Al}_2(\text{SO}_4)_3$ and rutil powder by homogeneous precipitation method using urea, then heat treated at 1200°C for 1 hr in order to convert it to α - Al_2O_3 -coated TiO_2 powder. The homogeneous precipitation method using urea was also applied to the synthesis of Al_2O_3 -coated Cr_2O_3 composite powders from aqueous solutions of $\text{Al}_2(\text{SO}_4)_3$, as well as $\text{Al}(\text{NO}_3)_3$, and heat-treatment at 1200°C for 1 hr converted them to α - Al_2O_3 -coated Cr_2O_3 composite powders.

1. Introduction

It is important to develop a new class of ceramic powders, such as powders coated with other kinds of substances. For example, Al_2O_3 -coated TiO_2 composite powder is of use as a starting material of aluminum titanate (Al_2TiO_5) which is well-known for its apparent low thermal expansion and high melting point [1]. To obtain improved, reliable composite ceramic powders, coating process is to be optimized. Aluminum titanate is ordinarily prepared from a stoichiometric mixture of alumina (Al_2O_3) and titanate (TiO_2) powders by conventional processing methods such as ball milling and isostatic pressing [2]. These method, however, often yield powders mixed inhomogeneously on a microscopic scale, and do not allow control of particle-size distribution and particle shape in a sintered body. The homogeneous precipitation method is one of the best methods to control pH and to form pure and dense precipitates, so that various ceramic powders such as TiO_2 , Al_2O_3 , MgAl_2O_4 , Fe_2O_3 , $\text{Fe}(\text{OH})_3$, and SnO_2 -coated TiO_2 composite powders were synthesized by this method using urea [3-10]. On the other hand, TiO_2 -coated Al_2O_3 composite powder was prepared from titanium alkoxide precursor and alumina powder by Okamura et al [11].

This paper deals with the synthesis of Al_2O_3 -coated TiO_2 and Al_2O_3 -coated Cr_2O_3 composite powders using the homogeneous precipitation method as a coating process.

2. Experimental procedure

16-hydrated aluminum sulfate and urea used were guaranteed grade (Wako Chemical Co.) and TiO_2 powder (rutil form) (Sakai Chemical Co.) consisted of approximately spherical particles with the average particle size of $0.2 \pm 0.04 \mu$

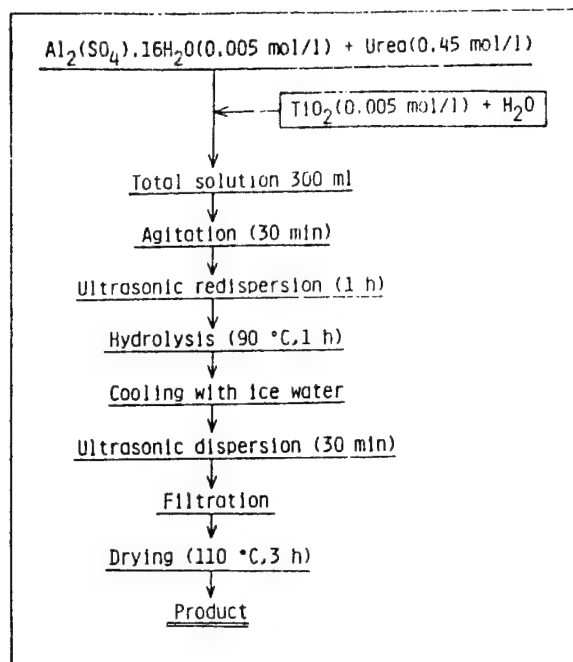


Fig. 1. Flow chart for preparation of hydrated Al_2O_3 -coated TiO_2 composite powder.

(fig. 2(a)). An aqueous solution of $\text{Al}_2(\text{SO}_4)_3 \cdot 16\text{H}_2\text{O}$ (0.005 mol/l) and urea (0.45 mol/l) was prepared in a three-neck flask with a capacity of 300 ml and TiO_2 (0.005 mol/l) was added. From this solution hydrated Al_2O_3 -coated TiO_2 composite powder was prepared according to the procedure shown in Fig.1. Agitation was required through the hydrolysis in order to disperse TiO_2 in the reaction solution.

To prepare hydrated Al_2O_3 -coated Cr_2O_3 composite powders, various amounts of Cr_2O_3 were added to 300 ml of the aqueous solution of $\text{Al}_2(\text{SO}_4)_3 \cdot 16\text{H}_2\text{O}$ (0.003 mol/l) and urea (0.45 mol/l). The solution was hydrolyzed at 90 °C for 3 hr and then cooled with ice water. The product was separated with a centrifugal separator and washed with deionized water. Finally, it was dried in an electric oven at 110 °C for 3 hr. This composite powder was also prepared from aqueous solution of $\text{Al}(\text{NO}_3)_3$. Agitation was required through the hydrolysis in order to disperse Cr_2O_3 in the reaction solution.

3. Results and discussion

Urea is hydrolyzed to ammonia and carbon dioxide as follow:



Urea is suitable to a hydrolytic process because of its very weak basic properties ($K_b = 1.5 \times 10^{-14}$) and its high solubility into water. It hydrolyzed easily at 80-100 °C and the hydrolysis can be quickly terminated at a desired pH by cooling the reaction mixture to room temperature.

In order to confirm the formation of hydrated Al_2O_3 -coated TiO_2 composite particle, it is preferable to observe the cross section of hydrated Al_2O_3 -coated TiO_2 composite powder. This experiment was nearly impossible because the product was submicron in size. Thus, this was confirmed indirectly by means

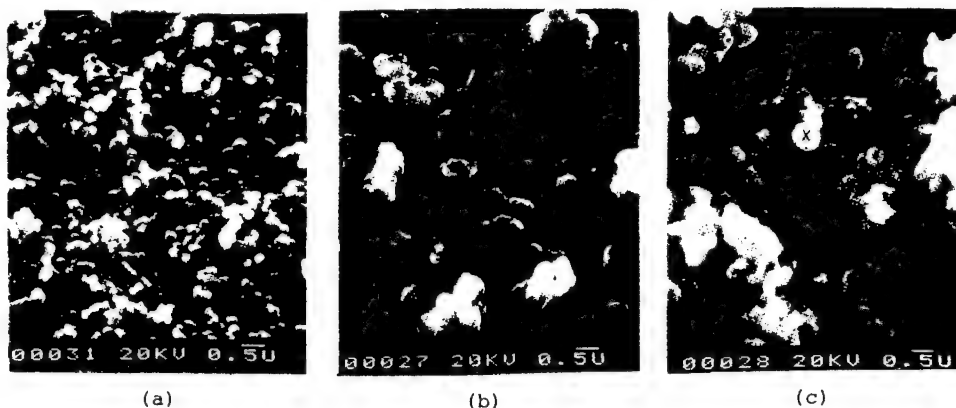


Fig. 2. SEM photographs of starting TiO_2 powder (a), hydrated Al_2O_3 -coated TiO_2 composite powder (b), and $\alpha\text{-Al}_2\text{O}_3$ -coated TiO_2 composite powder (c).

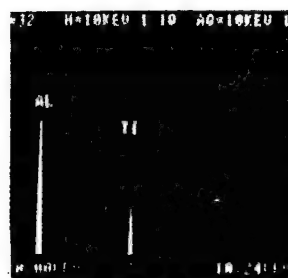


Fig. 3. EDX spectrum of spot analysis at the mark 'x' shown in Fig. 2(c).

of SEM (S-700, Hitachi Co.) observation and EDX (Kevex-7000) analysis. Hydrated Al_2O_3 -coated TiO_2 composite powder consisted of approximately spherical particles with some agglomeration and its average particle size was $0.29 \pm 0.09 \mu$ (Fig. 2(b)). By heating at 1200°C for 1 hr, the product was converted to $\alpha\text{-Al}_2\text{O}_3$ -coated TiO_2 composite powder with the average particle size of $0.27 \pm 0.08 \mu$ (Fig. 2(c)). The change in average particle size between this composite powder and the starting TiO_2 powder was indirect proof of the formation of hydrated Al_2O_3 -coated TiO_2 composite particle.

Figure 3 is the EDX spectrum of spot analysis at the mark 'x' shown in Fig. 2(c). X-ray count ratios of Al/Ti obtained for other particles had almost same value as the one shown in Fig. 3. This was also a proof of the formation of hydrated Al_2O_3 -coated TiO_2 composite particle.

It is difficult to describe a formation mechanism of hydrated Al_2O_3 -coated TiO_2 composite powder in detail. In general, TiO_2 powder has high dispersibility in an aqueous solution and its surface is more active, compared with other metal oxides such as SiO_2 , ZrO_2 , MgO , and ZnO etc [12]. It is supposed that TiO_2 particles dispersed in the solution act as seeds or accelerators in the formation of hydrated Al_2O_3 .

Hydrated Al_2O_3 -coated Cr_2O_3 composite powders were prepared from both solutions of $\text{Al}_2(\text{SO}_4)_3$ and $\text{Al}(\text{NO}_3)_3$. Figure 4 shows Al/Cr ratios of hydrated Al_2O_3 -coated Cr_2O_3 composite powders. Straight-line relations in Fig. 4 indicates that the products contained the amount of Al_2O_3 and Cr_2O_3 , which was expected from the compositions of the starting solutions. This relation was taken as an indirect proof of the formation of coated composite powder. These products were converted to $\alpha\text{-Al}_2\text{O}_3$ -coated Cr_2O_3 composite powders by heat

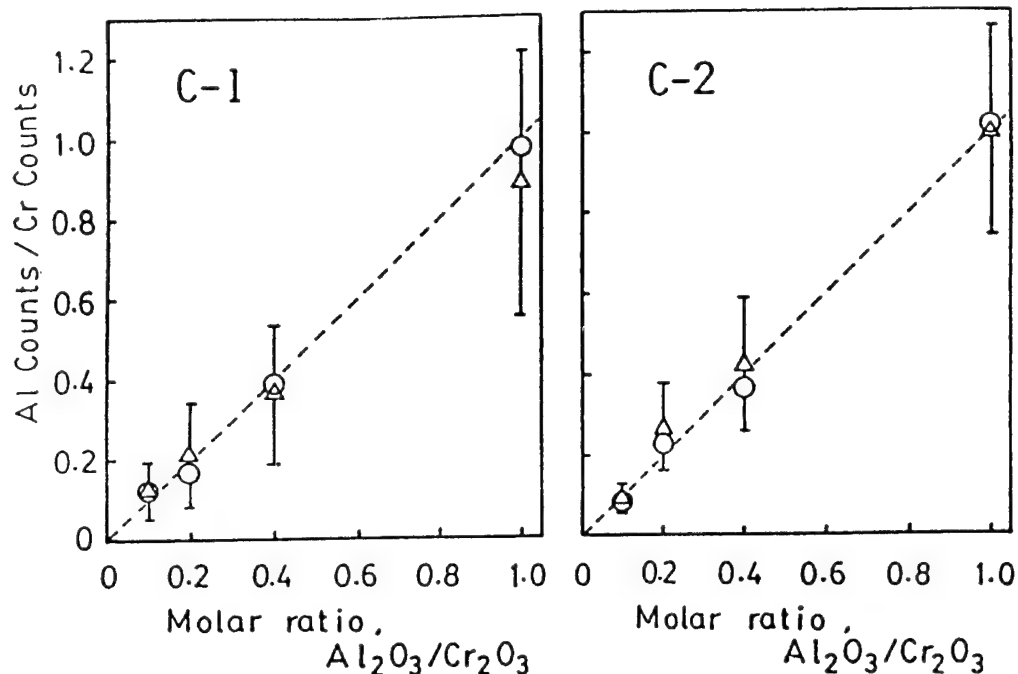


Fig. 4.

Count ratio of Al/Cr of Al₂O₃ coated Cr₂O₃ powders by EDX analysis

○ : plane analysis
 △ : arithmetic average and standard deviation of spot analysis

C-1 : synthesized from Al₂(SO₄)₃·16H₂O

C-2 : synthesized from Al(NO₃)₃·9H₂O

treatment at 1200 °C for 1hr.

4. Conclusion

The homogeneous precipitation method using urea as a coating process was applied to the synthesis of Al(OH)₃-coated TiO₂ composite powder as well as hydrated Al₂O₃-coated Cr₂O₃ composite powder. By heating at 1200 °C 1 hr, these composite powders were converted to α-Al₂O₃-coated TiO₂ and α-Al₂O₃-coated Cr₂O₃, respectively.

References

1. W.R. Bunssen, N.R. Thielke, and R.V. Sarakauskas, *Ceram. Age*, **60**, 38(1952)
2. K. Hamano, Y. Ohya, and Z. Nakagawa, *Yogyo Kyokai Shi*, **91**, 94(1983).
3. L. Gordon, M.L. Salutsky, and H.H. Willard, "precipitation from Homogeneous Solution", Wiley, New York (1959), p.1.
4. K. Kayama, *Shokubai*, **16**, 18(1974).
5. H. Suzuki, T. Iwai, H. Hasegawa, and I. Kayama, *Nippon Kagaku Kaishi*, **1977**, 1063.

6. K.Fujita, K.matsuda, and I.Kayama, Yogyo Kyokai Shi, 83 ,586(1975).
- 7 K.Fujita and I.Kayama, Yogyo Kyokai Shi, 86 ,433(1978).
8. K.Matsuda, Y.Iketani, U.Tamura, and I.Kayama, Nippon Kagaku Kaishi, 1982 ,697.
9. A.Kato and Y.MOrimistu, Nippon Kagaku Kaishi, 95 ,442(1987).
10. B.K.Kim and I.Yasui, J. Mater. Sci., 23 ,637(1988).
11. H.Okamura, E.A.Barringer, and H.K.Bowen, J. Am. Ceram. Soc., 69 , C22(1986).
12. M.Yoshizumi, Ceram. Jpn., 4 ,318(1986).

HIROAKI KATSUKI (勝木宏昭)

佐賀県窯業試験場 ファインセラミックス部

CERAMICS INDUSTRIAL RESEARCH INSTITUTE OF SAGA PREFECTURAL GOVERNMENT

〒844 佐賀県西松浦郡有田町3100

3100 ARITA-MACHI NISHIMATSUURAGUN SAGA PREF. (JAPAN)

1) Introduction

Needle-like crystals and whisker of oxides(Al_2O_3 , MgO , $\text{K}_2\text{O}\cdot 6\text{TiO}_2$), carbides(SiC) and nitrides(Si_3N_4) are now attracting interest as possible materials to improve the toughness and high-temperature strength of ceramics¹⁾.

It has been known for a long time that when alumina-silica minerals such as kaolin and silimanite which are raw materials for porcelain and refractories are fired at over 1200°C , needle-like mullite crystals several to tens of micrometers(μm) long and $0.5\text{--}3\ \mu\text{m}$ thick are formed in the glassy matrices²⁾⁻³⁾. And another methods of synthesizing mullite whisker that have been reported so far as follows: (1) heat treatment of a mixture of SiO_2 , Al and Al_2O_3 in an inert gas atmosphere, (2) hydrothermal synthesis of mixed alkoxides and (3) heat treatment of $\text{AlF}_3\text{--SiO}_2$ xerogels⁴⁾⁻⁶⁾. But there were no attempts to obtain only needle-like mullite crystals from fired kaolin minerals.

This study is intended to investigate the growth conditions of needle-like mullite from low-cost New Zealand kaolin as a raw material with good compactability and low impurity content, and to examine some properties of these crystals such as crystallographical characteristics, chemical composition, thermal expansion and thermal resistance.

2) Experimental procedure

The raw materials used in this study was commercial New Zealand kaolin powder (Ig. loss:13.79, SiO_2 :50.07, Al_2O_3 :35.75, Fe_2O_3 :0.26, TiO_2 :0.07, CaO : tr., MgO :0.08, Na_2O :0.07, K_2O :0.01 wt%). Raw sample was fired in air at $1500\text{--}1700^\circ\text{C}$ for 2hr. The heating and cooling rates were 2.2 and $5.7^\circ\text{C}/\text{min}$ respectively. In order to obtain needle-like mullite, fired sample were immersed in $4.6\text{--}18.4\%$ hydrofluoric acid (HF) and treated at $30\text{--}50^\circ\text{C}$ for $2\text{--}48\text{hr}$ to remove the glassy matrices. Phase structures and chemical composition of fired samples were examined by a powder X-ray diffraction and fluorescent X-ray analysis. Content of mullite, corundum and glass in samples fired at various temperatures were determined based on the method by Okuda et al.⁷⁾. The morphology of the needle-like mullite prepared after removing the glassy phase was observed by SEM and TEM. The growth direction of crystal was determined by a electron beam diffraction system. The specific surface area of mullite was measured by a BET method. The axial thermal expansions of the resulting mullite was studied for the temperature range from $25\text{--}800^\circ\text{C}$ using a high temperature X-ray diffractometer, and the angle of diffraction was calibrated with fine Pt powder based on (130), (201) and (230) lines of mullite. Thermal shock of mullite crystals was evaluated by quenching

crystals from 1150 to 0°C.

3) Results and discussion

3.1 Effect of reaction conditions on the formation of needle-like mullite

At first, New Zealand kaolin was fired at 1300-1700°C for 2hr to examine the effect of growth temperature on the formation of crystals. Fig.1 shows mullite crystals obtained at 1550, 1600, 1650 and 1700°C after treated in 4.6% HF. In addition, table 1 gives length, thickness, $\text{Al}_2\text{O}_3/\text{SiO}_2$ molar ratio, density and specific surface area.

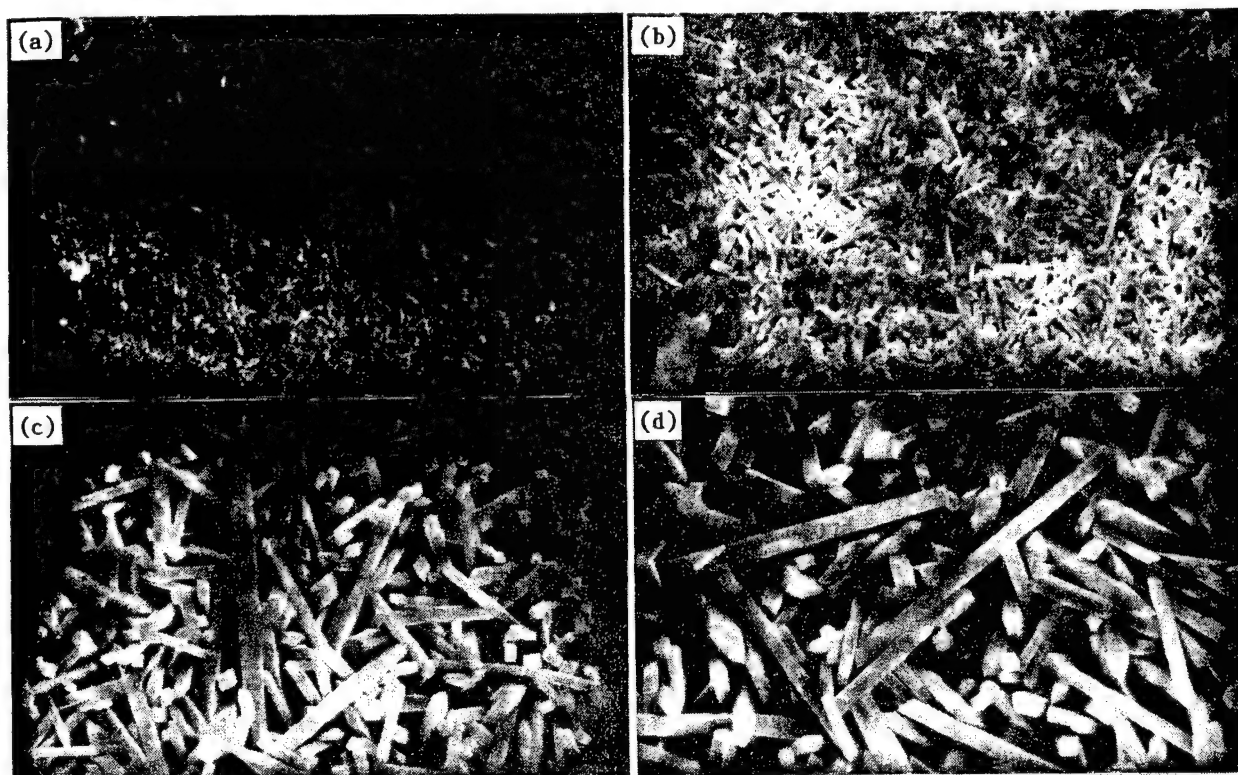


Fig. 1 SEM micrographs of needle-like mullite obtained from New Zealand kaolin.
(a) 1550, (b) 1600, (c) 1650 and (d) 1700°C

Table 1 Some properties of needle-like mullite obtained at 1550 - 1700 °C for 2 hr.

Growth temp. (°C)	Av. length (μm)	Av. thickness (μm)	$\text{Al}_2\text{O}_3/\text{SiO}_2$ (molar ratio)	Density (g/cm ³)	Specific surface area (m ² /g)
1550	1 - 3	0.1 - 0.4	1.48	3.14	8.2
1600	3 - 6	0.2 - 0.5	1.47	3.16	6.7
1650	10 - 20	0.8 - 1.1	1.48	3.15	4.1
1700	10 - 20	0.7 - 1.3	1.48	3.14	3.9

Below 1550°C, mullite was fine crystals less than 1 μm long and 0.1-0.2 μm thick, but not needle crystals. At 1550 and 1600°C, needle-like mullite 1-6 μm long, 0.1-0.5 μm thick, and 5-10 aspect ratio was formed as shown in Fig.1(a) and (b). On the other hand, at 1650 and 1700°C, the growth of needle crystals 10-20 μm long, 1-2 μm thick, and 10-15 aspect ratio, and having a square cross section was promoted but their formation density ($20-30 \times 10^4$ needles/mm²) was less than that of samples grew at 1550

and 1600°C. There were no influences of fired temperatures on $\text{Al}_2\text{O}_3/\text{SiO}_2$ molar ratio and the density of mullite crystals but the specific surface area decreased with fired temperatures.

It has been said that when the clay of porcelain raw materials is fired at 1200-1300°C, needle-like mullite several to tens of micrometers long and 0.5 to several micrometers thick is formed in the matrices²⁾, while in the case of New Zealand kaolin, the growth of needle crystals was not detected below 1500°C. Porcelain raw materials such as Amakusa clay usually contain 80-85% of SiO_2 along with 2-4% of K_2O and Na_2O , so that a glass phase tends to melt over 1300°C and the growth of mullite crystals is promoted in the presence of a liquid phase. On the other hand, the New Zealand kaolin used in this experiment has as low as 58wt% of SiO_2 and less than 0.1wt% of K_2O and Na_2O . This difference in temperature range for the formation of needle-like mullite between clay and New Zealand kaolin is probably due to a difference in components or the amount of a liquid phase, which leads to different solubility of mullite in the liquid phase formed. Subsequently, changes in the phase structure of New Zealand kaolin fired for 2hr at 1300, 1550, 1600, 1650 and 1700°C were examined by a X-ray diffraction. Fig.2 shows these diffraction patterns. At 1300°C, mullite and α -cristobalite were formed but the diffraction intensity of mullite was low and the crystal growth was premature. At 1550°C, the formation of mullite increased and the diffraction intensity of α -cristobalite was even greater, indicating further crystallization of the matrix. However, α -cristobalite remarkably melted and the peak of diffraction became broad over 1600°C. The reason why the growth of needle-like mullite was promoted at higher temperatures than 1600°C is not known, but it is presumed that the molten glassy phase (matrices) became a low viscosity liquid phase which increased the reactivity of SiO_2 and Al_2O_3 as well as the growth rate of mullite crystals in the matrices, thus promoting crystal growth.

Table 2 lists the amounts of mullite, corundum and silica glass contained in samples fired at 1500-1700°C after considering the solubility of each phase in HF. With a

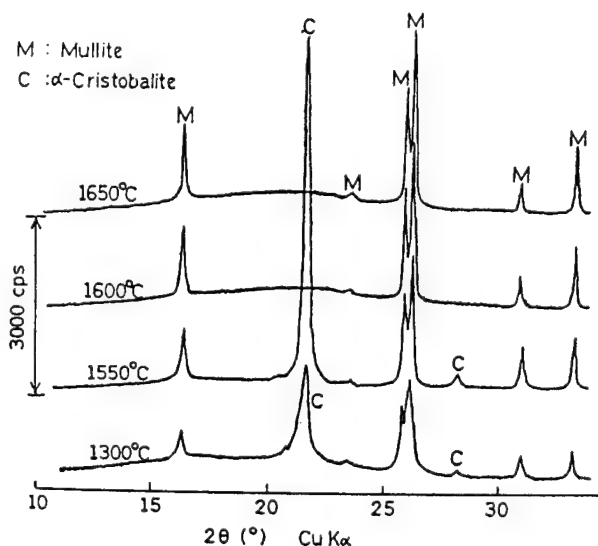


Fig. 2 X-ray diffraction patterns of New Zealand kaolin fired at 1300 - 1700°C for 2hr.

Table 2 The amount of mullite, corundum and glass in New Zealand kaolin fired at 1500 - 1700°C for 2 hr.

Growth temp. (°C)	Mullite (wt%)	Corundum (wt%)	Glass (wt%)
1500	48.02	3.33	48.68
1550	53.69	1.89	44.42
1600	56.80	1.54	41.66
1650	60.04	0.68	39.28
1700	59.14	0.71	40.15

rise in firing temperature, the amount of corundum and glass decreased but crystal growth of mullite was promoted. The amount of mullite is 59-60% at 1650-1700°C, which almost agrees with the theoretical mullite ratio (about 58%) in the case where the alumina component in New Zealand kaolin is converted completely into mullite. Moreover, the amount of corundum is about 0.7wt% and no diffraction peak of corundum is detected in almost converted into mullite crystals.

3.2 Some properties of needle-like mullite

Fig. 3 shows the transmission electron micrograph of needle-like mullite of which the glassy phase was removed completely, and the electron diffraction pattern. The growth direction of this crystals was [001], which coincided with that of single mullite crystal obtained by a Czochralski method^{8)~9)} using alumina and silica as raw materials. However, it was different from the growth direction of mullite whisker obtained by heat treatment of xerogel⁶⁾. Furthermore, a few dislocations which were perpendicular to [001] direction existed in these crystals. The composition of needle-like mullite was SiO₂ (28.33wt%), Al₂O₃ (71.27), Fe₂O₃ (0.23), TiO₂ (0.05), CaO (tr.), MgO (tr.), Na₂O (0.05) and K₂O (tr.); the amount of CaO, MgO, Na₂O and K₂O had decreased compared with those in the raw materials.

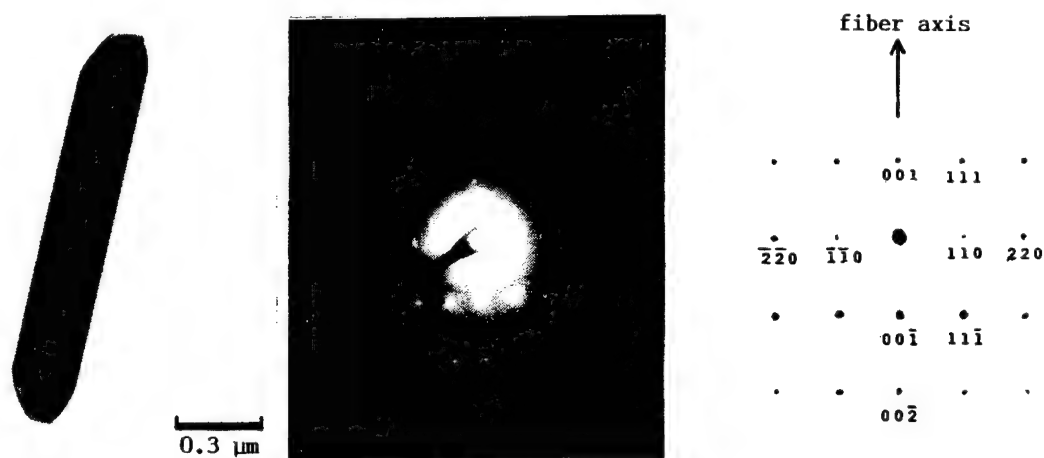


Fig. 3 Bright field image and electron diffraction pattern of needle-like mullite obtained at 1650°C.

It is usually said that mullite is stable oxide material under high temperature, and has comparatively low thermal expansion. Consequently, needle-like mullite obtained at 1550 and 1650°C was reheated at 1000-1700°C for 20-30hr to evaluate sintering property. The change of the specific surface area of needle-like mullite and the morphology of crystals after reheating at 1650 and 1700°C were shown in Fig. 4 and 5. There was no sintering among each needle crystals and deformation below 1600°C, but the specific surface area gradually decreased and the sintering was promoted above 1650°C. These needle-like mullite was relatively stable for reheating treatment at 1000-1650°C and it was assumed that there was no glassy phase such as SiO₂ around crystals.

Fig. 6 shows the directional thermal expansion behavior of needle-like mullite from 25 to 800°C. Thermal expansion coefficients computed from lattice parameters is as follows: $\alpha_a = +2.2 \times 10^{-6}/^\circ\text{C}$, $\alpha_b = +3.9 \times 10^{-6}/^\circ\text{C}$, $\alpha_c = +4.5 \times 10^{-6}/^\circ\text{C}$ and average thermal expansion coefficient and the volume expansion are $\alpha = +3.5 \times 10^{-6}/^\circ\text{C}$.

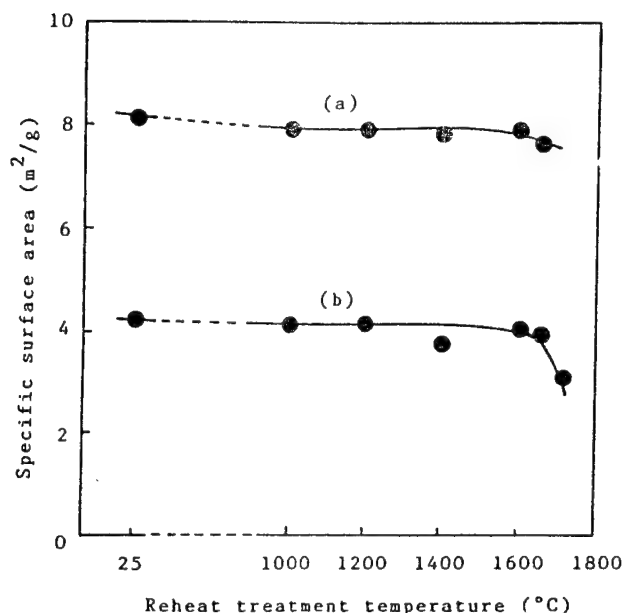


Fig. 4 The change of the specific surface area of needle-like mullite obtained at 1550 and 1650°C by reheat treatment. (a) 1550 and (b) 1650°C

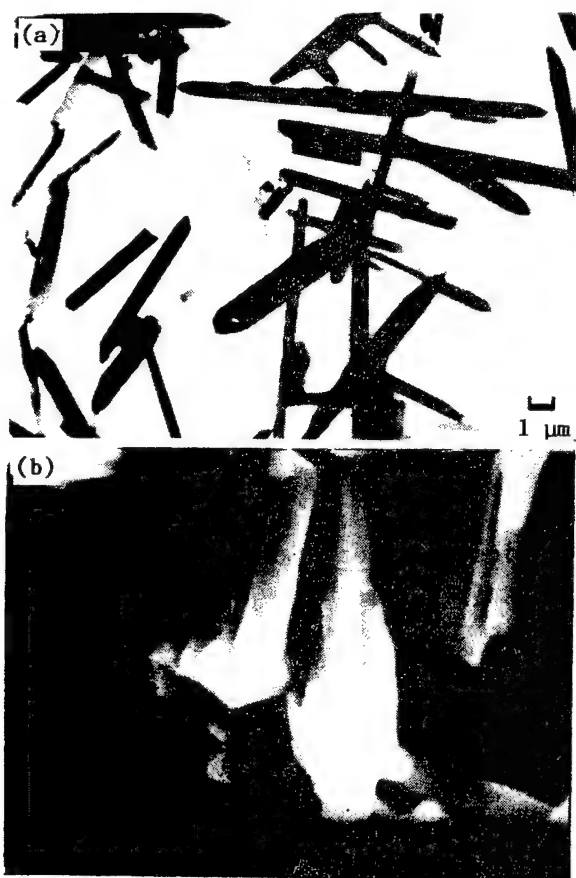


Fig. 5 Morphology of needle-like mullite obtained at 1650°C by reheat treatment (a) 1650°C - 30hr and (b) 1700°C - 4hr.

$\beta = +10.6 \times 10^{-6} / ^\circ\text{C}$ respectively. It was revealed that thermal expansion of c axis [001] direction was larger than that of a and b axis, but the difference of the directional thermal expansion is not yet clear.

It is expected that needle-like mullite has relative high thermal shock resistance because of its low thermal expansion, so needle-like mullite was quenched from 1150 to 0°C to investigate the quenching effect, but there were no evidences of fracture and crack in crystals as shown in Fig. 7.

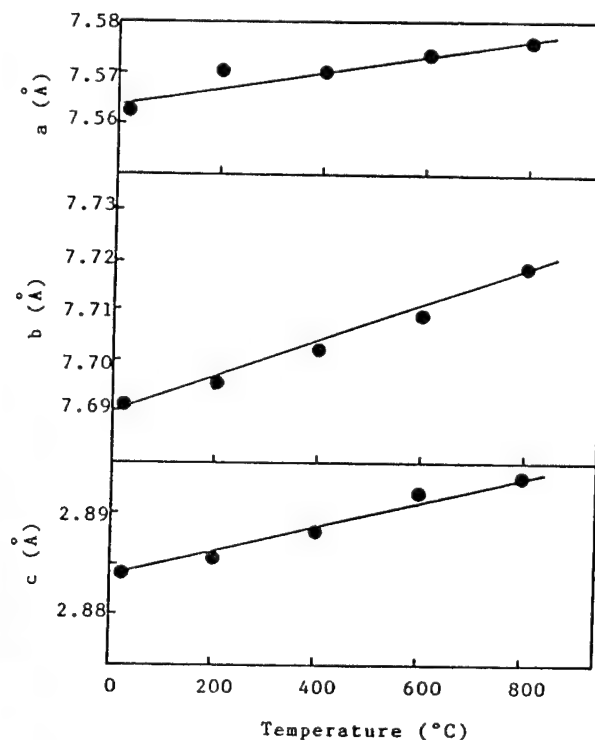


Fig. 6 Lattice constants of needle-like mullite with elevating temperatures measured by a high temperature X-ray diffractometer.



Fig.7 Morphology of needle-like mullite quenched from 1150 to 0°C.

4) Conclusion

The results are summarized as follows.

(1) Fine needle-like mullite crystals started to grow at 1550°C, and a molten glassy phase (matrices) became a liquid state with low viscosity over 1650°C, needle crystals of 10-20 μm long and 1-2 μm thick grown in the [001] direction were obtained. Additionally, over this temperature, most of alumina component in the raw material was converted into mullite, and the resultant composition was mullite (59-60wt%), glass (39-40), and corundum (0.6).

(2) The specific surface area of mullite crystals grew at 1550 and 1650°C were 3.2 and 4.1 m²/g respectively and did not decrease with reheating treatment at 1000 to 1650°C for 20-30hr. Axial thermal expansion coefficients of crystals at 25-800°C were

$\alpha_a = +2.2 \times 10^{-6}/^{\circ}\text{C}$, $\alpha_b = +3.9 \times 10^{-6}/^{\circ}\text{C}$, $\alpha_c = +4.5 \times 10^{-6}/^{\circ}\text{C}$ and crystals were expected to be thermally stable.

References:

- 1) Nikkei New Materials, No.63 (1989) pp.32-44.
- 2) K. Hamano, "Ceramic Research II", Gihodo (1961) pp.301-34.
- 3) B. Yoshiki, "Minerals Technology", Gihodo (1967) pp.392-94.
- 4) E. I. Du pont de Nemours & Co., US Pat. 3, 104, 943 (1960).
- 5) T. Yamaguchi, M. Suzuki, S. Hiraishi, M. Yoshimura and S. Somiya, Yogyo-Kyokaishi, 93, 101-D4 (1985).
- 6) K. Okada and N. Ootsuga, Abstracts from 26th Conference of Ceramics Society of Japan (1988) p.197.
- 7) H. Okuda, "Inorganic Materials and Its Application", ed. by H. Takagi, Kagaku Kagyo-sha, Supplement Volume, Vol.14, No.6 (1970) pp.219-39.
- 8) W. Guse, J, Crystal Growth, 26 (1974) 151-52.
- 9) D. Michel, L. Mazerolles and R. Portier, Abstract of 1st. Int. Workshop on Mullite, (1987) p.51.

EFFECTS OF ADDITIVES AND ATMOSPHERE ON MORPHOLOGY AND GROWTH OF SILICON CARBIDE WHISKERS

Thae-Khapp Kang, Soon-Dong Park, Chang-Kyu Rhee, and Il-Hyun Kuk.

Korea Advanced Energy Research Institute, Dept. Nuclear Chem. Eng.,
P.O.Box 7 Daeduk-danji, Daejeon 302-353, Korea

Co ABSTRACT

line of a new

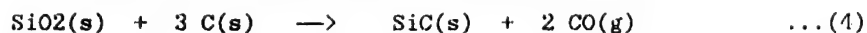
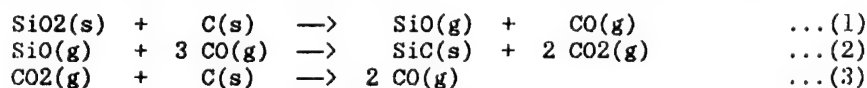
chapter The effect of catalyst addition, halide of an earth element addition, and atmosphere variation on the morphology and growth of silicon carbide whiskers was investigated. To simplify the carbothermic process, silicon mono-oxide powder and carbon mono-oxide gas were used as the raw materials. The addition of an iron containing catalyst induced very long thread-like growth of the whiskers, while that of sodium chloride resulted in spring-like curlings of the whiskers. Hydrogen addition to the non-oxidizing atmosphere enhanced the whisker formation for both additives.

INTRODUCTION

Silicon carbide whiskers are a promising reinforcement material for metallic and ceramic matrix composites. Silicon carbide whiskers can be manufactured by various methods [1-4]. The first process that succeeded in the commercialization of silicon carbide whisker manufacturing is the carbothermic process[1], which used rice hulls as the raw material. This process has been developed further to use various silicon containing solids as a raw material, such as volcanic sands[5] and silica gels[6].

For this carbothermic reaction some catalysts like Fe, Ni, and Co in forms of metals or compounds [7,8] and halides of earth or rare earth elements[8,9] are added. The atmosphere is mainly maintained in a non-oxidizing inert condition [1,5,6], but a slight reducing condition is often used[8].

The carbothermic process is based on the following reactions;



Among the above step reactions, reaction (2) is the principal reaction. In this experiment the carbothermic process is simplified into the reaction (2) by using SiO powder and CO gas as the raw materials. In order to investigate the role of the additives, iron nitrate and sodium chloride were added as a catalyst and a halide respectively. A slight reducing atmosphere was prepared by adding H₂ to the inert Ar atmosphere.

EXPERIMENTAL PROCEDURE

High purity amorphous SiO powder (Kojundo Chem.Lab.Co.,99.9%) and CO gas (Air Products and Chemicals,Inc.,99.3%) were used as the raw materials. To investigate the effects of catalyst and halide additions, 0.1 mole of Fe(NO₃)₃·9H₂O and 1 mole of NaCl were added separately in a form of a solution to 1 mole of SiO powder. The dried powders were put into a graphite crucible located in the center of a tube furnace of 50 mm in diameter and

heated up at a rate of 7 °C/min.

The CO gas, mixed with an Ar carrier gas, was supplied to the furnace. The flow rate and the partial pressure of the CO gas were 40 cc/min and 20%, respectively. To prepare a slight reducing condition in the atmosphere, 10% of H₂ gas was added after subtracting the partial pressure of the Ar. The reaction was carried out at 1500 °C for 1 h. At the end of the reaction the atmosphere was converted to 100% Ar. X-ray diffraction (XRD), scanning electron microscope (SEM), TYP and energy dispersive X-ray spectroscopy (EDX) analyses were carried out.

EXPERIMENTAL RESULTS

X-ray diffraction analyses showed strong peaks of SiC and SiO₂ in all specimens, as shown in Fig.1. Additionally, in the specimens with iron nitrate added, weak peaks of some iron silicides, iron carbides and silicon were detected. Those with sodium chloride added, weak peaks of sodium oxide and sodium silicide were detected. After a hydrofluoric acid leaching, a small amount of silicon could also be detected in all specimens.

Scanning electron microscope observations showed quite different whisker morphologies between specimens. Figure 2 reveals the SiC whisker formation of the specimen doped with iron nitrate. Whiskers were formed all over the specimen, but the whisker lengths were not as long, as shown in Fig. 2 (a). A higher magnification observation revealed, in Fig. 2 (b), smooth surfaces and homogeneous diameters of the whiskers. However, in this experiment, liquid drops could not clearly be detected on the tip of the whiskers. On the other hand, some liquid phases were found at triangles between the whiskers, as shown in Fig. 2 (a) and (b). The addition of H₂ to the inert atmosphere enhanced the formation of the whiskers. Whisker lengths and diameters were increased. The whisker lengths were so remarkably increased, that it was very difficult to find the end of a whisker. The whiskers were not linear and therefore seemed to be in tangles of endless threads, as shown in Fig.2 (c).

The addition of sodium chloride resulted in quite different whisker morphologies from those described above. Figure 3 (a) shows the formation of hair-like whiskers. The specimens exhibited larger diameters, rougher surfaces and more severe tanglings of the whiskers than those of iron nitrate addition, as shown in Fig.3 (b). A high magnification revealed spring-like curlings of the whiskers, as shown in Fig.3 (c). EDX analysis of the whiskers showed only the silicon element present. The analysis also found that the whiskers were electrically conductive. From these results the spring-like whiskers must be of SiC phase. The addition of H₂ to the inert atmosphere increased the amount of the whiskers formed. However, distinguished to the case of iron nitrate addition, diameters and the spring-like curlings of the whiskers were apparently not changed with presence of H₂. The amount of whiskers formed was always less than in the case of the iron nitrate addition.

DISCUSSION

SiO has a high partial pressure above 1200 °C[10]. This gaseous SiO reacts with CO gas to form SiC whiskers. However, according to the phase diagram[12], SiO is unstable at low temperatures. During the heat-up the amorphous SiO powder decomposed into SiO₂ and Si. This SiO₂ remained unchanged throughout the reaction, while the Si contributed to the whisker formations. The detections of SiO₂ in this experiment can be explained by this decomposition of SiO powder.

As shown in Fig. 2, the addition of iron catalyst enhanced the whisker formations in the carbothermic process. For the role of the catalyst, the VLS-mechanism is universally accepted[1,4]. Recently the birth-spread mechanism [13] is proposed. The essential evidence of these mechanisms is a presence of a liquid drop on the tip of a whisker and a rough whisker surface respectively. However, as mentioned above, liquid drops were not clearly found on the tip of the whiskers. Some liquid phases were found at triangles between the whiskers. And the whiskers exhibit smooth surfaces. In this experiment, the role of the catalyst on the growth of the whiskers is not clear and should be investigated further.

In contrast to the thread-like shape from the iron nitrate addition, the spring-like curled shape of the whiskers were the result of the sodium chloride addition. This kind of morphology has not been reported in silicon carbide whisker growths. Recently Motojima et al.[13] reported a formation of spring-like whiskers of silicon nitride. They used Si_2Cl_6 , NH_3 , and H_2 as gaseous raw materials, and Ni and Fe as catalysts.. They reported that the whiskers were amorphous and that the presence of iron impurity was essential for the spring-like whisker formation. But the growth mechanism of the whiskers was not explained.

In this experiment, however, the spring-like curled silicon carbide whiskers were not formed in the presence of iron impurity. They were formed only in the presence of sodium chloride and independent of the presence of hydrogen. Compared with the result of Motojima et al.[13], it is suspected that the formation of the spring-like whiskers should be closely related to the presence of chlorine impurity, which is common in both works. But the growth mechanism of the whisker curling should be investigated further.

Hydrogen enhanced the whisker growth of both iron nitrate and sodium chloride doped specimens. This can be explained by the role of hydrogen on the reduction of SiO . Hydrogen enhances the reduction of SiO into Si by forming H_2O . Hydrogen assists the decomposition of iron nitrate and sodium chloride forming nitric acid and chloric acid which accelerate the reduction of SiO . The enhanced reduction of SiO into Si increased the reaction with CO gas to form the whiskers. In addition, hydrogen cleans the surfaces of the whiskers and the liquid phase containing iron and this helps the formation of the whiskers.

CONCLUSIONS

1. The addition of catalyst in the form of iron nitrate resulted in the formations of thread-like long and tangled whiskers.
2. The addition of halide of an earth element in the form of sodium chloride resulted in the formations of spring-like curled whiskers.
3. The formation of the spring-like curled whiskers may be closely related to the presence of chlorine impurity.
4. The addition of hydrogen to the inert reaction atmosphere increased the formation of the whiskers remarkably.

REFERENCES

1. J.G.Lee and I.B.Cutler, Am.Ceram.Soc.Bull., 54 (2) 195 (1975).
2. J.P.86-291498, Shinetsu Co.
3. K.W.Park and S.S.Kim, J.Korean Inst.Metals, 25 (8) 579 (1987).
4. J.V.Milewski et al., J.Mater.Sci. 20, 1160 (1985).
5. J.P. 83-20799, Tateho Chem. Ind.
6. J.P.82-209813, Tokai Carbon Co.
7. J.P. 84-213700, Tokai Carbon Co.
8. J.P. 86-22000, Kanebo Co.
9. J.P. 83-45196, Tokai Carbon Co.
10. O.Kubaschewski and T.G.Chart, J.Chem.Thermodynamics, 6, 467 (1974).
11. Phase diagrams for ceramists, Vol.I, Fig.21, ed. E.M.Levin et al., Am.Ceram.Soc., Inc. (1964).
12. S.R.Nutt, J.Am.Ceram.Soc., 71 (3) 149 (1988).
13. S.Motojima et al., J.Crystal Growth, 96, 383 (1989).

Fig. 1.
X-ray diffraction analyses of specimens
doped with iron nitrate (lower) and
sodium chloride (upper): ● SiO_2 ; ○ SiC ;
△ Na_2O ; ▲ NaSi ; □ Fe-Si ; ■ Si ; ◆ Fe-C .

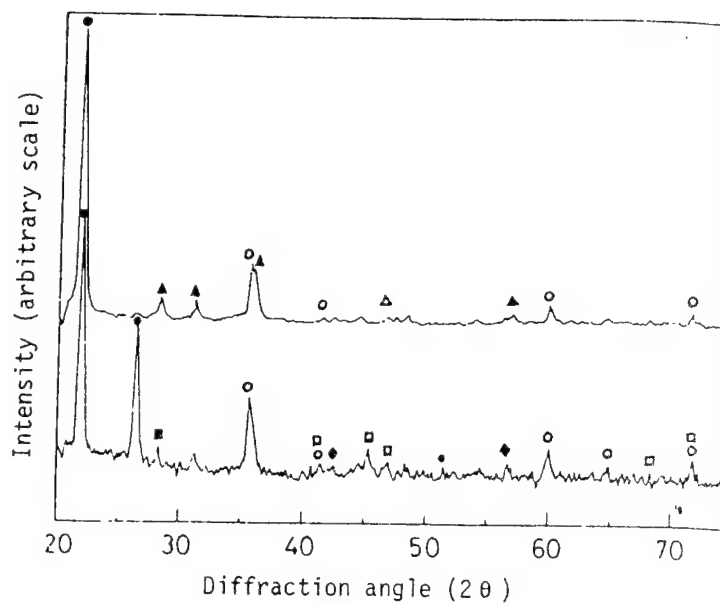


Fig. 2.
SiC whisker formation of specimens
doped with 0.1 mole of iron nitrate
to 1 mole of SiO at 1500°C for 1 h
under $\text{Ar} + \text{CO}$ atmosphere; (a) and
(b) without and (c) with H_2 addition.

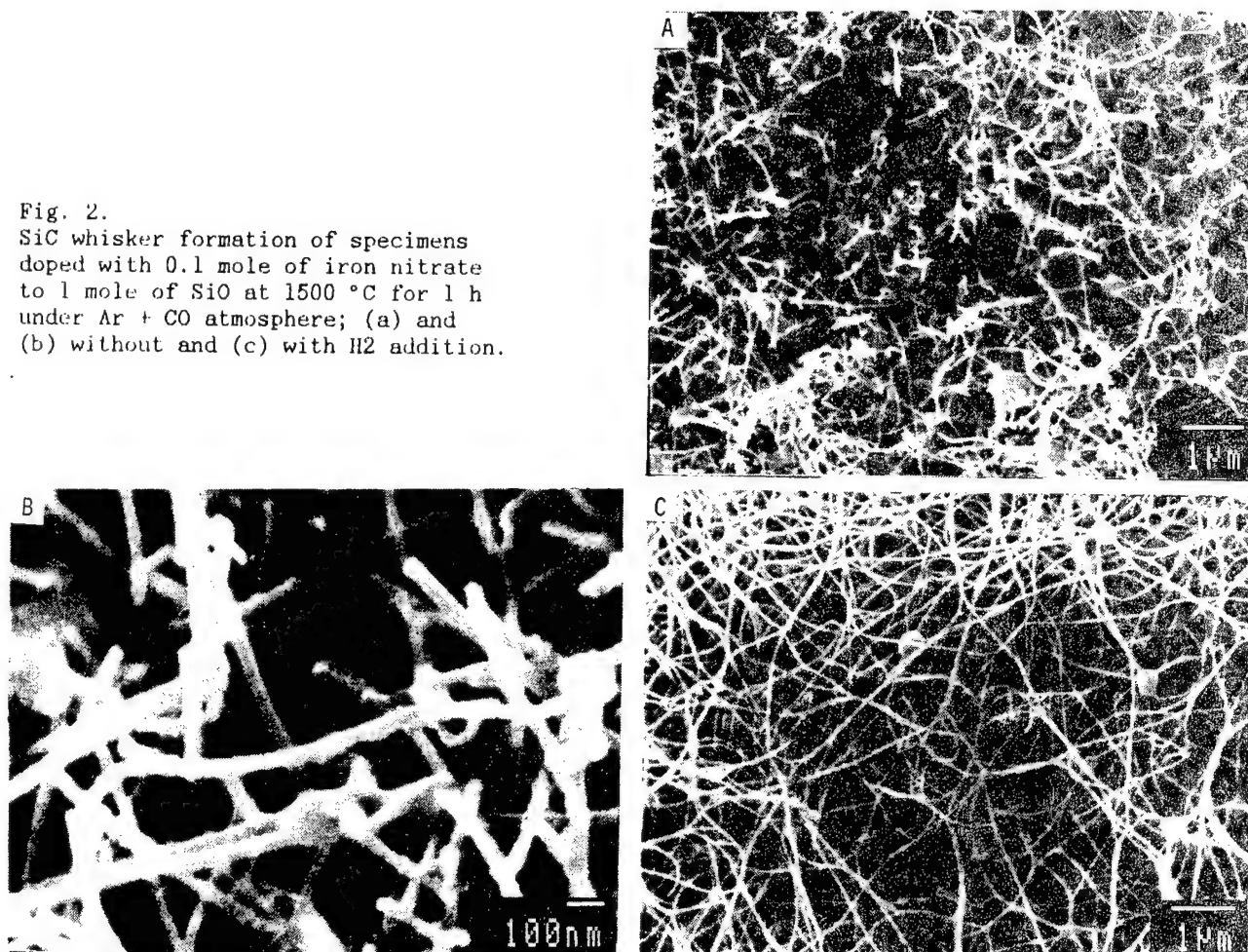
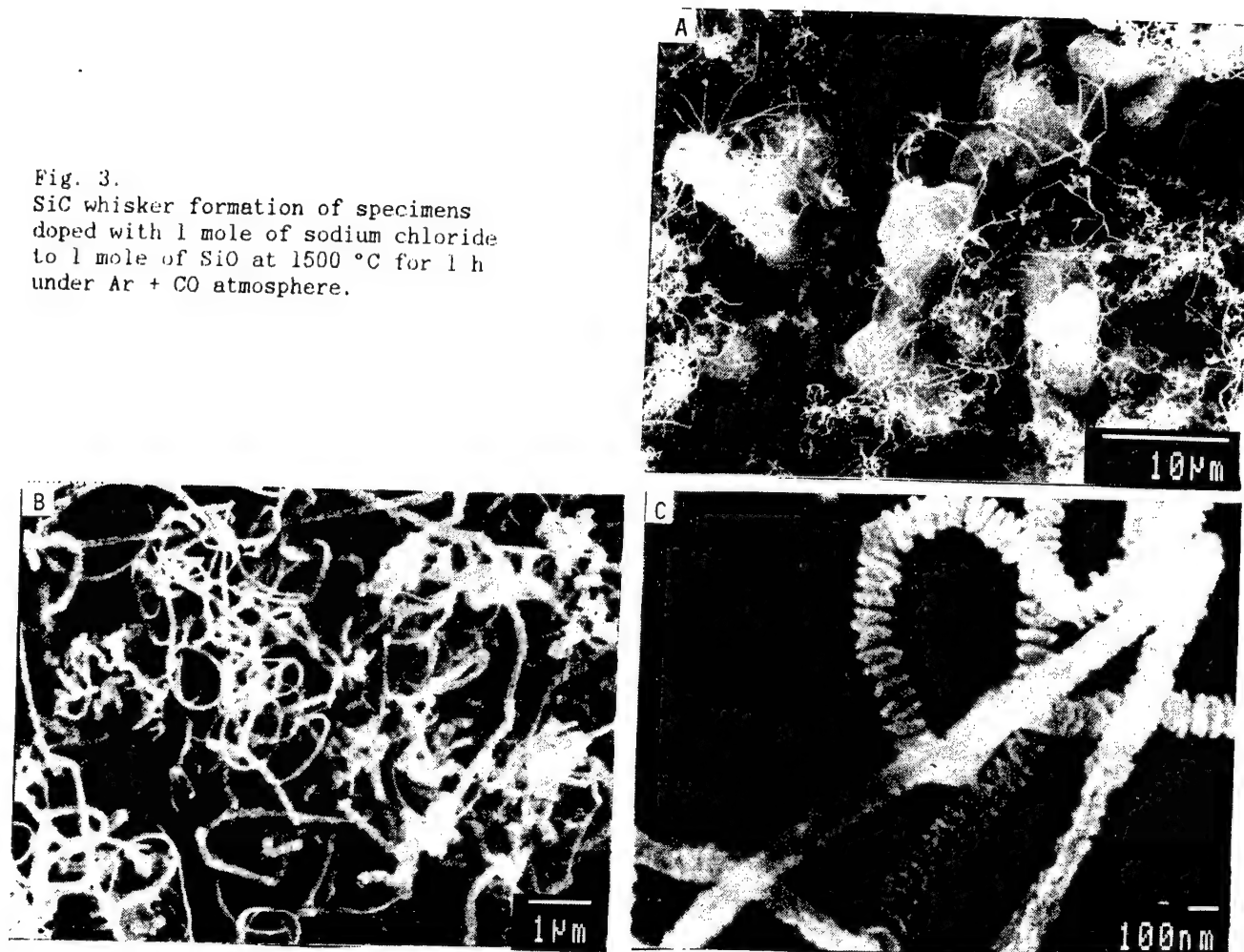


Fig. 3.
SiC whisker formation of specimens
doped with 1 mole of sodium chloride
to 1 mole of SiO at 1500 °C for 1 h
under Ar + CO atmosphere.



METALLIZATION OF ALUMINA CERAMICS BY ELECTROLESS PLATING

S.G. Kang,^{*} B.S. Jeon^{**} and K.J. Park^{**}

^{*}Dept. of Materials Engineering, Hanyang University
#17, Haengdang-dong, Sungdong-gu, Seoul 133-791, Korea
^{**} National Industrial Research Institute
#2, Joongang-dong, Kwachon 427-010, Kyunggi-do, Korea

ABSTRACT

An electroless nickel plating on ceramics as a means of metallization was studied using alumina substrates. It was revealed that pretreatment process, etching in particular, played an important role in obtaining good adhesion. The nickel-phosphorous and nickel-boron electroless plating were discussed in terms of the etching condition, deposition rate, adhesion strength, and surface structure.

KEY WORD

Electroless plating, Metallization, Alumina ceramics.

INTRODUCTION

The application of ceramics to electronic devices is increasing more and more recently. In such application of ceramics there are many cases where ceramics must be metallized for conduction electricity, soldering, fine line patterning, and so on.¹⁻⁵

There are several methods to metallize ceramics, such as utilizing heavy metal solder, oxide solder, evaporation, CVD and PVD methods. Electroless plating is known as a reliable method of metallization.

In this study two kinds of electroless nickel plating, nickel-phosphorous and nickel-boron were compared each other in terms of plating rate, adhesion strength and surface structures.

EXPERIMENTAL

Alumina ceramic substrate (90% Al_2O_3 , 10 X 10 X 2 mm) with roughness of Ra 0.60 μm was pretreated as shown in Table 1. Table 2 shows the chemical composition of electroless plating solutions.

Table 1. Chemical composition and treatment condition of pretreatment steps

Step	Process	Chemicals	Temp.(°C)	Time(min)
1	Cleaning	Acidic	Room temp.	5 (Ultrasonic)
2	Etching	10% HF 100 g/L NaCl	Room temp.	5
3	Sensitizing	0.5 g/L $SnCl_2$ 0.5 ml/L HCl	Room temp.	5
4	Activation	0.25 g/L $PdCl_2$ 5 ml/L HCl	Room temp.	5

Table 2. Basic bath composition for electroless Ni-P and Ni-B plating

Nickel-Phosphorous		Nickel-Boron	
Chemicals	Concentration	Chemicals	Concentration
$\text{NiCl}_2 \cdot 6\text{H}_2\text{O}$	0.1 M/L	$\text{NiSO}_4 \cdot 6\text{H}_2\text{O}$	0.15 M/L
$\text{NaH}_2\text{PO}_2 \cdot \text{H}_2\text{O}$	0.12 M/L	$(\text{CH}_3)_2\text{NHBH}_3$	0.1 M/L
$\text{Na}_3\text{C}_6\text{H}_5\text{O}_7 \cdot 2\text{H}_2\text{O}$	0.2 M/L	$\text{Na}_3\text{C}_6\text{H}_5\text{O}_7 \cdot 2\text{H}_2\text{O}$	0.1 M/L
		CH_3COONa	0.3 M/L

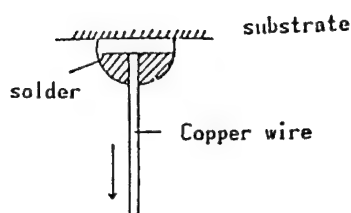


Fig. 1 Peeling test for measuring adhesion strength

Plating rate was determined by weight gain. Surface morphology and structure were studied by SEM (JSM-35CF, JEOL) and X-ray diffractometer (RAD-C, Rigaku). Adhesion strength was determined by peeling the nickel-plated area of 20 mm^2 as shown in Fig. 1.

RESULTS AND DISCUSSION

Plating conditions

Fig. 2 and 3 show the effects of pH and temperature on plating rate. Fig. 2 and 3 illustrate that deposition rate of electroless Ni-P and Ni-B plating increases with increasing pH and temperature. However, Ni-B had a peak at pH 7. The appearance of the plated film of Ni-B was very poor under pH 5.

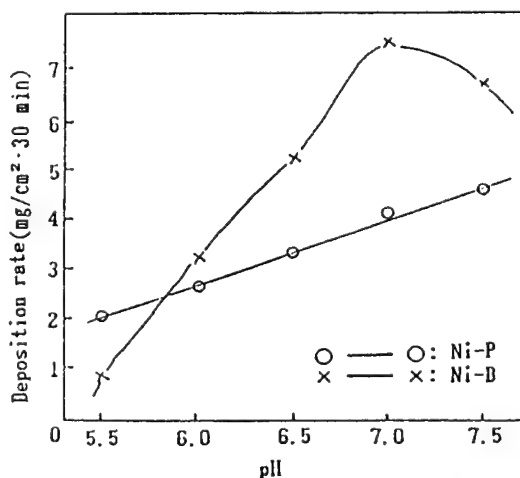


Fig. 2 Effect of pH on the electroless Ni plating

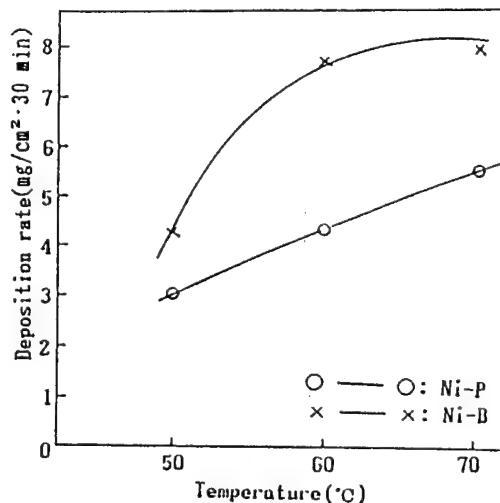


Fig. 3 Effect of plating temperature on electroless Ni plating

Adhesion strength

The effect of etching on adhesion strength is shown in Fig. 4.

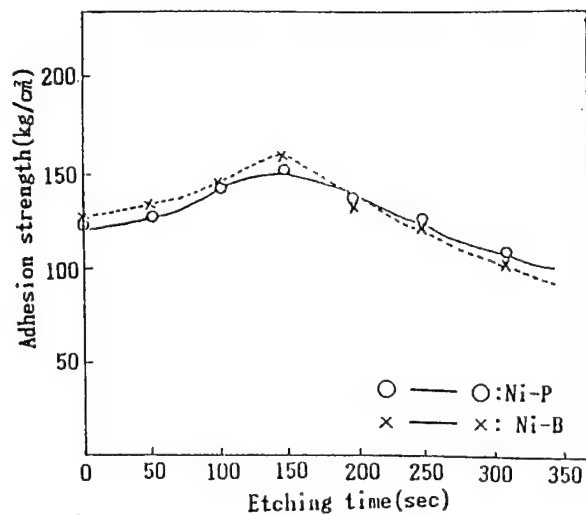


Fig.4 Adhesion strength vs. etching time

Fig. 4 shows that there is no difference in adhesion strength between Ni-P and Ni-B and that etching time affects the bonding strength. Adhesion strength had a maximum value of about 150 Kg/cm² at the etching time of 150 sec and decreased with longer etching time.

This diminution tendency of adhesion strength in the region of etching time > 150 sec was observed by surveying the surface microstructure (Fig. 5) and EDS analysis (Fig. 6) of alumina substrates. Due to glass phases of SiO₂, CaO and MgO unetched on the alumina surface and intergranular boundary, anchor effect was low in the beginning of etching.

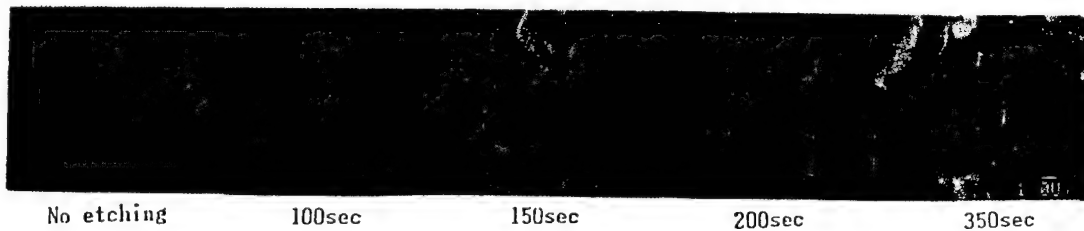


Fig.5 Microstructure of etched alumina substrate by HF+NaCl

However, in the region of etching time over 150 sec, the glassy phase was dissolved out completely and alumina remained only. Thus, the anchor effect did not increase any more. Since alumina is chemically inert, the poor adsorption of Sn, Pd catalysts reduced adhesion strength between metal and ceramic.

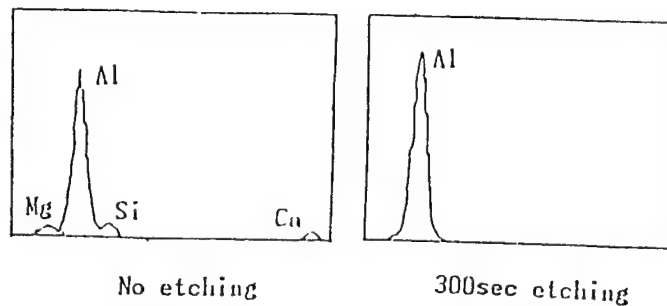
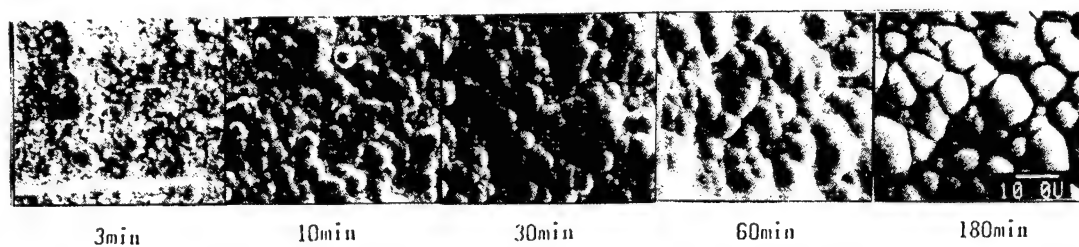


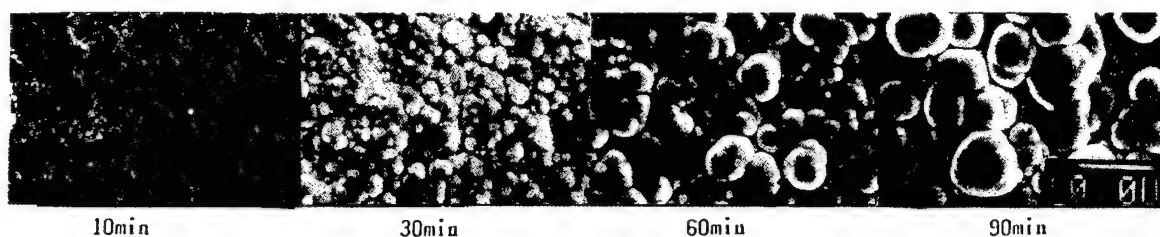
Fig.6 EDS Analysis of ceramic substrate

Surface microstructure

Fig. 7 shows the growth of electroless plated Ni particles with plating time.



(a) Ni-P (pH8, 70°C)



(b) Ni-B (pH7, 60°C)

Fig. 7 Scanning electron micrograph of the Ni-deposited on alumina at different time

At plating time of 3 min, bare alumina and scattered nickel were observed on the substrates. As plating progressed, small particles stuck together and grew larger forming large particles of uniform size. The structure changes of the deposit with heat treatment are shown in Fig. 8 and 9.

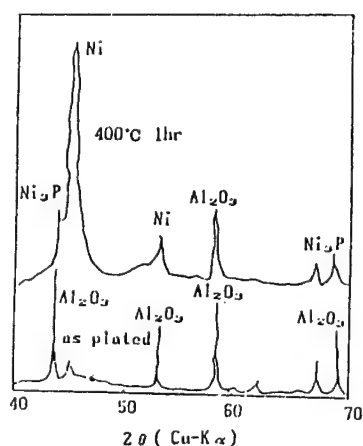


Fig. 8 X-ray diffraction patterns of electroless Ni-P film

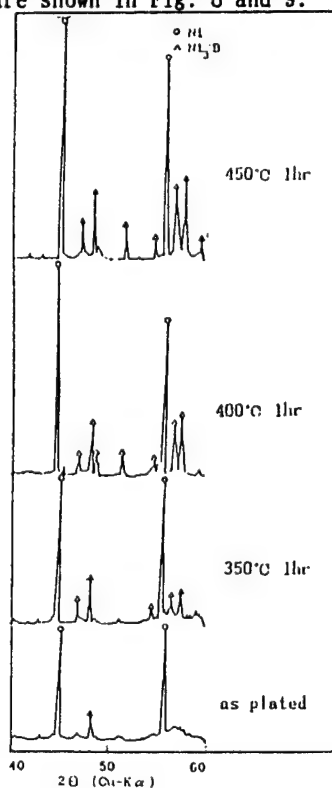


Fig. 9 X-ray diffraction patterns of electroless Ni-B film

The phases of Ni and Al_2O_3 were observed at plated film of Ni-P and Ni-B. After heat treatments, for 1 hr at temperatures ranging from 350 °C to 450 °C, the crystallization of Ni_3P and Ni_3B phases appeared and their intensity grew as the heating temperature increased.

CONCLUSION

Adhesion strength of Ni-P and Ni-B electroless plated film on alumina substrates had a maximum value of 150 Kg/cm^2 at the etching time of 150 sec and decreased with longer time. Two kinds of electroless nickel films did not show any difference in adhesion strength.

The microstructure of Ni-P on alumina showed crystalline Ni and Al_2O_3 in as-plated film. After heating Ni-P plated ceramics, the crystallization of Ni_3P appeared and the intensity of Ni_3P at X-ray diffraction pattern increased as the heating temperature increased. On the other hand, crystal Ni_3B also appeared in the Ni-B film and its intensity grew with heating temperature as in Ni-P.

REFERENCES

1. A. Kubota and N. Koura ; J. Metal Finishing Soc., Japan 37 [2] 694 (1986)
2. Randy Strauss ; Plating and Surface Finishing 1 34 (1985)
3. H. Honma and S. Mizushima ; J. Metal Finishing Soc., Japan 33 [8] 380 (1982)
4. J.E.A.M. Van den Meerakker ; J. Appl. Electrochem., 11 395 (1971)
5. G. O. Mallory ; Plating, 4 319 (1971)

MICROSTRUCTURE AND PHASE TRANSFORMATION OF PLASMA-SPRAYED $\text{ZrO}_2\text{-Y}_2\text{O}_3$ THERMAL BARRIER COATINGS

Dong - Soo Shur

Dept. of Materials Engineering, Chungnam National Univ.
Daeduck Science Town
220 Gung-dong, Yuseon-gu, Taejon 302-764, Korea

The microstructure and phase transformation of the plasma-sprayed NiCrAlY bond coating and $\text{ZrO}_2\text{-Y}_2\text{O}_3$ ceramic coating were investigated using XRD, SEM, EDAX and TEM. The overall microstructure of the as-sprayed ceramic coating was quite inhomogeneous due to the chemical inhomogeneity of Y_2O_3 in the starting powder. As-sprayed ceramic coatings consisted mainly of non-equilibrium tetragonal (T') grains with separated monoclinic and cubic grains. Three kinds of tetragonal phase microstructures were observed, i.e. APB structure, mottled structure and colony structure.

1. INTRODUCTION

Two-layer thermal barrier coatings consisting of a MCrAlY (where M= Ni, Co, Fe or combinations of these elements) inner metallic bond coating layer and an outer $\text{ZrO}_2\text{-Y}_2\text{O}_3$ ceramic coating layer have been investigated as a means to increase the durability of air-cooled gas turbine airfoils by preventing oxidation and corrosion of the Ni and Co base superalloy and reducing metal temperature.

The coating properties for turbine engine application are achieved through the selection of materials properties and coating process parameters. Desired ceramic material properties include low thermal expansion, thermodynamic stability in the gas turbine environment and mechanical stability during thermal cycling. Although a number of ceramic materials including ZrO_2 , ZrSiO_4 , Ca_2SiO_4 , and HfO_2 have been considered for potential application, today only ZrO_2 is still under serious consideration, because it has low conductivity and a coefficient of thermal expansion greater than most other oxides making it more compatible with metal substrates with regard to thermal expansion mismatch strains. However, pure ZrO_2 has poor mechanical stability toward thermal cycling because of the large volume change during the transformation from the tetragonal to the monoclinic phase. The largest

improvements in mechanical properties can be obtained by partially stabilizing the ZrO_2 with the additions of CaO , MgO or Y_2O_3 . Of these, Y_2O_3 performs best, in part because CaO and MgO tend to vaporize during plasma spraying.

2. EXPERIMENTAL PROCEDURE

ZrO_2 -7.9% Y_2O_3 ceramic coating was sprayed onto Ni-base superalloy (PWA 1422) specimens which were previously coated with a low pressure plasma sprayed Ni-17%Cr-14%Al-0.3%Y bond coating.

The plasma-sprayed specimens were thermally exposed at 1200°C in order to study oxidation and interdiffusion of the bond coating and phase transformations within the ZrO_2 - Y_2O_3 ceramic coating using optical microscope, SEM, EDAX, XRD and TEM.

3. RESULTS AND DISCUSSION

3.1. Oxidation of NiCrAlY Bond Coating

At the bond coating/ceramic coating interface, bond coating oxidation is noticeable after less than one hour exposure at 1200°C. A thin oxide scale is formed on the bond coating by diffusion of bond coating alloying elements outwards and interact with oxygen diffusing through the ZrO_2 - Y_2O_3 ceramic coating. The oxide scale is composed of many types of transient oxides. Near the bond coating interface, Al_2O_3 and spinel types of oxides (NiCr_2O_4 , NiAl_2O_4) are formed.

TEM work to study the oxidation of the bond coating was limited because the specimen tended to crack at the interface during TEM foil preparation of transverse sections, especially in thermally exposed specimens. Fig. 1 shows the TEM microstructure of the oxide scale after one hour static thermal exposure and the results of point EDAX analysis. Spinel types of oxide grains of about 0.7 μm thickness are observed between the ZrO_2 - Y_2O_3 ceramic coating and bond coating, and many voids are present at the oxide scale/ceramic coating interface. In some place, however, the oxide scale is adherent to the ceramic coating. Presumably, the bond coating is adherent to the ceramic coating in the as-sprayed condition and chemical reactions occur between the newly formed oxides and the bond coating.

After ten hours exposure, stable Al_2O_3 columnar grains have formed beneath the spinel-type oxide; the thickness of the Al_2O_3 columnar grain is about $1\text{ }\mu\text{m}$ as shown in Fig. 2. The presence of large voids (about $1\text{ }\mu\text{m}$) is evident at the Al_2O_3 oxide scale/bond coating interface. The voids grow further after ten hours exposure and subsequently the adhesive strength between the Al_2O_3 scale and the bond coating will not be enough to hold them together due to the decrease in load bearing contact area. Therefore, cracks can develop at the voids and propagate along the weakly bonded Al_2O_3 scale/bond coating boundary, and finally failure occurs by delamination at the Al_2O_3 scale/bond coating interface.

SEM analysis of the underside of the ceramic coating shows that Al_2O_3 scale adhered to a large area of ZrO_2 ceramic coating. The bottom surface of this spalled Al_2O_3 scale is quite smooth and there is no indication of crack propagation. However, the ceramic coating has a flaky appearance because of the splat morphology.

3.2. TEM of the Ceramic Coating

TEM micrographs of the as-sprayed $\text{ZrO}_2\text{-Y}_2\text{O}_3$ ceramic coatings showed gaps between splat boundaries and micro-pores formed from entrapped gases ($\text{Ar}+\text{H}_2$) and/or air. Columnar grains of small grain size ($0.1\text{-}0.2\text{ }\mu\text{m}$) of the non-equilibrium tetragonal (T') phase were formed near the bond coating/ceramic coating interface. Deeper into the ceramic coating, the grain size of the columnar grains was bigger than that of the columnar grains near the interface; large equiaxed grains ($1\text{-}2\text{ }\mu\text{m}$) were formed due to the slower cooling rate in this region. Grains of tetragonal, monoclinic and cubic phases were separated from each other and showed large variations in Y_2O_3 concentration from different regions. The results of XRD phase analysis of the as-sprayed ceramic coating showed that the tetragonal phase was the main phase.

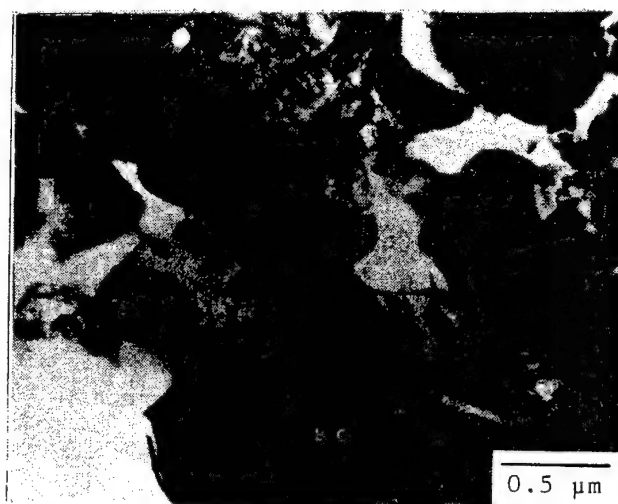
However, three kinds of tetragonal microstructures were observed in this study. First, most of the tetragonal phase existed as non-equilibrium tetragonal (T') columnar grains which were formed during rapid cooling of the splats without yttrium diffusion. The size of the columnar grains was small ($0.1\text{-}0.2\text{ }\mu\text{m}$) and anti-phase boundaries (APB) were observed within the tetra-

gonal (T') grains. Well developed APB's within large grains which had 11.5% Y_2O_3 concentration are shown in Fig. 3(a).

The second structure was a mottled structure due to tetragonal precipitates formed within large grains ($1.0\text{ }\mu\text{m}$) as shown in Fig. 3(b). The precipitates were aligned parallel to $\langle 211 \rangle$, $\langle 121 \rangle$ and $\langle 112 \rangle$ projected directions in this particular orientation and showed indication of tetragonal colony structure containing mottled tetragonal precipitates.

The third structure was a well developed tetragonal colony structure within the large grains ($2.0\text{ }\mu\text{m}$) which were located in the middle of the ceramic coating. The colonies was aligned parallel to $\langle 011 \rangle$ and $\langle 100 \rangle$ projected directions as shown in Fig. 3(c) and the Y_2O_3 concentration was analyzed to be 6.5% Y_2O_3 . APB's and mottled tetragonal precipitates were present within the colony structure. The colony structure consists of banded ellipsoidal particles composed of a alternating, twin related variants of the tetragonal phase.

TEM micrographs of the ceramic coating was similar to as-sprayed condition even after 100 hours exposure at 1200°C . Fig. 4 shows the regions of monoclinic and tetragonal grains remain separated even after 100 hours thermal exposure. The monoclinic grains were found to contain 2.1% Y_2O_3 and the tetragonal (T') grains contain 4.5% Y_2O_3 concentration. Strain contrast is evident within the monoclinic grains.



Position	Al_2O_3	SiO_2	Cr_2O_3	CoO	NiO
1	2.2	43.1	9.3	4.3	41.1
2	5.7	55.2	6.9	2.8	29.3
3	25.0	3.3	65.2	0.6	5.8

Fig. 1. TEM micrograph of oxide scale after 1 hour thermal exposure at 1200°C and the result of point EDAX analyses.

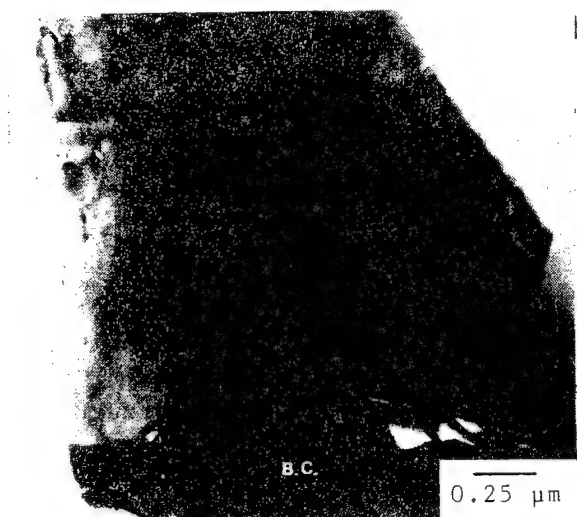
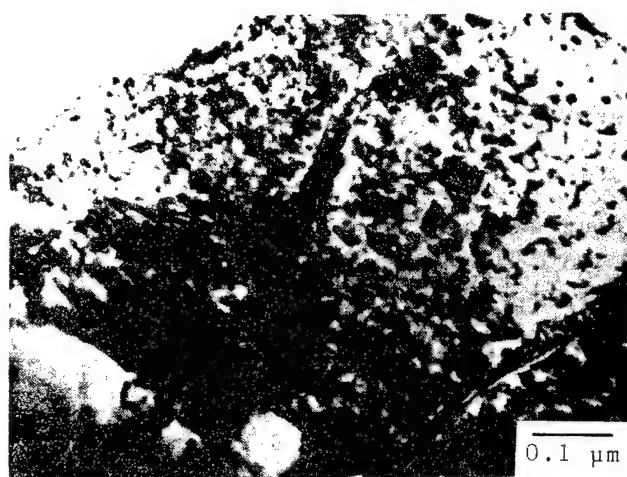


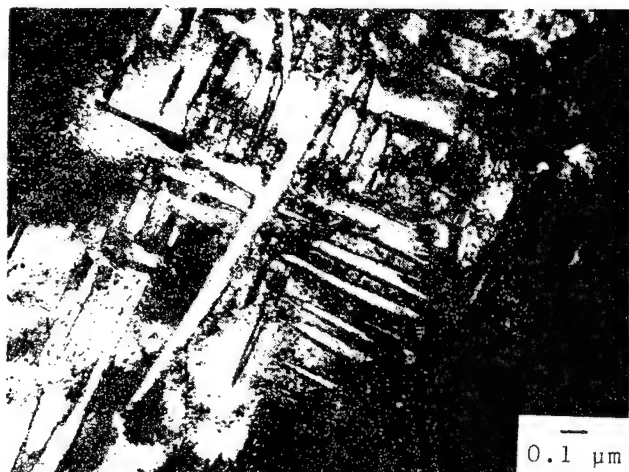
Fig. 2. TEM micrograph of oxide scale
after 10 hours thermal exposure
at 1200°C.



(a)

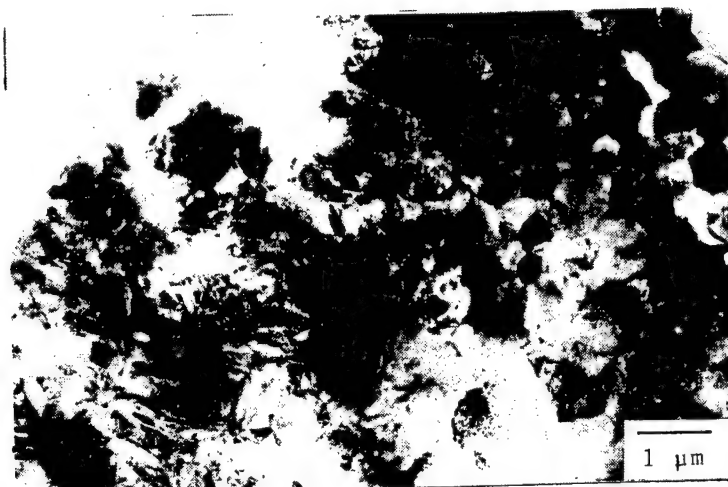


(b)



(c)

Fig. 3. (a)-(c) Three kinds of tetragonal phase TEM microstructure
(a) APB's
(b) Mottled structure
(c) Colony structure



(a)



(b)



(c)

Fig. 4. (a)-(c) TEM micrograph of ceramic coating after 100 hours thermal exposure at 1200°C showing separate regions of monoclinic and tetragonal grains.

Cutting Tool of SiC Whisker/ Al_2O_3 Composite

Kazuo Ueno, Tsutomu Yamamoto* and Makoto Asano*

Government Industrial Research Institute, Osaka
1-8-31 Midorigaoka, Ikeda-shi, Osaka 563 Japan
*Di jet Industry Co., 2-1-18 Kamihigashi, Hirano
-ku, Osaka 547 Japan

Silicon carbide whisker-reinforced Al_2O_3 matrix composites were fabricated. Homogeneous dispersion of the whisker in the starting powder mixture dominates both strength level and its reliability. Improvements both in strength and fracture toughness have been observed. Alumina matrix composite was applied as a cutting tool, which exhibited good performances.

1. Introduction

Improvements in both toughness and reliability are indispensable to the application of ceramics as a structural material. For this purpose, fiber-reinforcement, especially whisker-reinforcement attracts much attention today.

Whiskers in the FRC(Fiber-reinforced Ceramics) make the crack sensitivity of the matrix lower and then the composite tend to be tolerable against flaws on its surface or in the body. Whisker-reinforcement has also a prominent effect for improving reliability of the composite.¹⁻⁶⁾ In this paper, influences of whisker-reinforcement on the mechanical properties of the Al_2O_3 matrix-FRC and application as a cutting tool are described.

2. Experimental

On the fabrication of whisker-reinforced composite(Fig. 1) homogeneous dispersion of whiskers in the composite body is essential. If the mixing of the whisker and the matrix powder is not enough, it is often observed that fracture begins from a whisker entangle in the sintered body. Unless these defects are removed from the starting powder mixture, whisker-reinforcement cannot be expected; on the contrary, only strength degradation will be observed.

In our experiment silicon carbide whisker(SiC(w)) was first dispersed

in water by a mechanical stirring and then the suspension was filtered through a mesh having ca. 500 - 60 micrometer opening ¹⁾. By this filtration process almost all whisker lumps can be removed from the suspension.

The slurry of matrix powder with 10 - 40 wt% silicon carbide whisker doped with some sintering additives such as MgO, was mixed with the whisker suspension, dried and hot-pressed.

3. Results and discussion

Concerning with the fabrication process for SiC(w)-Al₂O₃ composite, dispersion method for untangling whisker lumps is a determinant for strength and its reliability.⁷⁾

For comparison, three kinds of alumina matrix FRC have been fabricated. One with as-received whisker, one with the whisker which was untangled by ultrasonic for 10 minutes under a mechanical stirring, and one with the whisker refined through a filter with 50 μ m opening after the ultrasonic treatment.

Figure 2 shows Weibull's plot of the strength values for FRC with as-received, ultrasonic-treated, and filtered whisker of 30 %. The average strength, ca. 470 MPa, of the FRC with as-received whisker is lower than even that for monolithic alumina. On the other hand, the whisker treatment improves both strength level and reliability. The composite with the filtered-whisker has an average strength of 1 GPa, which would be one of the highest values reported for alumina-based ceramics.

Fracture toughness is also improved as shown in Fig. 3. Toughness increases as increasing with the whisker content. Toughening mechanism is assumed to be crack deflection and/or crack bridging of whisker in the crack wake region. Fiber pull-out has not been observed so much on the fracture surface.

This alumina matrix FRC was applied to a cutting tool. Important characteristics for cutting tool material are high wear resistance and mechanical-shock resistance. Improved strength and crack resistance by

whisker incorporation seem to make the composite a promising candidate for the application.

Figure 4 shows wear curves of SiC(w)-alumina, Si_3N_4 and super-hard alloy on continuous cutting of heat-resistant alloy Inconel 718. Alumina FRC exhibits a superior wear-resistance than other materials.

Figure 5 shows spalling-resistance of alumina-SiC(w), Si_3N_4 , and alumina-TiC on the intermittent cutting of cast iron. The whisker composite has a longer life for repeated mechanical shocks than the particulate reinforced composite.

Figure 6 shows cutting performances of SiC(w)- Al_2O_3 , TiC- Al_2O_3 and Si_3N_4 on the intermittent milling of cast iron. Under such severe cutting condition with complex stress-state at the tip, whisker-reinforced alumina shows excellent behavior than other materials.

4. Conclusion

SiC whisker reinforced Al_2O_3 were fabricated. By the reinforcement, various mechanical properties were improved, such as bending strength, hardness, or fracture toughness.

It was found that the reinforcement of the whisker produced composites with high reliability. On the field tests as a cutting tool, SiC(w)- Al_2O_3 composite exhibited to be a high wear-resistant and shock-tolerable material in comparison with conventional ceramic cutting tools.

References

- 1) Y.Toibana and K.Ueno, USP. 4,507,224. Mar. 26, 1985.
- 2) K.Ueno, N.Tamari, T.Ogura and Y.Toibana, High Temperature Strength of Silicon Nitride Composite Reinforced with Silicon Carbide Whisker, Osaka Kogyougijutu Shikensho Kiho, 33(1), 114 (1982).
- 3) K.Ueno and S.Sodeoka, Fracture Toughness of SiC Whisker Reinforced Si_3N_4 Ceramics, Yogyo Kyokai-shi, 94(9), 981 (1986).
- 4) R.Hayami, K.Ueno, I.Kondou, N.Tamari and Y.Toibana, Si_3N_4 -SiC Whisker Composite Material, Tailoring Multiphase and Composite Ceramics, Edit. R.E.Tressler, G.L.Messing, C.G.Pantano and R.E.Newnham, Plenum Pub. Co., 1986.
- 5) K.Ueno and Y.Toibana, Mechanical Properties of Silicon Nitride Ceramic Composite Reinforced with Silicon Carbide Whisker, Yogyo Kyokai-shi, 91(11), 493 (1983).
- 6) I.Kondo, N.Tamari and Y.Toibana, Thermal Properties of Si_3N_4 -SiC Whisker Composite, Yogyo Kyokai-shi, 94(11), 1180 (1986).
- 7) T.Yamamoto, M.Asano, K.Ueno and N.Tamari, Submitted to Funtai Funmatsu Yakin Kyokai-shi.

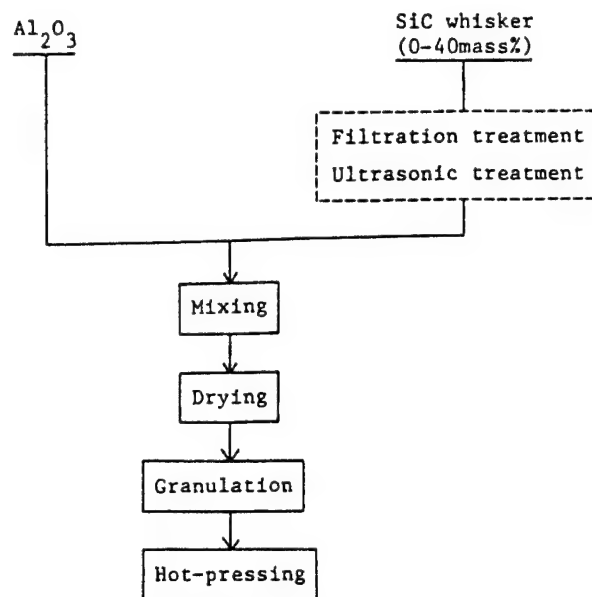


Fig. 1 Fabrication process of SiC(w)-Al₂O₃ composite.

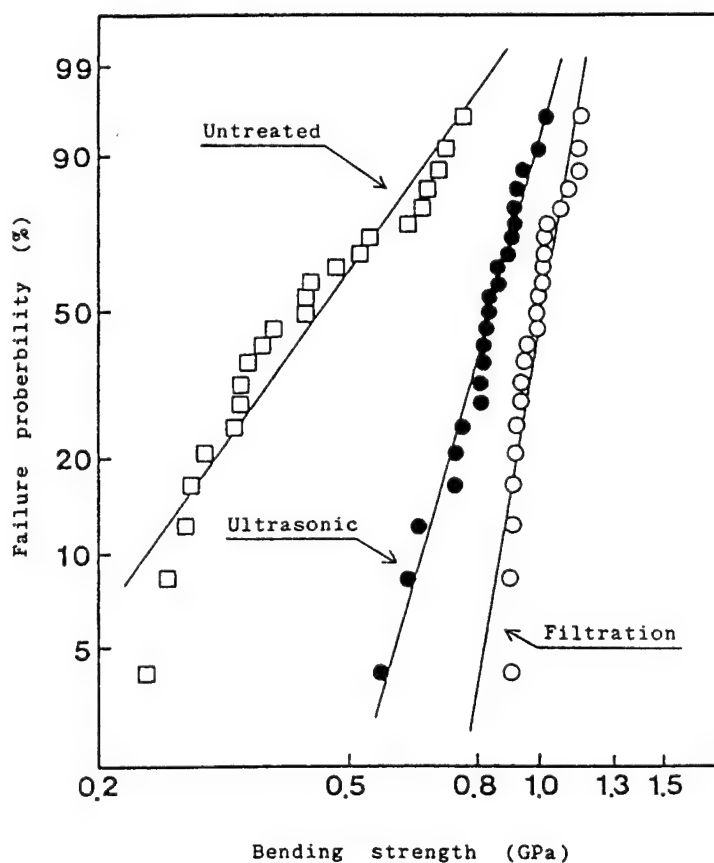


Fig. 2 weibull's plots of bending strength of 30 wt% SiC(w)-Al₂O₃ composite with as-recieved(□), ultrasonic-treated(●) and filtered(○) whisker.

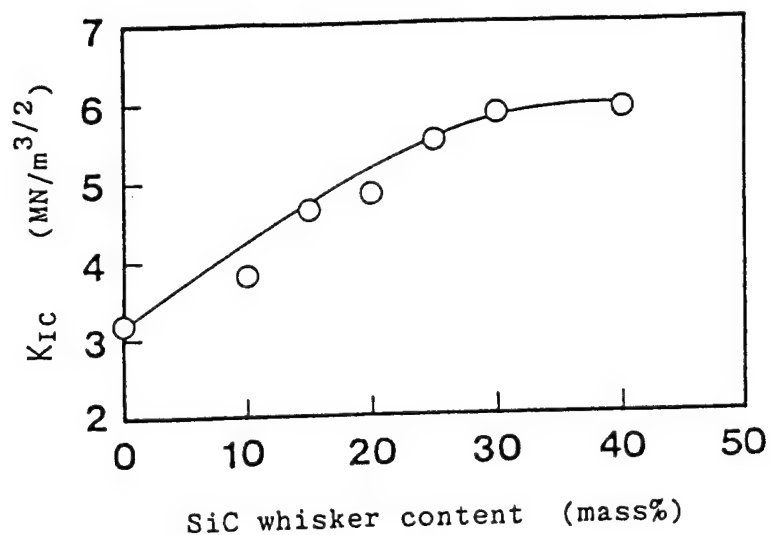


Fig. 3 Effect of SiC whisker content on fracture toughness of SiC(w)-Al₂O₃ composite.

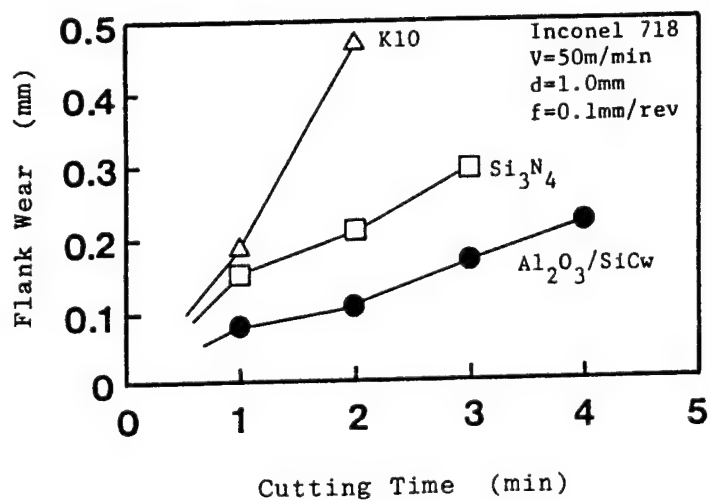


Fig. 4 Wear curves of SiC(w)-Al₂O₃, Si₃N₄ and hard metal on cutting of heat-resistant alloy.

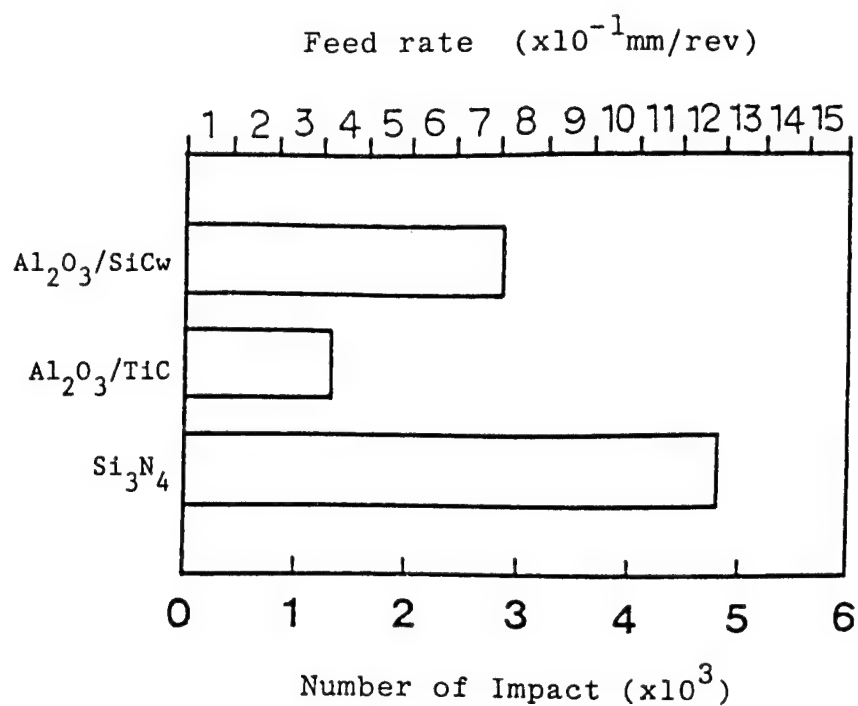


Fig. 5 Number of impacts up to failure of $\text{SiC(w)-Al}_2\text{O}_3$, $\text{TiC-Al}_2\text{O}_3$ and Si_3N_4 on intermittent cutting of cast iron.

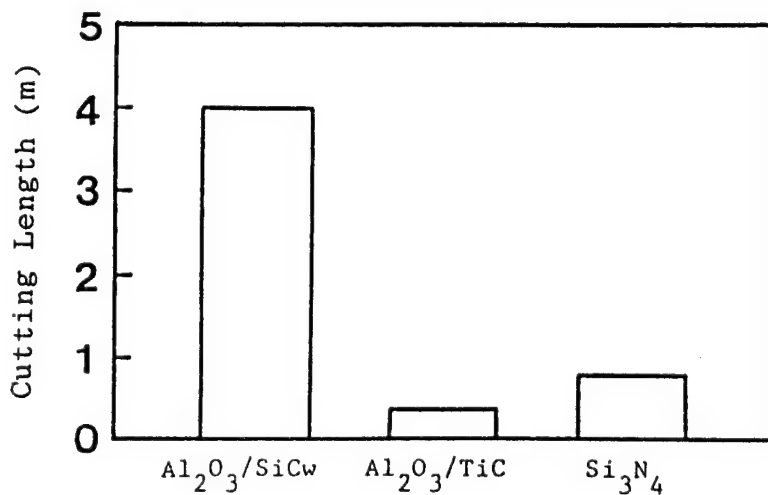


Fig. 6 Cutting length up to failure of $\text{SiC(w)-Al}_2\text{O}_3$, $\text{TiC-Al}_2\text{O}_3$ and Si_3N_4 on milling of cast iron.

Development and Application of High Thermal Conductivity AlN Substrates

Kurokawa Y., Shimada Y., and Takamizawa H.

Material Development Center, NEC Corporation

1-1, Miyazaki 4-chome, Miyamae-ku, Kawasaki city 213 Japan

Recent trend on the development of high thermal conductivity substrates is introduced first. High thermal conductivity AlN substrates, which have thermal conductivity of 160~260 W/mK, have been developed by NEC Corporation. The AlN substrates have several excellent characteristics at room temperature, such as high thermal conductivities over 10 times that of Al₂O₃, a thermal expansion coefficient close to silicon, high electrical insulation resistivity, low dielectric constant and loss, good mechanical properties and non-toxicity.

The AlN substrates were applied to several electrical and optical devices. AlN was found to be applicable as heat sinks to three kinds of semiconductor devices: 1) silicon transistor, 2), GaAlAs LED, and 3) InGaAsP laser diode. The multilayer AlN substrate was also developed by co-firing AlN green sheets with W conductor paste. New thick film conductor-resistor-glass encapsulant system with excellent performance was developed. This new thick film paste system consists of ZnO-B₂O₃-SiO₂ new glass-frits. Furthermore it was found that AlN with thermal conductivity of 260 W/mK is compatible with 99.5% BeO as a high power semiconductor package. Finally AlN is the most promising candidate for the advanced packaging material.

I. Introduction

The ever increasing demand for electronic circuit miniaturization is continuing for advanced electronic devices. However as a result of increasing circuit density and power on silicon chips, heat dissipation from the chips is becoming critical. In electronic devices, heat dissipation through the substrate is one of the best ways to achieve efficient management of heat from microcircuits. High thermal conductivity substrates will enable heat to be readily dissipated from the chips.

Nowadays, Al₂O₃ ceramics (alumina) with thermal conductivity of 20 W/mK at room temperature has been dominant among substrate materials. In some cases, BeO ceramics (beryllia) has been used, in spite of its toxic nature, because it has high thermal conductivity of 260 W/mK. Recently high thermal conductivity substrates, such as SiC and AlN substrates, have been developed in Japan [1,2,3,4,5,6]. Table 1 summarizes the recent trend on the development of high thermal conductivity substrates. The SiC substrate, which has excellent properties for packaging material, such as high thermal conductivity of 270 W/mK, high electrical insulation resistivity, a thermal expansion coefficient close to that of silicon chip, and high mechanical strength, has been developed. However, it has disadvantages that the dielectric constant and loss are extremely high and the multilayer substrate can not come true through a hot press process. On the other hand, aluminum nitride (AlN) substrates overcame these problems and showed superior properties to Al₂O₃, though the thermal conductivities were not as high as that of BeO at the first stage [2,3,4,5]. Recently the thermal conductivities of AlN increased remarkable in a few years in Japan by improvement of raw AlN powder and sintering process and by utilizing effective

sintering additives, such as CaC₂, CaO and Y₂O₃, and finally it became close to that of BeO[6,7,8]. Further, various applications and evaluations, such as heat sinks, cerdip package, flat package, multilayer multichip package, PGA package and multilayer PGA package, were investigated [5,6,7,8,9]. At last AlN seems to be the most promising candidate material for thermal management.

The thermal conductivity of AlN ceramics is greatly influenced by its chemical purity and density, while the theoretical value is predicted to be 320 W/mK at room temperature.

Table 1 Recent trend in the development of high thermal conductivity substrates

Year	Company	Material	Thermal Conductivity	Topics
1982	Hitachi	SiC	270w/mK	—
1983	Toshiba	AlN	60	Thyristor for Train
1984	Hitachi	SiC	270	ECL LSI Package
	Toshiba	AlN	100	Y ₂ O ₃ Additive
	Tokuyama Soda	AlN	110	High Purity AlN Powder Translucent AlN
	Heraeus	AlN	140~170	—
	NEC	AlN	160	Reducing Sintering
	NEC	AlN	160	Transistor, LED, Laser Diode
1985	Sumitomo Denko	AlN	220	—
1986	NEC	AlN	240~260	CaC ₂ Reductant
	NEC	AlN	160	Multilayer Substrate
	Tokuyama Soda	AlN	260	—
1987	Toshiba	AlN	260	Reducing Atmosphere
	Toshiba	AlN	70	Multilayer PGA

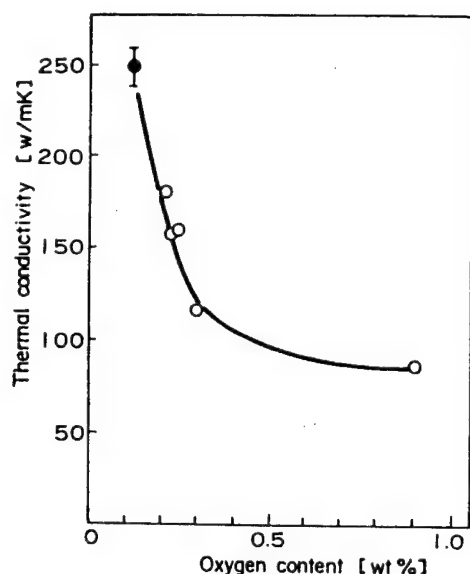


Fig.1 Relation between thermal conductivity and oxygen content of AlN ceramics.

Especially, a small amount of oxygen impurity markedly decreases thermal conductivity as shown in Fig. 1.

2. AlN Substrate Properties

Typical properties for the AlN substrate are summarized in Table 2. Table 2 compares properties for AlN and other substrates (Al_2O_3 , BeO, SiC) at room temperature.

The AlN substrate has a maximum thermal conductivity of 240~260 W/mK at room temperature, which is over 12 times as high as that of Al_2O_3 and 80% of the theoretical value.

The AlN substrate shows excellent thermal expansion matching to the silicon chip. The thermal expansion coefficient is closer to that of silicon than those of Al_2O_3 and BeO. As a result, there is little stress problem induced by thermal mismatch between silicon chip and AlN substrate.

The AlN substrate also has good electrical properties, as good as Al_2O_3 and BeO. It shows high electrical insulation resistivity, and low dielectric constant and loss, though SiC has the disadvantages of extremely high dielectric constant and loss [1].

The AlN substrate shows not only higher flexural strength but also easier machinable property than Al_2O_3 . The flexural strength at room temperature is 3500~4000 kg/cm², which is higher than those of Al_2O_3 and BeO. On the other hand, the vickers hardness is 1200 kg/mm².

3. AlN Substrate Applications

3-1. Heat sinks

The AlN substrate with thermal conductivity of 160 W/mK was first applied as a heat sink of the high power semiconductor devices shown in Fig. 2 [5]. Both surfaces of AlN substrate were metallized by the conventional Ti/Pt/Au sputtering technique. It was proved that AlN is able to be metallized with good stability and reliability by the pressure cooker test, the high temperature high humidity test, the high temperature test and the heat cycle test [6]. The thermal resistance, and electrical and optical properties for the three different semiconductor devices were measured. The thermal resistance for them are summarized in Table 3. Today toxic BeO, silicon crystal, silicon or expensive diamond crystals are used as heat sinks of silicon transistor, GaAlAs LED and

Table 2 Properties for AlN and other substrates at room temperature

Substrates	NEC-AlN	96% Al_2O_3	99.5%BeO	SiC
Properties				
Thermal Conductivity (W/mK)	160~260	20	260	270
Thermal Expansion Coefficient (r.t. ~ 400 °C) ($\times 10^{-6}/^\circ\text{C}$)	4.3	6.7	7.5	3.7
Electrical Resistivity (Ωcm)	$>10^{13}$	$>10^{13}$	$>10^{13}$	$>10^{13}$
Dielectric Constant at 1MHz	8.9	8.9	6.7	42
Dielectric Loss ($\times 10^{-4}$) at 1MHz	1	2	1	500
Flexural Strength (Kg/cm ²)	3500~4000	3000	2500	4500
Vickers Hardness (Kg/mm ²)	1200	3000	1200	3000

Thermal expansion coefficient of Si is $3.5\sim 4.0 \times 10^{-6}/^\circ\text{C}$.

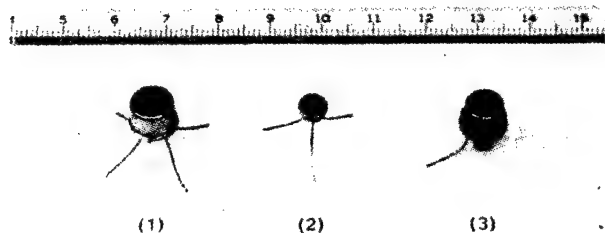


Fig.2 Semiconductor devices with AlN heat sink.

- (1) Silicon Transistor
- (2) GaAlAs Light Emitting Diode
- (3) InGaAsP Laser Diode

InGaAsP laser diode, respectively. The thermal conductivity of each heat sink is shown in Table 3. In case of AlN heat sinks thermal resistance were all small enough to be compatible with the conventional heat sinks in these devices. On the other hand, no great difference was detected in the significant electrical and optical properties on the device, such as the total dissipation power, the output power, the rise time, the fall time, etc. Finally it was assured that AlN is applicable to these electrical and optical devices.

3-2. Multilayer AlN Substrate

A co-fired multilayer AlN substrate is a significant breakthrough for AlN substrate application. Multilayer AlN substrates were successfully developed by co-firing the AlN green sheets with W conductor pastes. Characteristics for the test sample are summarized in Table 4. Sheet resistivities of external and internal conductors were 20 and 25 mΩ/□, respectively. These values are satisfactory for practical use. The adhesion strength of the external W

conductors was higher than 2kg/mm². In addition, the camber of the multilayer AlN substrate was measured to investigate any shrinkage mismatch between the AlN substrate and the W conductor. The camber of 20 μm/20 mm is as good as that of the standard AlN substrate. These preliminary results indicate that the multilayer AlN substrate is feasible for use in place of a conventional Al₂O₃ package.

A multilayer AlN substrate, with three metallized layers, is shown in Fig. 3. It is an example of a multichip package (MCP), which is capable of mounting 10 LSI chips. Microstructural characterization was carried using TEM (transmission electron microscope). BF image, DF image and SAD (Fig. 4) revealed that there was no reaction between AlN and W at the interface. It was concluded that the high adhesion strength between W conductor and the AlN substrate was not due to any secondary phase but to mechanical interlocking of AlN and W during cofiring.

Table 4 Characteristics for the multilayer AlN substrate with co-fired W conductor

Test		Result
Sheet resistivity	External conductor	20mΩ / □
	Internal conductor	25mΩ / □
Adhesion strength		> 2 kg/mm ²
Camber		20 μm / 20 mm

Table 3 Thermal resistance for semiconductor device with AlN heat sink

Semiconductor Device	Heat Sink				
	92%Al ₂ O ₃	Silicon Crystal	AlN	995% BeO	Diamond Crystal (1a)
Thermal Conductivity (RT)	17w/mk	150	160	260	1000
Silicon Epitaxial Transistor (< 50°C/W)	77°C/W	—	39	34	—
GaAlAs Light Emitting Diode	—	95°C/W	86	—	—
InGaAsP Laser Diode	—	105°C/W	88	—	70

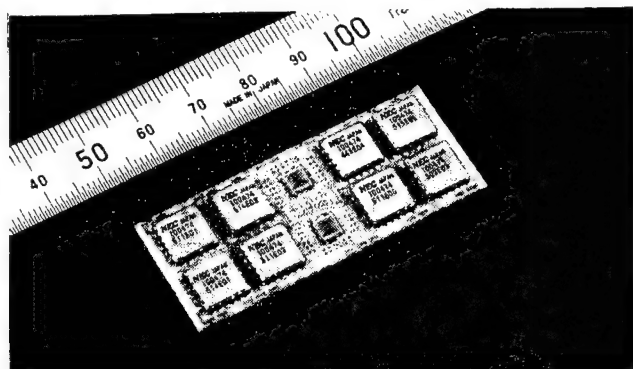


Fig.3 Multilayer AlN substrate with 3 metallized layer.

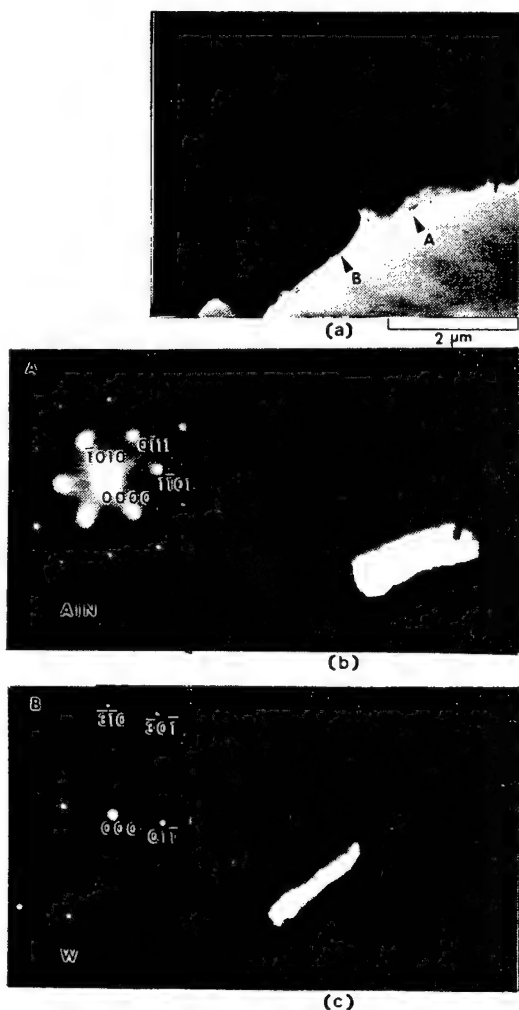


Fig.4 TEM images and SAD patterns at the AlN-W interface:
(a) BF image (b) SAD pattern and DF image from region B (c) SAD pattern and DF image from region C

3-3. Hybrid IC module

A thick film paste system, using conductor and resistor pastes, is very popular for making hybrid integrated circuits. The commercial thick film pastes for Al_2O_3 substrates are not generally compatible with AlN substrates. Fundamental problems are that most glasses in thick film paste sometimes decompose AlN into nitrogen gas and there is a great thermal expansion mismatch between AlN and glass-frits.

The new thick film paste system for AlN substrates consists of new $\text{ZnO-B}_2\text{O}_3\text{-SiO}_2$ glass-frits. The thermal expansion coefficient for new glass-frits is close to that for AlN substrates.

Thick Film Paste System Process

All thick films were printed onto AlN substrates using a 200 mesh stainless steel screen. After drying at 150°C for 10~50 minutes, conductor and resistors were fired in a belt furnace at 850°C peak temperature for 10 minutes in air. The glass encapsulant was fired in a belt furnace at 600°C for 5 minutes in air.

Thick Film Conductor

This thick Ag-Pd film conductor did not blister and was applicable for use with AlN substrates. The conductor adhesion strength was 1.7 kg/mm^2 , which was measured by pulling nailhead pins soldered onto 2 mm square pads. This value was higher than the practically available lower limit of 1.5 kg/mm^2 . Table 5 summarizes the typical properties on the conductor film. These results indicate that the thick film conductors have excellent reliability.

Thick Film Resistors and Glass Encapsulant

New thick film resistor series have been developed with excellent performance on AlN substrates. The resistors mainly consist of RuO_2 and devitrifiable solder glass of $\text{ZnO-B}_2\text{O}_3\text{-SiO}_2$

Table 5 Properties of thick film conductor

Thickness (μm)	8.9
Adhesion (Kg/mm^2)	1.7
Resistivity ($\text{m}\Omega/\square$)	4.1
Solder Wettability (%)	100
Solder Leaching (cycle)	>10

n=10

Table 6 Properties of thick film resistors

Resistivity (Ω/\square)		10	100	1K	10K	100K	1M
TCR (ppm/ $^{\circ}\text{C}$)	HOT	160	20	-10	-70	-140	-300
	COLD	120	-20	-20	-80	-170	-350
Variations In Resistivity by Glass Encapsulant (%)		-1.7	0.3	-1.5	-0.6	0.4	4.2

HOT : $25^{\circ}\text{C} \sim 125^{\circ}\text{C}$ COLD : $25^{\circ}\text{C} \sim -55^{\circ}\text{C}$

system. Resistivity values for the resistors are 10, 100, 1 K, 10 K, 100 K and 1 M Ω/\square . Table 6 shows properties of newly developed resistors for AlN substrates. Thick film resistor layers did not have bubbles or blisters. The TCR for 1 M Ω/\square resistor needs improvement, because it is less than $-250 \text{ ppm}/^{\circ}\text{C}$. These facts indicate that the new resistors for AlN substrates have excellent reliability.

The glass encapsulant has also been developed for AlN substrates. It mainly consists of glasses having low thermal expansion coefficient, close to that for AlN substrates. The encapsulant did neither produce any bubbles and cracks, nor change color due to silver migration.

Thick Film Metallization Application

Figure 5 shows a AlN hybrid IC module for a car telephone, with the new thick film paste system.

3-4. High Power Semiconductor Package

AlN substrates were applied to the package for high power semiconductor devices shown in Fig. 6.

Their thermal resistances are summarized in Table 7. Today, toxic 99.5% BeO is used for this high power semiconductor device packages. Standard specifications on the device indicate that the thermal resistance $R_{th(j-c)}$ is less than $0.55^{\circ}\text{C}/\text{W}$ and the total dissipation power is 200 W. In case of AlN package W heat sink was used in stead of 80wt%W/20wt%Cu heat sink. The thermal resistance in case of AlN substrates, which have 260 W/mK thermal conductivity was $0.42^{\circ}\text{C}/\text{W}$. On the other hand the thermal resistance for 99.5% BeO was $0.38^{\circ}\text{C}/\text{W}$. The thermal resistance in case of AlN was higher than that of BeO, because W heat sink was brazed onto the AlN substrates. The results indicate that the thermal resistance for the AlN is close to that for 99.5% BeO, which is in good agreement with the thermal conductivity

magnitude and the AlN package is applicable to the device.

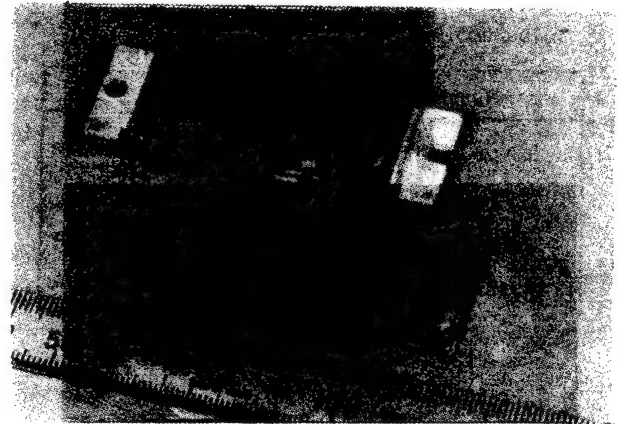


Fig.5 AlN hybrid IC module for a car telephone.

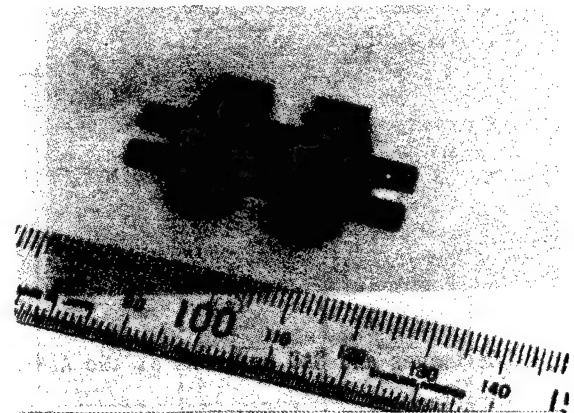


Fig.6 AlN high power semiconductor package.

Table 7 Thermal resistance for high power semiconductor devices

Package	AlN + W	BeO + 80W/20Cu
Property	260 W/mK 170	260 250
Thermal Resistance (°C/W)	0.42	0.38

Standard Specification; (0.55°C/W)

4. Conclusion

Heat dissipation from silicon chips is becoming ever more critical from year to year. The advanced AlN substrate has properties superior to Al₂O₃, and does not have the thermal expansion mismatching to the silicon chip and toxicity that appear for BeO. Therefore, the AlN substrate seems to be the most promising candidate. The AlN substrate will be applied to high density, high power and high frequency microcircuits, such as LSI, VLSI, hybrid IC, high power transistors and diodes.

5. Acknowledgement

The authors would like to thank the members in the Electronics Division, Sumitomo Metal Mining Co., Ltd. for their development of thick film paste system. The authors are very grateful to M. Yonezawa, general manager of the Material Development Center, for his guidance and encouragement. The authors wish to thank their co-workers in the Material Development Center, NEC Corporation, for their contribution to AlN substrates fabrication and metallization.

REFERENCES

- [1] S. Ogiwara, T. Yasuda, K. Otsuka and F. Kobayashi, "Application to LSI Packages of SiC Ceramics with High Thermal Conductivity," Proc. 3rd Internat. Microelectronics Conf., p. 423, 1984.
- [2] N. Iwase, A. Tsuge and Y. Sugiura, "Development of a High Thermal Conductive AlN Ceramic Substrate Technology," *ibid.*, p. 180, 1984.
- [3] W. Werdecker and F. Aldinger, "High Performance Aluminum Nitride Substrate by Tape Casting Technology," Proc. 35th Electronic Components Conf., p. 26, 1984.
- [4] N. Kuramoto and H. Taniguchi, "Transparent AlN Ceramics," J. Mater. Sci. Lett., 3, p. 471, 1984.
- [5] Y. Kurokawa, K. Utsumi, H. Takamizawa, T. Kamata and S. Noguchi, "AlN Substrates with High Thermal Conductivity," IEEE Trans. Components, Hybrids and Manufacturing Technology, CHMT-8, 2, p. 248, June 1985.
- [6] Y. Kurokawa, H. Hamaguchi, Y. Shimada, K. Utsumi, H. Takamizawa, T. Kamata and S. Noguchi, "Development of Highly Thermal Conductive AlN Substrate by Green Sheet Technology," Proc. 36th Electronic Components Conf., p. 412, 1986.
- [7] N. Kuramoto, H. Taniguchi and I. Aso, "Translucent AlN Ceramic Substrate," *ibid.*, p. 424, 1986.
- [8] N. Iwase, T. Yanazawa, M. Nakahashi, K. Shinozaki, A. Tsuge and K. Anzai, "Aluminum Nitride Multilayer Pin Grid Array Packages," Proc. 37th Electronic Components Conf., p. 384, 1987.
- [9] N. Iwase, K. Anzai and K. Shinozaki, "Aluminum Nitride Substrates Having High Thermal Conductivity," Solid State Technology, vol. 29, No. 10, p. 135, 1986.
- [10] Y. Kurokawa, H. Hamaguchi, Y. Shimada, K. Utsumi and H. Takamizawa, "Highly Thermal Conductive Aluminum Nitrides," Proc. ISHM 1987, p. 654.
- [11] H. Yamamoto, Y. Kurokawa, Y. Shimada and T. Kamata, "Metallization Development and Application for Aluminum Nitride Substrates," Proc. 39th Electronic Components Conf., p. 23.
- [12] Y. Kurokawa, C. Toy, and W.D. Scott, "Characterization of the AlN-W Interface in a Cofired Multilayer AlN substrate," J. Am. Cer. Soc., Vol. 72, No. 4, p. 612, 1989.

SUPERCONDUCTING CERAMIC ARTIFICIAL SUPERSTRUCTURED FILMS

超伝導セラミック人工格子

Kenji Kawaguchi, Mitsugu Sohma, Shigemitsu Shin

National Chemical Laboratory for Industry

Tsukuba, Ibaraki 305, Japan

Artificial superstructured films (ASF's) composed of transition metal nitrides were prepared by alternate reactive deposition method using electron-beam guns (E-guns). The ASF of the combination of MoN and TiN were epitaxially grown on MgO{100} single crystal substrate. Those artificial superstructures of [MoN(2 atomic planes)/TiN(2 atomic planes)], [MoN(monatomic plane) /TiN(17 atomic planes)], and [MoN(12 atomic planes)/TiN(monatomic plane)] were successfully synthesized and it was confirmed that the synthesis of ASF on the atomic scale is possible for ceramic materials. The structural analysis indicates the formation of B1-MoN which is a non-equilibrium phase and is predicted to be a high superconducting transition temperature (T_c) material. However, the ASF's containing B1-MoN layers showed lower T_c 's than those of ASF's with γ -Mo₂N. The combination of superconducting material (NbN) and ferromagnetic material (FeN_x) was also attempted.

INTRODUCTION

Transition metal nitride films have been used for protective and wear-resistive coating and the application for the micro-electronic and cryo-electronic materials has been remarkable recently. Since extremely thin nitride films and their heterostructures are used for the electronic materials, such studies as the thickness control on the atomic scale, microscopic structural properties, and the physical properties are important. Artificial superstructured film (ASF) is a good model sample for the basic studies. The ASF often shows unusual structural and physical properties different from those of bulk material derived from interface effects, two-dimensional effects, one-dimensional superstructure, etc., and hence the ASF also attracts attention as a new material.

Molybdenum mono-nitride with the B1-structure is expected to be a high- T_c superconductor. The T_c is predicted to be about 30 K from empirical estimation /1/ and theoretical calculation /2,3/. Since the B1-MoN is a non-equilibrium phase, it is difficult to be synthesized by conventional methods. We have tried to stabilize B1-MoN by multilayering with B1-TiN, because the lattice constant of B1-TiN is approximately equal to the estimated value of B1-MoN (0.422 nm /1/ - 0.425 nm /3/).

The ASF with the combination of ferromagnetic material (FeN_x) and superconducting material (NbN) is also interesting. Some information about the competing correlation between ferromagnetic ordering and superconducting coherence and the possibility of their coexistence is expected from the study of the ASF. The study of MoN-TiN ASF's is mainly described and the tentative results of NbN-FeN_x ASF's are also presented in this report.

PREPARATION OF MoN-TiN ASF'S

Samples of MoN-TiN ASF's were prepared by an alternate reactive deposition method using

electron-beam guns. Nitride films are generally prepared by sputtering, because the pressure of reactive gas atmosphere is higher in sputtering than in reactive deposition and hence the nitrogen composition of the sample prepared by sputtering is expected to be higher than that by reactive deposition. While the reactive deposition method is convenient to control preparing conditions such as deposition rate, substrate temperature, and atmospheric pressure over a more wide range and precisely. Main part of sample preparation system is schematically shown in Fig. 1. The preparation chamber was first evacuated to the base pressure of 10^{-8} Torr. Each metal ingot (99.99% Mo, Ti) was alternately electron-beam evaporated in an ammonia atmosphere. The atmospheric pressure ($P(\text{NH}_3)$) was in the range of 10^{-5} to 10^{-4} Torr. The substrate temperature (T_s) was varied between 50 C and 700 C. Crystal thickness monitors were normally placed halfway between the substrate and the evaporation sources. Since the thickness monitor is strongly affected by thermal radiation, the monitor for Mo source was placed far from the crucible. For the purpose of precise thickness control and enough nitridation, samples were deposited fairly slowly, typically about 0.01 nm/s. Cleaved single crystal $\text{MgO}\{100\}$ plates were used as substrates, because the lattice mismatch between MgO and Bi-TiN is very small (0.6%) and epitaxial growth is expected.

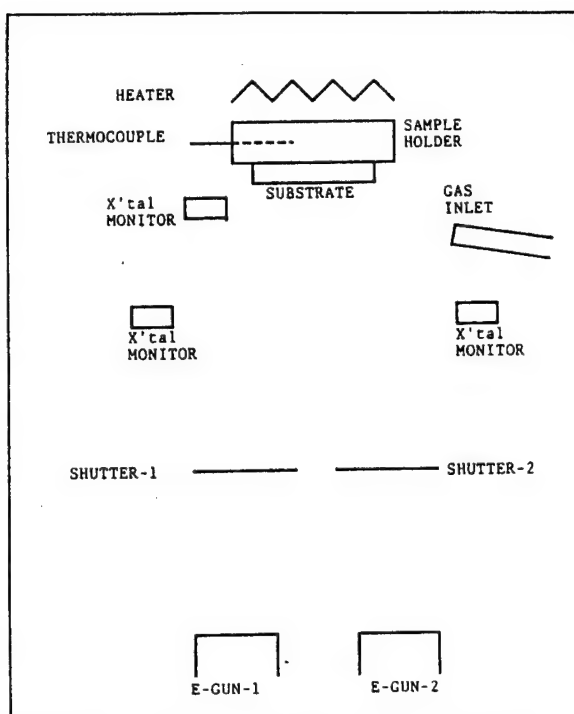


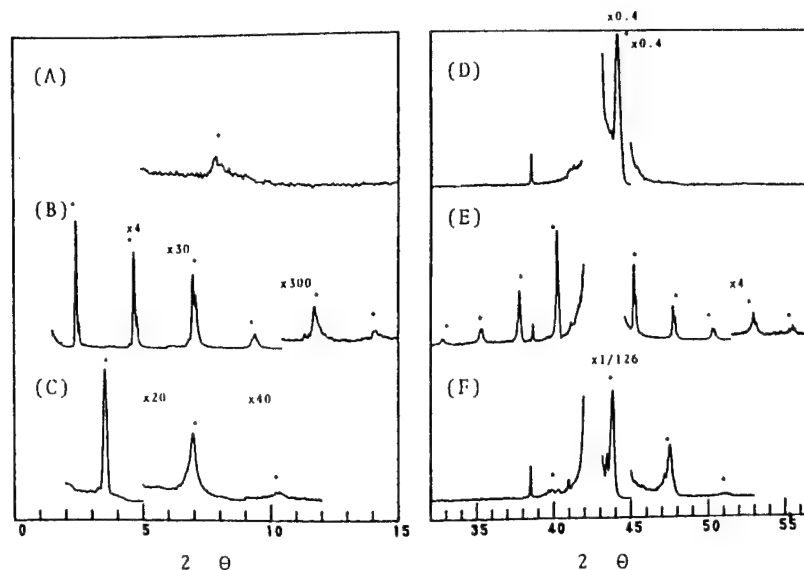
Fig.1 Schematic representation of reactive deposition system.

STRUCTURAL PROPERTIES OF MoN-TiN ASF'S

Structural properties of ASF's were investigated mainly by X-ray diffraction (XRD) using ordinary powder diffractometer. Typical XRD patterns of MoN-TiN ASF's are shown in Fig.2. Reflections derived from artificial periodicity are indicated by (*) marks. Though the fundamental $\{200\}$ reflection of the MoN-TiN ASF was usually superposed on the intense substrate $\text{MgO}\{200\}$ reflection and could not be distinguished, satellite peaks shown in Fig.2 (D)-(F) indicate the preferred orientation of MoN and TiN $\{100\}$ planes. Some samples were removed by dissolving the MgO substrate in hot HCl and examined by transmission electron diffraction. The expected epitaxial growth with the direction of $\text{ASF}\{100\}/\text{MgO}\{100\}$ was confirmed by the observation of the spot diffraction pattern. Artificial periodicity of ASF's were evaluated by low-angle reflections (Fig.2 (A)-(C)) and middle-angle satellites (Fig.2 (D)-(F)). The shortest periodicity of $[\text{MoN}(0.4 \text{ nm})/\text{TiN}(0.4 \text{ nm})]$ which is nominally composed of two atomic MoN planes and TiN planes each, was successfully formed as shown in Fig.2 (A) and (D). The ASF's composed of monatomic MoN plane (Fig.2 (B) and (E)),

[MoN(0.2 nm)/TiN(3.4 nm)] and monatomic TiN plane (Fig.2 (C) and (F)). [MoN(2.4 nm)/TiN(0.2 nm)] show higher order reflections. Those reflections imply a well regulated artificial superstructure. These results proved that the thickness of each deposited layer was controlled accurately on the atomic scale.

In the case of ASF, it is well known that a single fundamental reflection is observed when the artificial periodicity is short enough and lattice spacings of both stacking layers are very close. Though the fundamental reflections were generally not observed directly as described above, we could calculate the position from their satellite peaks on the basis of a simple step-model /4/. The calculated position represents a compositionally averaged spacing of stacking atomic planes. The averaged lattice constants are plotted against MoN composition (X_{MoN}) in Fig.3. The linear relationship between the averaged lattice constant and the MoN composition indicates that the lattice constant of each MoN and TiN layer does not vary. Therefore each lattice constant is estimated from the intercept ($X_{\text{MoN}}=0.0$ or 1.0) of the straight line. The MoN layers of the ASF prepared under the condition (C) ($T_s=300$ C, $P(\text{NH}_3)=10^{-5}$ Torr, open triangles) are composed of $\gamma\text{-Mo}_2\text{N}$ judging from the intercept at $X_{\text{MoN}}=1.0$. The MoN lattice constant of high- T_s samples (B) ($T_s=500$ C, $P(\text{NH}_3)=10^{-5}$ Torr, crosses) came to be larger, however it is not enough to be B1-MoN. The estimated MoN lattice constant of high- T_s and high- $P(\text{NH}_3)$ samples (A) ($T_s=500$ C, $P(\text{NH}_3)=10^{-4}$ Torr, open circles) is within the range of pre-



cal XRD patterns of MoN-TiN ASF's.

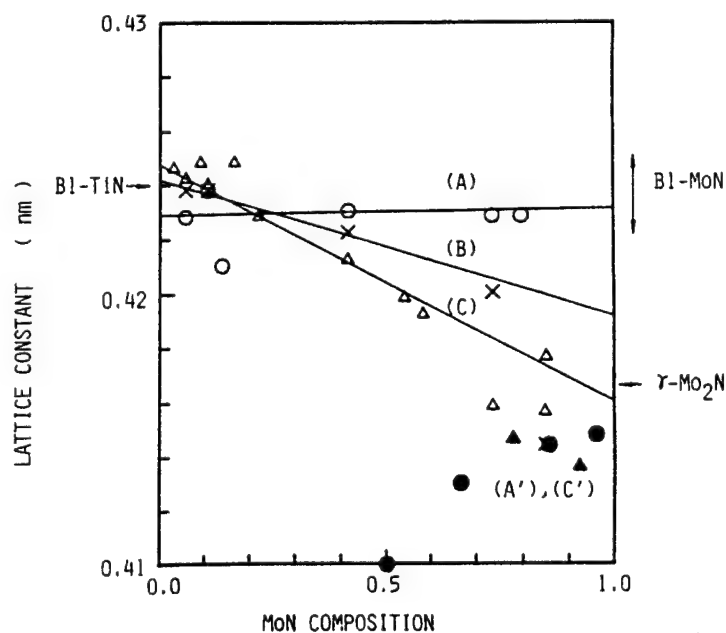


Fig.3 Lattice constant of ASF as a function of MoN composition.

dicted Bi-MoN value /1,2/. All the extrapolations to $X_{\text{MoN}}=0.0$ approximately agree with the lattice constant of Bi-TiN. Closed circles (A') and closed triangles (C') are from the samples which were prepared under the same condition (A) and (C) each and the TiN layers are thinner than 0.4 nm. Those data deviate from the straight lines significantly. In the case of such extremely thin TiN layers, it is considered that the TiN layers shrink to form the coherent TiN/ γ -Mo₂N interface.

SUPERCONDUCTING TRANSITION TEMPERATURES OF MoN-TiN ASF's

Electrical resistance of the samples was measured by a conventional four-probe method. The superconducting transition temperature (T_c) was defined as the mid-point of residual resistance. The relationship between T_c and MoN lattice constant ($a_0(\text{MoN})$) of ASF's is shown in Fig.4. Since the measured lattice constant is an averaged value as mentioned above, the MoN lattice constant is calculated by assuming a linear dependence on the composition. Contrary to the prediction, T_c decreases with increasing of $a_0(\text{MoN})$. The result indicates that the T_c of Bi-MoN is lower than that of γ -Mo₂N. Though several problems such as structural strain and nitrogen may be responsible for the low T_c , the relationship between T_c and lattice constant is considered to be essential.

It is important to distinguish the contribution from impurity phase, because molybdenum nitride has several other superconducting phases such as δ -MoN ($T_c=15$ K), γ -Mo₂N ($T_c=5.5$ K), and bcc-MoN_x ($T_c=1-5$ K). Actually, a single layer film (SLF) of MoN showed some weak XRD reflections derived from impurity phases. While any other XRD reflections were observed for the ASF prepared under the same condition. The T_c of SLF is higher than that of ASF, however the transition width of the SLF is much broader. Those results prove that the ASF method is effective for the preparation of single-phase Bi-MoN.

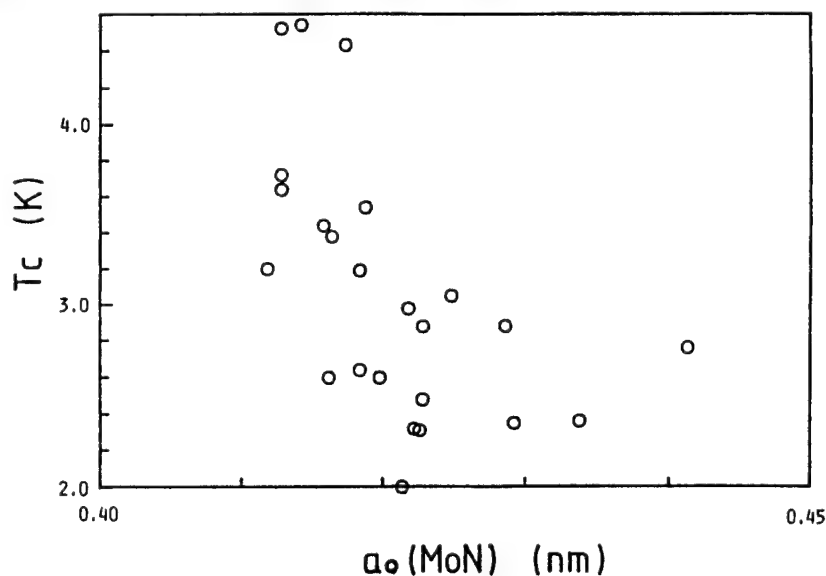


Fig.4 The relationship between T_c and MoN lattice constant ($a_0(\text{MoN})$).

NbN-FeN ASF's

The combination of superconducting nitride and ferromagnetic nitride has been also attempted. Niobium nitride (NbN) and iron nitride (FeN) were deposited alternately in nitrogen atmosphere activated by r.f. plasma. Another deposition apparatus equipped with the r.f. plasma generator was designed in order to promote nitridation during deposition. The base pressure is about 10^{-7} Torr and nitrogen atmospheric pressure during deposition is 10^{-3} Torr. Three XRD patterns are shown in

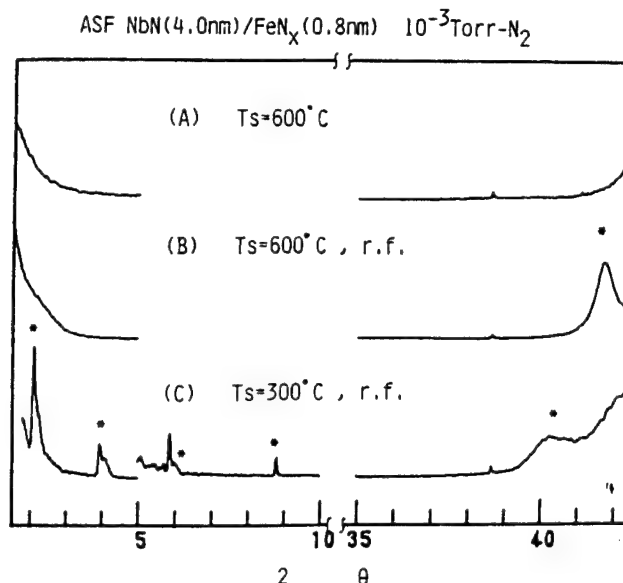


Fig.5 XRD patterns of NbN-FeN ASF's.

Fig.5. No diffraction peaks were observed for the sample prepared in non-activated atmosphere (Fig.5 (A)). The reflections around $2\theta=41^\circ$ in Fig.5 (B),(C) are considered to be B1-NbN{200}. Since any other reflections were not observed without B1-NbN{200} and {400}, B1-NbN{100} planes stacked preferentially. The rocking curves of the reflections were, however, fairly broad. The ASF is considered to have a textured structure with a mosaic structure. Information about the structure of iron nitride has not been obtained yet. The low-angle reflections derived from the artificial periodicity were observed clearly in the case of low-Ts (Fig.5 (C)). The research of optimum preparing condition is under way.

SUMMARY

Artificial superstructured films of MoN and TiN were successfully synthesized using alternate reactive deposition method. The thickness was controlled on the atomic scale. The formation of non-equilibrium B1-MoN single-phase was confirmed under an optimum condition. The ASF's containing B1-MoN layers showed lower T_c than the ASF's composed of γ -Mo₂N layers. A combination of NbN and FeN has been also attempted and the artificial periodicity was confirmed.

ACKNOWLEDGMENTS

The authors would like to thank I.Kojima and N.Fukumoto and N.Nomura for fruitful discussions.

REFERENCES

1. Z.You-xiang and H.Show-an, Solid State Commun., 45, 281 (1983)
2. W.E.Pickett, B.M.Klein, and D.A.Papaconstantopoulos, Physica, 107B, 667 (1981)
3. D.A.Papaconstantopoulos, W.E.Pickett, B.M.Klein, and L.L.Boyer, Phys.Rev.B, 31, 752 (1985)
4. S.Shinjo and T.Takada, Metallic Superlattices (Elsevier Science Publisher, Amsterdam, 1987)

MICROSTRUCTURE AND PROPERTIES OF HOT-WORKED $\text{YBa}_2\text{Cu}_3\text{O}_{7-x}$ SUPERCONDUCTING WIRE

Song J. T., Chang H. J., Akihama R.*

Dept. of material Engineering
Hanyang University,

17 Haengdang-dong, Seongdong-gu, Seoul 133-791, Korea

* Chichibu Cement Co., LTD., Japan

Commence the first

We report on a powder-in-tube method using hot extrusion plus hot drawing to prepare a Y-Ba-Cu-O oxide superconducting wire and on the relation between microstructure and properties of $\text{YBa}_2\text{Cu}_3\text{O}_{7-x}$ superconductor. Sample of $\text{YBa}_2\text{Cu}_3\text{O}_{7-x}$ oxide superconductor was first prepared by the solid state reaction and wire samples of $\text{YBa}_2\text{Cu}_3\text{O}_{7-x}$ superconductors were fabricated by hot extrusion plus hot drawing. It is confirmed that there was no difference in the crystal structure of $\text{YBa}_2\text{Cu}_3\text{O}_{7-x}$ compound between bulk sample and the core compound in wire samples. Furthermore, hot working brought not only a considerable promotion of (00 ℓ) preferential crystal orientation of superconducting wire, but also the larger grain structure and the reduction of porosity in microstructure, with the result that the dense structure was formed with enhanced connectivity of each grain. It seems the increase of J_c in hot-worked wire ^{is} attributed to these microstructural combined effects.

Since Bednorz and Muller[1] reported possible high T_c Superconductivity in the La-Ba-Cu-O System, oxide superconductors have been the subject of tremendous research and development interest throughout the scientific groups. Thereafter, superconducting compounds with high critical temperature and critical magnetic field such as Y-Ba-Cu-O[2] and Bi-Sr-Ca-Cu-O Oxides[3] were found and they became of great interest among many scientists because of their own feasibility for the application of superconductors in the field of powder transmission lines, superconducting magnets, electronic devices, and so on. These superconducting compounds, however, need to be fabricated into fine wires or thin films for the practical applications. In general, oxide superconducting materials are mechanically hard and brittle and not easily drawn into desirable fine wires or filament forms. Some possible fabrication method have recently been proposed and demonstrated, for example, a powder-in-tube method, a powder-coating method, or a melt-textured growth technique. But, it is likely that all they are no more than outpost techniques for the future commercial process for obtaining oxide-superconducting wires or filaments. In this paper, we report on a powder-in-tube method using hot extrusion plus hot drawing to produce a Y-Ba-Cu-O oxide superconducting wire and on the relation between microstructure and properties of $\text{YBa}_2\text{Cu}_3\text{O}_{7-x}$ superconductor.

Experimental

Sample of $\text{YBa}_2\text{Cu}_3\text{O}_{7-x}$ oxide superconductor was first prepared by the solid state reaction method using Y_2O_3 , BaCO_3 and CuO powders with high purity (99.99%). Mixtures of these powders were calcined in air at 910 °C for 16 hours two times and were reground into powders. The powder was pressed in a die under the pressure of 1 ton/cm² to prepare disk-pellets with 20mm in diameter and 2 mm in height, and the disk-pellets were sintered at 900 °C for 24 hours in oxygen atmosphere. After then, sintered compacts were cooled in the furnace and held at 600 °C for 3 hours in flowing oxygen before being slowly cooled in the furnace to room temperature. Wire samples of $\text{YBa}_2\text{Cu}_3\text{O}_{7-x}$ superconductors were fabricated by hot working of the powder-in-tube.

That is, the sintered $\text{YBa}_2\text{Cu}_3\text{O}_{7-x}$ compound powder was packed into 20 ϕ silver tube. The initial diameter ratio of compound core to Ag tube was 1/2. This composite was hot-extruded into the outer diameter of 5 mm at 950°C and subsequently drawn into 4.0, 3.45, 2.55, 1.45, and 1.2 mm at 540°C, respectively. After hot working, all drawn-wire samples were heated at 900°C for 16 hours and then held at 600°C for 2 days in oxygen atmosphere followed by cooling in the furnace. X-ray diffraction analysis was carried out for the crystal structure of hot-worked $\text{YBa}_2\text{Cu}_3\text{O}_{7-x}$ compounds and their microstructures were observed by optical, polarized, and scanning electron microscope. The critical temperature (T_c) and critical current density (J_c) were measured using a standard four probe technique without removing Ag sheath of wire samples and the criterion for the critical current was 0.1 $\mu\text{V}/\text{cm}$.

Result and Discussion

Fig.1. shows X-ray diffraction analyses of the superconducting compound in the wire samples fabricated by hot working and heat-treated at 900°C after hot working, in which (a) indicates a diffraction pattern of sintered bulk sample, (b) a pattern of core compound in the wire sample hot-drawn into 3.45 mm, and (c) a pattern of hot-drawn into 2.55 mm after hot extrusion.

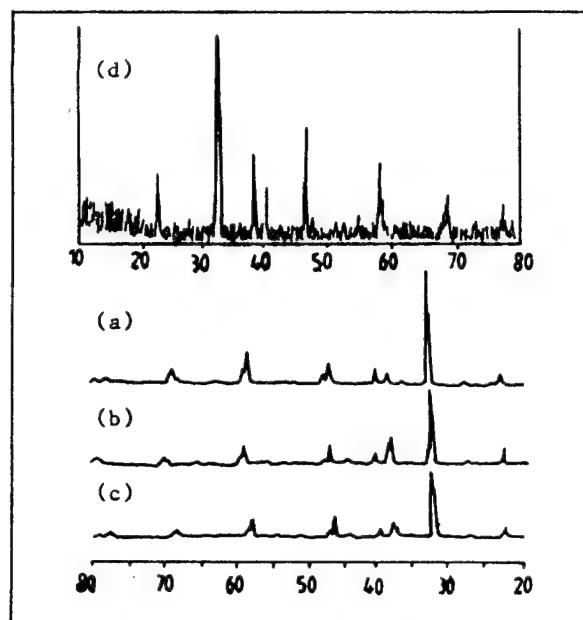


Fig.1. X-ray diffraction patterns of (a) bulk sample, (b) hot drawn (3.45 ϕ), (c) hot drawn (2.55 ϕ), (d) forged sample

They show the Cu-O based oxygen deficient perovskite compound structure and there was no difference in the X-ray diffraction patterns between bulk sample and the core compound in the wire samples. Therefore, it is confirmed that the initial crystal structure of the $\text{YBa}_2\text{Cu}_3\text{O}_{7-x}$ compound in the wire was maintained through the hot working. Furthermore, it should be noted that they show a considerable promotion of (00 l) preferential crystal orientation, such as at (003), (005), and (006) peaks. According to this result, we are confident that significantly higher grain alignment or texture of $\text{YBa}_2\text{Cu}_3\text{O}_{7-x}$ superconducting compound in the wire samples will be obtained if we have hot extrusion and hot drawing with a bigger extrusion ratio and a more suitable grain structure. We believe the extra peaks near $2\theta = 38^\circ$ and 44° are ones due to Ag powder mixed when we raked out the core compound from the finished wires for the preparation of X-ray diffraction powders.

Fig.2. shows the electrical resistance vs. temperature curves for the samples sintered and hot-worked. Curve (a) is for the bulk sample before hot extrusion, (b) is for a sample hot-extruded into 5 mm and (c) and (d) are for wire samples hot-drawn into 3.45 mm and 1.2 mm after hot extrusion, respectively. The on-set temperature of bulk sample was 95 K, but the ones of wire samples were 92 K and 91 K. On the other hand, the off-set temperature of bulk sample and wire samples are 90 K, 80 K, and 84 K, respectively. These large transition temperature width (ΔT_c) in the wire samples may be ascribed to the oxygen deficiency resulting from incomplete oxygen diffusion due to Ag sheath and partially ascribed to incomplete optimization of crystal structure of hot-worked superconducting compound.

Bulk samples had the typical microstructure of stoichiometric compound. It exhibited plate-like or rectangular grains and randomly oriented microstructure with an average grain diameter of about 5 μm . Fig.3. shows microstructures of hot-extruded wire superconductors.

They had the similar microstructure to sintered bulk sample, but their grain sizes increased with increasing the cross-sectional area reduction of hot working. This may be attributed to the enhancement of atom diffusion and reduction of porosity resulting from the increment of the total amount of working. In fact, the increase of reduction ratio of hot working not only reduced porosity, but also enhanced grain growth. Porosity was measured on micrographs by linear analysis [4]. The measured porosities of each wire sample having the diameter of 5, 3.45, 2.55, and 1.2 mm were 17.2, 14.4, 13.3, and 12.7%, respectively.

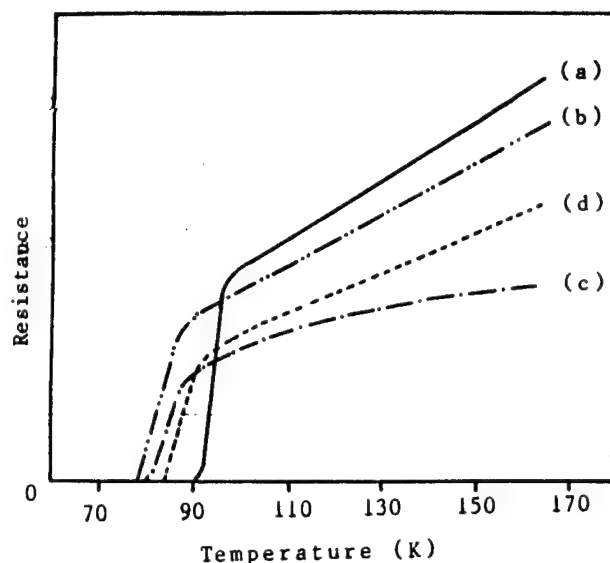


Fig.2. Resistance-temperature Curves of (a) Sintered only, (b) hot-extruded sample(5 ϕ) (c) hot-drawn sample (3.45 ϕ), (d) hot-drawn (1.2 ϕ)

While, the critical current density J_c also increased as the cross-sectional area reduction of hot working becomes larger. The J_c at 77 K and in zero field of Ag-sheathed wire hot-drawn into 1.45 mm and 1.2 mm in outer diameter were roughly 114 A/cm² and 162 A/cm², respectively. These results may be explained by the larger grain structure and the reduction of porosity in microstructure.

As Ekin[5] reported, there are four possibilities for optimizing the transport current density of YBa₂Cu₃O_{7-x} superconductors. They are grain alignment, reduction of number of grain boundaries, increased area for current transfer, and reduction of non-high-T_c phase at grain boundaries.

Although we expected the development of grain alignment or texture through hot extrusion and hot drawing of YBa₂Cu₃O_{7-x} compound in this experiment, we could get only a little, as shown in X-ray diffraction analysis (Fig.1). However, as shown in Fig.3, the grain sizes of superconducting wire fabricated by hot extrusion and hot drawing were larger than bulk samples. From their results, we suggest that hot working brings the formation of fewer grain boundaries as well as the formation of dense structure with enhanced connectivity and the foregoing J_c improvement by hot working is attributed to the combined effect of them. But, we ignored, in this experiment, the effect of crack occurrence on J_c , which occurs from the difference of thermal expansion between Ag sheath and superconducting core materials during heat treatment, because their harmful effect might be outweighed by the beneficial effect for the transport current with the increment of contact area between grains caused by the grain growth and reduction of porosity volume mentioned above.

Conclusion

YBa₂Cu₃O_{7-x} superconducting wire samples with silver sheath were successfully fabricated through hot extrusion at 950°C with the diameter of 5 mm and

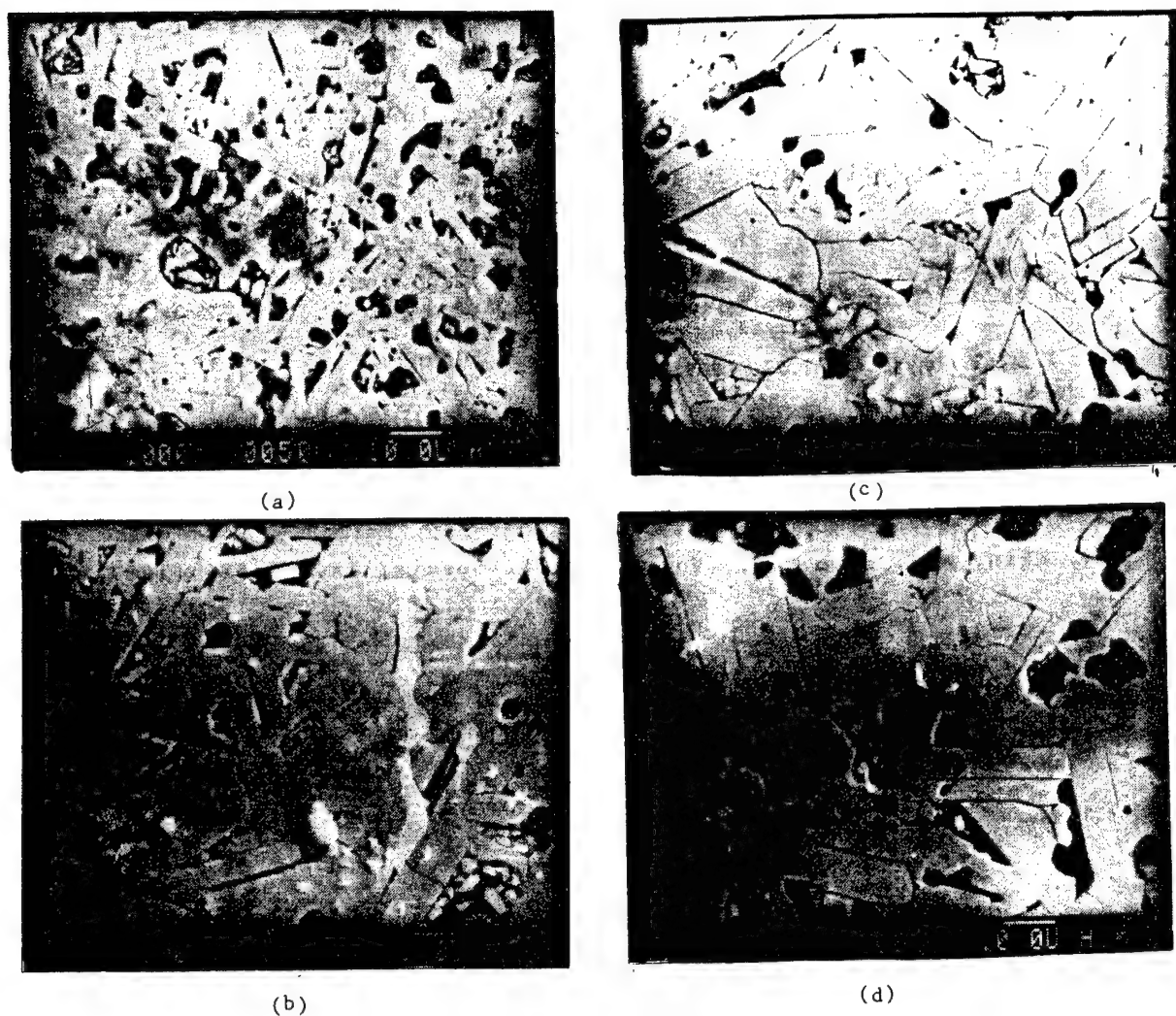


Fig.3. SEM Photographs compared at different diameters with same magnification($\times 1000$)

(a) 5.0 ϕ , (b) 3.45 ϕ , (c) 2.55 ϕ , and (d) 1.2 ϕ

then hot drawing at 540°C with the diameter of 4.0, 3.45, 1.45, 1.2 mm, respectively. Through the X-ray diffraction analysis, it is confirmed that there was no difference in the crystal structure of $\text{YBa}_2\text{Cu}_3\text{O}_{7-x}$ compound in the wire samples fabricated by hot working consisting of hot extrusion and hot drawing.

Furthermore, hot working brought a considerable promotion of (00 $\bar{1}$) preferential crystal orientation of $\text{YBa}_2\text{Cu}_3\text{O}_{7-x}$ superconducting wire samples, such as at (003), (005), and (006) peaks. It is found that the larger grain structure and the reduction of porosity in microstructure through hot working have helped in raising critical current density (J_c).

The two on-set temperatures, one bulk sample and the other hot-drawn wire, had almost similar values of above 90 K, but the off-set temperature of hot-drawn wire were lower than those in the bulk samples.

REFERENCES

1. J.G. Bednorz and K.A. Muller, Z. phys. B64, 189 (1986)
2. M.K. Wu, J.R. Ashburn, C.J. Torng, P.H. Hor, R.L. Meng, L. Gao, Z.L. Huang, Q. Wang, and C.W. Chu, Phys. Rev. Lett., Vol. 58, 908 (1987)
3. H. Maeda, Y. Tanaka, M. Fukutomi and T. Asano, Jpn. J. Appl. Phys., Vol. 27, L209 (1988)
Commence the first
4. G. F. Vander Voort, Metallography, Principles and Practice, Ch 6. McGraw-Hill, New York. 1984
5. J.W. Ekin, Adv. Ceram. Mat., Vol. 2, No 3B, Special Issue, 586 (1987)

Properties of Carbon Ceramic Composite Made by Pressureless Sintering

Yoshio Takashima*, Ichitaro Ogawa**, Mitsuhiro Furukawa*, Hisayoshi Yoshida**

*Nippon Tungsten Co. Ltd. Shimizu 2-20-31, Minami-ku, Fukuoka, 815 Japan.

**Government Industrial Research Institute, Kyushu. Tosu-shi, Saga-ken 841, Japan.

I Introduction

The pressureless sintering method for carbon ceramic composites was developed by the Government Industrial Research Institute, Kyushu. This method uses a process that involves raw material mixing and grinding, compacting, and pressureless sintering. Carbon Silicon Carbide (SiC) - Boron Carbide (B_4C) composite, which is one of the carbon ceramic composites made by this process, has high mechanical strength and low combustibility. In this paper we report the physical properties of this material, the effects of the manufacturing conditions, incombustibility, and machinability.

II Experimental Procedure

Crushed raw coke, SiC, and B_4C was mixed and ground. The composition was C-(0 to 30)vol%(SiC+ B_4C), SiC to B_4C was 1:1.38 by weight, for example C-20%(SiC+ B_4C) = C-15.5wt%SiC-20wt% B_4C . The mixed powder was compacted and sintered at various temperatures for an hour in an Ar atmosphere.

We measured the transverse rupture strength (TRS), shore hardness, and other physical properties. Incombustibility was evaluated by weight loss after oxidation in an electric furnace. For the machinability test the workpieces (ϕ (70-30) x 200) were turned in a lathe with cemented carbide (K10), CBN, and diamond inserts. Tool life was judged by flank wear length. The insert type was SNGN432, and cutting angles were (5° 5° -5° -5° 15° 15° 0.8).

III Results

1. Physical Properties

The physical properties of C-SiC- B_4C composite (C-20vol%(SiC+ B_4C)) are shown in Table 1 and are compared with other carbon materials. C-SiC- B_4C composite has high strength and high coefficient of thermal expansion because of its low porosity, and has low thermal conductivity due to

Table.1 Physical Properties of C-SiC-B₄C Composite.

	C-SiC-B ₄ C composite	Common carbon	Common graphite	High density isotropic graphite
Specific gravity	1.95~2.05	1.7	1.6	1.8
Shore hardness	70~100	62	25	54
Transverse rupture strenyth(kg/mm ²)	15~20	4.7	2	4
Thermal expansion coefficient($\times 10^6$ /deg)	4.5~5.5	3.6	2.0	4.6
Thermal conductivity (Cal/cm \cdot deg \cdot sec) (Kcal/m \cdot deg \cdot hr)	0.04~0.08 14.3~28.6	0.056 20	0.36 130	0.28 100
Resistivity (m Ω \cdot cm)	1~10	—	0.85	1.1
Thermal shock resistance, $\Delta T(^{\circ}\text{C})$	600	—	>1000	>1000

less graphitization. This composite was nearly isotropic for all properties.

2. Effects of manufacturing conditions

1)

Fig. 1 shows the effect of sintering temperature on transverse rupture strength. Pure C showed maximum transverse rupture strength at 1400°C. In contrast, C-SiC-B₄C was at its minimum strength at 1400°C, and then increased at increased sintering temperature. It seems that above 1400°C the decrease in the pure C transverse rupture strength is caused by the progress of graphitization, and the increase for C-SiC-B₄C is caused by sintering of (SiC-B₄C) powder. The decrease in rupture strength of C-SiC-B₄C below 1400°C is probably caused by degradation of interface strength between C and SiC due to CO gas and SiO which are made by the reaction between the matrix carbon and SiO₂ on the surface of the SiC particles.

Although it is not dealt with here, the transverse rupture strength increased and the shore hardness decreased with the increase of ceramic content, and we also observed the significant effect of compacting pressure on properties.

3. Incombustibility

2)

Fig. 2 illustrates the incombustibility of C-SiC-B₄C composite. 5%vol or more (SiC-B₄C) showed less weight loss due to oxidation because of the reaction of SiC and B₄C with atmospheric oxygen to form a thin film of SiO₂-B₂O₃ boron silicate glass on the surface which prevented the passage of oxygen and thus oxidation.

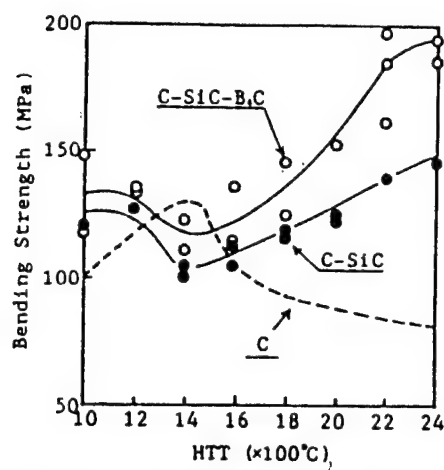


Fig.1 Change of transverse rupture strength of composites and pure carbon solid with sintering temperature.

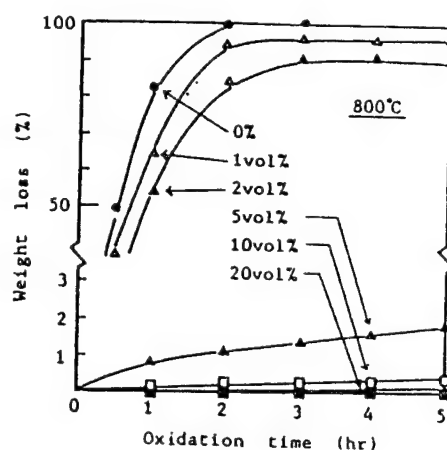


Fig.2 Changes with weight loss with oxidation time at 800°C of the C-SiC-B₄C composite with various initial contents of the carbide.

4. Machinability

For the machinability test, the workpieces contained 0 to 30vol%(SiC-B₄C) and were sintered at 1400°C or 2050°C .

Fig. 3 shows flank wear (VB) against cutting time (T) for cemented carbide cutting of C-SiC-B₄C composite. With the 1400°C sintered workpieces, the life of the inserts reached a minimum at 20vol%. With low ceramic content, the life of inserts cutting 2050°C workpiece was longer than for the 1400°C sintered workpieces due to the progress of graphitization. However, the ceramic content had more influence on lifetime, and the lifetime was shorter with the 2050°C sintered workpiece with 30vol% ceramic content.

The cutting speed (V) against lifetime (T) for the cemented carbide insert is shown in Fig. 4. Here, the exponent 'n' of Taylor's formula is 1, which means the life of the insert has no relation to the cutting speed, but only to the cutting length. From this result it is clear that insert wear is abrasive wear.

We also cut with CBN and diamond insert. Both inserts had a much longer life (over 20 minutes with a cutting speed of 120m/min) than cemented carbide insert. Their lives were too long to be considered in this test. Feed had to be less than 0.1 mm/rev because of tearing of the machined surface.

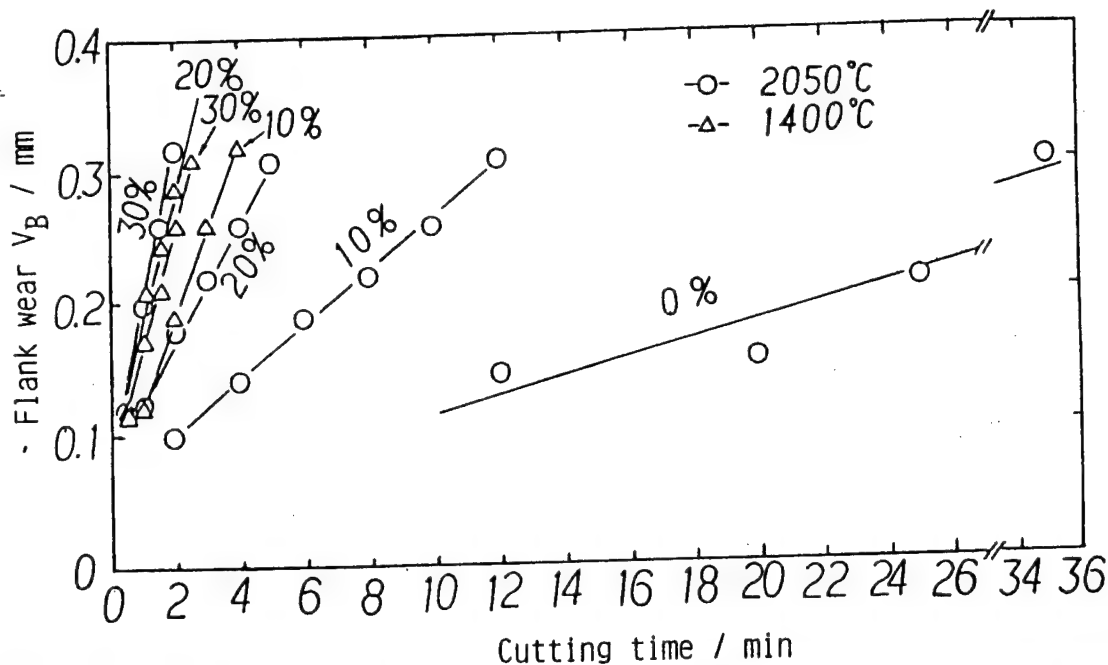


Fig.3 Comparison of machinability of C-SiC-B₄C composite, cutting with cemented carbide(K10) insert. Cutting conditions : $V=30\text{m/min}$, $d=1.0\text{mm}$, $f=0.1\text{mm/rev}$

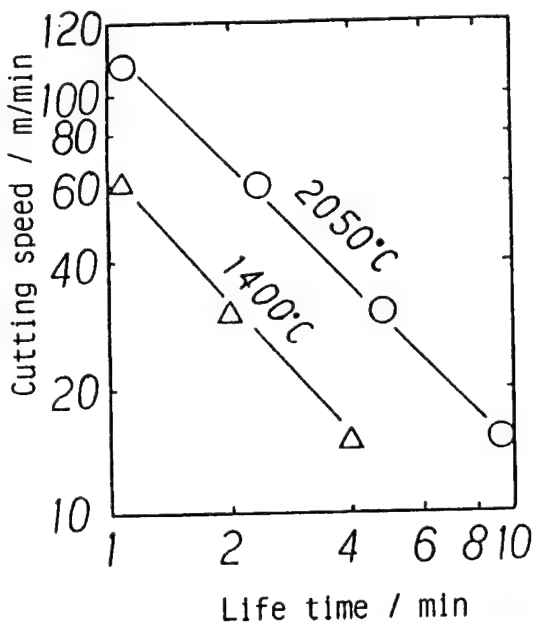


Fig.4 Taylor's tool live diagram of cemented carbide(K10) insert, cutting C-20vol%(SiC+B₄C) composite sintered at 1400°C or 2050°C.

Photo 1 shows two typical wear patterns of cemented carbide. Uniform wear was found after cutting 1400°C sintered workpieces. In contrast, grooved wear at the minor flank and boundary wear at the major flank were observed in 2050°C sintered workpieces. This type of boundary wear is commonly observed in the cutting of tough materials. As discussed above, an increase in ceramic content of the 1400°C workpiece had little effect on tool life, but an increase in the 2050°C workpiece dramatically reduced tool life. From these observations, it is thought that only the coke content sintered at 1400°C, with essentially no ceramic grain sintering, while at 2050°C the ceramic grains also sintered to create strong bonding.

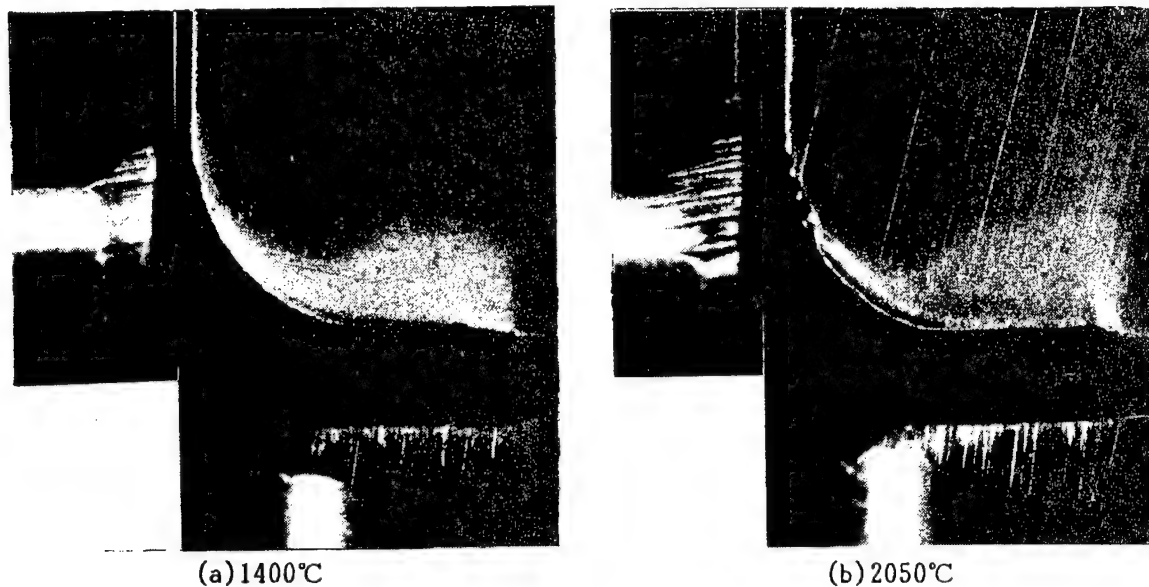


Photo.1 Wear pattern of cemented carbide insert after cutting C-20vol%(SiC+B₄C) composite sintered at (a)1400°C or (b)2050°C.

IV Conclusions

1. The effect of sintering temperature, ceramic content, and compaction pressure on the properties of C-SiC-B₄C composite is evident.
2. C-SiC-B₄C composite is incombustible in an air atmosphere because of a thin film of SiO₂-B₂O₃ boron silicated glass forms on the surface.
3. Machining of C-SiC-B₄C is possible using a small feed and cemented carbide, CBN and diamond inserts. The life of the cemented carbide insert decreases with the increase in ceramic content, but it is not related to cutting speed.
4. The effect of ceramic content on machinability with cemented carbide is more evident in 2050°C sintered workpieces than with 1400°C sintered workpieces, and cutting 2500°C sintered workpieces gave rise to grooved wear in the minor flank.

V References

- (1) Ogawa et. al. : "Preparation of Carbon-Ceramic Composite Materials by Use of Raw Coke (Part 3)", *Yogyo-kyoukai-shi*, 93[10](1985), 612.
- (2) Ogawa et. al. : " ibid (Part 4), Oxidation Resistance of C-SiC-B₄C composite in Air", *Yogyo-kyokai-shi*, 94[4](1986), 409.

The Grain-Growth Behavior and Mechanical Properties of Al₂O₃-TiC Composite

H.S. Song and Y. H. You

Ssang-Yong Research Center
P.O.Box 12 Yuseong, Daejeon, KOREA

The grain-growth behavior and mechanical properties were investigated in Al₂O₃-30 TiC composite according to the sintering temperature, time and schedule. An earlier productions of Al₂O₃-TiC composite were made by hot-pressing because of the existence of sintering barrier which was known as the gas formation between Al₂O₃ and TiC. But in this study, above reaction was inhibited by embedding powder having same composition with the specimen in Ar atmosphere. This study describes the grain-growth behavior and mechanical properties in respect of average grain size and porosity in Al₂O₃-30 TiC system being used as the ceramic cutting tool. All the sintered Al₂O₃-30 TiC specimens being more than 96% TD could be fully densified by HIPping at 1600°C, 0.5 hr, 1500 bar in Ar atmosphere.

1. Introduction

During the past few years, ceramic materials have been used as the cutting tool because of the high wear resistance and cutting ability. But these ceramic cutting tools intrinsically have the weak properties in toughness and reliability. Recently, a lot of research have been focused on the development of Si₃N₄-based material, CBN and particle reinforced composite such as Al₂O₃-TiC materials which are generally used as the cutting tool for hard metal cutting.

All commercial Al₂O₃-TiC cutting tool are reportedly produced by hot pressing, but these materials can be made by sin/hip process with the appearance of easy sinterable Al₂O₃ powder and the addition of sintering additives. Although, a lot of reports were published to improve the sintering and mechanical properties of Al₂O₃-TiC materials, there were few reports concerning the sintering and grain growth behavior according to the sintering condition. This study investigated the sintering behaviors and the mechanical properties of Al₂O₃-30 TiC composite being generally used for cutting tool materials according to the sintering temperature, time and schedule.

2. Experimental Method

2.1 Raw Materials

Raw materials being used in this study were Al₂O₃ made by Sumitomo Co. grade AES 11C with 0.4 μm average particle size and TiC made by Hermann C. Strak Co. with 0.8 μm average particle size.

2.2 Preparation of Specimen

The powders for specimen were mixed at a ratio of (wt %) 70 Al₂O₃:30 TiC and ball milled in Al₂O₃ jar with methanol for 24 hours.

The mixed slurry was dried and uniaxially pressed at 300 kg/cm² and uniaxially pressed at 300 kg/cm² and isostatically pressed at 2000 kg/cm².

Sintering was conducted in graphite furnace using graphite crucible. Sample was embedded with powders having the same composition with sample and sintered in Ar atmosphere (20/min). In this study the weight loss was observed less than 1 wt%. Such a small weight loss was highly effective on densification of Al₂O₃-30 TiC system. The sintered specimen was cut and polished with diamond paste and etched in hydrogen atmosphere. The average grain size was measured with image analyzer (KIT 500, PIAS) in terms of Heywood diameter

3. Results and Discussion

3.1 Sintering Behavior and Grain Size

Table 1. represents the whole sintering conditions and results.

Table 1. Sintering Conditions and results

EXP. No.	Sin. Temp (°C)	Holding Time (min)	Heating Schedule (°C/min)	Average Density [*] (g/cm ³)	Hardness (kg/mm ²)	Toughness (MPaM-1/2)	Grain Size ^{***} (μm)
AT 1	1750	5	20 °C/min	3.75	1160		0.96
AT 2	1800	"	"	3.88	1340	3.29	1.10
AT 3	1850	"	"	4.06	1670	2.89	1.39
AT 4	1900	"	"	4.16	1750	2.71	1.59
AT 5	1950	"	"	4.18	1740	2.63	3.55
AT 6	1850	0	"	3.94	1400	3.12	1.14
AT 7	"	30	"	4.15	1760	2.66	1.65
AT 8	"	60	"	4.15	1800	2.54	1.74
AT 9	"	120	"	4.17	1780	2.54	1.88
AT10	"	240	"	4.17	1770	2.63	1.89
			^{**}				
AT11	"	5	40 °C/min	4.10	1680	2.81	1.50
AT12	"	"	10 °C/min	4.04	1590	2.86	1.56
AT13	"	"	5 °C/min	4.02	1450	2.90	1.71

* Density was measured in water immersion method

** For AT 11, AT 12, AT 13, the indicated heating schedules are from 1100°C to 1850°C and the heating schedules for less than 1100 °C is 20°C/min

*** Heywood diameter, evaluated by Image Analyzer

Fig. 1 shows the density variation and grain size according to the sintering temperature. Generally, Al₂O₃-TiC composite was known as the difficult material to densify only with increasing the sintering temperature as the TiC contents increase up to 30 wt%. (2)

But, in this study, a group of samples with 99% TD density (true density was evaluated from lever rule of mixture) were obtained. However, it was unreasonable to densify above 1950 °C because of the vaporization of Al₂O₃ from the surface of specimen.

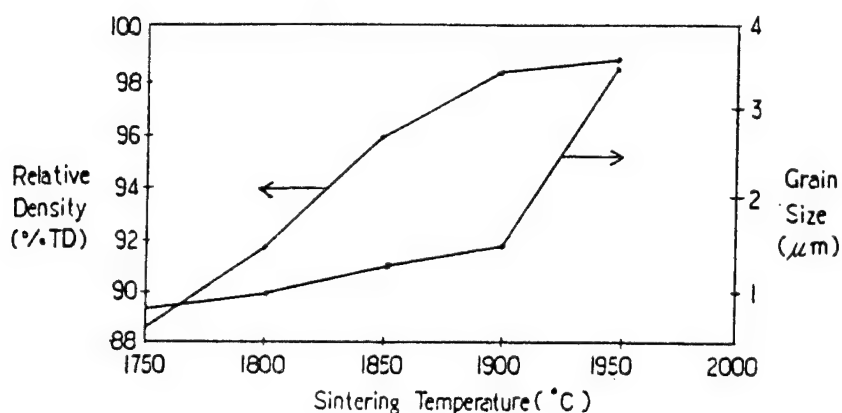


Fig. 1. Relative density and average grain size of Al_2O_3 -TiC composite according to sintering temperature (Table 1. AT1 ~ AT5)

On the other hand, the coarsening rate of alumina grain was significantly higher above 1900 °C for the same temperature gradient. Many explanations for the grain-growth inhibiting effect of TiC in Al_2O_3 -TiC composite were based on the dragging effect of secondary particle, TiC. Therefore, if the phenomena of congregation of TiC particles occur during sintering, there will be reduction of dragging effect of alumina grainboundary and higher grain growth results. Fig. 3 shows the above phenomena of congregation of TiC particles.

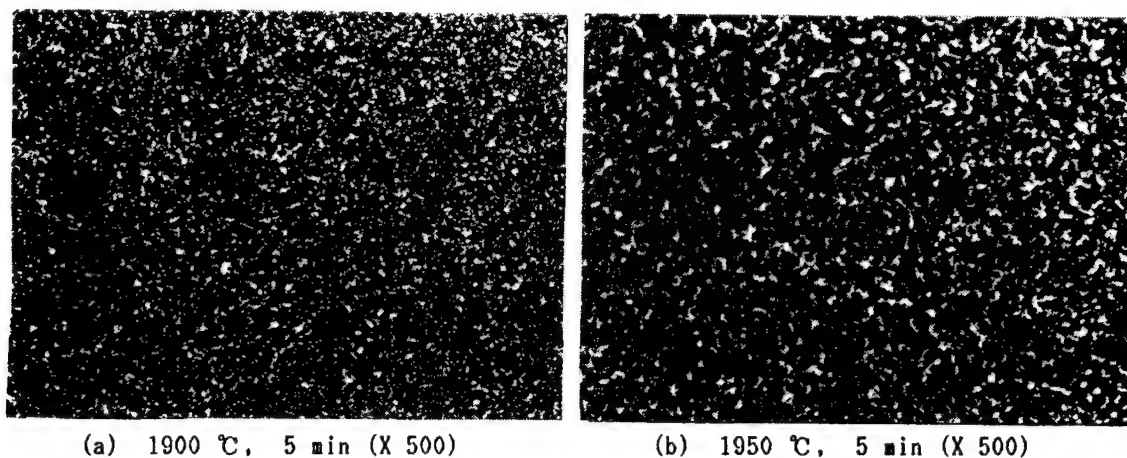


Fig. 3. Optical microstructure of Al_2O_3 -TiC according to the sintering temperature. The average grain size is (a) 1.6 μm (b) 3.5 μm

Fig. 4 shows the grain size variation according to the sintering time.

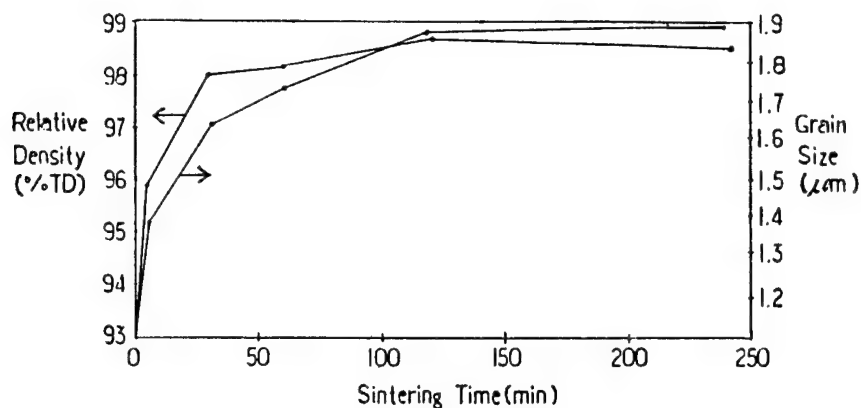


Fig. 4. Density and grain size of sintered $\text{Al}_2\text{O}_3\text{-TiC}$ according to the sintering time at 1850°C (Table 1, AT6~AT10)

The time dependence of grain growth could be described as following relation ship.

$$\{G(T)\}^n - \{G(0)\}^n = k_1 t \quad \text{-----} \quad (1)$$

$G(t)$: Average grain size at time t .

k_1 : Temperature dependent growth-rate constant

$G(0)$: Initial grain size

Generally, the value of n was known as $2 \sim 3$ (6) for the pure alumina grain growth, however the value of n was estimated approximately as 10 in $\text{Al}_2\text{O}_3\text{-30 TiC}$. This higher value could be considered as the result of inhibition of alumina grain growth by secondary TiC particle. (7)

The grain-growth of the $\text{Al}_2\text{O}_3\text{-TiC}$ composite was also dependent on the sintering schedule (Fig.5). The higher heating rate, the higher density and the smaller grain size results.

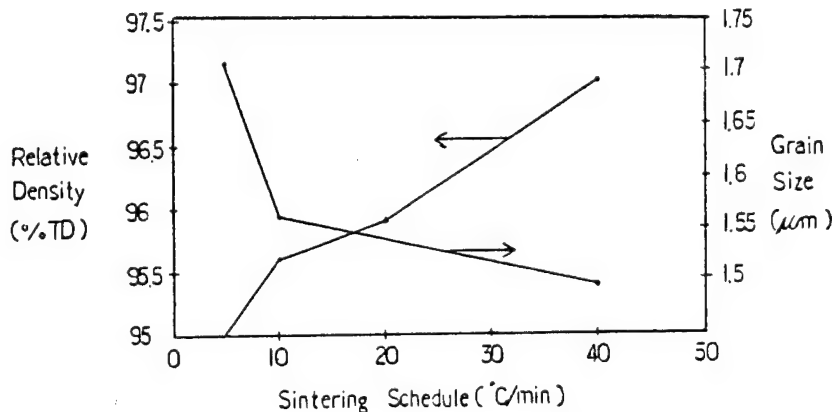
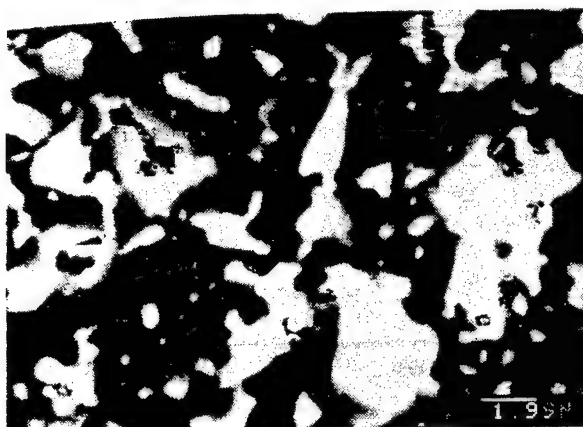
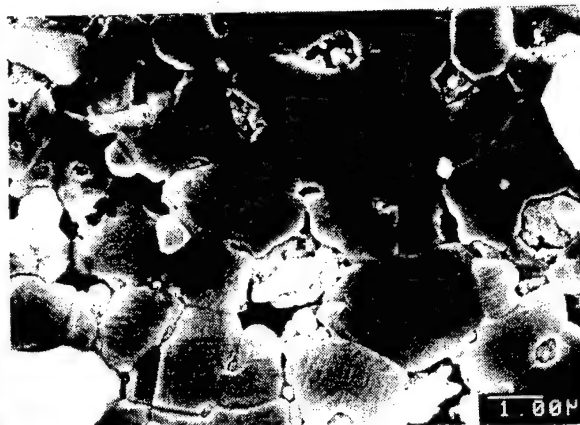


Fig. 5. Density and grain size variation at 1850°C 5 min, according to sintering schedule.

This experimental result could be explained in terms of evolution of gas phase reaction products between Al_2O_3 and TiC. As the heating rate increase, the gas reactions are suppressed and the higher density and smaller grain size can be obtained. Lee and Borom (3) reported that the gas phase was the Al_2O and CO gas and developed around the TiC particle and remained as the pore shown in Fig. 6.



(a) polished section (X 5,000)



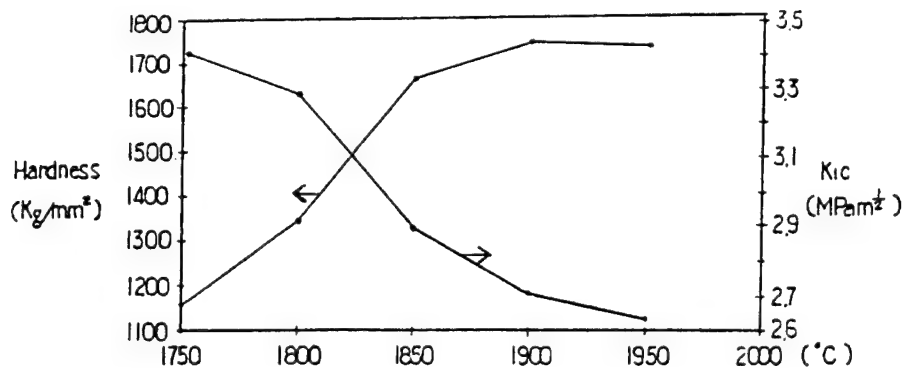
(b) etched section (X-10,000)

Fig. 6. SEM of polished and etched Al_2O_3 -30 TiC composite (rather white parts are TiC)

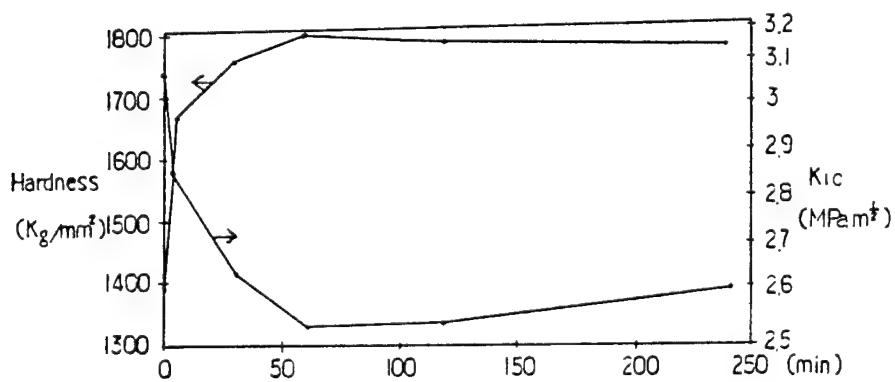
3.3 Mechanical Properties.

The mechanical properties were evaluated using by vicker's indenter. Hardness and toughness were directly dependent on the degree of densification.

Fig. 8 shows the hardness and toughness variation according to the sintering temperature, time and schedule.



(a) sintering temperature (AT1 ~ AT5)



(b) sintering time (AT6 ~ AT10)

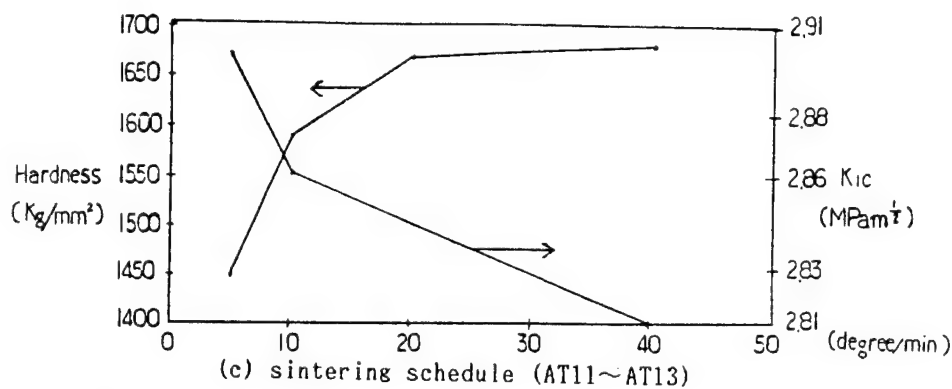


Fig. 8. Hv and K_{IC} variations according to the sintering conditons.

For the specimens having been densified more than 97% TD, the hardness value were not changed but the toughness value (K_{IC}) were decreased as the grain size of the sample increased. This toughness decrease can be considered as the reduction of the effect of crack deflection as the grain size increase (5). The congregation of the secondary TiC particles, which were shown on Fig. 3 also reduce the effect of crack deflection.

All the specimens, which were densified more than 96% TD, could be fully densified by hipping at 1600°C, 30 min, 1500 bar Ar atmosphere. Fig. 9. represents the fully densified specimen by hipping. After hipping, there were no great change in grain size comparing to that of sintered specimens.



Fig. 9. SEM of polished section of Al₂O₃-30 TiC after hipping (rather white is TiC)

4. Conclusion

- (1) The densification of Al₂O₃-30 TiC composite could be obtained up to 99% TD with increasing the temperature in Ar atmosphere with powder bed method. And the resultant weight loss was less than 1 wt%.
- (2) Comparing to the grain size of sintered sample at 1900°C, the grain size of the sintered sample at 1950 °C was very large. This grain growth can be considered as the results of congregation of secondary TiC particles.
- (3) The dependence of the average grain size on sintering time was represented as the kinetic relationship, and the value of n was approximately 10.
- (4) As the heating rate increases, the higher sintering density obtained.
- (5) All the sintered Al₂O₃-30 TiC composites whose density were greater than 96% TD were fully densified by hipping.
- (6) In Al₂O₃-30 TiC system, the hardness and toughness (K_{IC}) were directly dependent on porosity. But the hardness of sintered specimens whose density were greater than 97% TD was less dependent on grain size than toughness. In high density specimens (> 97% TD), the larger the grain size, the lower the toughness resulted.

Reference

- (1) R.P. Wahi and B. Ilschner, "Fracture behavior of composites based on $\text{Al}_2\text{O}_3\text{-TiC}$ ", Jour. of Mat. Sci., Vol. 15, PP 875~885 (1980).
- (2) J. Hojo, H. Yokoyama, R. Oono and A. Kato, "Sintering behavior of $\text{Al}_2\text{O}_3\text{-TiC}$ composite using ultrafine powders", Tran. JSMC, Vol. 9(2), PP 37~44 (1983).
- (3) M. Lee and M. P. Borom, "Rapid rate sintering of $\text{Al}_2\text{O}_3\text{-TiC}$ composites for cutting tool applications", Advanced Ceramic Materials, 3(1), PP 38~44 (1988).
- (4) J. S. Choi, S. Y. Park, D. J. Kim and S. J. Kang, "Sintering and Mechanical Properties of Y_2O_3 added $\text{Al}_2\text{O}_3\text{-TiC}$ composites" J. of Korean Ceram. Soc. Vol. 26(3), PP 438~444 (1989).
- (5) K. T. Faber and A. G. Evans, "Crack deflection processes" Acta Metall., 31(4), PP565~576 (1983).
- (6) K. S. Venkataraman and R. A. Dimilia, "Predicting the grain size distributions in high-density, high-purity alumina ceramics" J. Am. Ceram. Soc., 72(1), PP33 ~ 39 (1989).
- (7) C. S. Smith, "Grains, phases and interfaces : " An interpretation of microstructure", Trans. AIME, 175, PP 345 (1984).

Sintering Behavior and α/β Transformation of Si_3N_4 in $\text{Si}_3\text{N}_4 - \text{ZrO}_2$ Composite

Chong Hee Kim , Jae Ryong Kim and Chae Hyun Lee

Department of Materials Science and Engineering
Korea Advanced Institute of Science and Technology
P.O. Box 131, Cheongryang, Seoul 130-650, Korea

In $\text{Si}_3\text{N}_4 - \text{ZrO}_2$ composite, the effects of zirconia and Y_2O_3 dissolved in zyttrite on the densification and the α/β phase transformation of Si_3N_4 were studied by using hot-pressing of Si_3N_4 with the addition of pure, 3, 6, and 8 mol% Y_2O_3 -doped zirconia. The addition of pure zirconia was not effective to obtain the full density of $\text{Si}_3\text{N}_4 - \text{ZrO}_2$ composite, but almost all α/β phase transformation of Si_3N_4 occurred through $\text{Si}_2\text{N}_2\text{O}$ phase which was the reaction phase between Si_3N_4 and ZrO_2 . On the other hand, Y_2O_3 in zyttrite promoted the densification of composite by diffusing from the zyttrite; the added zirconia itself did not contribute to densifying the composite, but nearly full density (>97%) could be obtained in Si_3N_4 with 5 vol% of 6 and 8 mol% Y_2O_3 -doped zirconia.

Densities of Si_3N_4 with 3 mol% Y_2O_3 -doped zirconia composite could not exceed 80 % of theoretical, even though much zirconia was added. From EDS analysis in AEM, it is suggested that the formation of Y - Zr - Si oxynitride glass in grain boundary occur local equilibrium and restrict the diffusion of Y_2O_3 in zyttrite.

1. Introduction

Silicon nitride is a well known candidate material for heat engine and cutting tools, because of its good thermal shock resistance, high temperature strength and oxidation resistance. Generally, a dense silicon nitride body is fabricated by pressureless sintering, hot-pressing or hot isostatic pressing process with the addition of sintering aids, such as MgO , Y_2O_3 , CeO_2 etc. Also, it has been reported that the dispersion of ZrO_2 is effective on toughening other ceramic matrix, because of its useful tetragonal - monoclinic ZrO_2 phase transformation. Since 1975, several researchers have studied of hot-pressed Si_3N_4 with the addition of monoclinic-zirconia or zyttrite (yttria stabilized zirconia) [1-9]. These $\text{Si}_3\text{N}_4 - \text{ZrO}_2$ composites were shown to be superior to hot-pressed Si_3N_4 with MgO with regard to room and high temperature strength, oxidation resistance and cutting capability [6-8]. And it was reported that toughness could be increased by compressive surface stress resulting from the oxidation of $\text{Si}_3\text{N}_4 - \text{ZrO}_2$ composite [4].

But previous workers were primarily concerned about the beneficial effects

of added zirconia on the properties of Si_3N_4 ceramics, therefore, it has been little known about the details of the role of zirconia in the densification and the α/β phase transformation of Si_3N_4 [4-10]. Moreover, the behavior of Y_2O_3 dissolved in zyttrite has almost been neglected in Si_3N_4 - zyttrite composite.

In the present work, the effects of ZrO_2 and Y_2O_3 dissolved in zyttrite on the densification and the α/β phase transformation of Si_3N_4 were studied by using pure, 3, 6, and 8 mol % Y_2O_3 -doped zirconia powder without any other sintering aids. In order to observe the diffusion behavior of Y_2O_3 in zyttrite, EDS work in AEM (Analytical Electron Microscope) was performed.

2. Experimental procedure

The commercially available Si_3N_4 powder^{*} and 0, 3, 6, 8 mol % Y_2O_3 -doped zirconia⁺ (denoted 0Y, 3Y, 6Y, and 8Y, respectively) powders were used to prepare the mixtures of Si_3N_4 and 5, 10, 15, 20, and 30 vol % of various zirconia. The mixtures were centrifugally mixed in acetone for 2 h using zirconia balls and jar[&]. For increased uniformity of mixing, these mixtures were again vibratively mixed[§] for 10 min in teflon coated container with zirconia balls, and then dried in oven.

The dried mixtures screened to - 60 mesh were hot-pressed in a tungsten mesh heater furnace^{**} using BN coated graphite die (2cm in ID). One atm N_2 atmosphere was maintained during hot-pressing, which was done at 1750°C and 35MPa.

Microstructural characterization of the composites was made by scanning electron microscope (SEM)^{***}, and phase identification was performed by x-ray diffraction (XRD)⁺⁺. EDS work in AEM^{&&} was performed to determine the Y_2O_3 content in zyttrite. The electron transparent specimen for AEM was obtained by argon ion bombardment technique^{&&&}. The specimen was thinned from both side with the incident beam angle of 15° at an average voltage of 5 KV. Densities of hot-pressed bodies were determined by Archimedes method, and theoretical density was calculated by the rule of mixture.

* LC-12, H.C. Starck, Berlin, FRG; max 0.7 μm particle size, ratio of α to β is 94 to 3, and contained less than 0.1 wt % free Si.

+ TZ-0 and TZ-3Y, 6Y, 8Y, respectively, Toyo Soda Co., Tokyo, Japan; 160 - 250 Å cryt. size.

& Pulverisette 6, Fritsch, FRG.

§ Spex 8000 mixer/mill, Edison, N.J., USA.

** Model 60 series, Centorr Associate, Inc., Suncook, N.H., USA.

*** ETEC Autoscan, co., Hayward, CA.

++ Rigaku, Japan.

&& Model 200CX, Jeol, Tokyo, Japan.

&&& MIM, Technics Inc., USA.

3. Results and discussion

3.1. Effect of Added Zirconia on the Densification

Pure Si_3N_4 and the mixtures of Si_3N_4 and 5 vol % of 0Y, 3Y, 6Y, and 8Y ZrO_2 were hot-pressed to investigate the effect of zirconia on the densification. Fig. 1 shows the final densities obtained. The additions of only 5 vol % of 6Y and 8Y ZrO_2 increased density upto 97% and 99% of theoretical, respectively. However, the density of pure Si_3N_4 was low (57%), which shows substantial densification did not take place during hot-pressing of pure Si_3N_4 . The density of Si_3N_4 with 5 vol % of 0Y ZrO_2 was higher (71%) than that of pure Si_3N_4 , but not dense enough. From these results, it can be assumed that Y_2O_3 in zyttrite played the dominant role in densification rather than ZrO_2 phase.

Figure 2 shows the density variations of hot-pressed Si_3N_4 - zyttrite composite with the amount of added 3Y, 6Y, and 8Y zirconia. Si_3N_4 with 6Y and 8Y ZrO_2 show high densities (>97%) regardless of the amount of added zyttrite, but the densities of Si_3N_4 with 3Y ZrO_2 can not exceed 80% of theoretical to even the range of 20 vol % of zyttrite addition. These results support the fact that the densification of these composites are mainly affected by the contents of Y_2O_3 in zyttrite. According to Fick's 1st law, the total amount of Y_2O_3

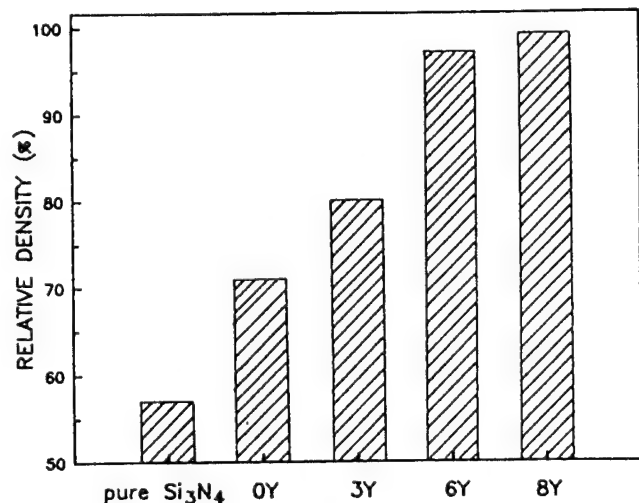


Fig.1. Relative density of hot-pressed Si_3N_4 with 5 vol % of various ZrO_2 and hot-pressed pure Si_3N_4 .

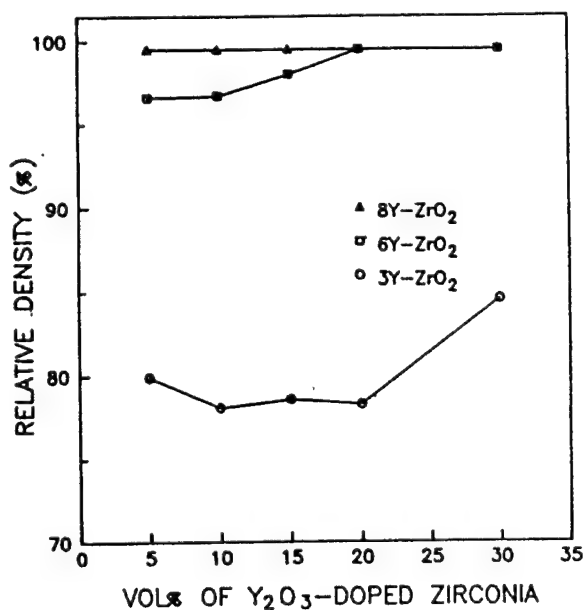


Fig.2. Relative density variations of hot-pressed Si_3N_4 with 3Y, 6Y, and 8Y ZrO_2 composite with the amount of added ZrO_2 .

diffusing out from zyttrite depends on the ΔC (concentration gradient) and temperature. Therefore, significant densification could not sufficiently proceed when 3Y ZrO_2 was added to Si_3N_4 , because ΔC of 3Y ZrO_2 was lower than that of 6Y and 8Y ZrO_2 . So, it is believed that Y_2O_3 diffusing from zyttrite promoted the densification of Si_3N_4 - zyttrite composite, when zyttrite having more than 6 mol % of Y_2O_3 content was added. But the density variations with the amount of added 3Y ZrO_2 could not be simply explained as described above, because Si_3N_4 and zyttrite system involve various chemical reaction processes. This will be discussed in detail in later section.

3.2: Microstructure

Figure 3 shows the fracture surface of hot-pressed pure Si_3N_4 (a), Si_3N_4 -5 vol% of 3Y(b), 6Y(c), 8Y(d) ZrO_2 specimens. Microstructure of hot-pressed pure Si_3N_4 was composed of the agglomerates of equi-axied α - Si_3N_4 grains. In Si_3N_4 -zyttrite composites, more dense microstructures were evolved with the increased

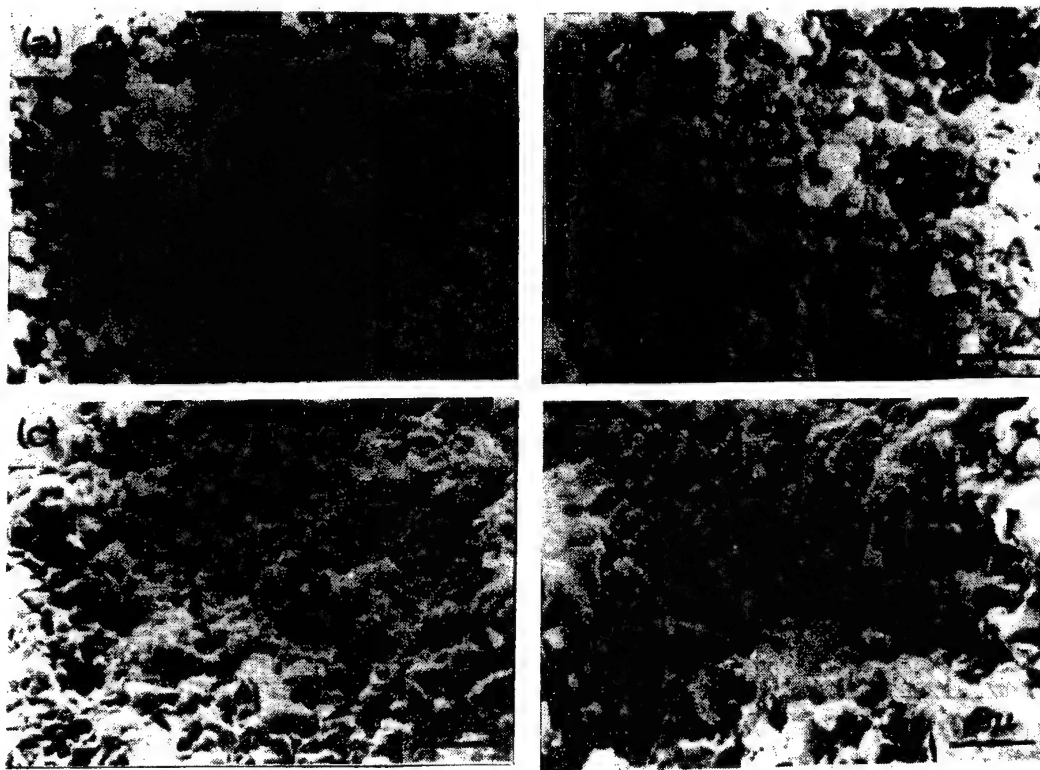


Fig.3. Scanning electron micrographs of the fracture surface of hot-pressed (a) Si_3N_4 and Si_3N_4 - 5 vol% of (b) 3Y, (c) 6Y and (d) 8Y ZrO_2 composite (arrow markings in (c) and (d) indicate the intergranular site of elongated β - Si_3N_4 grains).

content of Y_2O_3 in added zyttrite, and elongated $\beta-Si_3N_4$ grains appeared (arrow markings in Fig.3 (c) and (d) indicate the intergranular fracture sites of elongated $\beta-Si_3N_4$ grains). Zirconia particles located at grain boundaries and in grains can be seen in Fig.4.

3.3. Phase Identification

In order to evaluate the role of the zirconia on the α/β phase transformation of Si_3N_4 , X-ray diffraction analysis was performed. Significant α/β ratio change could not be detected in hot-pressed pure Si_3N_4 ^{\$\$} compared with starting powder ^{\$\$\$} (Fig.5(a),(b)). But in Si_3N_4 - 0Y ZrO_2 composite, most of α phase had transformed to β phase, and ZrO_2 , Si_2N_2O (silicon oxynitride) peaks were detected together (Fig.5 (c)). Zirconia existing in this composite was found to be a mixture of monoclinic and cubic phases. For this cubic phase, "Nitride Stabilized Cubic Zirconia"[10], or in other terms "Zirconium Oxynitride ($ZrO_{2-2x}N_{4x/3}$: $0.25 \leq x \leq 0.43$)"[4,11] has already been reported.

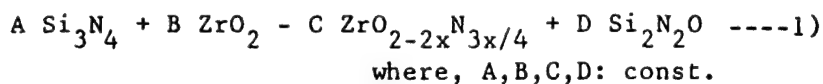
In Si_3N_4 - 0Y ZrO_2 composite, ZrO_2 phase seems to be concerned with the formation of Si_2N_2O phase, and the α/β phase transformation of Si_3N_4 also seems to be caused by this Si_2N_2O phase. If cubic zirconia in Si_3N_4 is present in the form of zirconium oxynitride as early reported[4,10], the formation of silicon oxynitride can be considered as follow.



Fig.4. Scanning electron micrograph of the etched surface of Si_3N_4 - 10 vol % of 8Y ZrO_2 (t and p marking indicate zirconia in Si_3N_4 grains and grain boundary, respectively).

^{\$\$} β fraction was determined by comparing the intensities of $\alpha(210)$ and $\beta(210)$ diffraction peaks, in a manner described by Gazzara[12]. In this case, β fraction was 0.203

^{\$\$\$} β fraction was 0.044, calculated by Gazzara method[12].



;oxygen atoms in ZrO_2 are substituted by nitrogen atoms in Si_3N_4 , and silicon oxynitride phase can be formed. The formation of $\text{Si}_2\text{N}_2\text{O}$ phase was also reported by Terao[9] and Gauckler[14], and Terao showed that $\text{Si}_2\text{N}_2\text{O}$ phase content increased with the amount of added ZrO_2 in hot-isostatically pressed Si_3N_4 .

It is conceivable that the density of Si_3N_4 with 0Y ZrO_2 compared with that of the hot-pressed pure Si_3N_4 , is increased by $\text{Si}_2\text{N}_2\text{O}$ phase, but yet far from full density. The α/β phase transformation of Si_3N_4 is known to be reconstructive

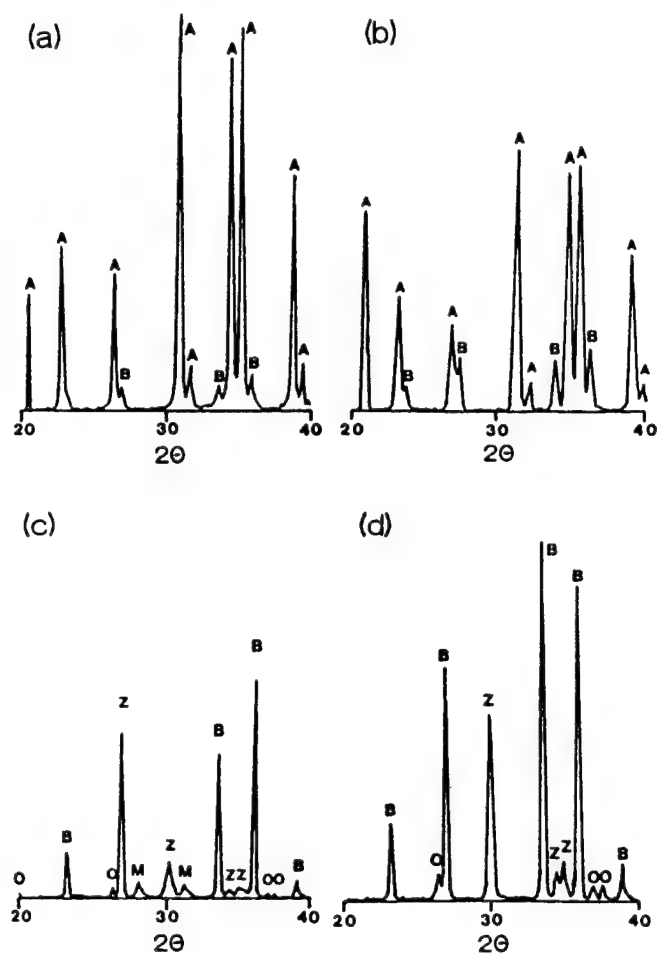


Fig.5. XRD patterns of (a) as received Si_3N_4 powder, (b) hot-pressed pure Si_3N_4 , (c) hot-pressed Si_3N_4 with 5 vol% of pure zirconia composite, and (d) hot-pressed Si_3N_4 with 5 vol % of 6 mol % Y_2O_3 -doped zirconia composite (A: $\alpha\text{-Si}_3\text{N}_4$, B: $\beta\text{-Si}_3\text{N}_4$, O: $\text{Si}_2\text{N}_2\text{O}$, Z:cubic or tetragonal zirconia, M:monoclinic zirconia peaks).

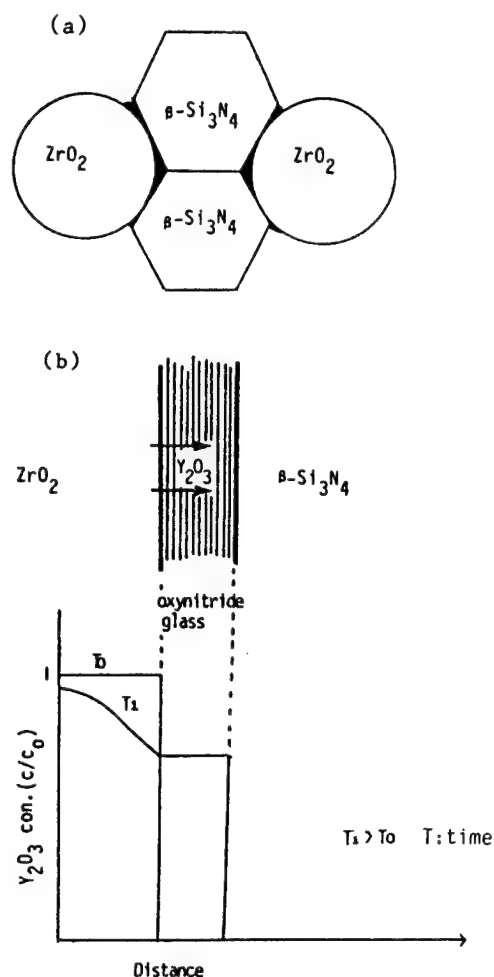


Fig.6. Diffusion model in Si_3N_4 - zyttrite composite. (a) Y_2O_3 diffusing from zyttrite forms a liquid phase and (b) oxynitride phase in grain boundary is acted as a immobilized substance for Y_2O_3 dissolved in zyttrite.

and catalyzed by the existence of small amount of liquid phase. But the densification is another problem and do not always accompany the phase transformation[13]. The $\text{Si}_2\text{N}_2\text{O}$ phase, being probably a liquid at the hot pressing temperature, influenced the phase transformation rather than the densification of Si_3N_4 .

XRD pattern of Si_3N_4 with 3Y ZrO_2 is composed of cubic or tetragonal- ZrO_2 , β - Si_3N_4 and $\text{Si}_2\text{N}_2\text{O}$ peaks(Fig.5,(d)). The XRD patterns of Si_3N_4 with 6Y and 8Y ZrO_2 were similar to those of Si_3N_4 with 3Y ZrO_2 .

3.4. Diffusion Behavior of Y_2O_3

In diffusion process, if the reaction by which the immobilized reactant is formed proceeds rapidly compared with the diffusion process, local equilibrium may exist between the free and immobilized components of the diffusing substance[15]. In this case, the concentration S of immobilized substance is proportional to the concentration C of substance free to diffuse. This can be simply expressed as follow;

$$S = R \cdot C \quad \text{---2)} \quad \text{where, } R:\text{const.}$$

In this view point, it can be considered that local equilibrium can exist between zyttrite and Si_3N_4 matrix by the formation of oxynitride grain boundary phase during the sintering of Si_3N_4 -zyttrite composite, i.e. Y_2O_3 diffusing from the zyttrite forms an oxynitride phase in grain boundary, and diffusion of Y_2O_3 is restricted by oxynitride phase as shown in Fig.6. The results of the EDS

Table 1. Yttrium Content in Zyttrite Measured by EDS Analysis in AEM.

			(wt%)
Sample Name		Theoretical Value	Measured Value
As Received Powder	3Y ZrO_2	5.4	4.9±0.6
	6Y ZrO_2	10.2	10.2±0.6
	8Y ZrO_2	13.7	13.9±0.8
Hot-Pressed	Si_3N_4 -6Y*	-	8.5±0.8
	Si_3N_4 -8Y*	-	8.3±0.6

* amount of added zyttrite is 10 vol %.

analysis of zyttrite phase in Si_3N_4 - 6Y and 8Y zyttrite composite show that the same concentrations of Y_2O_3 are remained (Table 1); as-received powders were also analyzed to determine the accuracy of this analysis. The concentration of yttrium dissolved in Si_3N_4 matrix is very low, and the grain boundary phase is composed of Y, Zr, and Si element (Fig.7 and Table 2). This grain boundary phase is thought to be Y - Zr - Si oxynitride. The concentration of yttrium in grain boundary phase is about 9.6 wt%. This value is similar to the concentration of Y_2O_3 remained in 6Y and 8Y zyttrite (Table 1) and is higher than that of Y_2O_3 existing in 3Y zyttrite. On the basis of these results, it is suggested that the formation of Y - Zr - Si oxynitride existing as a grain boundary phase bring local equilibrium and restrict the diffusion of Y_2O_3 from zyttrite. As a result, it seems that the density of Si_3N_4 -3Y ZrO_2 composite could not increase by even much additions of 3Y ZrO_2 .

Tabel 2. EDS Analysis of Si_3N_4 -15 vol% of 8Y ZrO_2 Composite.

(wt%)				
Point#	Element	Si	Zr	Y
A		101.38	-	-
B		6.4	83.6	9.6
C		53.9	36.5	9.6

corresponding in Fig.7.

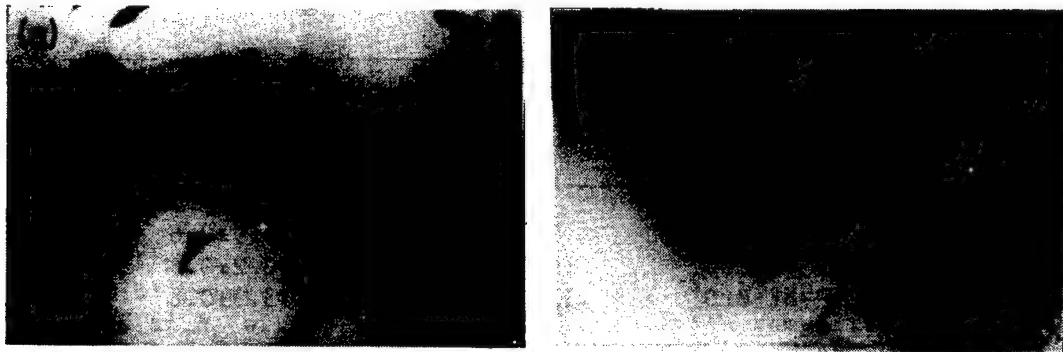


Fig.7. Transmission electron image of Si_3N_4 - 15 vol% of 8Y ZrO_2 ((b) is magnified image of (a) and A, B, C in (b) indicate the EDS analysis point).

3.5 Y - Zr - Si Oxynitride

In Si_3N_4 - 5 vol% of 6Y ZrO_2 composite, 0.93 wt% Y_2O_3 was totally involved. Among these, the amount of Y_2O_3 related to densification was about 0.2 wt%; this value was obtained by the EDS analysis as shown in Table 1, assuming that the concentration of Y_2O_3 remained in zyttrite is constant regardless of the amount of added zyttrite. So, in order to observe the effect of ZrO_2 with Y_2O_3 on the densification, following experiments were performed. 0.2-1.5 wt% of Y_2O_3 was added to Si_3N_4 in the form of yttrium nitrate. And 5 vol% of 0Y ZrO_2 was also added to these mixtures, respectively. These mixtures were hot-pressed after calcining at 700°C for 2h under N_2 atmosphere. When only Y_2O_3 was added, density changed from 90.6 to 96.6 % of theoretical with the amount of added Y_2O_3 (Table 3). In the case of the addition of ZrO_2 and Y_2O_3 , all densities increased above 97% of theoretical as like Si_3N_4 - 5 vol% of 6Y ZrO_2 . Therefore, although full density could not be obtained by the only addition of ZrO_2 , it is suggested that ZrO_2 act as an important role in the formation of Y - Zr - Si oxynitride resulting in increase the density of Si_3N_4 - zyttrite composite.

Table 3. Relative Density of Si_3N_4 with the Addition of Y_2O_3 (and ZrO_2).

Addition	Density	Addition	Density
0.2 wt% Y_2O_3	90.6 %	0.2 wt% Y_2O_3 + 5 vol% 0Y ZrO_2	97.9 %
0.5 wt% Y_2O_3	91.6 %	0.5 wt% Y_2O_3 + 5 vol% 0Y ZrO_2	97.1 %
1.0 wt% Y_2O_3	95.3 %	1.0 wt% Y_2O_3 + 5 vol% 0Y ZrO_2	97.1 %
1.5 wt% Y_2O_3	96.6 %	1.5 wt% Y_2O_3 + 5 vol% 0Y ZrO_2	98.2 %

Summary

1. The addition of pure ZrO_2 was not effective to obtain full density of Si_3N_4 - ZrO_2 composite, but most of $\alpha\text{-Si}_3\text{N}_4$ phase was transformed to $\beta\text{-Si}_3\text{N}_4$, accompanying the formation of $\text{Si}_2\text{N}_2\text{O}$ phase.

2. In Si_3N_4 - zyttrite composite, nearly full density (97%) could be obtained by the addition of 5 vol % of 6Y or 8Y ZrO_2 , but the densification was not sufficient in the case of the addition of 3Y ZrO_2 . From these results, it is suggested that Y_2O_3 diffusing from the added zyttrite promote the densification of Si_3N_4 - zyttrite composite, and the densification depend on the content of Y_2O_3 in zyttrite.
3. On the basis of EDS analysis in AEM, it is suggested that the formation of Y - Zr - Si oxynitride glass in grain boundary bring local equilibrium and restrict the diffusion of Y_2O_3 in zyttrite.

References

1. R.W.RICE and W.J. McDONOUGH, J.Am.Ceram.Soc.58(1975)264.
2. Y.INOMATA, Y.HASEGEWA, T.MATSUYAMA, and Y.YAJIMA,Yogyo Kyokai Shi 84(1976)600.
3. N.CLAUSSEN and J.JAHN, J.Am.Ceram.Soc.61(1978)94.
4. F.F.LANGE, J.Am.Ceram.Soc. 63(1980) 38.
5. D.A.SHOCKEY and K.C.DAO,Am.Ceram.Soc.Bull.60(1981)256.
6. S.DUTTA and B.BUZEK,J.Am.Ceram.Soc.67(1984)89.
7. W.A.SNADERS and D. M. MIESKOWSKI, Adv. Ceram. Mater. 1 (1986) 166.
8. G. W.BABINI, A. BELLOSI, R. CHIARA, and M. BRANO, Adv. Ceram. Mater.2 (1987)146.
9. K. TERA0, J. Am. Ceram. Soc.71(1988)C-167.
10. N. CLAUSSEN, R. WAGNER, L. J. GAUCKLER, and G. PETZOW, J. Am. Ceram. Soc. 61(1978)369.
11. F. F. Lange, L. K. L. Falk and B. I. Davis, J.Mater.Res. 2(1987)66
12. C. P. GAZZARA and D. R. MESSIER, Am. Ceram. Soc. Bull. 56 (1977) 777.
13. J.R. KIM and C.H. KIM, J. Korean Ceram.Soc.23(1986)67.
14. L.J.GAUCKLER, J.WEISS and G.PETZOW," Energy and Ceamics," edited by P. VINCENZINI (Elsevier Scientific Pub., Netherlands, 1980) p.671.
15. J. Crank, "The Mathematics of Diffusion", 2nd edition, Clarendon Press, Oxford, England(1975)

PROPERTIES OF Al_2O_3 -15v/o ZrO_2 (+3m/o Y_2O_3) CERAMICS PREPARED
BY A PRECIPITATION METHOD

Hong Lim Lee and Gi Gon Hong

Department of Ceramic Engineering, Yonsei University, 134 Shinchon-Dong,
Seodaemoon-Ku, Seoul 120-749, Korea

Very fine alpha-alumina and alumina-zirconia powders with a narrow particle size distribution were prepared by a precipitation method using $\text{Al}_2(\text{SO}_4)_3 \cdot 18\text{H}_2\text{O}$, $\text{ZrOCl}_2 \cdot 8\text{H}_2\text{O}$ and $\text{YCl}_3 \cdot 6\text{H}_2\text{O}$ as the starting materials. Alpha-alumina was prepared by calcining aluminum hydroxides which were formed through hydrolysis under various PH values. ZrO_2 (+3m/o Y_2O_3) powder was prepared by a coprecipitation technique from $\text{ZrOCl}_2 \cdot 8\text{H}_2\text{O}$ and $\text{YCl}_3 \cdot 6\text{H}_2\text{O}$. Al_2O_3 -15v/o ZrO_2 (+3m/o Y_2O_3) ceramics was prepared by a mechanical mixing of these two powders and also by a coprecipitation technique from the three chemicals. The sinterability and mechanical properties of the former was observed to be superior to the latter. The addition of 0.03 wt% MgO to the prepared alumina-zirconia enhanced the sinterability of the ceramics.

1. Introduction

Powder preparation techniques are broadly categorized according to whether they involve solutions, vapor phases, or the solid-state decomposition of salts. For the solution techniques, there are subcategories according to how the solvents are removed (1).

Precipitation technique is generally known as a method by which numerous ceramic powders can be prepared easily and cheaply. In this study, therefore, a precipitation technique was adapted for the preparation of pure and fine alpha-alumina and alumina-zirconia (+3m/o yttria) powders, using the aluminum sulfate, zirconium oxychloride and yttrium chloride as the starting materials.

The powder characterization and mechanical properties of the Al_2O_3 -15v/o ZrO_2 (+3m/o Y_2O_3) ceramics prepared through the precipitation technique were studied.

2. Experimental Procedure

2.1 Alumina

$\text{Al}_2(\text{SO}_4)_3 \cdot 18\text{H}_2\text{O}$ was hydrolyzed in water with various pH values using an ammonia-water (28wt% NH_3) to precipitate aluminum hydroxides.

The obtained aluminum hydroxides were dried at 100°C for 24 hours before characterized and heat-treated to prepare alpha-alumina via transition aluminas.

Table 1 Phase Change of Precipitated Materials (hydrated aluminas) as a Function of pH.

pH	Hydrated aluminas
5	Amorphous
6	Amorphous
7	Amorphous
8	Pseudo-boehmite
9	Pseudo-boehmite
10	Pseudo-boehmite, Nordstrandite, Bayerite, Gibbsite, Hydrargillite.
11	Nordstrandite, Bayerite, Gibbsite, Hydrargillite.

Table 2. The Relative Density of Green Body as a Function of pH.

	pH	Relative Density (%)
Green Body Undoped with MgO	7	43.42
	9	43.54
	10	43.57
	11	38.26
Green Body Doped with 0.03 wt % MgO	7	42.67
	9	43.67
	10	44.80
	11	38.52

2.2 Alumina-Zirconia System

$ZrO_2(+3m/oY_2O_3)$ powder was prepared by coprecipitating $ZrOCl_2 \cdot 8H_2O$ and $YCl_3 \cdot 6H_2O$ with an ammonia water (28wt% NH_3) before washing the precipitate and calcining it at $600^\circ C$.

$Al_2O_3-15v/oZrO_2(+3m/oY_2O_3)$ ceramics was prepared by two kinds of technique. One is the mechanical mixing of the alpha-alumina and zirconia(+3m/o yttria) powders, which were separately prepared by a precipitation technique (we call it Series A). The other is a coprecipitation technique, by which three chemicals, $Al_2(SO_4)_3 \cdot 18H_2O$, $ZrOCl_2 \cdot 8H_2O$ and $YCl_3 \cdot 6H_2O$ were precipitated together with the ammonia water before washing the precipitate and calcining it (we call it Series B).

3. Results and Discussion

3.1 Aluminum Hydroxides

In Table 1 are presented the phases of aluminum hydroxides as a function of pH value. The specific surface areas of the hydroxides are given in Table 2. The phase changes from $AlOOH$ to $Al(OH)_3$ type hydroxides as pH value increases. But the specific surface area decreases as the pH value increases.

3.2 Alumina Powder

The specific surface area changes of alumina powder on heat-treatment are shown in Table 2. The specific surface area increases with pH when the hydroxides were heat-treated at $600^\circ C$ for 2 hours, which is an opposite tendency to that of the hydroxide powders dried only at $100^\circ C$ for 24 hours. This is probably attributed to the mechanism that $Al(OH)_3$ type hydroxides evolve more water than $AlOOH$ type hydroxide during drying at $600^\circ C$, as schematically shown in Fig.1. The particle size distributions are given in Table 3. It can be seen that the particle size was much reduced after ball-milling.

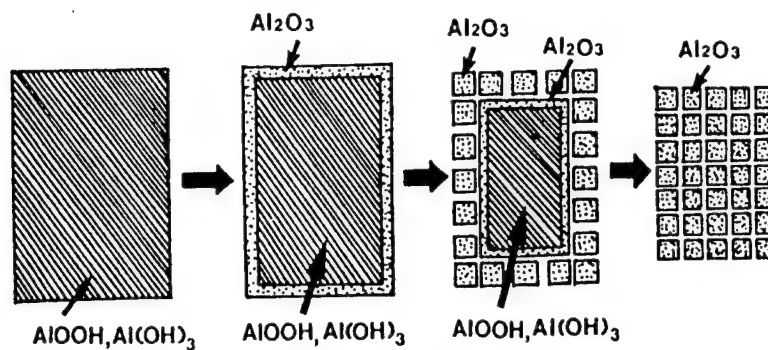


Fig. 1. The schematic representation of the increase of specific surface area with dehydration process in the precipitation method ($\text{pH} > 7$).

In Fig.2 was shown the relative density of the alumina ceramics when alumina ceramic bodies were sintered at 1650°C . It was observed that the MgO addition enhanced the sinterability of alumina ceramics.

3.3 Alumina-Zirconia Powder

Particle size distributions before and after and after ball-milling are given in Table 4 as a function of pH . Particle sizes of the Series A are smaller than those of the Series B. Relative densities and shrinkages of the alumina-zirconia ceramics sintered at 1650°C for 4 hours are shown in Fig.3. It can be understood that the Series A specimens are much more densified than the Series B and MgO effectively acted as the sintering aid for the alumina-zirconia ceramics. In Table 5 are given the tetragonal ZrO_2 contents as a function pH , from which it can be seen that the tetragonal zirconia can be retained higher than 94% for all pH values.

4. Conclusions

1) Very fine and narrow size distributed alpha-alumina and alumina-zirconia powders could be prepared by a precipitation method.

2) Mechanical mixing of separately precipitated alpha-alumina and zirconia powders was more effective for fabrication of densified alumina-zirconia ceramics than coprecipitation from Al and Zr salts.

3) MgO doping was found to be effective for densification of alumina and alumina-zirconia ceramics.

5. References

- 1) D.W.Johnson, Jr., " Nonconventional Powder Preparation Techniques," Am. Ceram. Soc. Bull., 60(2) 221-24 (1981).

Table 3 Particle Size Distributions before and after Ball Milling as a Function of pH.

Condition				Data	
pH	Calcination Temp. (°C)	Soaking Time (min)		Mean Particle Size (μm)	Particle Size Range (μm)
7	1200	8	Before Ball Milling	0.85	0.32 - 2.21
9	1150	60		1.15	0.37 - 1.43
10	1150	50		1.49	0.44 - 2.47
11	1150	85		0.74	0.41 - 2.28
7	1200	8	after Ball Milling for 48 h	0.09	0.04 - 0.20
9	1150	60		0.12	0.03 - 0.20
10	1150	50		0.11	0.04 - 0.24
11	1150	85		0.06	0.01 - 0.07

Table 4 Particle Size Distributions before and after Ball Milling as a Function of pH.

(a) Series A

	pH	Calcination Temp. (°C)	Soaking Time (min)		Particle Size Range (μm)	Mean Particle Size (μm)
Al ₂ O ₃	7	1200	8	before Ball Milling	0.32-2.21	0.85
	9	1150	60		0.37-1.43	1.15
	10	1150	50		0.44-2.47	1.49
	11	1150	85		0.41-2.28	0.74
ZrO ₂	7	600	60		0.28-1.60	0.74
Al ₂ O ₃	7	1200	8	after Ball Milling for 48 h	0.04-0.20	0.10
	9	1150	60		0.03-0.20	0.12
	10	1150	50		0.04-0.24	0.11
	11	1150	85		0.01-0.19	0.06
ZrO ₂	7	600	60		0.09-0.48	0.27

(b) Series B

pH	Calcination Temp. (°C)	Soaking Time (min)		Particle Size Range (μm)	Mean Particle Size (μm)
7	1250	60	before Ball Milling	0.37-3.01	0.87
9	1250	90		0.93-2.93	1.71
10	1250	60		0.49-2.27	0.69
11	1250	120		0.47-3.17	0.76
7	1250	60	after Ball Milling for 48 h	0.13-0.75	0.28
9	1250	90		0.30-1.14	0.46
10	1250	60		0.15-0.56	0.31
11	1250	120		0.12-0.54	0.27

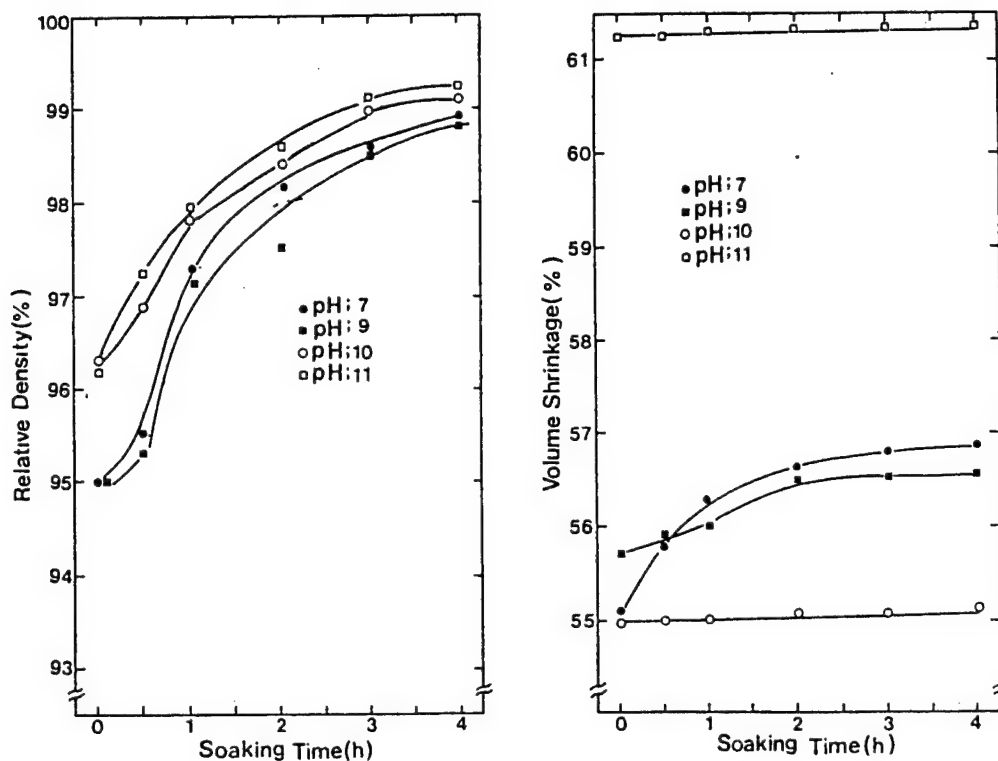


Fig.2 The change of relative density and volume shrinkage as functions of pH and soaking time at 1650°C. (Doped with 0.03 wt%MgO)

Table 5. Tetragonal-to-Monoclinic ZrO_2 Ratio as a Function of pH in As-Fired Surface of Al_2O_3 -15 v/o ZrO_2 (+3 m/o Y_2O_3) Composite Sintered at 1650°C for 4 h.

		pH	Tetragonal (%)	Monoclinic (%)
Series A	Composite Undoped with MgO	7	94.05	5.95
		9	97.79	2.21
		10	98.70	1.30
		11	98.27	1.73
	Composite Doped with MgO	7	98.08	1.92
		9	96.66	3.34
		10	98.30	1.70
		11	98.87	1.13
Series B	Composite Undoped with MgO	7	97.81	2.19
		9	97.67	2.33
		10	93.30	6.70
		11	95.72	4.28
	Composite Doped with MgO	7	98.46	1.54
		9	97.44	2.56
		10	97.87	2.13
		11	98.35	1.65

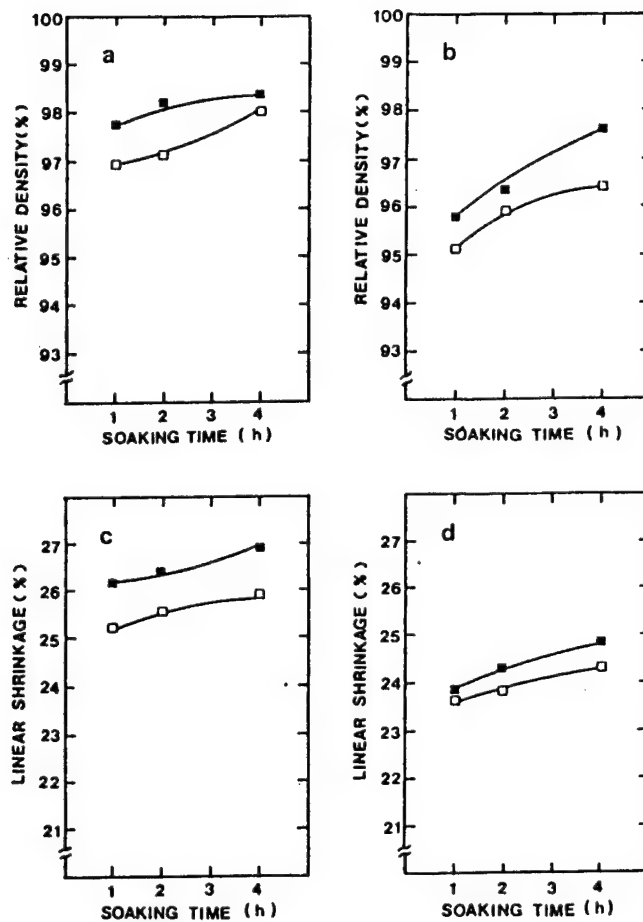


Fig.3 Relative densities and linear shrinkages as a function of soaking time at 1650°C (pH=11).
 (Closed marks are specimens doped with MgO and open marks are specimens undoped with MgO.)
 (a) and (c) ; Series A.
 (b) and (d) ; Series B.

PREPARATION OF Al_2O_3 AND Si_3N_4 CERAMICS BY LOW PRESSURE INJECTION MOLDING METHOD.

K. MIYAMOTO, Y.TAKAHASHI, S.INAMURA and H.MIYAMOTO

Osaka Prefectural Industrial Technology Research Institute
2-1-53, Enokojima, Nishi-ku, Osaka 550, Japan

Four different mixing methods were tested ; stirrer equipped in the low pressure injection molding apparatus, automatic agate mortar, ceramic three roll mill and ball mill. It is concluded that the ball mill mixing method prepares the most uniform slurry among the four mixing methods. The specimen sintered at $1700^{\circ}C$ for 3hrs, after being shaped in the horizontal flow type mold from the slurry of the ball mill mixing method, shows a strength of $40.0kgf/mm^2$ and its Weibull constant is 6.9. Furthermore, the flexural strength of the sintered specimens increased from $40.0kgf/mm^2$ to $46.2kgf/mm^2$ and their Weibull constant increased from 6.9 to 14.5, as the metal mold was changed from horizontal into vertical flow type.

A transparent mold with a window of a strengthened glass was devised. This mold enables to visualize the dynamic flow of the Si_3N_4 slurry through the glass window by VTR. A turbulent flow of the slurry was observed, when the flow rate increases abruptly. It was made clear that this turbulence gives rise to a lot of voids in the Si_3N_4 green compact, which result in low Weibull constant of bending strength of Si_3N_4 sintered body. By controlling the flow of the slurry without turbulet flow, the flexural strength of the sintered specimen increased from $77.1kgf/mm^2$ to $99.1kgf/mm^2$ and their Weibull constants incleased from 5.6 to 11.9 .

The injection molding method is able to prepare green compacts of complicated shape with high precise dimension and good productivity. In this method, there is no need to mechanically process the compacts after molding. It is expected that this method will become a principal technology processing complicated ceramic structural parts. However, the ordinary injection molding method needs such a high pressure (200 to $2000 kgf/cm^2$) for shaping the compacts that the molding apparatus and mold must have high wear resistivity against flow of the slurry used. Therefore, the ceramic parts, when the ordinary injection molding is applied for fabrication of many species-small rot parts, become prohibitively expensive. On the contrary, low pressure injection molding makes the life of mold ten or fifteen times longer than that of ordinary injection molding because of applying lower pressure (3 to $5 kgf/cm^2$). But studies on the fabrication of ceramics by low pressure injection molding using fine powder are scarcely reported.

In the present investigation, the possibility of low pressure injection molding for processing the high strength-ceramics sintered from raw material of fine particles was examined. Especially the following three articles,

(1) the effect of the mixing method of the slurry on the flexural strength and its Weibull constant of sintered body¹⁾, (2) the effect of the shape of the mold on the flexural strength and its Weibull constant of sintered body^{2,3)}, (3) observation of the dynamic flow of the slurry using a transparent mold with a window of strengthened glass⁴⁾, were studied.

Experimental

(1) The effect of the mixing method of the slurry on the flexural strength and its Weibull constant of sintered body.

The process of preparing Al_2O_3 ceramics by the low pressure injection molding method is shown in Fig.1.

The green compact was prepared by a low pressure injection molding machine made by Peltzman Co., Ltd. (type MIGL-28) as illustrated in Fig.2. A mixture of starting powder and binder provides the slurry in the heated tank. The tank and guiding pipe are kept at temperatures in the range from 80°C to 100°C. After the bubbles remaining in the slurry are evacuated by the vacuum pump, the slurry is transferred into the metal mold by gas pressure up to 5 kgf/cm^2 of the compressor. The slurry gives rise to a green compact shaped in the water cooled mold.

A Al_2O_3 fine powder, AL-160SG, of a mean particle diameter of 0.6 μm , supplied by Showa Keikin-zoku Co., Ltd. was used after being heated at 900°C to remove water adsorbed on the surface of the particles. An organic binder, SE-146, supplied by Chukyo Yushi Co., Ltd. was used.

Fine particles of raw material powder need to be dispersed homogeneously into the binder in order to obtain high strength ceramics. When the size of particles of raw material is smaller than about 1 μm , the particles tend to make a large agglomerate. In order uniformly to disperse the particles into the organic binder, four different mixing methods were tested; (1) a stirrer equipped in the low pressure injection molding apparatus, (2) an automatic agate mortar, (3) a ceramic three roll mill and (4) a ball mill. The content of Al_2O_3 powder to the slurry was 85 wt%.

(1) Stirrer; the organic binder of SE-146 of 150g was put in the tank of the hot molding machine and heated at 90°C. Then the Al_2O_3 powder of 850g was gradually added into the molten wax and mixed by the stirrer of the hot molding machine for 6 hrs.

(2) Automatic agate mortar; an Ishikawa-type automatic agate mortar was used. While the binder was melted by a hot blower, Al_2O_3 powder was added and mixed for 4 hrs.

(3) Ceramic three roll mill; a ceramic three roll mill, type 9x18G (the ratio of rotation rate is 1:3:9) produced by Inoue Seisakusho Co., Ltd. was used. A small amount of methyl ethyl keton was added to the slurry premixed by the automatic agate mortar to give the slurry adequate plasticity. The slurry thus prepared was passed through the rolls four times.

(4) Ball mill; a Al_2O_3 ball mill Type HD pot-mill B (capacity 7300 ml) produced by Nippon Kagaku Togyo Co., Ltd. was used. 1700g of Al_2O_3 powder, 300g of the binder and 1000ml of methyl ethyl keton were introduced into the pot with Al_2O_3 balls, and milled for 24 hrs. Methyl ethyl keton plays the role of solving the wax. After milling, the solvent was evaporated by heating the suspension at 70 °C.

The viscosities of these slurries were measured with a temperature from 65 °C to 90 °C by a B Type Viscometer by Tokyo Keisoku Co., Ltd.

The green compacts were molded by using a mold that was a plate of 50mmx50mmx5mm. The conditions of molding are shown in Table 1.

The temperature program for dewaxing was as follows ; RT-200°C:heating rate 5°C/h, 200°C:holding time 0.1h, 200°C-400°C:heating rate 2°C/h and 400°C-900°C:heating rate 5 °C/h. The temperature program for sintering was as follows ; RT-1200°C:heating time 3h, 1200°C-1700°C:heating time 1.5h, 1700°C : holding time 3h, and 1700°C-1200°C:cooling time 1h.

The flexural strength of Al_2O_3 ceramics at 1700 °C for 3 hrs was measured by a three point bending test at room temperature and Weibull constants were calculated.

Result

Fibers of a diameter of about 100 μm were prepared from the four kinds of molten slurries kept at 80 °C, which were prepared by four kinds of mixing method, by abruptly pulling a glass stick from the slurries after it had been in contact with them. The presence of agglomerate on the surface of the fiber was detected by the naked eye or optical microscope. The results are summarized in Table 2. This Table shows that the ball mill mixing method prepares the most uniform slurry of the four slurries above described.

Fig.3 shows the measured viscosity of the slurries. The slurry prepared by the stirrer mixing method showed the lowest viscosity while the other slurries showed nearly the same high value. The more uniformly dispersed the particles are, the higher the viscosity of the slurry is. Therefore, the slurries prepared by the above methods except the stirrer mixing one were thought to be homogeneous so far as observed from their viscosity.

The results of the three point bending test and Weibull constants are shown in Table 3. The flexural strength of the sintered specimen from the ball mill mixing method shows the highest value, 40kgf/mm², while that of the test pieces from the stirrer mixing method shows the lowest value, 22.1kgf/mm². Similarly, the sintered specimen from the ball mill mixing method shows the highest Weibull constant, 6.9, while that from the stirrer mixing method shows the lowest value, 3.7. The high Weibull constant results from the small probability of the presence of defects which give rise to fracture under an external stress. The sintered specimen from the ceramic three roll mill shows the second highest value of flexural strength and Weibull constant. The order

of homogeneity of the slurry as shown Table 2 coincides well with that of the Weibull constant.

From these experimental results, it is concluded that the most homogeneously dispersed slurry prepared by the ball mill mixing method gives the highest strength sintered Al_2O_3 ceramics with the highest Weibull constant.

(2) The effect of the shape of the mold on the flexural strength and its Weibull constant of sintered body.

The specimen sintered at 1700°C for 3hrs, from the slurry of the ball mill mixing method, shows a strength of 40.0kgf/mm^2 and its Weibull constant is 6.9 as shown in Table 3. The low Weibull constant results from the large probability of the presence of defects which give rise to fracture under an external stress. The variation of the average flexural strength of the sintered Al_2O_3 ceramics with the positions of specimens were analyzed to find out the origin of the low Weibull constant observed. Fig.5 shows that the flexural strength of the center of the specimens, particularly from the ceramic three roll mill mixing method and the ball mill mixing method, has lower value than that of the other positions. The injecting gate of this metal mold used is in the center. It is thought that the defects of voids became incorporated into the green compact. Therefore, a new metal mold, named vertical flow type mold was made as shown in Fig. 5. The flexural strength of the sintered specimens increased from 40.0kgf/mm^2 to 46.2kgf/mm^2 and these Weibull constants increased from 6.9 to 14.5, as the metal mold was changed from horizontal into vertical flow type.

(3) Observation of the dynamic flow of the slurry using a transparent mold with a window of strengthened glass.

Experimental

89.3wt% of Si_3N_4 powder, N4-F, of mean particle diameter of $0.9\mu\text{m}$, supplied by Nippon Denkou Co., Ltd., 5.7wt% of Al_2O_3 powder, AKP30, supplied by Sumitomo Chemical Co., Ltd. and 5wt% of Y_2O_3 powder, supplied by Shinetsu Chemical Co.,Ltd. were used. The content of ceramic powder to the slurry was from 17 to 20wt%. The slurries were prepared by the ball mill mixing method which makes the most homogeneously dispersed slurry as above described. A transparent mold with a window of a strengthened glass was devised. The dynamic flow of the Si_3N_4 slurry was observed through the glass window by VTR.

Result

A turbulet flow of the slurry was observed, when the flow rate increases abruptly. It was made clear that this turbulence gives rise to a lot of voids in the Si_3N_4 green compact, which result in low Weibull constant of bending strength of Si_3N_4 sintered body, 5.6 . By controlling the flow of the slurry without turbulet flow, the flexural strength of the sintered specimens

increased from 77.1kgf/mm² to 91.6kgf/mm² and its Weibull constant increased from 5.6 to 11.2 .(summarized in Table 4)

Reference

- 1) K.Miyamoto, H.Miyamoto, Y.Takahashi and H.Taguchi: Bull.Inst.Chem.Res., Kyoto Univ., 64 (1986), 287
- 2) K.Miyamoto, Y.Takahashi, S.Inamura and H.Miyamoto: Journal of the Japan Society of Powder and Powder Metallurgy 34 (1987), 378
- 3) K.Miyamoto, Y.Takahashi, S.Inamura and H.Miyamoto: Journal of the Japan Society of Power and Power Metallurgy 35(1988), 633
- 4) K.Miyamoto, Y.Takahashi, S.Inamura and H.Miyamoto: Journal of the Japan Society of Power and Power Metallurgy 36 (1989), 192

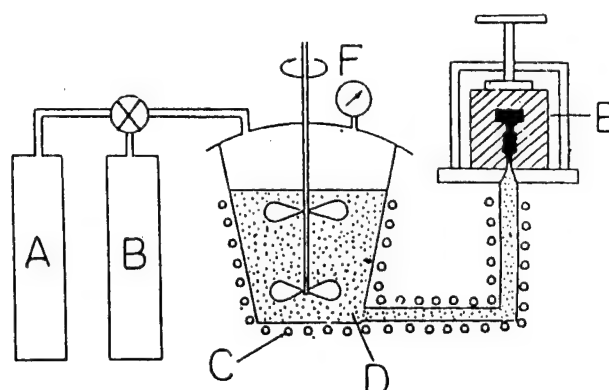
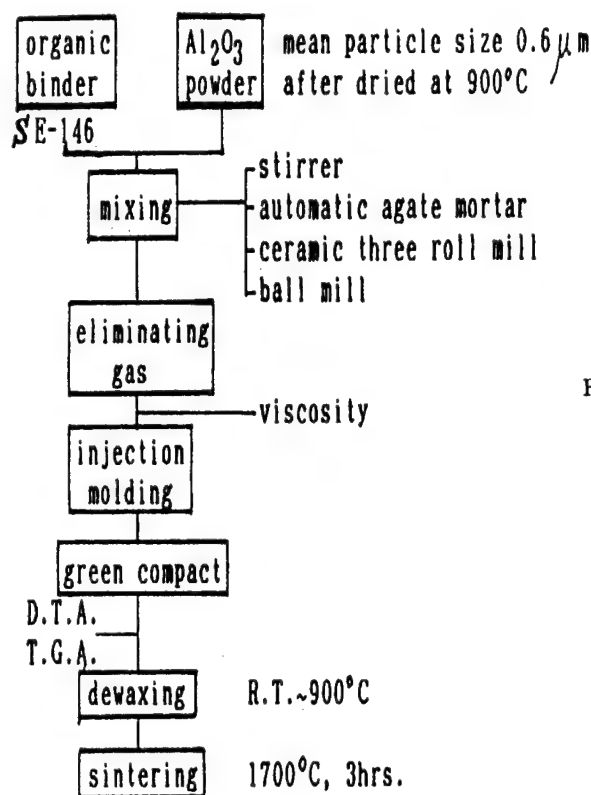


Fig. 2 Schematic diagram of low pressure injection molding machine.

(A) compressor (B) vacuum pump (C) heater (D) slurry (E) metal mold (F) pressure gauge

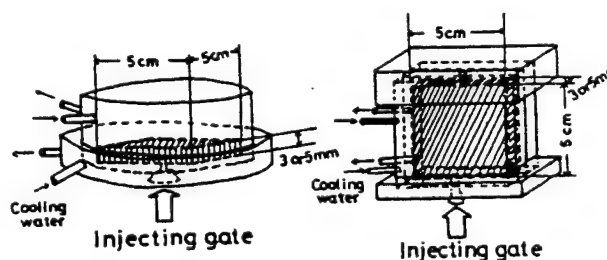


Fig. 1 Process to prepared Al₂O₃ ceramics by low pressure injection molding method. Fig. 5 Illustration of the two kinds of metal molds used.

Table 1 Conditions of molding.

Thickness of plate	Temperature of tank	Temperature of pipe	Molding time	Molding pressure
3 mm	100°C	90°C	20 sec	5 Kgf/cm ²
5 mm	100°C	90°C	30 sec	5 Kgf/cm ²

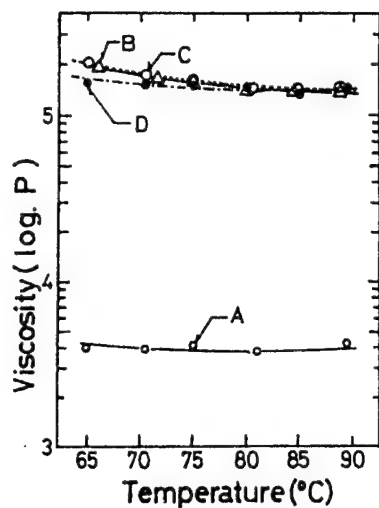


Fig. 3 Viscosity of four kinds of slurries.
(A) stirrer (B) automatic agate mortar (C) ceramic three roll mill (D) ball mill

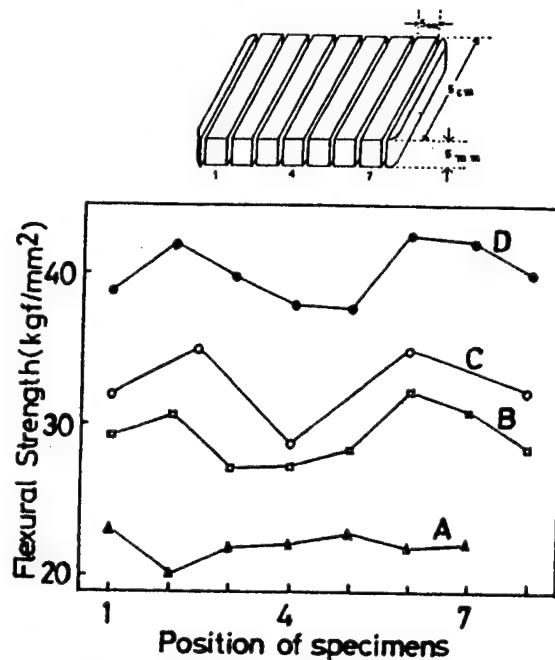


Fig. 4 Variation of the flexural strength of sintered Al_2O_3 with the positions of specimens.
(A) stirrer (B) automatic agate mortar (C) ceramic three roll mill (D) ball mill

Table 2 Appearance of four kinds of slurries.

Mixing method	Mixing time	Fiber formation	Agglomerates
Stirrer	6 hr	Difficult	Large Amount Observed
Agate mortar	4 hr	Easy	Trace
Ceramic three roll mill	15 min	Easy	Trace
Ball mill	24 hr	Easy	Not detected

Table 3 Flexural strength of sintered Al_2O_3 ceramics and their Weibull constants.

Mixing method	Sintering temperature °C	Average of flexural strength Kgf/mm²	Number of specimens	Weibull constant
Stirrer	1700	22.1	24	3.7
Automatic agate mortar	1700	28.3	26	4.6
Ceramic three roll mill	1700	32.5	47	5.2
Ball mill	1700	40.0	26	6.9

Table 4 Flexural strength of sintered Si_3N_4 ceramics and their Weibull constants

Content of SE-146 wt%	Controlling the flow of the slurry without turbulence	Molding pressure kgf/cm²	Average of flexural strength kgf/mm²	Weibull constant
17	----	3	74.8	---
17	----	5	86.7	7.2
20	----	3	80.9	---
20	----	5	77.1	5.6
20	done	5	91.6	11.9

SYNTHESIS OF β -SIALON FROM POROUS GLASS AND PROPERTIES OF ITS SINTERED BODY

Kim, Byong-Ho, Lee, Gun-Hun, and Jun, Hyung-Woo

Department of Materials Science, Korea University
5-1 Anam-Dong, Sungbuk-Ku, Seoul, 136-701, Korea

Introduction

In reduction-nitridation method for synthesizing Sialon from Si-Al-O-C system, it is of prime importance to give sufficient reduction and enhance the reactivity of raw materials.

Synthesis of β -Sialon powder was attempted with reduction-nitridation of porous glass-carbon mixture. Porous glass was prepared by heat (for phase separation) and hydrothermal treatments of $\text{Li}_2\text{O}-\text{B}_2\text{O}_3-\text{SiO}_2-\text{Al}_2\text{O}_3$ glass as a starting material.

The porous glass has a specific surface area more than $330 \text{ m}^2/\text{g}$ as well as softening point higher than 1200°C . And then, the porous glass is thought to be an ideal material which can maintain porous structure up to carbothermal reduction temperature. In addition, if carbon pyrolyzed from hydrocarbon is deposited on the surface and interior of porous glass, the degree of contact between porous glass and reducing agent is increased and the good reduction effect can be expected.

In this study, carbon pyrolyzed from propane gas was deposited on the porous glass and thereafter synthesis of β -Sialon was performed.

Experimental Procedure

The mother glass composed with $37.2\text{SiO}_2 \cdot 46.5\text{B}_2\text{O}_3 \cdot 9.32\text{Li}_2\text{O} \cdot 6.98\text{Al}_2\text{O}_3$ was crushed and heated at 480°C for 10hr. The heat treated glass was pulverized into various kind of particle size and hydrothermally treated with distilled water at 98°C for 4hr. Carbon pyrolyzed from propane gas was deposited on porous glass and activated carbon was added to sufficient amount as a reducing agent.

The mixed gas of H_2 and N_2 was passed through the tube furnace with carbon/porous glass at each temperature. After reduction temperature, the products were heated at $700^\circ C$ for 1hr to remove remaining carbon and identified by X-ray diffractometer.

The reaction product with 6 wt% Y_2O_3 as a sintering agent was pressurelessly sintered at $1750^\circ C$ for 1hr in nitrogen atmosphere. The bulk density, M.O.R. and K_{IC} of the sintered bodies were determined.

Results

The amount of carbon deposited on porous glass linearly increased with the pore size. The reduction effect of carbon deposited was better than that of carbon mechanically added.

As the reaction products, β -Sialon, X-phase, α -SiC and Si_2ON_2 were observed. The kinds of reaction products and their amounts were altered according to carbon/porous glass ratio, reaction temperature, time and flow rate. The amount of β -Sialon in reaction product was increased with the reaction temperature, time and pore size of porous glass as shown in Fig.1.

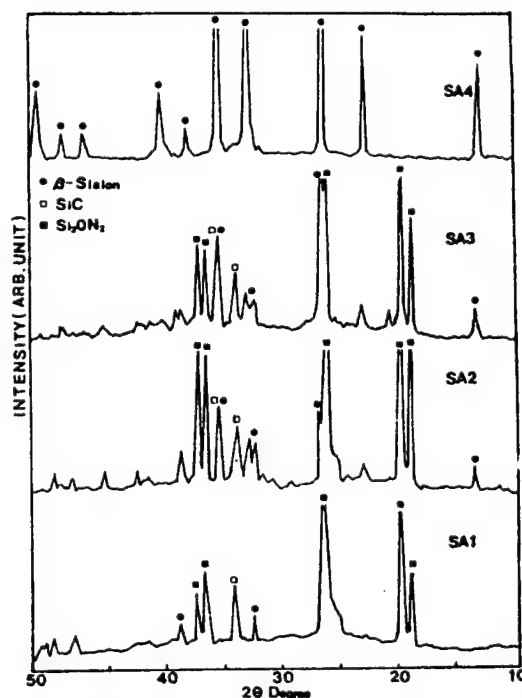


Fig. 1 X-ray diffraction patterns of reaction products for SA1($1350^\circ C$, 5 h), SA2($1400^\circ C$, 5 h), SA3($1400^\circ C$, 10 h), SA4($1450^\circ C$, 5 h) in N_2+H_2 gas = 120 cc/min.

The particle shape of the reaction products showed fibrous in $3 \times 0.4 \mu\text{m}$. The bulk density and M.O.R. of the sintered bodies were $2.25 \sim 3.17 \text{ g/cm}^3$ and $290 \sim 434 \text{ MPa}$, respectively. The values were increased with the amount of β -Sialon in the reaction products. The values of K_{IC} were $3.4 \sim 4.0 \text{ MPa} \cdot \text{m}^{1/2}$.

Table 1. Physical properties of sintered bodies (1750 °C, 1hr)

	Weight loss (%)	Linear shrinkage (%)	Density (g/cm ³)	M.O.R. (MPa)	K_{IC} (MPa·m ^{1/2})
SA1	32	22	2.25	—	—
SA2	8	21	3.12	289.6	3.41
SA3	5	19.5	3.16	393.1	3.96
SA4	2	16.2	3.17	434.4	4.00

Conclusions

- 1) The mean pore size of porous glass was distributed in $9 \sim 16 \text{ \AA}$ range and the amount of carbon deposited on porous glass linearly increased with the pore size.
- 2) The reaction product obtained at 1450 °C for 5hr was β -Sialon single phase.
- 3) The values of M.O.R. and K_{IC} of the sintered body prepared from optimum conditions were 434.4 MPa , $4.00 \text{ MPa} \cdot \text{m}^{1/2}$, respectively.

Effect of Carbide Addition on Sintering of SiC-B-C System

Toshiaki MIZUTANI & Akihiko TSUGE

Toshiba Co. Ltd., Research & Development Center.

1, KomukaiToshiba-Cho, Saiwai-Ku, Kawasaki-Shi, 210, JAPAN

Densification properties of TiC, ZrC, HfC, VC, NbC, TaC or WC dispersed SiC-B-C composites were investigated by pressure-less sintering. Not only could densification to more than 93 %TD be achieved in the TaC-SiC-B-C system by sintering at relatively higher temperature, but also the dispersed TaC particles had suppressed grain boundary movement. The 10mol%TaC-90mol%SiC-B-C composite had twice the toughness as the non-dispersed SiC, in the same sintering batch.

1. INTRODUCTION

SiC-B-C Ceramic Systems are interesting in regard to their excellent strength and heat resistivity at high temperature, around 1500°C. However, the low toughness, around 3 GPa \sqrt{m} for this system, was the greatest problem to be overcome to achieve structural application to heat engines. Therefore, many toughening methods were proposed.1) Initially, the TiC particulate dispersed SiC-Al-C ceramic system was studied by hot-pressing, in order to achieve sufficient densification to make evaluating mechanical properties worthwhile. Then, toughening and strengthening mechanisms were recognized and considered to originate from the larger thermal expansion coefficient of TiC particles than that of SiC matrix.2) However, pressureless sintering is preferable to hot-pressing for structural applications of these ceramics. This study was made to determine some other particulate materials which didn't disturb the SiC-B-C matrix densification. Seven heat resistive metal carbide powders (TiC, ZrC, HfC, VC, NbC, TaC, WC) were selected as dispersed particles candidate in this study.

2. EXPERIMENTAL

Table 1 shows the characters of starting raw powders and the material properties of the related metallic carbides. The sources of B and C aids for sintering are, respectively, amorphous-B powder, produced by Herman C. Starck, and Phenol resin powder, furnished by Dainippon Ink & Chemicals Co. Ltd.

The B aid addition quantity is fixed to 0.7 atm% for main composition (SiC-Metallic Carbide), and the C aid addition quantity is fixed to 2.25 times the weight as the oxygen impurity amount in the main composition. The metallic carbide content in main compositions was selected up to 20 mol%.

A slurry was made from mixed SiC, boron and metallic carbide powders, using an acetone solution of phenol resin and binder. The slurry was dried, granulated and pressed into a 33-43-7mm shape. At 800°C under nitrogen, the binder was degreased and resin was carbonized. Sintering was carried out in a carbon heated vacuum furnace for 2 hours at 1950-2200°C. Sintered bodies were cut and polished to the standard size of JIS R1601.

The densities of sintered bodies were obtained by liquid displacement or size measurement. Standard X-ray diffraction techniques were used to determine the crystalline phases present in the sintered bodies. Scanning electron microscopy etc. were used to observe the polished or fractured surfaces. The fracture toughness values were measured only for TaC-SiC-B-C composites, since they were sufficiently densified by 2200°C sintering to more than 93% of theoretical density, which was estimated from the composition by using the only densities of SiC and each metallic carbide in Table 1. Toughness K_{1C} and hardness H_v were evaluated from more than 10 Vickers indent measurements. Niihara's Equation 3) was used in calculating toughness K_{1C} under the previously postulated Young's modulus E=410 GPa, that could usually be obtained in dense single phase SiC ceramic.

3. RESULTS AND DISCUSSION

Figure 1 shows the effects of each metallic carbide addition and its quantity on 1950°C sintering. Density was normalized by the theoretical density. Every metallic carbide more or less disturbs the densification for each mixture. However, TaC and HfC additions respectively provide higher densities than the additions of other carbides, with IVa and Va elements in the periodic table.

Figure 2 shows the 2050°C sintering results for TaC or HfC dispersed composites, with and without B aid. The densification degradation becomes significant around the 5/8 mol% addition of each metallic carbide, that closely corresponds to the B aid atomic quantity (0.7 atm%). The density becomes slightly higher with increasing the TaC quantity from 5/4 mol%, in spite of the fact that the densification does not occur anymore in the TaC-SiC-C composition without B aid.

In the X-ray diffraction patterns for every sintered body, peaks for each metallic boride were detected. As an example, Table 2 shows the relative peak strengths between SiC, TaC and TaB₂. It seems clear that most of TaC has reacted with the B aid to form TaB₂ at 5/8 mol% TaC addition, and the formed TaB₂ quantity varies little with the excess TaC amount. Even though the low carbon pressure exists in sintering (0.015Pa at 2300K), the B aid would be stabilized by forming metallic borides and lose the aid effect. Therefore, the

SiC-B-C system densification would be deteriorated by metallic carbide addition.

Figure 3 shows SEM photographs of the polished surfaces on sintered body of TaC-SiC-B-C system. Dispersed bright grains are TaC. They have sharp edged rectangular shapes, similar to those for the raw starting powder.

Figure 4 shows the variations on density, toughness and hardness for the TaC-SiC-B-C system, sintered at around 2200°C. The hardness is almost 25 GPa, which seems constant between non-dispersed SiC and 20 mol% TaC dispersed composite. On the other hand, the toughness is increasing with TaC addition, especially quick between 0 mol% and 5 mol% TaC addition.

Figure 5 shows fracture surfaces for each composite. Abnormal exaggerated SiC grain growth appeared and fracture surface is flat on the micro-scale, in the case of no TaC addition. On the contrary, in the TaC added bodies, there is no such exaggerated grain growth, and fracture surfaces are rough on the micro-scale. Dispersed TaC particles seem to suppress the grain growth by pinning the grain boundary movement.

REFERENCES

- 1) K.T.Faber and A.G.Evans, "Crack Deflection Processes-1,2," Acta Metal. 31(4), p.565,p.577, (1983)
- 2) G.C.Wei and P.F.Becher, "Improvements in Mechanical Properties in SiC by the Addition of TiC Particles," J.Am.Ceram.Soc., 67(8), p.571-574, (1984).
- 3) K.Niihara, R.Morena and D.P.H.Hasselmann, "Further Reply to Comment on Elastic/Plastic Indentation Damage in Ceramics: The Median/Radial Crack System," J.Am.Ceram.Soc., 65(7), c.116,(1982).

Table 1. Related metallic carbide characters.

Material	Density g/cc	Molar Vol. cc/mol	Melt. Point °C	F.P.E. KJ/mol	T.E.C. ppm/°C	Young's Modulus GPa	M.P.S. μm	Oxygen Maker Imp. wt%
TiC	4.910	12.5	3,067	-151.4	8.56	470	1.45	0.13 JNM
ZrC	6.633	16.0	3,427	-178.7	7.0	550	1.09	0.81 JNM
HfC	12.657	15.6	3,830	-203.6	7.0	750	3.05	0.01 HCS
VC	5.81	10.8	2,800		6.7	420	1.59	0.40 JNM
NbC	7.801	13.4	3,608	-134.4	7.25	540	1.10	0.39 JNM
TaC	14.497	13.3	3,825	-145.3	6.96	720	2.69	0.13 JNM
WC	15.668	12.6	2,785	-67.0	5.5	700	0.61	0.17 JNM
SiC	3.217	12.5	subl.	-35.4	4.7	386	0.62	1.28 LNZ
BC	2.52	22.0	2,450	-27.3	5.2	450	0.03	CLV

Table 2. Relative X-ray

diffraction peak heights.

TaC Content	(200)TaC (104)6H-SiC	(101)TaB (104)6H-SiC	(200)TaC (101)TaB
5/8 mol%	0.03	1.0	0.03
5/4 mol%	0.81	1.1	0.71
5/2 mol%	2.6	1.3	1.9
5 mol%	5.8	0.98	5.9
10 mol%	14.	0.93	15.
20 mol%	25.	0.61	41.

Referred from JANAF Thermochemical Tables, "D.R.Stull, et al., (1971).
and "Особо тугоплавкие элементы и соединения."
Р. Б. Жотельников, et al., Москва, (1969).

F.P.E. : Formation free Energy at 2300K.

T.E.C. : Thermal Expansion Coefficient from RT. to 2000K.

M.P.S. : Mean Particle Size.

JNM : Japan New Metal Co. Ltd., HCS : Herman C. Starck Co. Ltd..

LNZ : Lonza Co. Ltd., CLV : Callery Co. Ltd..

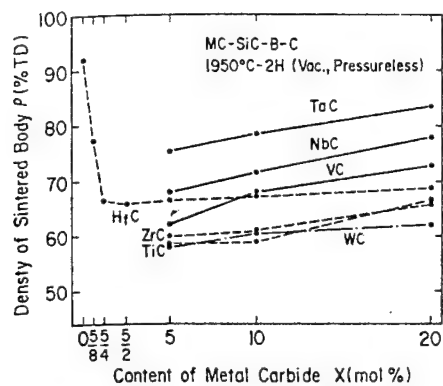


Fig. 1. Density for SiC-Metallic Carbides in 1950°C sintering.

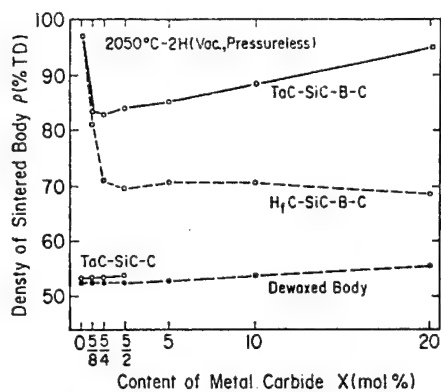


Fig. 2. Density for SiC-TaC and SiC-HfC in 2050°C sintering.

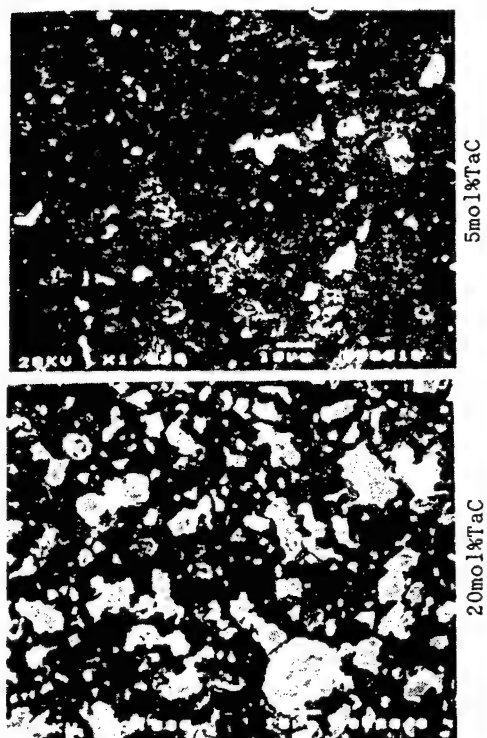


Fig. 3. The polished surfaces of TaC-SiC-B-C, sintered at 2200°C.

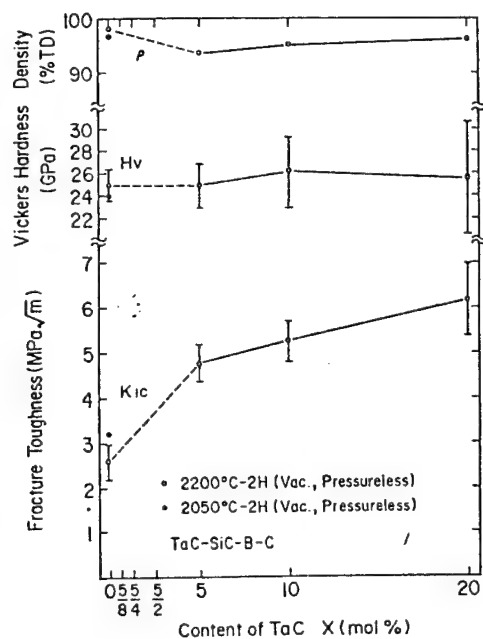


Fig. 4. Density, Hardness and Toughness for TaC-SiC-B-C in 2200°C sintering.



Fig. 5 Fractured surfaces for TaC-SiC-B-C, sintered at 2200°C.

MORPHOLOGY OF COILED WHISKERS OF Si_3N_4 AND THEIR MECHANICAL PROPERTIES

Iwanaga H.^{A)}, Iwasaki T.^{A)}, Motozima S.^{B)}, Hattori T.^{C)} and Takeuchi S.^{D)}

A) Faculty of Liberal Arts Nagasaki University, Nagasaki 852, Japan

B) Faculty of Engineering, Gifu University, Gifu 501-11, Japan

C) Toagosei Chemical Industry Co., Ltd., Nagoya 455, Japan

D) Institute for Solid State Physics, University of Tokyo, 106, Japan

Morphology of regularly coiled whiskers of amorphous Si_3N_4 grown by chemical vapor deposition on a quartz or graphite substrate coated with iron impurity has been examined by scanning electron microscopy. The typical diameter and the pitch of the coils are $10\mu\text{m}$ and a few μm , respectively. Various features of the growth morphology suggest a VLS mechanism of the whisker growth. The coils have been elongated with a special tensile device and observed by SEM. It was found that the coils can be elongated elastically up to three times of its initial length, indicating an excellent spring character of the coils. τ_{max}/G value (τ_{max} : the maximum shear stress in the coil; G : the shear modulus) reaches 0.035 at the fracture stress. Preliminary tensile tests of the coils to obtain load-elongation curves have also been performed using a special tensile device on an optical microscope.

Since silicon nitride (Si_3N_4) possesses high strength and toughness at high temperatures, Si_3N_4 whiskers have attracted much attention as a possible material for fiber reinforcement of high temperature structural materials. In previous papers [1,2], it has been shown that Si_3N_4 whiskers of a special shape, i.e. a regularly coiled helical shape, can be grown by a chemical vapor deposition (CVD) method. In the present paper, we present some morphological features of the coiled whiskers and their excellent spring character which has been measured by use of special devices.

Morphology of coiled whiskers

The details of the production method have been described in the previous paper [2]. Here we summarize the procedure only briefly. Si_3N_4 whiskers have been produced by a CVD method from a gas mixture of Si_2Cl_6 , NH_3 and H_2 on a quartz or graphite substrate coated with a metal as an impurity dopant. The best regularly-coiled whiskers have been obtained at 1200°C on a graphite

substrate with iron impurity. Figure 1 shows an example. The coil pitch is 2-5 μm and the coil diameter is 10-15 μm . The cross section of the whiskers is circular with a uniform diameter. The electron diffraction pattern from the whiskers, an example being given in the inset of fig. 1(b), shows a halo characteristic of amorphous structure. An interesting feature is that after having coiled 20-30 turns, most of the whiskers stopped coiling for a while and then continued coiling again. At several positions in a whisker, spherical droplet-like nodules are observed as indicated by Q in fig. 1(b). Although iron impurity was not detected in such nodules by EPMA analysis, these rounded nodules seem to be related to a VLS mechanism in the growth process of the coiled whiskers. Sometimes, another whisker grew into a coiled whisker as shown in fig. 2(a). The fact that the threading whisker has also a uniform diameter strongly suggests a VLS mechanism; in the case of direct vapor growth the diameter should be affected sensitively by the surrounding situation. In fig. 2(a), branching of the whisker is seen as indicated by X. The branching occurs also with almost the same diameter. This phenomenon is again difficult to be understood if this happens as a result of impingement of two vapor-growing whiskers, but can be understood if we assume that the branchings take place by a VLS mechanism at the droplet-like nodules as given in fig. 1(b). Figure 2(b) is a special case where the coil diameter is gradually decreased and the coil ends with a rounded tip, which also suggests a VLS growth mechanism.

We find both the right-handedly winding coils and the left-handedly winding ones with the same probability. We often find the whiskers whose winding

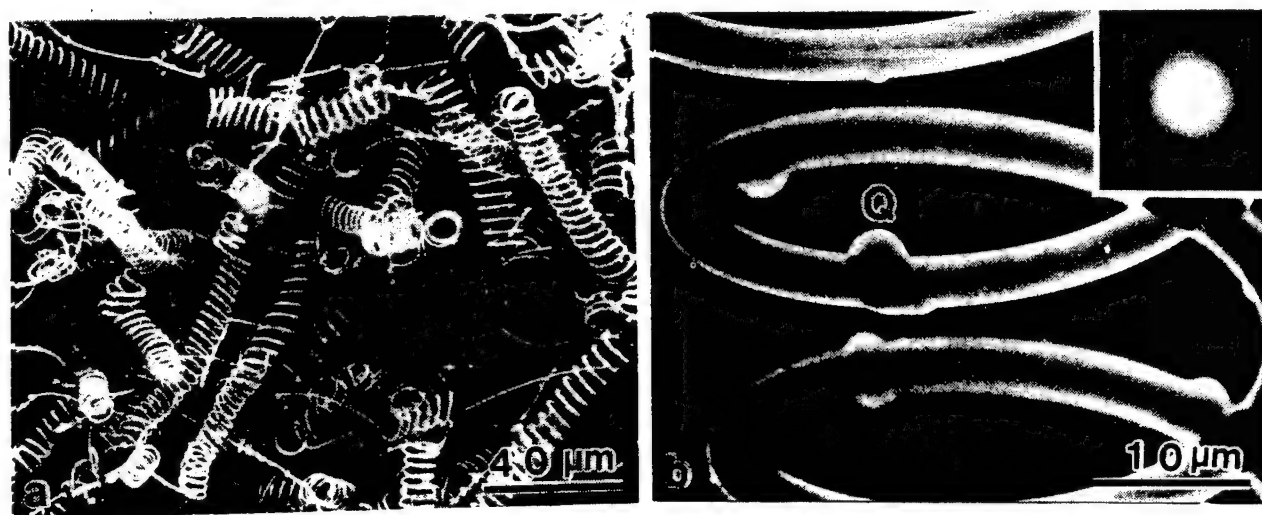


Fig. 1. (a) A SEM micrograph of regularly coiled whiskers grown on a graphite substrate with an iron impurity. (b) An enlarged view showing droplet like nodule Q on coiled whisker. Inset is the electron diffraction pattern.

direction changes several times during their growth, as shown in fig. 3. There is a joining point with a nodule at the point where the winding direction changes, as indicated by an arrow in fig. 3(b), and that the coil diameter is almost the same even if the winding direction changes. These observations would provide us with important suggestions as to the mechanism of the coiling of the whisker.

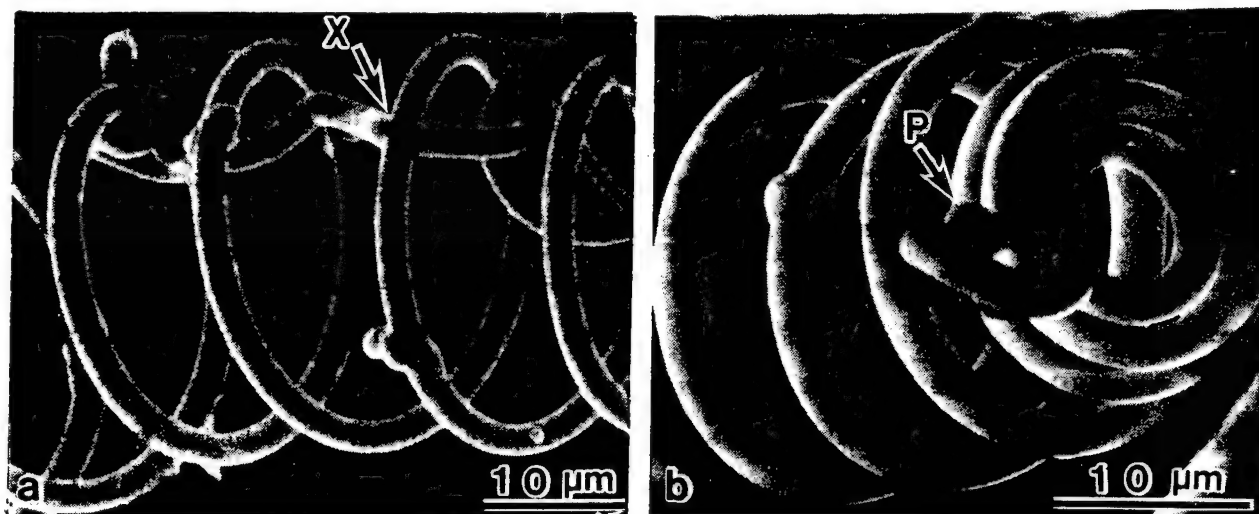


Fig. 2. (a) Branching and interpenetrating complex growth of whiskers. (b) A special shape of a coiled whisker with decreasing coil diameter. Note a rounded tip of the end of the whisker.

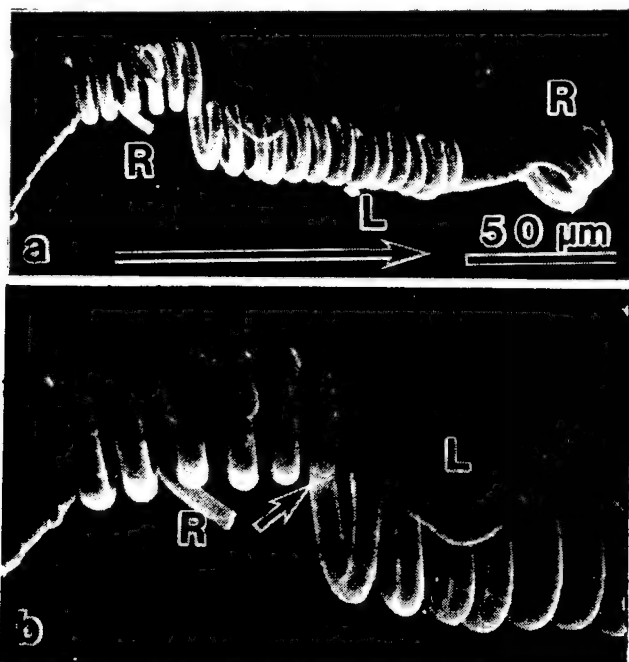


Fig. 3. (a) A SEM micrograph showing changes of winding direction in a coiled whisker. (b) An enlarged view showing a joining point with a nodule at the turning point indicated by an arrow. R and L mean the direction of winding.

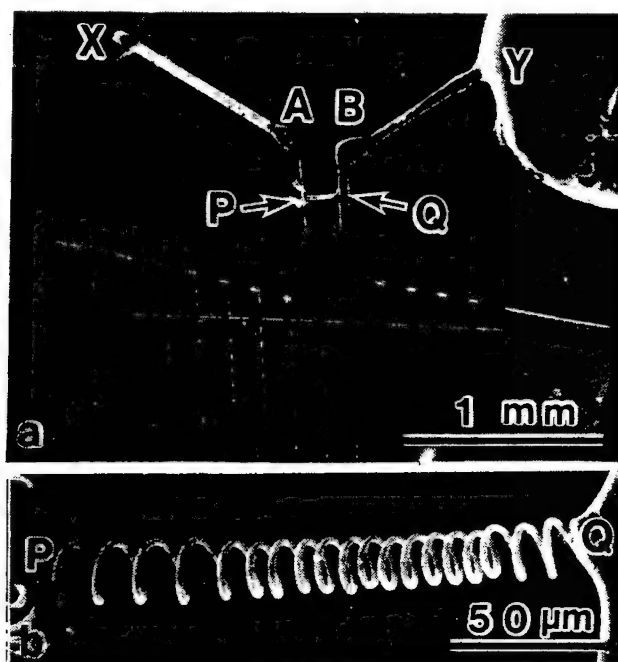


Fig. 4. (a) A special tensile device for coiled whisker, see the text. (b) An enlarged view of the specimen of which the two ends are glued at P and Q.

Mechanical properties

In order to clarify the spring characteristics of the coiled whiskers, we performed two kinds of tensile experiments by using special devices: one is the observation of large elongation of the coils by SEM and the other is the tensile tests under an optical microscope.

In the first experiment, we at first cut a usual parallel-grid metal mesh for TEM observation into the shape shown in fig. 4(a), where the mesh was cut in a half leaving two long filaments of the grid. To the points P and Q on the two long filaments we glued a coil specimen as shown in fig. 4(b), and to the top ends of the filaments A and B we glued thin metal wires. These metal wires were then fixed to supports by an adhesive at X and Y. These points are separated step by step and the stretched coiled whisker was observed by SEM at each step. Figure 5 shows an example of the results. Values X given in the figures indicate the coil length with respect to the initial length. In this particular case, the coil fractured at $X=2.2$. Figure 5(e) shows the coil after the fracture. By comparing the distance of two nodules A and B on the coil between the initial state (a) and the final fracture state (e), it is found that no plastic deformation took place during stretching until fracture. Figure 6 shows an enlarged view of the fracture point. We see the nodule B near the fracture point, meaning that the fracture was initiated at the stress concentration site at the nodule. It is found that the fractured surface is oblique to the growth direction. When a coil is elongated, a torsion stress is exerted to each part of the specimen. In the torsion stress of a wire, maximum tensile stress component is 45 deg to the torsion axis. Thus, fig. 6 indicates that the fracture took place almost along the maximum tensile stress plane, which is the usual case in brittle materials. According to the elasticity theory, the ratio of the maximum shear stress acting at the surface of the whisker, τ_{max} , to the shear modulus of the material G is given by the following equation:

$$\tau_{max}/G = d\delta / (4\pi nr^2)$$

Here, d is the whisker diameter, r the coil diameter, δ the amount of elongation and n is the number of turns. In the case of fig. 5, τ_{max}/G value at the fracture stress is calculated to be 0.023. In a thinner whisker, the τ_{max}/G value is as large as 0.035, which is extremely high value.

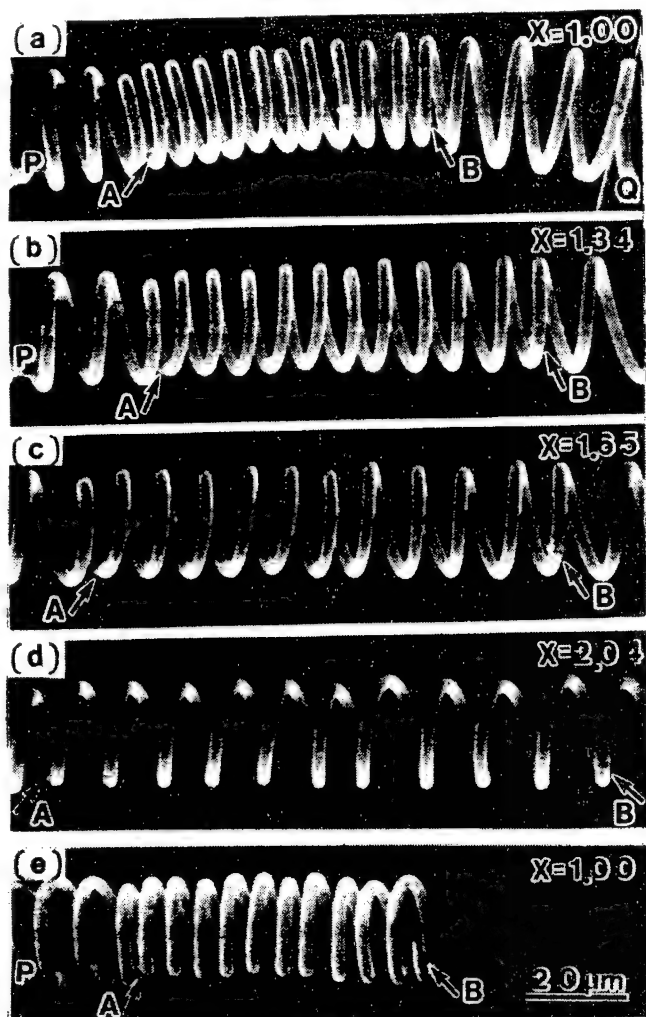


Fig. 5. A series of SEM micrographs showing elongation of a coiled whisker.

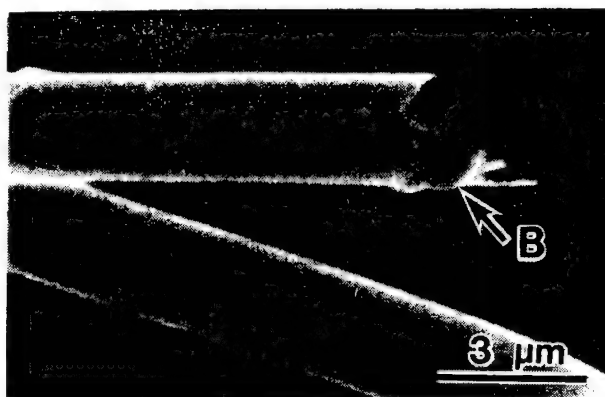


Fig. 6. Shape of fractured point of a coiled whisker. Note the existence of a small nodule indicated by an arrow.

In the tensile experiments on an optical microscope, load was applied by a weight, which was actually a piece of cover glass in our experiments. The weight was connected to one end of a coil specimen of which the other end was fixed. By inclining the optical microscope gradually together with the microscope stage on which the specimen with the weight was placed, the weight was slid on a slide glass by the gravity to apply a load on the specimen. Alumina powder was used as a lubricant between the weight and the slide glass. The threshold inclination angle of the microscope for initiation of sliding of the weight is 20-25 deg, which corresponds to the static friction coefficient of 0.35-0.5. Figure 7 shows optical micrographs of a coil under tensile test on the microscope stage. The specimen fractured in this case at the inclination angle of 55 deg at which the elongation $\delta = 80 \mu\text{m}$. In fig. 8, we plot load elongation relation for the case of fig.7. Here the load was estimated on the

assumption of the constant friction of 0.35 or 0.5. The calculated shear modulus from the slope of the load-elongation relation is $G=13-16 \times 10^3 \text{ kg/mm}^2$. More details of the tensile tests of the whiskers will be reported in the near future.

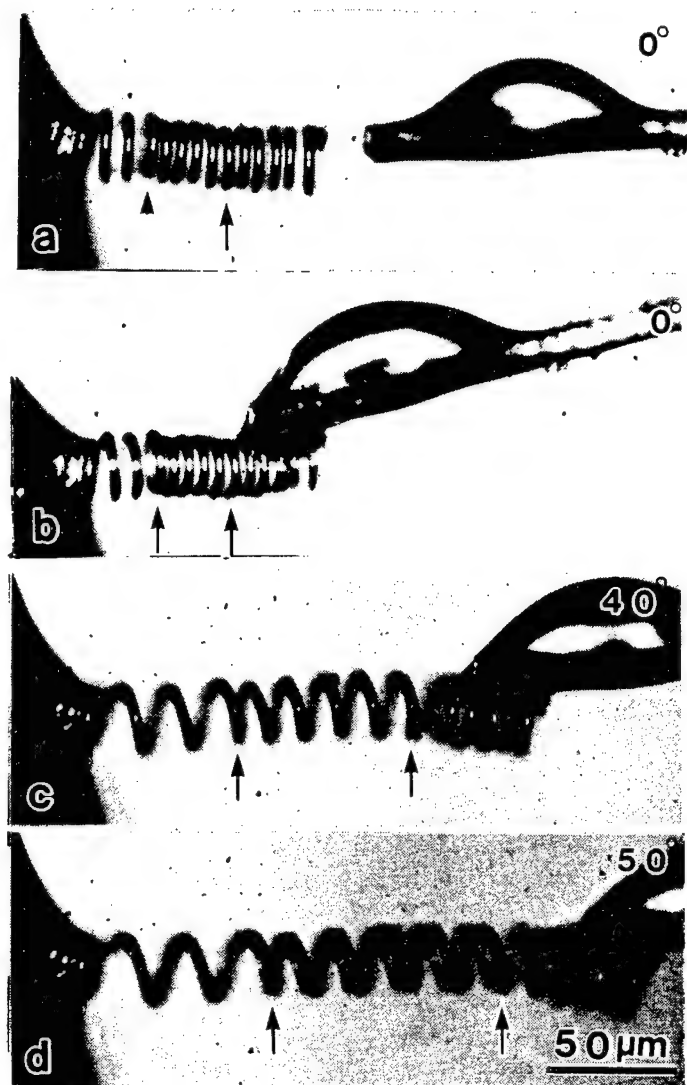


Fig. 7. A series of optical micrographs showing elongation of a coil during tensile experiment. (a) and (b) show the initial state. (c) and (d) are in inclined angles 40° and 50° respectively.

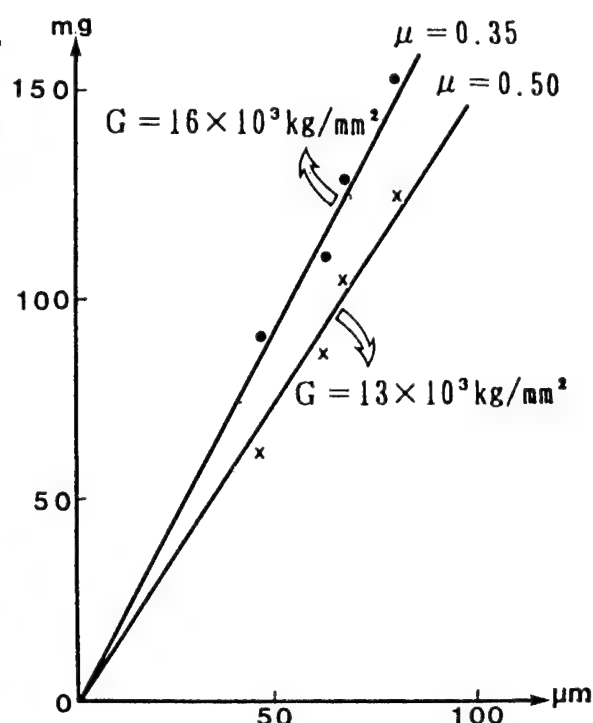


Fig. 8. Load-elongation relations assuming a constant friction coefficient of 0.35 or 0.5.

References

- [1] S. Motojima, S. Ueno, T. Hattori and K. Goto: Appl. Phys. Lett. 54 (1989) 1001.
- [2] S. Motojima, S. Ueno, T. Hattori and H. Iwanaga: J. Crystal Growth 96 (1989) 383.

DYNAMIC FATIGUE PROPERTIES OF MULLITE SILICA FIBER CERAMICS

Yonemura M., Kusuda T. and Wakamiya M.*

LSRC, AVRC* Matsushita Electric Ind. Co., Ltd
3-15, Yagumo-nakamachi, Moriguchi, Osaka, 570, Japan

Dynamic fatigue properties of a Mullite silica fiber ceramics developed for the material of diesel particulate filter were examined by tensile strength test in the temperature range of 25°C to 600°C. It became clear that the tensile strengths and the fatigue parameters of 61 to 72 varied little in that temperature range, but decreased with increasing of water vapor pressure. The Mullite silica fiber ceramics is advantageous to the thermal stress design from the viewpoint of filter durability.

INTRODUCTION

Regulation of diesel particulate emission is discussed in various countries, which has already started and is scheduled to become more stringent in the U.S.A.. In order to meet with this situation, we have developed diesel particulate filter of corrugated honeycomb fabricated with the Mullite silica fiber ceramics and regeneration systems using the filter, in which diesel particulates are collected to incinerate repeatedly.¹⁾²⁾ Both the filter and the regeneration system need durability of more than 10^5 vehicle kilometers as the diesel engine does. Therefore, it is necessary to estimate durability of the filter material under applied stress. A major portion of stress is constituted by thermal stress primarily caused by the temperature gradients both in radial and axial directions during regeneration. Fracture mechanics is an useful means to predict the above-mentioned durability for the filter material.

This work describes fatigue data and the durable stress design of the filter by taking fatigue degradation into account.

In fracture mechanics based on Griffith flaw propagation, dynamic fatigue test is available method to characterize the properties of material. The relation described in dynamic fatigue is given by

$$\sigma = \sigma_0 \{1 - (n+1)\} \quad \text{--- (1)}$$

where σ , $\dot{\sigma}$ and n denote the strength, the stress rate and fatigue parameter respectively. Fracture mechanics also describes the relationship between dynamic fatigue, static fatigue and n , as is given by

$$\frac{\sigma_s}{\sigma_d} = \left(\frac{1}{n+1} \cdot \frac{t_d}{t_s} \right)^{1/n} \quad \text{--- (2)}$$

where σ_s and σ_d are the applied static strength and dynamic strength, t_s and t_d are the times to failure of static and dynamic strength respectively.

The optimized condition of diesel filter design can be obtained by the application of these equations. In other words, the fatigue parameter n obtained by dynamic fatigue gives the calculation of maximum allowable stress for any required failure time. The durability of the filter will be forecasted afterwards.

EXPERIMENTAL PROCEDURE

A Mullite silica fiber ceramic sheet was prepared to measure the fatigue properties, which was 0.5mm thick. Test specimens were cut off to be rectangle of 13mmX45mm, followed by making notches of radius 3mm at each center of the long side. The both short sides of the specimen were sandwiched by alumina plates and bonded by an inorganic adhesive, as shown in Figure 1.

The tension test machine (CATY-2000YL) with a infrared furnace was used for measurement. All dynamic fatigue data were obtained by tensile strength test at each of the four temperatures; 25°C, 200°C, 400°C and 600°C. The stress rate was changed at each temperature in nitrogen atmosphere; 5.4MPa/s, 0.54MPa/s, 0.054MPa/s and 0.011MPa/s. The atmosphere was obtained by supplying

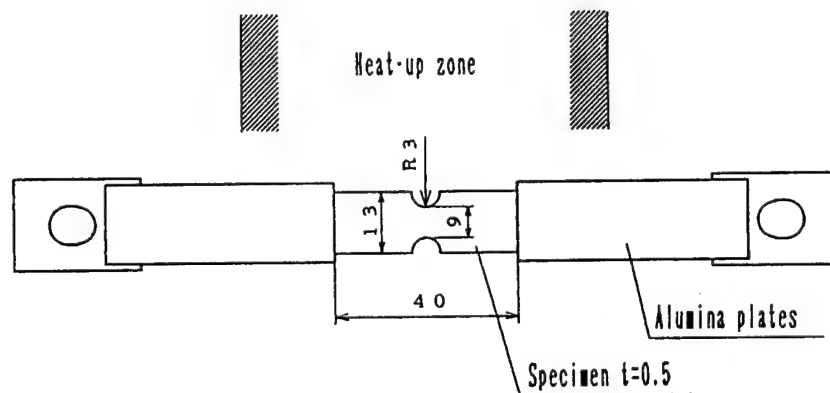


Fig.1 Specimen for tensile strength test.

nitrogen gas into the infrared furnace. The vapor pressure of nitrogen gas was 0.11kPa. Ten to sixteen specimens per rate were tested at each temperature. Effect of atmospheric water vapor on fatigue was also examined at 25°C by changing the vapor pressure from 0.11kPa to 3.17kPa (saturated vapor pressure).

RESULTS AND DISCUSSION

Data of the dynamic fatigue were characterized by Weibull statistics. In each tensile strength test, rupture was so fast that plastic flow region could not be specified. The results of the tensile strength test were listed in Table 1. The m values of 8.2 to 15.8 indicate that the tensile strength of the Mullite silica fiber ceramics exhibits narrow distribution in each temperature and stress rate. Little change in the filter strength is observed in the temperature range of 25°C to 600°C.

The n value is estimated from Eq.(1) by plotting the tensile strength vs. the stress rate on log-log axes. Figure 2 shows an example for a test temperature of 200°C. The n values listed in Table 1 were estimated using the method of least squares at each temperature. The n values of 62 to 71 suggest

Table 1 Tensile strength and fatigue parameter of Mullite silica fiber ceramics in nitrogen atmosphere

Temp. [°C]	Stress rate [MPa/s]	Strength (WEIBULL)		Fatigue parameter n
		parameter m	average [MPa]	
25	.011	10.2	2.89	62
	.054	10.2	3.04	
	.54	12.9	3.11	
	5.4	9.2	3.23	
200	.011	15.8	3.07	64
	.054	10.0	3.09	
	.54	10.6	3.19	
	5.4	12.8	3.37	
400	.011	9.0	2.95	71
	.054	13.4	3.15	
	.54	9.2	3.14	
	5.4	11.9	3.27	
600	.011	8.2	3.11	66
	.054	9.6	3.10	
	.54	12.5	3.29	
	5.4	11.5	3.37	

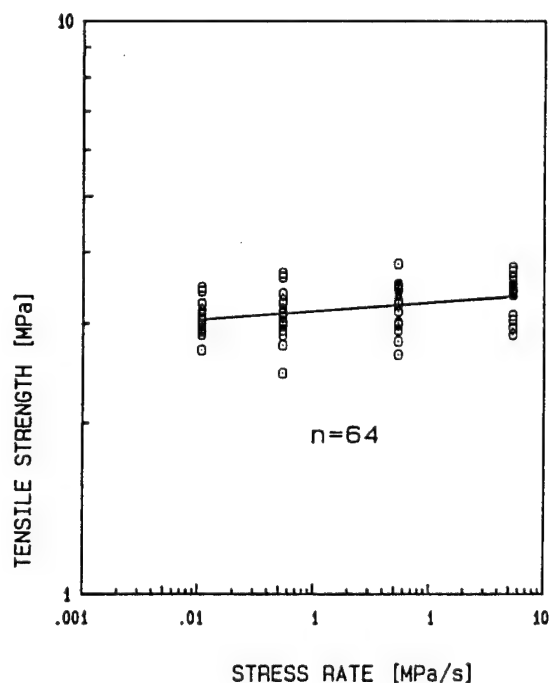


Fig.2 Relationship between tensile strength and stress rate of the Mullite silica fiber ceramics; at 200°C in nitrogen atmosphere.

that the similar fatigue behavior of the Mullite silica fiber ceramics is occurred in the temperature range of 25°C to 600°C. Almost all thermal stress is supposed to be occurred in the filter during regeneration in this temperature range.

The above-mentioned results suggest that the dynamic fatigue properties of the Mullite silica fiber ceramics can be represented by the data obtained at 25°C. The influence of water vapor on the tensile strength was also examined at 25°C in the similar manner, as is shown in Fig.3. The tensile strengths at all stress rates and the n values were decreased with the increasing the water vapor pressure from 0.11kPa to 3.17kPa. These behaviors are considered to be due to enhancement of stress corrosion cracking. The minimum n value of 33 was obtained at the water vapor pressure of 3.17kPa.

Durability forecast

As mentioned previously, the n value gives the allowable stress of the filter. That is, the maximum value of thermal stress occurred in the filter during regeneration can be derived for the required failure time from Eq.(2). In this case, the failure time of the filter was assumed to be equal to the cumulative time experienced the maximum thermal stress during regeneration.

Assuming half of regeneration period as the time applied the maximum thermal stress, 10^5 vehicle kilometers corresponded to 3×10^5 seconds cumulative time in our newly developed regeneration system. Considering the effect of water vapor in the actual usage, the minimum n value of 33 was chosen, which is larger than one of conventional ceramics. The durability forecast is shown in Fig.4, in which a failure time of 3×10^5 sec gives the ratio of σ_s/σ_a or about 0.7. If the regeneration system is designed for the thermal stress to be below 0.7 to the tensile strength, the filter is

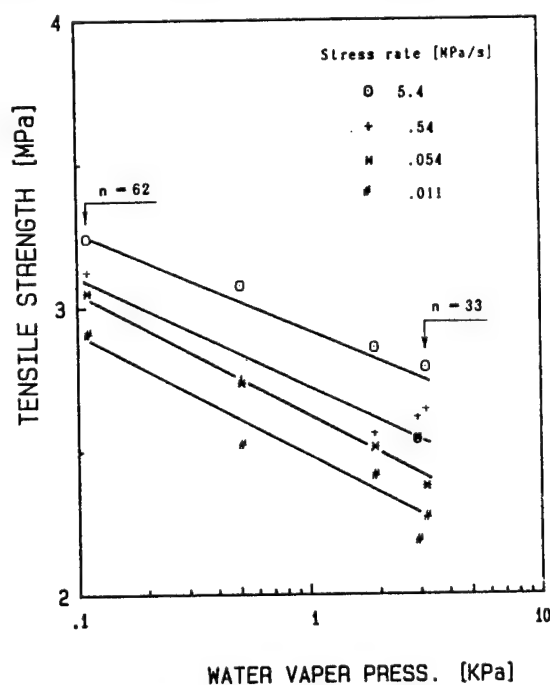


Fig.3 Relationship between tensile strength of the Mullite silica fiber ceramics and water vapor pressure for four stress rates at 25°C.

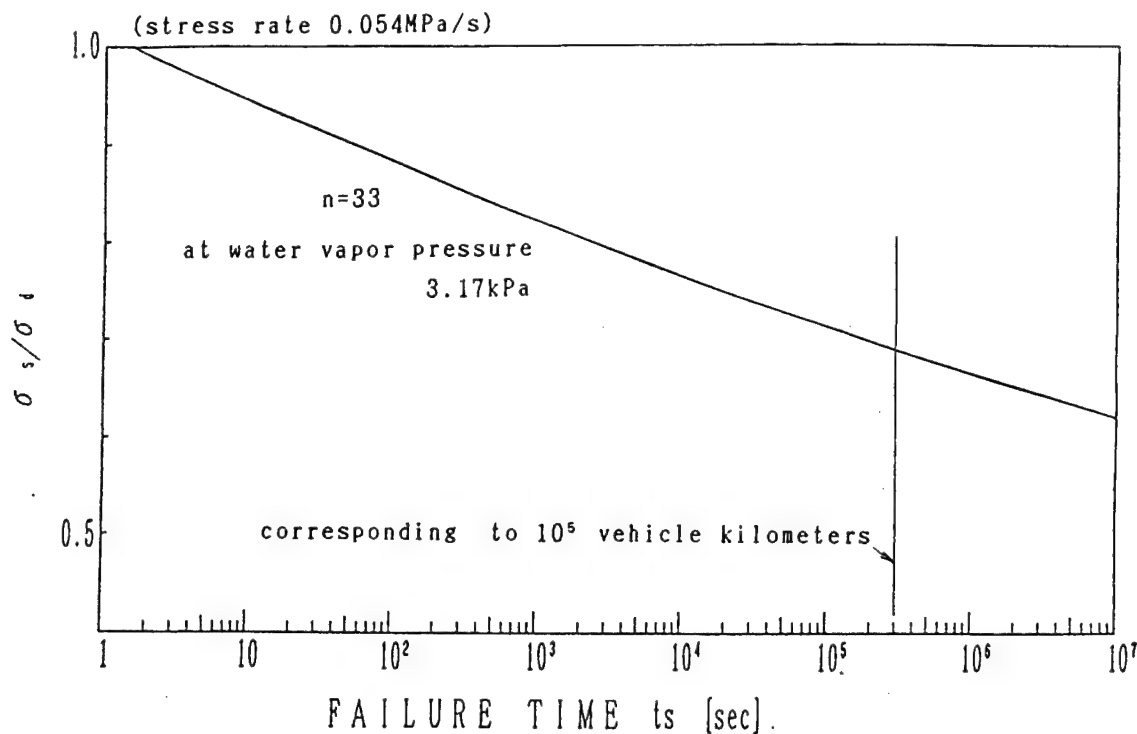


Fig.4 Failure time prediction of the Mullite silica fiber ceramics.

expected to be able to withstand 10^5 vehicle kilometers.

CONCLUSIONS

The dynamic fatigue properties of the Mullite silica fiber ceramics were investigated by the tensile strength test in the temperature range of 25°C to 600°C. The influence of water vapor on the properties was also examined at 25°C. Results are as follows:

(1) The Weibull parameters of 8 to 16 and the fatigue parameters of 62 to 71 was obtained for the Mullite fiber ceramics. In nitrogen atmosphere (water vapor pressure; 0.11kPa), these values vary little in the temperature range of 25°C to 600°C, in which the similar fatigue behavior is considered to be occurred.

(2) In existence of water vapor, both the tensile strength and the fatigue parameter were decreased with increasing water vapor pressure by stress corrosion cracking.

(3) On account of large fatigue parameter, the Mullite silica fiber ceramics has an advantageous feature in the thermal stress design during regeneration from the viewpoint of filter durability.

REFERENCES

- 1) T. Mihara et al., SAE Paper 860010; February, 1986.
- 2) T. Kusuda, M. Yonemura and H. Shimoda, National Tech. Rept. 34, 389-396(1988).

EVALUATION OF FRACTURE TOUGHNESS BY A SINGLE EDGE V-NOTCHED BEAM METHOD

Watanabe, T., Awaji, H., Yamada, T., Sakaida, Y.,
Tamiya, H., and Nakagawa, H.*

Japan Fine Ceramics Center, Mutsuno,
Atsuta-ku, Nagoya, 456, JAPAN

*Tottori Univ., Koyama-cho, Tottori,
680 ,JAPAN

1. Introduction

Structural ceramics has excellent mechanical properties such as high strength even at elevated temperature. Despite several advantages, ceramics is very sensitive to microscopic defects because of its low fracture toughness. Therefore, one of the primary subjects for the development of structural ceramics is how to evaluate its fracture toughness accurately. Among a number of techniques for evaluating fracture toughness of ceramics, the single edge precracked beam (SEPB) method^{1),2)} is regarded as the most reliable technique in Japan³⁾. The technique is based on the single edge notched beam (SENB) method, and takes advantages of the indentation technique. The procedure of the technique to create a precrack is as follows. A crack starter is made on the specimen surface along a line which is perpendicular to the specimen tensile axis. Vickers indents or a straight-through notch is suitable for a starter. Then radial cracks or a notch propagates unstably (pop-in) forming a precrack by a bridge indentation loading fixture¹⁾. Therefore, a very sharp precrack is created like natural defects. This technique, however, has a limit such that precrack making is difficult in some toughened ceramics and it needs to measure a precrack length on a fracture surface. In limited case, it is hard to measure a precrack.

On the other hand, the SENB method has been used widely because of its simple concept, simple procedure and applicability of wide variety of materials. But the fracture toughness evaluated by the SENB method depends on the notch root radius^{4),5)}.

The indentation strength (IS) technique¹⁰⁾ has also some advantages; it does not need to measure a precrack length on a fracture surface. But the fracture toughness depends on the indented load.

In this report, we propose a new SENB technique using a V-shaped notch with very sharp root radius to evaluate a fracture toughness of ceramics precisely. We made a special shaped diamond wheel for grinding the V-notch. Fracture toughness obtained by the SENB(V) technique for several kinds of ceramics are compared with the values measured by the SEPB method and the IS technique.

2. Stress distribution around a V-notch root

It is well established by the linear elastic fracture mechanics that the stress distribution around a crack tip has a square root singularity and is characterized by the stress intensity factor (SIF) exactly. Likewise, the stress distribution around V-notch has a singularity. For a finite plate with V-notch under tension, it is known that the distribution keeps the inverse square root property when the notch angle is below 30 degrees^{7),6)}. Then, the stress distribution around a V-notch is also characterized by the SIF explicitly.

A notch with finite root radius, has no singularity at the tip. However, the stress distribution around the tip can express by a SIF like a crack tip, by shifting the origin of the coordinates from the tip, 0, to the inside with $\rho/2$, 0', and by taking a distance r' instead of r to the point considered, as is shown in Fig. 1. The longitudinal (vertical) stress along the X-axis at the vicinity of the notch tip, $\sigma_{y,n}$ is expressed as follows,

$$\sigma_{y,n} = \frac{K_{I,n}}{(2\pi r)^{1/2}} \cdot \frac{1+\rho/r}{(1+\rho/2r)^{3/2}}, \quad 0 \leq r \leq \rho/2 \quad (1)$$

where, $K_{I,n}$ is a SIF for the notch, and ρ is a root radius. The SIF for the notch, $K_{I,n}$, depends on the notch root radius, and approaches the SIF for the sharp crack, K_I , as the notch root radius approaches zero. Therefore, it is expected that the fracture toughness would be evaluated precisely by the SENB method with a V-shaped notch of very sharp root radius, if the unstable fracture initiates in a similar way to that for a sharp precrack.

3. Grinding of V-notch

A specially formed diamond wheel has been developed for the purpose of grinding the above mentioned V-notch, as shown in Fig.2. The bonding material of this wheel is metal, the diamond grit size is under $12/25 \mu\text{m}$ (1000 mesh) and the concentration is 100 (4.4 carats/cm³), which was produced by Osaka diamond industrial Co., Ltd. The machine used for grinding V-notches was a computerised numerical controlled slicer equipped with hydrostatic air bearing and its workpiece table can be driven at minute speed.

Figure 3 shows the sectional profile of the ground V-notch on a silicon nitride specimen. The curvature of the root is $16 \mu\text{m}$. In this grinding, setting feed rate was under 1 mm/min, depth of cut in rough grinding was 1 mm per pass and in finishing 0.05 mm per pass.

4. Testing method and results

Specimen configurations were 3 width x 4 height x 40 (mm)length (referred as full size), and 3 x 4 x 20 (mm)(half size). The surface roughness of the specimen was less than 0.8S. Materials used were gas pressured sintering silicon nitride (NTK,EC-141), zirconia alumina composite(ZAC) (NTK,UTZ-20),

99.5% PLS alumina (NTK,KP-990), PLS silicon carbide (Showa Denko,Shoceram-C), TiC-Cr₃C₂ based composite (Fujikoshi) and three kinds of toughened zirconia; material A with Y₂O₃, material B with CeO₂, and material C with MgO.

Three-point bending procedure is used to measure fracture toughness. For the full size specimen, 30mm span was used. Wakai's equation⁸⁾ was suitable for the stress intensity coefficient. For the half size specimen, 16mm span and Srawley's equation⁹⁾ were used. Cross head speed was selected as 0.5mm/min.

As the starter of the precrack for the SEPB method, one 10kgf Vickers indent was used as a rule to avoid the effect of the residual stresses around the indent on the fracture toughness. The exceptions were the TiC-Cr₃C₂ based composite for which three 20kgf indents were used, and the toughened zirconia for which three 50kgf indents or shallow slit (0.1mm width and 0.5mm depth) were used. The precracks from the starter were introduced by the BI Precracker(Maruto). To introduce an unstably propagated precrack (pop-in crack), we cemented an AE sensor on the precracker which was connected with an oscilloscope to catch a start point of the pop-in crack. After precracking, a dye was permeated with acetone to improve the visibility of the precrack. The length of the precrack was measured by a optical microscope. Requirements for the precrack measurements were complied with ASTM standards (E399-81).

Fracture toughness obtained by the SENB(V) and SEPB method are in Table 1 and 2. Table 1 shows the results for the several kinds of structural ceramics on the market. In the table, n is number of specimens tested. The fracture toughness obtained by the SENB(V) method is lower than the ones by the SEPB method except for silicon carbide. The differences between the two methods are quite small except for alumina.

Table 2 shows the results for the toughened zirconia. The SEPB method did not work for the materials B and C, because the precrack did not propagate from the starter by the BI Precracker. The fracture toughness of the material A used 50kgf Vickers indents is smaller than others by its residual stresses around the indents.

Figure 4 shows the indented load dependency on the fracture toughness measured by the IS method for silicon nitride. Specimens had JIS-typed 3 x 4 x 40(mm) configuration. The values are higher than the one of the SEPB method, 5.8 MPam^{1/2}, and show a little dependence of the indented load. The IS method is regarded as a suitable technique, particularly under high temperature, because of unnecessary of measuring the precrack length. However, the precrack length is not enough to avoid the residual stresses around the indent, and the IS technique is based on a semi-experimental equation¹⁰⁾.

Figure 5 shows the results obtained at high temperature in vacuum for silicon nitride. The error bar in the figure shows a standard deviations of the fracture toughness. Four or five specimens were used at each temperature. The values of the SENB(V) method, which is shown by empty circle, are always lower a little than the ones of the SEPB method, shown by solid circle.

Takahashi et al^{11),12)} have obtained the relation of fracture toughness between a cracked specimen and a notched specimen as follows, based on a concept of the local fracture criterion¹³⁾ for unstable cleavage fracture. Their thought is that a cleavage cracks will propagate in an unstable manner when the local tensile stress at a point of the distance r_0 from the crack tip exceed a critical stress σ_0 . The relation of the stress intensity factor K_{Ic} is expressed as follows at a crack tip,

$$\sigma_0 = \frac{K_{Ic}}{(2\pi r_0)^{1/2}} \quad (2)$$

By the same manner, when the stress at the distance r_0 from a notch tip reaches to the critical value, a crack will propagate unstably from the notch tip. Then following relation is obtained from eq.(1),

$$\sigma_0 = \frac{K_{C,n}}{(2\pi r_0)^{1/2}} \cdot \frac{1+\rho/r_0}{(1+\rho/2r_0)^{3/2}} \quad (3)$$

where, $K_{C,n}$ is a critical stress intensity fracture of the notch. From Eqs.(2) and (3), the relation of the fracture toughness between a crack and a notch is shown as,

$$\frac{K_{C,n}}{K_{Ic}} = \frac{(1+\rho/2r_0)^{3/2}}{1+\rho/r_0} \quad (4)$$

The relation is expressed in Fig.6.

Table 3 shows the calculated ρ/r_0 and r_0 (assuming ρ is $16 \mu m$) from Eq.(4), using the evaluated $K_{C,n}/K_{Ic}$ ratio for each materials. In the table, grain sizes of some materials are also shown. The value of critical distance r_0 is almost the same as the grain size for silicon carbide and is about 6 times of the grain size for silicon nitride. Takahashi et al¹¹⁾ reported that the values of r_0 were almost 2 times of the grain size independently of the materials. Kishimoto et al¹⁴⁾ have mentioned that r_0 was about 6 times of the grain size for silicon nitride. From the table, critical distances r_0 seem to be depend on the aspect ratio of the grain size, on the characteristics of the grain boundary layer, or on the amount of stable crack growth.

The mark, Δ , in Fig.5 shows the modified fracture toughness of the SENB(V) method using eq.(4), where $6.0 \mu m$ is used as the critical distance r_0 . These modified values are agree quite well with the SEPB values independently on the temperature.

5. Conclusions

We have developed a single edge notched beam technique using a very sharp V-notch for evaluating fracture toughnesses of ceramics. The technique has several advantages such as simple procedures of testing, applicability to a wide variety of materials and suitability for high temperature testing. Results obtained by the technique agree quite well with the values of SEPB technique for several ceramics by using the modification proposed by Takahashi et al, except for alumina.

References

- 1) T.Nose and T.Fujii; J. Am. Ceram. Soc., 71 (1988),328
- 2) T.Sadahiro ; J. Japan Inst. Metals, 45 (1981),291 (in Japanese)
- 3) Japan Fine Ceramics Association; "Report on study of Standarization for fine ceramics" (1987,1988) (in Japanese)
- 4) T.R.Lai, C.L.Hogg and M.V.Swain ; ISIJ International, 29 (1989),240
- 5) C.Rief and K.Kromp; "Mechanical Testing of Engineering Ceramics at High Temperature" edited by B.F.Dyson et al., Elsevier Applied Science (1989)
- 6) H.Awaji, A.T.Yokobori,Jr. and T.Yokobori; Computers & Structures 22 (1986), 25
- 7) B.Gross and A.Mendelson; Int. J. Frac. Mech. 8 (1972), 267
- 8) F.Wakai, S.Sakaguti and Y.Matsuno; Yogyo-Kyokai-shi, 93 (1985), 479
- 9) J.E.Srawley ; Int. J. Fracture, 12 (1976),475
- 10) P.Chantikul, G.R.Anstis, B.R.Lown, and D.B.Marshall; J. Am. Crem. Soc., 64 (1981),539
- 11) I.Takahashi, S,Usami, K.Nakakado, H.Miyata and S.Shida; Yogyo-kyokai-shi, 93 (1985),30 (in Japanese)
- 12) S.Usami, H.Kimoto, I.Takahasi and S.Shida; Engng.Fract.Mech. 23 (1986),745
- 13) R.O.Ritchie, J.F.Knott and J.R.Rice ; J. Mech. Phys. Solids, 21 (1973),395
- 14) H.Kishimoto, A.Ueno, H.Kawamoto and S.Ura; J. Soc. Material Science, Japan, 38 (1989),32 (in Japanese)

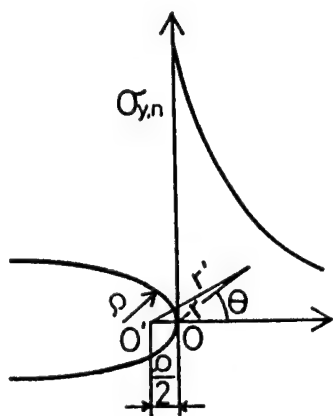


Fig.1. Coordinate around a notch tip.

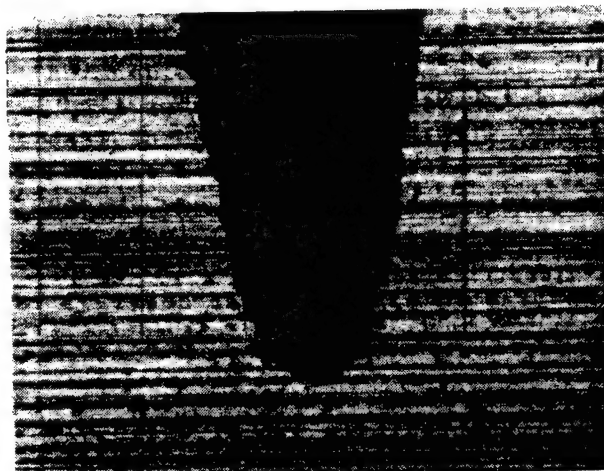


Fig.3. A feature of the V-notch for Si_3N_4 .

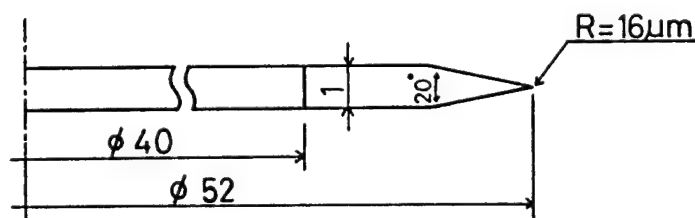


Fig.2. Special shaped diamond wheel for a V-notch.

Table 1. Fracture toughness obtained by SENB (V) and SEPB method. (MPa $m^{1/2}$)

Materials	SENB (V)	SEPB (indents)
Si ₃ N ₄	6.85±0.17 n=10 full	6.80±0.13 n=9 half
Z A C	6.54±0.18 n=10 half	6.55±0.18 n=8 half
Al ₂ O ₃	3.92±0.14 n=10 half	4.48±0.24 n=9 half
S i C	2.51±0.14 n=6 half	2.23±0.05 n=3 full
TiC-Cr ₃ C ₂	5.04±0.28 n=8 half	5.19±0.11 n=2 half

Table 2. Fracture toughness for toughened zirconias. (MPa $m^{1/2}$)

Materials	SENB (V)	SEPB (slit)	SEPB (indents)
A (Y ₂ O ₃)	7.03±0.07	7.11±0.10	6.88±0.27
B (CeO ₂)	7.62±0.07	unable	unable
C (MgO)	5.48±0.12	unable	unable

Table 3. Results of the SENB (V) Method. Ratio of the fracture toughness, $K_{c,n}/K_{ic}$ and a critical distance r_c .

Materials	$\frac{K_{c,n}}{K_{ic}}$	ρ/r_0	r_c (μ m)	Grain dia. (μ m)
Si ₃ N ₄	0.8741	2.71	5.9	1.2
Z A C	0.8885	3.20	5.0	—
TiC-Cr ₃ C ₂	0.8711	2.85	6.0	—
S i C	1.1258	5.88	2.8	2.6
* Si ₃ N ₄ (20°C)	0.8470	2.11	7.6	1.2
" (810°C)	0.9615	2.44	6.6	1.2
" (1000°C)	0.8593	2.40	6.7	1.2
" (1200°C)	0.8488	2.15	7.4	1.2

* in vacuum (10^{-6} ~ 10^{-5} torr)

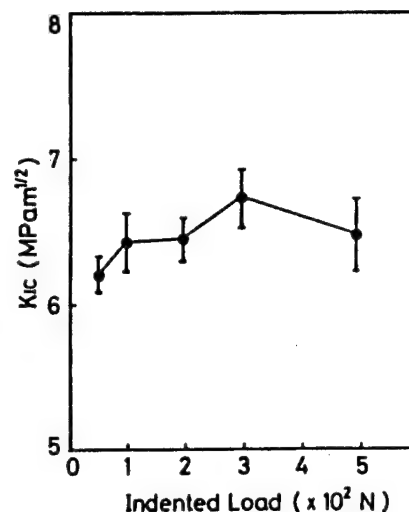


Fig.4. Indented load dependence on the fracture toughness.

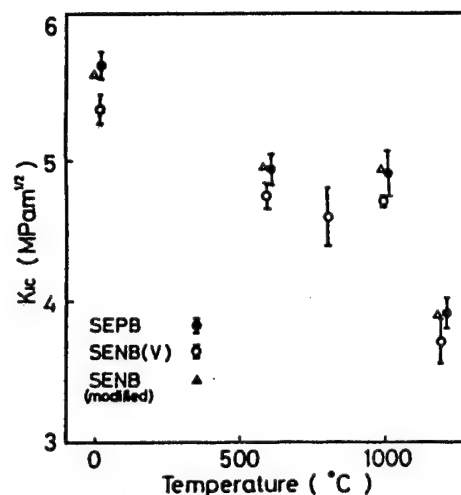


Fig.5. Fracture toughness at high temperature.

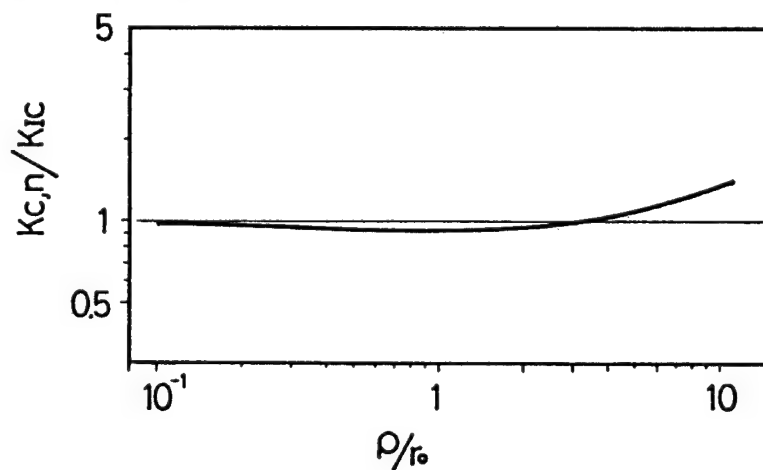


Fig.6. Relation between $K_{c,n}/K_{ic}$ and ρ/r_0 .

MULTILAYER CERAMIC CAPACITOR FABRICATION BY INFILTRATION PROCESS OF INTERNAL ELECTRODE MATERIAL

Moon G. Kim, J.W.Ko, Y.H.Kim*

Department of Inorganic Materials Eng., Seoul National Univ.
Seoul 151-742, Korea

* Fine Ceramic Materials Lab., KAIST
39-1 Hawueol.KOK-dong, Seongbuk-gu, Seoul 136-791, Korea

Abstract

Multilayer ceramic capacitor was fabricated by infiltration of liquid tin through porous NiO of which the surface was reduced to Ni. Observed morphology of fractured surface indicated a perfect infiltration of tin metal. The measured capacitance and dielectric loss factor imply that the infiltrated tin serves the purpose of internal electrode.

Introduction

There are mainly two methods for the fabrication of internal electrode of multilayer ceramic capacitor (MLC), i.e., the co-sintering of dielectric material and internal electrode material and the infiltration process of internal electrode material through porous layer after the sintering of the dielectric material[1-3].

The co-sintering method is commonly used for the fabrication of MLC. However the co-sintering method has some problems such that expensive noble metal like Ag-Pd alloy should be used to prevent the reduction of BaTiO_3 -based dielectric materials and the poor adhesion between dielectric layer and electrode layer often results in. In order to overcome the cost and adhesion problem the infiltration process has been invented. Although the cost of electrode materials is not a major factor for the fabrication of MLC since this process uses the relatively cheap and low melting metals like Pb-Sn alloy, more elaborated system is required to infiltrate the molten metal into porous layers. High pressure system is needed to push the molten metals into porous layers because the molten metals do not wet on the surface of ceramic dielectric materials.

Using the infiltration process for the fabrication of MLC a new method was tested in this study to infiltrate the molten metal not by high pressure system but by capillary rise of molten metal wetted on the surface of the porous layer material. To this end the surface properties of porous layer material should be altered to be wetted by the infiltrated molten metal. The porous layers can be formed by many methods such as the decomposition of inorganic salts or the burning of the mixture of organic binder and oxide materials. In any case the porous layer material should result in high porosity, mechanical stability, thermal stability at the sintering temperature of the dielectric materials, and reducibility at low enough temperature to prevent the reduction of dielectric materials.

In this study nickel basic carbonate, which decomposes to porous NiO, was selected as the precursor material for the porous layer material since the product, NiO is thermally stable at the sintering temperature (1200-1300°C) and is easily reduced to Ni of high surface energy in reducing atmosphere at low temperature. Wetting behavior of molten Pb, Sn, and Pb-Sn

alloy was tested by Sessile drop method[4]. Improved wetting with the alteration of surface properties made the infiltration possible under 1 atmosphere. The fabricated MLC by this infiltration process indicated good enough physical and electrical properties so that this method has the high potential for the commercialization.

Experimental

In this study two major experiments were carried out; i.e., wetting contact angle measurement and MLC fabrication by infiltration.

In order to test wettability of possible internal electrode materials on the surface of porous layer, reagent grade NiO powder was formed as the disk of 1/2 inch diameter and sintered at 1330°C for 2 hours, and then annealed at 500-800°C under the mixed gas of CO₂/CO (5:1).

Rectangular parallelepiped pieces of Pb, Sn, and Pb-Sn(37:63 wt%) were placed on the NiO disk of which the surface had been reduced. Heating the sample in an apparatus for infiltration process shown in Fig.1 formed liquid drop on the disk. The contact angle between liquid and solid was measured by silhouette technique[4].

The slurry for the dielectric layer and porous layer casting was prepared by mixing the powder and organic binders as is indicated in Table 1. Tape casting was used to form thin layer of dielectric materials on which the porous layer materials were to be screen-printed. After sequential stacking, laminating, and cutting, the green form was heated to burn-off the organic additives to 600°C with a heating speed of 30°C/hr. The calcined sample was sintered in air at 1200°C for 2 hours and annealed at 750°C in the gas mixture of CO₂/CO(5:1) for 2 hours. The molten liquid metals were infiltrated by dipping the evacuated sample in the apparatus shown in fig.1 MLC fabrication was completed with attaching the external electrode material(Ag-Pd paste) by heating at 850°C.

X-ray diffractometer (XRD), SEM, and Multi-Frequency LCR meter were used for the characterization of phases, morphology, capacitance, and dielectric loss factor.

Results and Discussion

The phase in the surface region of NiO disk was characterized by XRD after the reducing treatment at 700°C in CO₂/CO(5:1) gas mixture for 0.5, 1, 2, and 3 hours.

The samples reduced for more than 2 hours showed Ni XRD peaks in addition to the NiO peaks.

Fig.2 shows the wetting characteristics for low melting liquid alloys of Sn, Pb-Sn alloy and Pb. As seen in the figure Sn is most easily wetted with the smallest wetting angle.

After the infiltration at 310°C of Sn into the porous layer of sintered and reduced sample the sample was fractured to observe the cross sectional morphology and infiltrated tin distribution. SEM micrograph and tin mapping (Fig.3) clearly show the path and distribution of infiltrated tin. Measured capacitance for MLC having infiltrated tin inner electrode was about 70% of MLC capacitance calculated with the known relative dielectric constant, 1850 of the dielectric material used in this study.

The measured capacitance may reflect that the infiltrated tin plays perfectly as the internal electrode since the contact area covered by insulating NiO in the porous layer lineally reduces the capacitance. The measured dielectric loss factor for the MLC fabricated.

in this study was slightly higher than the one for the MLC fabricated by the co-sintering process. This higher loss factor might be resulted from higher conductivity of the infiltrated MLC due to a slight reduction of BaTiO_3 -based dielectric material at reducing stage.

Conclusion

MLC was successfully fabricated by infiltration of inner electrode material through porous layer without applying high pressure.

NiO , which is easily reduced to Ni having high surface energy, was found to be good porous material meeting the various criteria for the fabrication of MLC based on BaTiO_3 as the dielectric material.

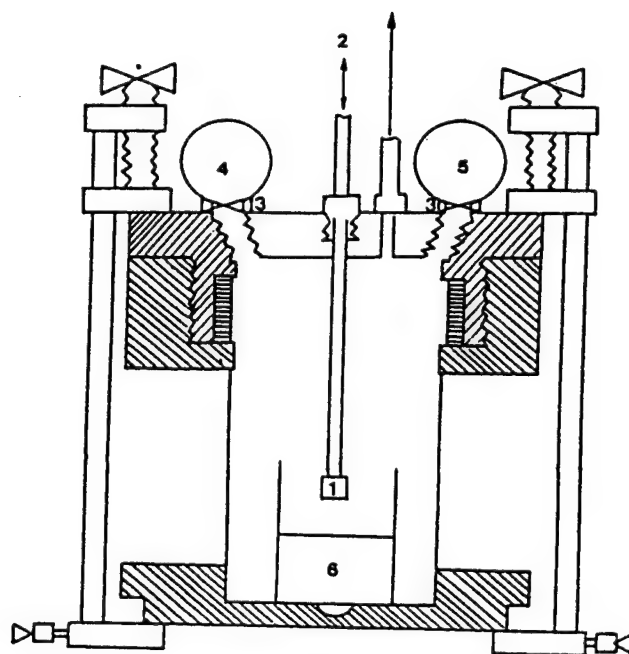
Among the tested liquid metals tin was most easily wetted and infiltrated through the porous layer of the NiO of which the surface had been reduced to Ni .

References

1. J.H.Alexander, D.A.Jackson, and E.L.Bush, "The Preparation and Properties of 4.7 μF 2220 size 50V Z5U Relaxor Multilayer Ceramic Capacitors," IEEE Trans. Comp., Hybrids, and Manufact. Tech., Vol. CHMT-9 [4], 468-469 (1986).
2. F.Goodenough, "Lead Electrodes Slash Field Failures for Multilayer Ceramic Capacitors," Electronic Design, 30[9], 35-37 (1982).
3. T.C.Rutt and J.a.Stynes, "Fabrication of Multilayer Ceramic Capacitors by Metal Impregnation," IEEE Trans. Parts, Hybrids, and Packaging, pHp[3], 144-147 (1973).
4. G.H.Zeising, "Determination of Surface Tension by Sessile Drop Measurements with Application to Mercury," Aust. J. Phys., 6[1] 86-95 (1953).

Table 1. Slurry compositions of dielectric and porous layer materials (unit:wt%)

Dielectric layer material	BaTiO ₃	Bi ₂ O ₃	Nb ₂ O ₅	TiO ₂	MuCO ₃	PVA	dibutyl phthalate	iso-butanol	metyl isobutyl Keton
	85.6	11.2	1.9	1.1	0.16	13.0	4.0	34.0	34.0
Porous layer material	2NiCO ₃ ·3Ni(OH) ₂ ·4H ₂ O			carbon black		PVA	dibutyl phthalate	iso-butanol	metyl isobutyl Keton
	80.0			20.0		25.44	33.54	20.51	20.51



- | | |
|-----------|-------------------|
| 1. sample | 4. vacuum guage |
| 2. rod | 5. pressure guage |
| 3. cock | 6. liquid |

Fig. 1. Apparatus for infiltration process.

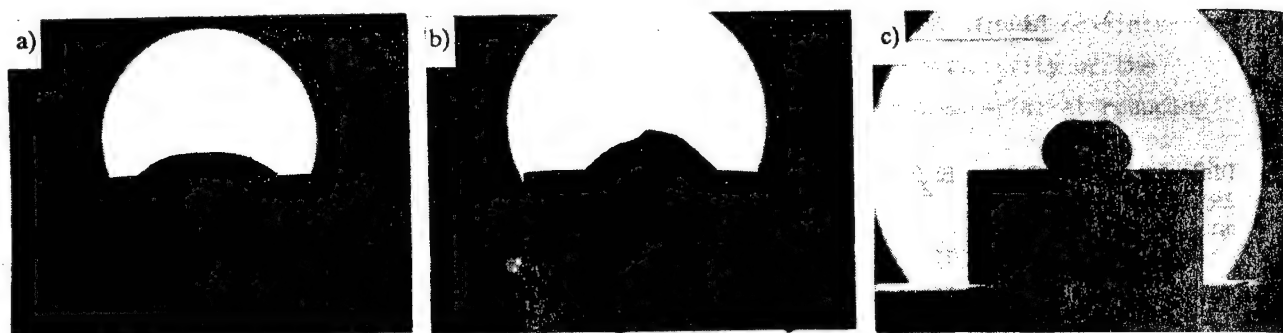


Fig. 2. Silhouette photographs of low melting liquid metals; a) tin, b) lead -tin alloy, and c) lead on smooth nickel substrate in Ar atmosphere reduced from nickel oxide for two hours at 700°C under the mixed gas of CO_2/CO (5:1).

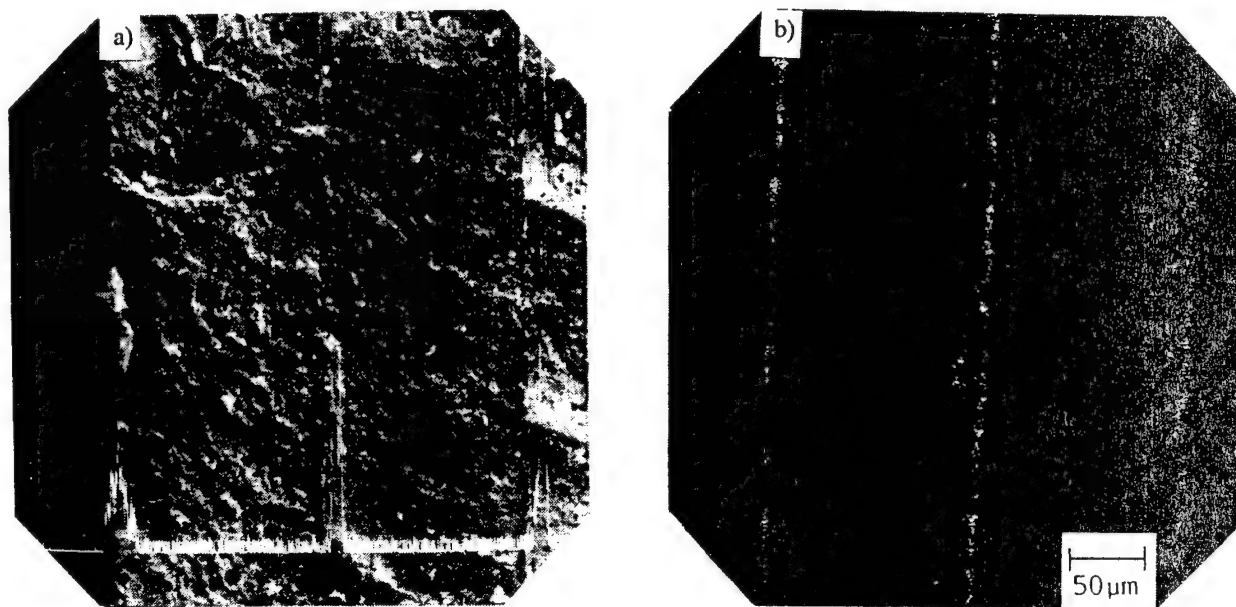


Fig.3. SEM micrograph (a) and tin mapping (b) of the fracture surface of tin-infiltrated MLC.

DIELECTRIC MATERIAL WITH RESISTANCE TO REDUCTION AND MULTILAYER CERAMIC CAPACITOR WITH COPPER ELECTRODE

KAGATA H. and KATO J.

Materials and Devices Research Laboratory,
Audio Video Research Center
YOKOTANI Y. and KUGIMIYA K.
Central Research Laboratory,
Matsusita Electric Industrial Co.,Ltd.,
Moriguchi,Osaka 570,Japan

A multilayer CERAMIC capacitor (MLC) with copper electrode has been realized by developing new dielectric material and unique fabrication process.

The dielectric material is Pb-based perovskite ceramics with a²⁺ site excess composition. It has high density when fired at the temperature below copper's melting point(1083°C) and has high resistivity even when exposed in the atmosphere of the equilibrium oxygen partial pressure of copper's oxidation at firing temperature.

The features of the MLC's fabrication process are to use copper oxide for the starting material of the inner electrode and to fire in the atmosphere controlled oxygen partial pressure.

In the obtained capacitor, the thickness of the dielectric layers was 17 micron meter, and the temperature characteristic of capacitance met to Z5U specification of EIA standards. Furthermore, it was stable under d.c. bias voltage and high a.c. field, and it was reliable at humidity load life test.

INTRODUCTION

Recently, in the MLC's market, the requirement for miniaturization and large capacitance has been growing rapidly. It is possible to meet the requirement by multiplying inner electrode layers. However, the cost of palladium used for present inner electrode is very high, then the cost of the capacitor becomes high when multiplying the inner electrode layers. Many efforts have been carried out for that problem.

One of the efforts is to use nickel for inner electrodes and modified BaTiO₃-based ceramics for dielectric materials¹. The BaTiO₃-based dielectrics have resistance to reduction. However, nickel is magnetic metal and the BaTiO₃-based dielectrics are not as stable as Pb-based dielectrics under d.c. bias voltage and high a.c. field.

The other one of the efforts is to use Ag-Pd alloy for inner electrodes and Pb-based dielectrics that can be sintered at low temperature². The Pb-based dielectrics are more stable under d.c. bias voltage and a.c. field than the BaTiO₃-based dielectrics. Additionally, Ag-Pd alloy can be fired in air. However, Ag migrates easily under d.c. bias voltage, and Ag-Pd alloy is more expensive than base-metal.

Nickel does not migrate easily, but the equilibrium oxygen partial pressure of its oxidation is lower than that of lead's oxidation. So nickel can not be fired with Pb-based materials. The equilibrium oxygen partial pressure of copper's oxidation is higher than that of lead's oxidation. Additionally, copper has low cost and low electrical resistivity. Therefore we have investigated to use the

copper for MLC's inner electrode³⁻⁵.

In this paper, we describe about the resistance to reduction of the Pb-based dielectrics that we have developed, the unique fabrication process of the MLC with copper inner electrode, and the influence that the process gives to the MLC's characteristics.

EXPERIMENTAL PROCEDURE

1. Measurement of electrical conductivity at high temperature

The composition of the dielectrics using for the measurement was a solid solution of $\text{Pb}(\text{Mg}_{1/3}\text{Nb}_{2/3})\text{O}_3$ - PbTiO_3 - $\text{Pb}(\text{Ni}_{1/2}\text{W}_{1/2})\text{O}_3$ ternary system. The curie point is near room temperature, and the temperature characteristic of the dielectrics meets to Z5U specification of EIA standards. We investigated two kinds of composition. One was chemical stoichiometric composition; (a) $\text{Pb}_{1.0}(\text{Mg}_{1/3}\text{Nb}_{2/3})_{0.8}\text{Ti}_{0.125}(\text{Ni}_{1/2}\text{W}_{1/2})_{0.075}\text{O}_{3.0}$, and the other one was a-site excess composition of perovskite adding calcium; (b) $\text{Pb}_{1.0}\text{Ca}_{0.03}(\text{Mg}_{1/3}\text{Nb}_{2/3})_{0.8}\text{Ti}_{0.125}(\text{Ni}_{1/2}\text{W}_{1/2})_{0.075}\text{O}_{3.03}$.

The calcined powder of the dielectrics was obtained as followed. Firstly, MgO and Nb_2O_5 powders were mixed and calcined at 1000°C to obtain MgNb_2O_6 . The obtained MgNb_2O_6 and other starting oxides or carbonate were mixed, calcined at 750 - 800°C for 2 hours, ground, and pressed into rectangles. The pressed bodies were put into MgO vessel with many amount of the calcined powder of same composition to prevent the vaporization of PbO , and then sintered in air. Sintering temperature was 1050°C for the composition (a) and 900°C for the composition (b). The sintering bodies were polished into rectangle of $10 \times 4 \times 0.6\text{mm}$, then electroded with platinum paste not containing glass frit.

One of that was fit to the device as shown in Fig.1, then inserted into a tube furnace. The electrical conductivities at high temperature were measured by four probe method. The oxygen partial pressure was monitored by oxygen sensor of partial stabilized zirconia set above the sample, and controlled by changing the ratio of CO_2 and CO gases in carrier N_2 gas.

By that method, we measured the change of electrical conductivity versus oxygen partial pressure at various temperatures from 700 to 925°C .

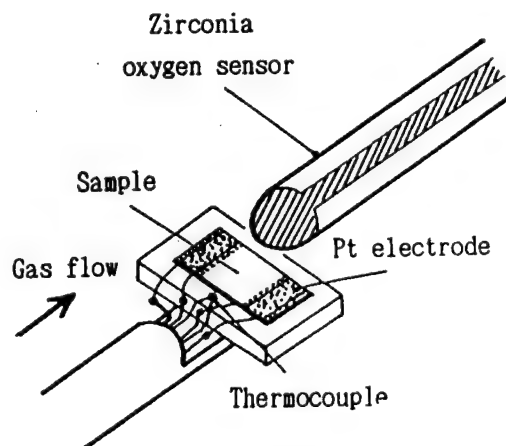


Fig.1 Device of measuring conductivity at high temperature.

2. Fabrication process of MLC

The calcined powder of the dielectrics was obtained as described before. The composition was $\text{Pb}_{1.0}\text{Ca}_{0.01}(\text{Mg}_{1/3}\text{Nb}_{2/3})_{0.8}\text{Ti}_{0.125}(\text{Ni}_{1/2}\text{W}_{1/2})_{0.075}\text{O}_{3.01}$. The obtained powder, butyral resin, and organic solvent were mixed to make slurry. After making green sheets

by doctor-blade method, the paste composed by CuO and ethyl-cellulose was printed on them, and they were laminated. Then they were pressed and cut into individual raw chips. The chips were burned out in air. If using copper metal for inner electrode paste, it is oxidized and expands during burning out in air, then the laminated bodies are broken. In the case of burning out in the atmosphere not to oxidize copper metal, the organic components are carbonized, then they reduces the dielectrics strongly during firing process. For that reasons, we have chosen the CuO paste for inner electrode. After that, the CuO of inner electrode in the chips was reduced to metal by heating at 600°C in the atmosphere of N₂ flow gas containing several hundreds ppm of H₂ gas. The chips were put in MgO vessels with covers, inserted into a tube furnace, and then fired at 1000°C. The oxygen partial pressure in the furnace was controlled by changing the ratio of H₂ and O₂ gases in carrier N₂ gas. The fired chips were coated with copper paste, and baked in N₂ gas to form terminations.

We investigated the influence that H₂ content in N₂ gas during reducing the inner electrode and partial oxygen pressure at firing gave to characteristics of obtained MLCs.

RESULTS AND DISCUSSION

Fig.2 shows a comparison of the conductivity change versus the oxygen partial pressure for stoichiometric composition (a) and a-site excess composition (b) at various temperatures.

In stoichiometric composition (a), with decreasing of the oxygen partial pressure, the conductivities decreased, then soon increased. That implies electrical conduction type changes from p-type to n-type. In a-site excess composition (b), there were the regions that conductivities did not change to oxygen partial pressures, therefore the oxygen partial pressure that n-type conduction appeared was shifted to lower than in stoichiometric compositions. The n-type conduction is due to electron formed by the oxygen removed from crystal lattice. It is considered that the a-site excess compositions has resistance to reduction, since the removal of oxygen is suppressed.

Fig.3 shows changes of the oxygen partial pressure that n-type

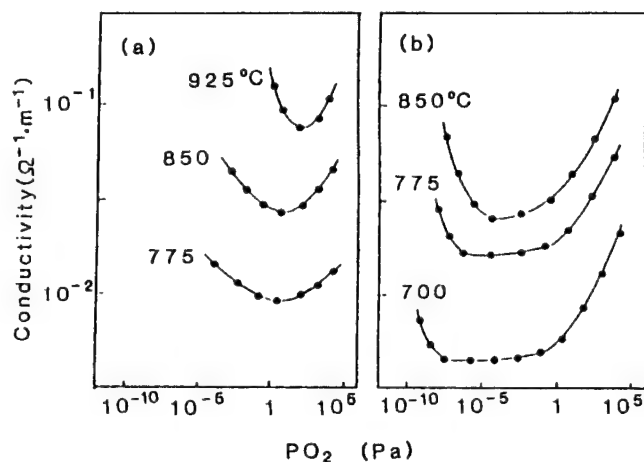


Fig.2 Change of conductivities to oxygen partial pressure at various temperatures.

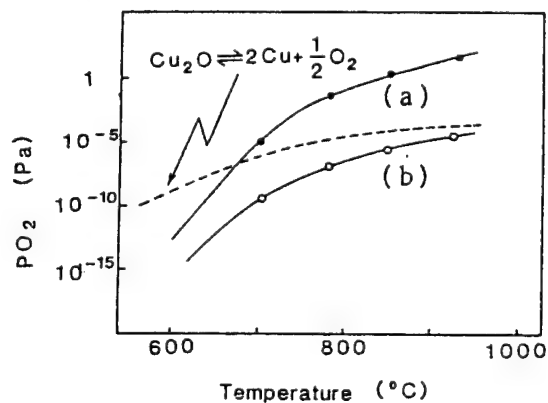


Fig.3 Temperature dependence of the oxygen partial pressure that n-type conduction appears.

conduction appeared to temperature for the composition (a) and (b). Simultaneously, equilibrium oxygen partial pressure of copper's oxidation is shown by dashed line. In a-site excess composition, the oxygen partial pressure that n-type conduction appears is in the region that metal copper is stable. The results show, exposing in the equilibrium oxygen partial pressure of copper's oxidation, the dielectrics with a-site excess composition doesn't show n-type conduction and keeps high resistivity. Therefore the dielectrics can cofire with copper electrode.

Fig.4 shows the capacitance and CR product of MLCs fired after reduced inner electrode to metal at various H_2 gas contents. In this experimental conditions, good characteristics were obtained when reduced at the H_2 gas content between 600 and 650 ppm. In order to reduce inner electrode to metal without reducing the dielectrics, it is necessary to control H_2 gas content exactly.

Fig.5 shows the capacitance and resistance of MLCs fired at various oxygen partial pressures after reduced through best condition. When fired at the oxygen partial pressure above 10^{-1} Pa, the capacitance and resistance became low. The reason is considered as follow. The inner electrode was partial oxidized and diffused to dielectric layers, since the oxygen partial pressure is higher than the equilibrium oxygen partial pressure of copper's oxidation during firing. Therefore, continuity and area of electrode was lost. When fired at the oxygen partial pressure below 10^{-5} Pa, the capacitance became low. The reason is considered as follow. PbO containing in dielectric layers is reduced to metal Pb, since the oxygen partial pressure is lower

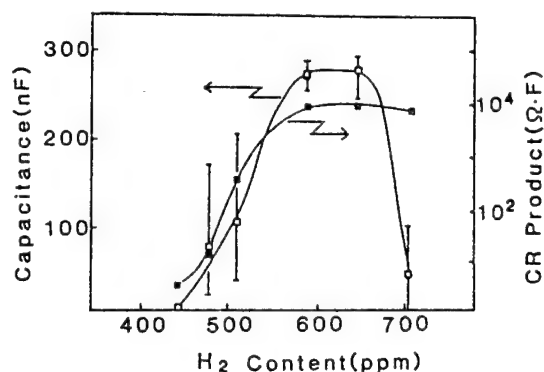


Fig.4 Relation between H_2 gas content of reducing inner electrode and obtained capacitance and CR product of the MLCs.

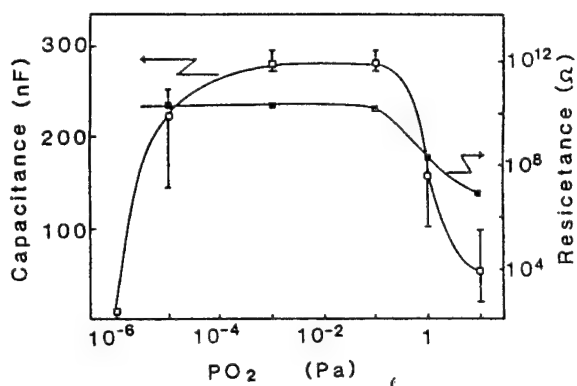


Fig.5 Relation between oxygen partial pressure at firing and obtained capacitance and resistance of the MLCs.

Table 1 Example of characteristics in the obtained MLC.

Capacitor size (mm)	3.2x1.6x0.7		
Number of layer	20		
Thickness of dielectrics (μm)	17		
Capacitance (nF)	280		
tan δ (%)	0.6		
Insulating resistance (Ω)	5×10^{10}		
CR product (ΩF)	14000		
Break down voltage (V)	>500		
Temperature coefficient of capacitance (%)	-25	20 °C	-14
	20	85	-52
Capacitance change rate under d.c. bias voltage (%)	15 V		+ 9
	25		-28
	50		-61

than the equilibrium oxygen partial pressure of Pb's oxidation during firing. The metal Pb contacted with inner electrode reacts with copper of inner electrode to form the liquid phase of Pb-Cu alloy, and then becomes segregated droplets. The best region of oxygen partial pressure at firing was between 10^{-4} and 10^{-1} Pa. It contains the region that expected by the results of Fig.3.

Table 1 shows an example of MLC's characteristics obtained through the best fabrication process. The MLC had good characteristics. The temperature coefficient of capacitance met to Z5U specification of EIA standards.

Fig.6 shows the change of capacitance with d.c. bias voltage and Fig.7 shows the change of capacitance and loss tangent under high a.c. field comparing with that of BaTiO₃-based systems. The both characteristics of the obtained MLC's were better than that of the BaTiO₃-based systems.

The equivalent serial resistance that obtained by measurement of frequency dependence of the impedance was about 22×10^{-3} ohm. Furthermore, in the humidity load life test of MLCs without molding, it was good reliability over 2000 hours. The migration as shown in Ag-based electrode was not observed.

SUMMARIES

- (1) The Pb-based dielectrics, that we had developed, had a-site excess composition, could be sintered below copper's melting point, and had resistance to reduction. They could cofire with copper.
- (2) We developed a unique process fabricating MLCs with copper electrode. It was the process that the printed CuO electrode was reduced to metal after burned out in air and then fired in the atmosphere controlled oxygen partial pressure.
- (3) The obtained MLCs had many excellent characteristics. They showed superiorities of copper and Pb-based dielectrics comparing with other materials.

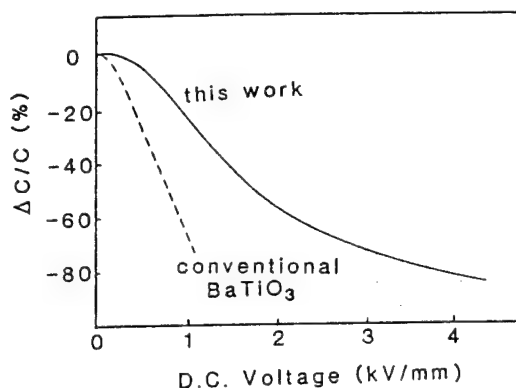


Fig.6 Capacitance change rate under d.c. bias voltage.

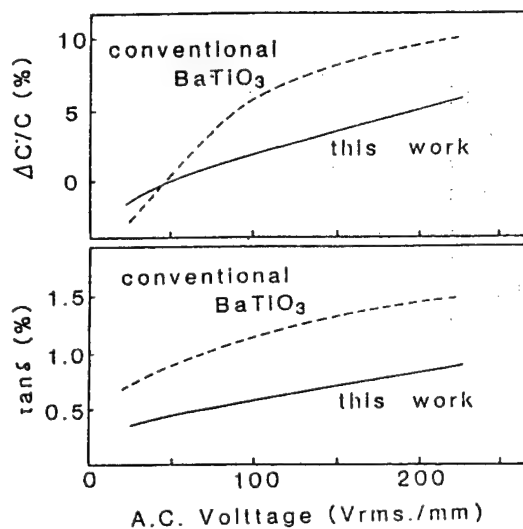


Fig.7 Capacitance change rate and loss tangent under various a.c. field.

REFERENCE

1. Sakabe Y., Minai K., and Wakino K., "High-Dielectric Constant Ceramics for Base Metal Monolithic Capacitors," Jap. J. Appl. Phys. 20 Suppl. 20-4 147-150 (1981).
2. Yonezawa M., Utsumi K., and Ohno T., "Properties of $\text{Pb}(\text{Fe}_{2/3}\text{W}_{1/3})\text{O}_3$ - $\text{Pb}(\text{Fe}_{1/2}\text{Nb}_{1/2})\text{O}_3$ Ceramics," Proc. 1st Meeting on Ferroelectric Materials and Their Applications pp.297-301 (1977).
3. Kato J., Yokotani Y., Kagata H., and Niwa H., "Multilayer Ceramic Capacitor with Copper Electrode," Jap. J. Appl. Phys. 26 Suppl. 26-2 90-92 (1987).
4. Kato J., Yokonani Y., and Kgata H., "Resistance to Reduction of a Lead-based Perovskite and Its Application to Multilayer Capacitor with Copper Electrode," to be published in Ferroelectrics (1989).
5. Kato J., Yokotani Y., Kgata H., Nakatani S., and Kugimiya K., "Dielectric Material and Fabrication Process for Multilayer Ceramic Capacitor with Copper Electrode," to be published in Proceedings of the Symposium on Ceramic Dielectrics and Capacitor-Related Topics (1989 Indianapolis).
6. Swartz S. L. and Shrout T. R., "Fabrication of Perovskite Lead Magnesium Niobate," Materials Reas. Bull. 17 1245-1250 (1982).

EFFECT OF EXCESS MgO ON THE DIELECTRIC PROPERTIES OF

$\text{Pb}(\text{Mg}_{1/3}\text{Nb}_{2/3})\text{O}_3$ CERAMICS

Kang D. H. and Yoon K. H.

Yonsei University, Department of Ceramic Engineering

134 Shinchon-dong, Seodaemun-gu, Seoul 120-749, Korea

The dielectric properties, such as dielectric constant, dissipation factor, tor, diffuseness coefficient, remanent polarization, coercive field, and phase analysis of lead magnesium niobate (PMN) ceramics have been studied as a function of the amount of excess MgO in the range of 0 to 90 m/o. With the addition of up to 5 m/o excess MgO, the pyrochlore phase was eliminated, and the dielectric constant increased greatly. However the dielectric constant decreased for greater than 10 m/o excess MgO even when no pyrochlore phase was found to be present. The dielectric constant decreased with increasing diffuseness of the phase transition.

Introduction

It is well known that the perovskite relaxor ferroelectric lead magnesium niobate (PMN, $\text{Pb}(\text{Mg}_{1/3}\text{Nb}_{2/3})\text{O}_3$) exhibits unusually high dielectric constants making it attractive material for various dielectrics and electrostrictive applications(1). However, reproducible fabrication of PMN ceramics is difficult due to the inevitable appearance of a stable pyrochlore phase ($\text{Pb}_3\text{Nb}_4\text{O}_{13}$, $\text{Pb}_3\text{Nb}_2\text{O}_8$, $\text{Pb}_2\text{Nb}_2\text{O}_7$ etc.). A number of methods have been tried to eliminate the pyrochlore phase (2,3). Moreover earlier studies have shown that the dielectric properties of PMN ceramics are generally influenced by ceramic fabrication processing, powder purity and composition (excess PbO, MgO contents) etc.(4,5,6)

In this study, PMN ceramics with both 40 m/o excess PbO and excess MgO in the range of 0 to 90 m/o were prepared and their dielectric properties and microstructures investigated with compositions.

Experimental

Ceramic specimens were prepared from reagent grade PbO, MgO and Nb_2O_5 powders. Compositions were selected so that the effect of excess MgO could be determined, as shown in Table 1. The fabrication process for PMN is referred to as the mixed oxide procedure, apart from the addition of excess PbO after the calcining step at 800°C for 4 hrs. Polyvinyl alcohol was added as a binder and the powder was cold-pressed into disks. Following binder burn out at 500°C , the pellets were sintered for 4 hrs. at 900°C (P-0 to P-7), but the 3PMN specimen with no excess PbO added (NP) was sintered at 1000°C . The pellets were buried in powder of the same composition to minimize material loss during sintering. The phase present in the sintered pellets were analyzed by X-ray diffraction pattern and the relative amounts of the pyrochlore phase and the perovskite phase were determined by measuring the major X-ray peak intensi-

ties for the perovskite and pyrochlore phases, (110) and (222) respectively, using the formula, (2)

$$\% \text{perovskite} = \frac{I_{\text{perov.}} \times 100}{(I_{\text{perov.}} + I_{\text{pyro.}})}$$

Polished and fractured sections were examined by a SEM equipped with an EDX. And etching with 5% HCl + 0.5% HF for 10 mins. were used to reveal the grain boundary. The mean grain sizes were determined by the linear intercept

method. For dielectric measurements were carried out using a LCR meter and the dielectric hysteresis loop were observed by using the Sawyer - Tower circuit.

Results and Discussion

Fig. 1 shows XRD patterns of 3PMN specimen and 3.4PMN series specimens. The phase present, density and grain size variation with compositions is also shown in Fig. 2. The formation of pyrochlore phase which mainly caused by the volatilization of PbO during sintering process was suppressed with excess PbO addition (Fig.1 (A),(B)). Furthermore the density and grain size increased slightly due to the liquid phase sintering as shown in Fig.1, 2.(7) The relatively large amount of pyrochlore phase (9%) present initially was eliminated completely above the 5 m/o excess MgO added PMN (Fig.1 (C)). No pyrochlore phase was observed with further addition of excess MgO. Such a complete elimination of the pyrochlore phase can be explained as a consequence of the compensation for poor dispersability and reactivity of MgO through the addition of excess MgO(4). In the compositions with higher than 70 m/o excess MgO, the MgO peak appeared as shown in Fig. 1 -(E).

In Fig. 2 shows that the density tends to increase with excess MgO nearly up to 5-10 m/o and then decrease sharply with increasing excess MgO. Also grain size increased to 3.4P1.05MN (8) and then grain growth inhibition occurred in PMN above 10 m/o excess MgO, which is shown in SEM photographs of the polished and etched surfaces in Fig. 3.

Table 1 Composition of Specimens

Specimen No.	Excess MgO	Composition
NP	0 (m/o)	3PMN
P-0	0	3.4PMN
P-1	2	3.4P1.02MN
P-2	5	3.4P1.05MN
P-3	10	3.4P1.1 MN
P-4	20	3.4P1.2 MN
P-5	50	3.4P1.5 MN
P-6	70	3.4P1.7 MN
P-7	90	3.4P1.9 MN

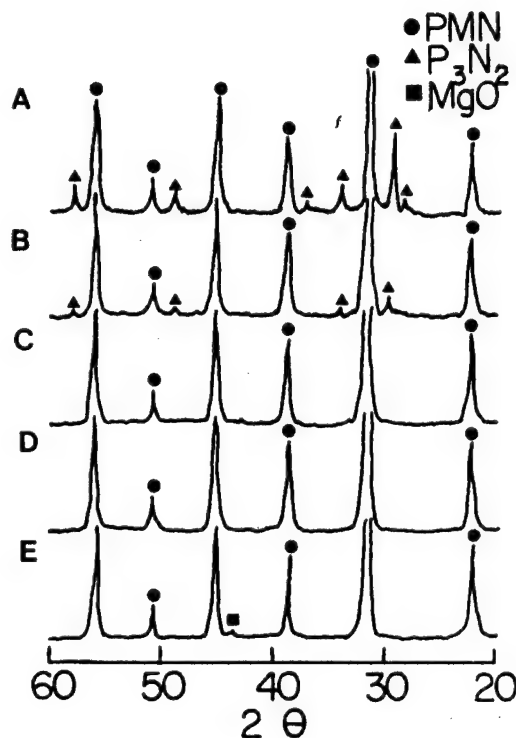


Fig. 1 XRD patterns of (A) 3PMN sintered at 1000°C, and (B) 3.4PMN, (C) 3.4P1.05MN, (D) 3.4P1.2MN, (E) 3.4P1.7MN sintered at 900°C.

We could not find a precipitated second phase when the excess MgO was added. However the fractured surfaces in Fig. 4 show the precipitated MgO rich second phase (b) which was analyzed by EDX. The reason for the increase of grain size up to 3.4P1.05MN is probably due to the fact that the pyrochlore phase distributed in grain boundaries was removed by the addition of excess MgO(4). But when the excess MgO exceeded 10 m/o, the grain growth was inhibited due to the precipitation of the MgO rich second phase(9).

The dielectric properties, such as K_{max} , $\tan \delta$, ϵ' , ϵ'' , P_r , and E_c with compositions are reported in Table 2. The increase in K_{max} with addition of excess PbO can be attributed to the decrease in the pyrochlore phase and the improvement in sinterability(7). However, the behavior of the dielectric properties in all of these compositions can not be simply explained by the pyrochlore phase, because the K_{max} decreased with the addition of MgO in excess of 10 m/o even no pyrochlore phase was found to be present. So in this work, the increase of K_{max} in the range of 0 - 5 m/o excess MgO can be explained by the increase of grain size, density and also the removal of the pyrochlore phase.

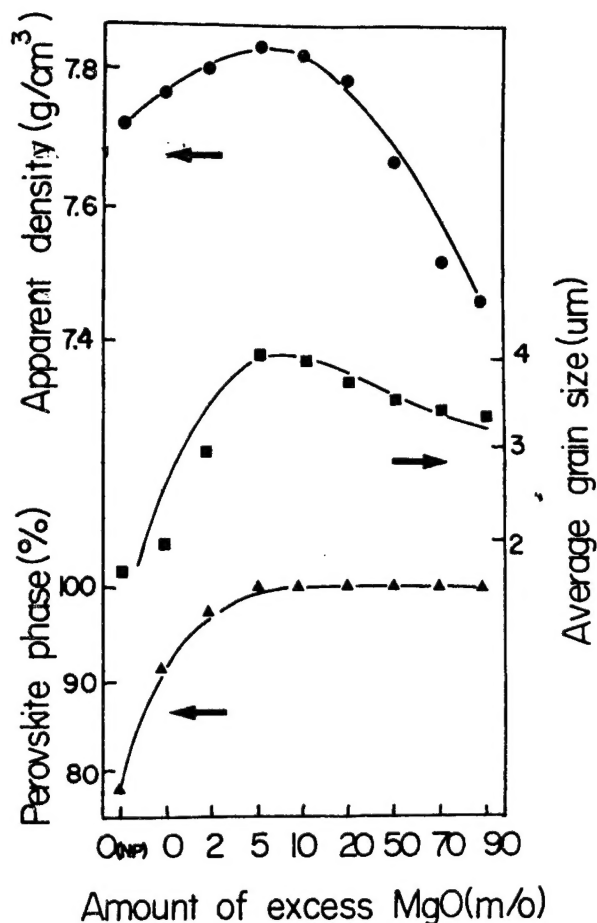


Fig. 2 Density, Grain size and Perovskite phase vs. amount of excess MgO in 3.4PMN series specimens.

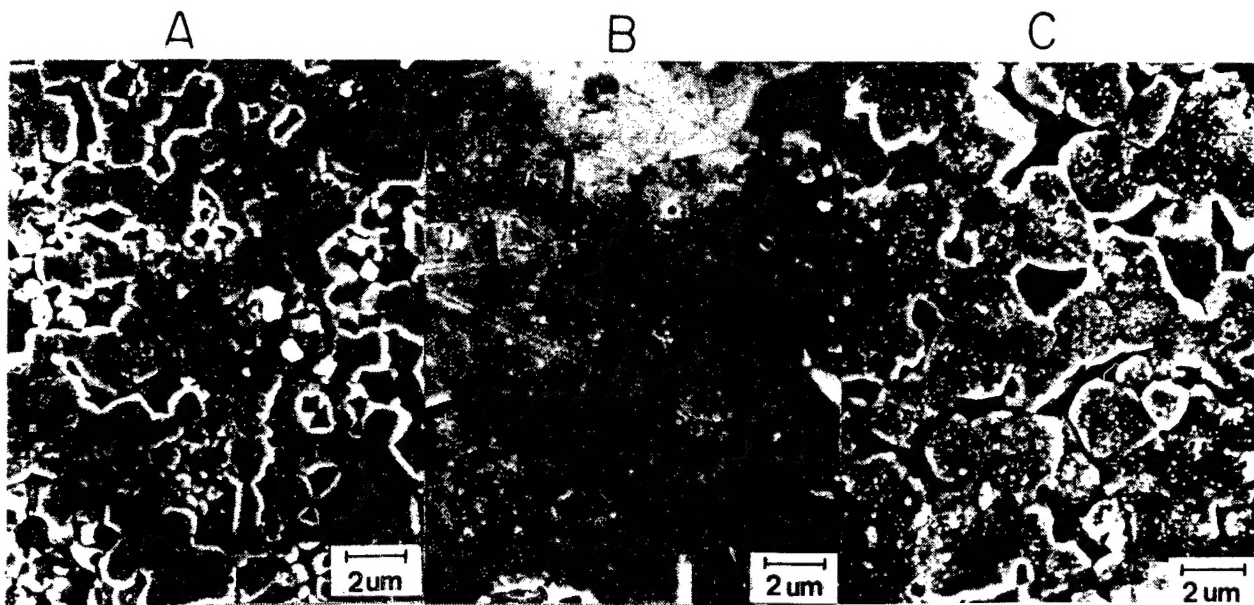


Fig. 3 SEM photographs of (A) 3.4PMN, (B) 3.4P1.05MN and (C) 3.4P1.7MN. (polished and etched)

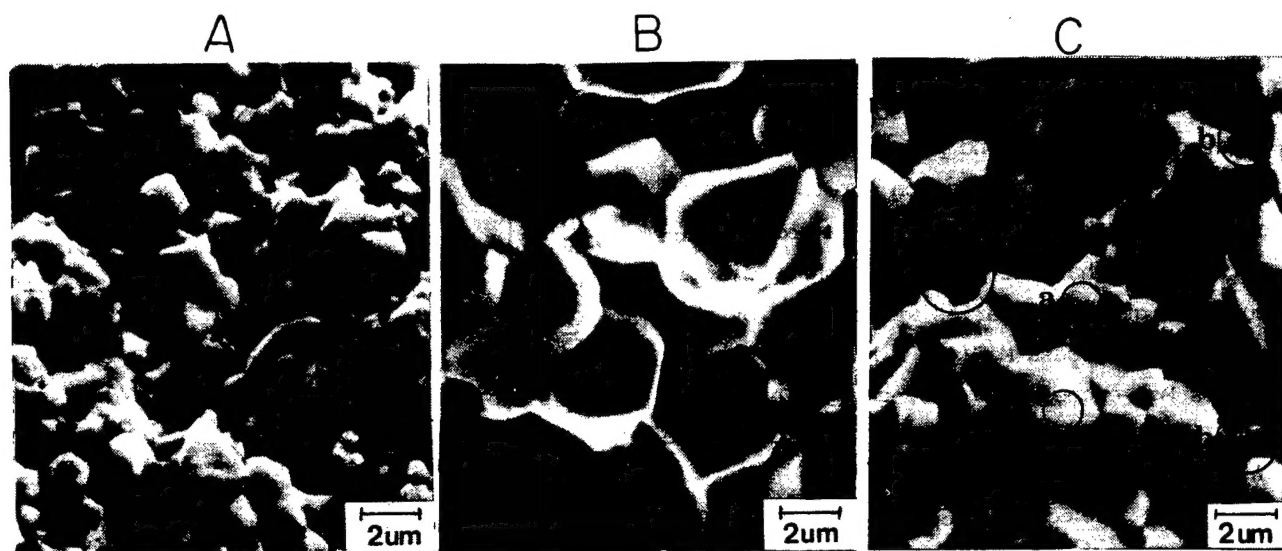


Fig. 4 SEM photographs of (A) 3.4PMN, (B) 3.4P1.05MN and (C) 3.4P1.7MN (fractured surfaces)
(a ; PMN matrix , b ; MgO rich second phase)

The grain size dependency is related to the relative volume of grain boundary with lower K (pyrochlore, MgO, PbO, impurities etc.), which is electrically connected in series with the bulk of the grain (8). For greater than 10 m/o excess MgO the decrease in K_{\max} is believed to be due to the decrease of grain size and density, especially the precipitation of the second phase as indicated in Fig. 4.

The value of $\tan \delta$ at 25°C increased slightly with increase in excess

Table 2 Dielectric properties of the PMN series specimens.

Specimen No.	K_{\max}	$\tan \delta_{25^\circ\text{C}}$	δ	P_r (uC/cm ²)	E_c (kV/cm)
NP	4500	0.006	81	5.1	4.4
P-0	10200	0.003	59	5.7	4.2
P-1	10800	0.002	55	6.2	4.2
P-2	13200	0.001	52.8	6.6	4.0
P-3	12500	0.001	53.4	6.4	3.92
P-4	12010	0.003	59.2	5.2	3.8
P-5	10780	0.002	61.6	5.3	3.95
P-6	10060	0.004	62.3	5.0	3.98
P-7	9980	0.004	63.4	5.2	4.1

MgO, which is related to microstructural losses arising from the precipitation of second phase and the decrease in density(3). The diffuseness coefficient(δ), which indicates the intensity of the diffused phase transition has been calculated and is presented in Table 2. The lower K_{\max} corresponded to an increase in δ . The P_r determined from the hysteresis loop near -40°C increased up to a composition of 5-10 m/o excess MgO addition and then decrease, which probably can be explained by the grain size effect(10). Also the value of the temperature coefficient of capacitance (TCC) for all compositions were found to be within the limits of Z5U capacitor specifications.

Conclusions

With the addition of up to 5 m/o excess MgO, the pyrochlore phase in PMN ceramics was completely eliminated. Also the dielectric constant and remanent polarization increased with increasing grain size and density. But for greater than 10 m/o excess MgO.

the dielectric constant decreased with excess MgO, mainly due to the increase in concentration of the precipitated MgO rich phase as the second phase, and decrease of density and grain size.

Acknowledgement

This work was supported by the Korea Science and Engineering Foundation.

References

1. G. A. Smolenskii and A. I. Agranovskaya, *Sov.Phys.Sol.State*, 1(10)1429 (1960).
2. S.L. Swartz and T. R. Shrout, *Mater.Res.Bull.*, 17, 1245 (1982).
3. M. Lejeune and J. P. Boilot, *Ceram.Inter.*, 9 (4) 119 (1983).
4. T. R. Shrout and A. Halliyal, *Am.Ceram.Soc.Bull.*, 66 (4) 704 (1987).
5. J. Chen, A. Gorton, H. M. Chan and M. P. Harmer, *J.Am.Ceram.Soc.*, 69 (12) C-303 (1986).
6. D. H. Kang and K. H. Yoon, *Ferroelectrics*, 87, 255 (1988).
7. M. Lejeune and J. P. Boilot, *Ferroelectrics*, 54, 191 (1984).
8. S. L. Swartz, T. R. Shrout, W. A. Schulze and L. E. Cross, *J.Am.Ceram.Soc.*, 67 (5) 311 (1984).
9. J. P. Guha, *J.Am.Ceram.Soc.*, 68 (3) C-86 (1985).
10. G. H. Haertling, *Am.Ceram.Soc.Bull.*, 43 (12) 875 (1964).

- END -

10

This is a U.S. Government publication. Its contents in no way represent the policies, views, or attitudes of the U.S. Government. Users of this publication may cite FBIS or JPRS provided they do so in a manner clearly identifying them as the secondary source.

Foreign Broadcast Information Service (FBIS) and Joint Publications Research Service (JPRS) publications contain political, economic, military, and sociological news, commentary, and other information, as well as scientific and technical data and reports. All information has been obtained from foreign radio and television broadcasts, news agency transmissions, newspapers, books, and periodicals. Items generally are processed from the first or best available source; it should not be inferred that they have been disseminated only in the medium, in the language, or to the area indicated. Items from foreign language sources are translated; those from English-language sources are transcribed, with personal and place names rendered in accordance with FBIS transliteration style.

Headlines, editorial reports, and material enclosed in brackets [] are supplied by FBIS/JPRS. Processing indicators such as [Text] or [Excerpts] in the first line of each item indicate how the information was processed from the original. Unfamiliar names rendered phonetically are enclosed in parentheses. Words or names preceded by a question mark and enclosed in parentheses were not clear from the original source but have been supplied as appropriate to the context. Other unattributed parenthetical notes within the body of an item originate with the source. Times within items are as given by the source. Passages in boldface or italics are as published.

SUBSCRIPTION/PROCUREMENT INFORMATION

The FBIS DAILY REPORT contains current news and information and is published Monday through Friday in eight volumes: China, East Europe, Soviet Union, East Asia, Near East & South Asia, Sub-Saharan Africa, Latin America, and West Europe. Supplements to the DAILY REPORTs may also be available periodically and will be distributed to regular DAILY REPORT subscribers. JPRS publications, which include approximately 50 regional, worldwide, and topical reports, generally contain less time-sensitive information and are published periodically.

Current DAILY REPORTs and JPRS publications are listed in *Government Reports Announcements* issued semimonthly by the National Technical Information Service (NTIS), 5285 Port Royal Road, Springfield, Virginia 22161 and the *Monthly Catalog of U.S. Government Publications* issued by the Superintendent of Documents, U.S. Government Printing Office, Washington, D.C. 20402.

The public may subscribe to either hardcover or microfiche versions of the DAILY REPORTs and JPRS publications through NTIS at the above address or by calling (703) 487-4630. Subscription rates will be

provided by NTIS upon request. Subscriptions are available outside the United States from NTIS or appointed foreign dealers. New subscribers should expect a 30-day delay in receipt of the first issue.

U.S. Government offices may obtain subscriptions to the DAILY REPORTs or JPRS publications (hardcover or microfiche) at no charge through their sponsoring organizations. For additional information or assistance, call FBIS, (202) 338-6735, or write to P.O. Box 2604, Washington, D.C. 20013. Department of Defense consumers are required to submit requests through appropriate command validation channels to DIA, RTS-2C, Washington, D.C. 20301. (Telephone: (202) 373-3771, Autovon: 243-3771.)

Back issues or single copies of the DAILY REPORTs and JPRS publications are not available. Both the DAILY REPORTs and the JPRS publications are on file for public reference at the Library of Congress and at many Federal Depository Libraries. Reference copies may also be seen at many public and university libraries throughout the United States.